Exploring variability in the luminescence properties of feldspars

Svenja Riedesel

A thesis presented for the degree of
Doctor of Philosophy

Department of Geography and Earth Sciences
Aberystwyth University
Wales, United Kingdom

September 2020

Abstract

Feldspars are the most abundant minerals in the Earth′s crust and they have the ability to store charge within defects in their crystal lattice over geological time scales. This allows their use as natural dosimeters in luminescence dating studies, which enables chronologies of past geomorphological, geological and archaeological events to be established.

Despite the routine use of feldspars in luminescence dating studies over the past decades, many key questions regarding the physical processes leading to luminescence of feldspars remain unanswered. For example, the crystal defects functioning as electron trapping centres in feldspars are still unknown, and the causes of variability seen in anomalous fading rates of the blue emission (∼410 nm) in feldspars have not been fully identified. Since feldspars are complex framework silicates with a variety of chemical compositions and mineralogical properties, linking properties inherent to the feldspar to particular luminescence characteristics is challenging. This thesis aims at establishing a better understanding of potential relationships between feldspar chemical composition, structural state and the number of phases present within a crystal and the luminescence properties of selected feldspar samples. To achieve this goal, this thesis investigates the luminescence properties of a selection of single crystal feldspars and feldspars of grain mixtures extracted from sediment and bedrock, by using a combination of excitation and emission spectroscopy, photo- radio-, thermo- and infrared stimulated luminescence and anomalous fading measurements.

Electron trap depths ranging from 2 eV to 2.4 eV were found in chemically and structurally different feldspars. The IR resonance peak, likely reflecting the first excited state of IR-sensitive electron trapping centres, is located ∼1.45 eV above the ground state of the trap. Similarities in energies measured for the ground and excited state energies across the sample suite indicate that defects functioning as electron trapping centres are likely located on the Si,Al-framework. Site-selective infrared photoluminescence (IRPL) excitation-emission spectroscopy revealed up

to three different lattice environments in which the investigated electron trapping centres might be located. A comparison of chemically and structurally different alkali feldspars indicated the presence of K^+ ions on M sites as one likely influence of the lattice environment of electron trapping centres in feldspars. Disorder of the tetrahedral site occupancy of Al^{3+} ions has only little effect on electron trapping centres and related IRPL emissions, and no correlation was found between the number of phases present in a single crystal feldspar (i.e. whether it is single phase or perthitic) and electron trapping centres. Thus, observed differences in electron trap depths and IRPL emissions are influenced by additional factors, not explored in this thesis.

The width of the sub-conduction band-tail states range from 0.2 to 0.8 eV in the samples investigated. This suggests different impacts on charge mobility, and stability of trapped electrons in these samples.

The intensity and stability of the blue luminescence emission ($\sim$410 nm), the emission most commonly used in luminescence dating studies, is suggested to be influenced by the degree of order of Al^{3+} ions on the framework. It is proposed that crystal defects giving rise to the blue luminescence emission are not only related to feldspars from geological environments where the high structural state (disorder of Al^{3+} ions on the framework) is retained during rapid cooling of the magma (e.g. volcanic origin), but is also related to perthites. In perthites the interfaces between K- and Na-feldspar lamellae are likely to host a high density of defects, resulting not only in intense blue emission, but also in high anomalous fading rates, making fading correction of luminescence ages inevitable.

Research in this thesis shows the complexity of factors influencing luminescence properties in feldspars, which has to be kept in mind, when trying to further improve the use of feldspars as natural luminescence dosimeters.

Acknowledgments

As a farewell gift before my first big trip on my own, my mum gave me a postcard, which pictured a blue camper van on a narrow stone bridge; the postcard was entitled with the words

Nur wer das Außergewöhliche wagt, der kann das Außergewöhliche erleben
(Only who dares the extraordinary, can experience the extraordinary)

I still use this postcard as a bookmark. Personally, I would consider moving abroad and doing a PhD as extraordinary. I dared the extraordinary and most importantly: I experienced the extraordinary. Here I would like to thank all those people who made my time as a PhD student at Aberystwyth University to an extraordinary time.

My PhD research was funded through an AberDoc PhD scholarship. During the course of my PhD, I have received funding from the Royal Geographical Society, the Quaternary Research Association and the Department of Geography and Earth Sciences at Aberystwyth University. I am very grateful to have received this financial support, which enabled my studies.

I would like to acknowledge my supervisors: I would like to thank Prof Dr Helen Roberts for her encouragement, scientific and academic advice. Although it was the hardest lesson for me to learn, she advised me to slow down, and this was one of, if not the most important advice I received during my PhD. Thank you to Prof Dr Geoff Duller, who with his restless excitement for luminescence research motivated me throughout my studies and never got tired of answering my last (it was never the last) question. Despite this being a luminescence PhD thesis, I owe a big thank you to Prof Dr Nick Pearce, who always had an open ear for all my concerns and time for a cup of coffee. Thank you for sharing your mineralogy and geochemistry knowledge and for asking non-luminescence questions, which were important to ask, so I did not forget to look beyond.

My PhD project developed throughout the course of my PhD and took a very different path than originally anticipated. The project as it is now, would not have happened without the support and encouragement of Prof Dr Georgina E. King (Université de Lausanne). Thank you Georgina for many fruitful discussions and your support throughout this project.

I visited the Risø Campus in Roskilde, Denmark, several times during my PhD studies. During these visits I worked under the supervision of Dr Mayank Jain and with great help from many people. I would like to thank the whole Risø family for making me feel welcome. Especially I would like to thank Dr Mayank Jain, who enabled all my visits and who I had very fruitful discussions with. I thank Amit Prasad and Raju Kumar for their help with COLUR and for sharing their experience with the instrument, spectroscopy and IRPL. I would also like to thank Karsten Bracht-Nielsen for his help with the Andor spectrometer.

Thank you to Prof Dr Adrian Finch (University of St. Andrews) for providing me with selected "pet" feldspar samples and for sharing his feldspar knowledge with me. Thank you to Dr Tony Bell (Sheffield Hallam University) for doing the XRF and XRD measurements for me and especially for quick email responses and last minute measurements.

My work at the Aberystwyth Luminescence Research Lab and in the geochemistry laboratories of the Department of Geography and Earth Sciences at Aberystwyth University would not have been possible without the help and support of Hollie Wynne and Andy Brown. Thank you both for your help and for always having time for a little chat (including cake). I would like to thank Robyn Pinder, Melissa Chapot, Geraint Jenkins and Nina Ataee for their great company in F1 (and beyond). I would like to thank Prof Dr Milja Kurki (International Politics, Aberystwyth University) for having an open ear and giving great academic advice from a perspective outside of geoscience.

Since my PhD project was originally designed to be very different from the actual outcome, I would like to thank some people for their support during the first phase of my PhD: Dr Jim O'Connor (USGS), Prof Dr Vic Baker and Tao Liu (both University of Arizona), Dr Andrea Balbas (Caltech) and Dr Tess Harding (USGS) for their help during an amazing field campaign in the Channelled Scablands and Dr Britta Jensen, Dr Lauren Davies and Dr Andrew Locock (all University of Alberta) for teaching me electron microprobe analysis of glass shards. Thank you to Lauren for making my time in Edmonton (and Canmore) very enjoyable.

Besides studying for my PhD, I spent a great amount of time at the Lluest Equine Centre at Aberystwyth University. Being able to bring my best (and fluffy) friend Cebi with me to Aberystwyth had a large influence on my wellbeing during my PhD. I would like to thank Faye, Caitlin, Annabel, Jess, Chrissy, Kelly, Rachel, Caryl, Hannah, Jen, Alyx and Joan for their friendship and help during the past three years. Thank you especially to Faye, Caitlin, Annabel and Rachel who all took great care of Cebi when I was away from Aberystwyth to "make sand glow in the dark".

Thank you to my friends in Germany, Britta, Michèle, Leonie and Carina, who stayed in contact with me and who always had time for a Skype call.

A very special thank you goes to my entire family, but especially my parents and my Omma, who always believe in me and support me in everything I do. Last but not least I would like to thank Martin for your love and for being my best friend.

Contents

One

Introduction

1.1 Background and aim of this thesis

Feldspars are used as natural dosimeters in luminescence dating studies, due to their ability to store charge within crystal defects over geological time scales. This trapped charge can be released as light (referred to as *luminescence*) by thermal or optical stimulation (Aitken, 1985; Huntley et al., 1985) and the emitted light intensity has some proportionality to the stored charge, which allows the construction of a dose response curve and the use of feldspars as a chronometer. Most commonly luminescence dating of feldspars is performed using the infrared stimulated luminescence (IRSL) signal (Hütt et al., 1988), with an emission recorded in the blue wavelength range (e.g. Thomsen et al., 2008; Buylaert et al., 2012; Reimann and Tsukamoto, 2012; Riedesel et al., 2018). This method relies on the release of trapped electrons from electron traps due to IR stimulation ($\sim$1.45 eV). The released electrons will move through the crystal until they finds trapped holes, with which they recombine (Jain and Ankjærgaard, 2011). Radiative recombination, with a specific defect functioning as the blue recombination centre, results in the emission of blue photons. Whilst this blue emission ($\sim$410 nm) is generally the emission of interest in luminescence dating studies, isolation of this emission using different optical filters (usually a combination of a Schott BG 39 and a Schott BG 3 filter) results in the transmission of not only this particular wavelength, but also other wavelengths, which are within the transmission window of the selected filters. Thus, it should be noted that the just described transmitted wavelength range might contain emissions that arise from a number of different defects.

The application of IRSL dating to a wide range of sedimentary environments

(e.g. Wallinga, 2002; Fuchs and Owen, 2008; Roberts, 2008) and different time scales (e.g. Thiel et al., 2011; Reimann et al., 2012) has shown large sample-to-sample and intra-sample variability in the luminescence signal intensities of the blue IRSL signal (e.g. Smedley et al., 2012), its thermal stability (e.g. Tsukamoto et al., 2012), equivalent doses (e.g. Buylaert et al., 2018) and also in the rate signal loss at room temperature over laboratory time scales (Neudorf et al., 2012; Trauerstein et al., 2012; Valla et al., 2016). This loss in luminescence signal intensity over time is commonly referred to as anomalous fading (e.g. Wintle, 1973). It is known that the feldspar mineral group consists of structurally and chemically different feldspars (e.g. Deer et al., 2013, p. 248). Previous studies have tried to link IRSL signal intensities (Smedley et al., 2012) or the rate of fading (e.g. Huntley and Lian, 2006) with the chemical composition of feldspars. And suggestions have been made regarding relationships between anomalous fading and structural disorder of the feldspars, particularly in samples of volcanic origin (e.g. Visocekas and Zink, 1995). However, further developments in luminescence dating of feldspars are challenged by limited knowledge of the interaction between the chemistry and structure of feldspars and their luminescence properties, particularly how mineralogical properties of the samples influence the electron trapping centre and the recombination centre in various feldspars.

The recently developed method of infrared photoluminescence (IRPL, Prasad et al., 2017) might become a promising alternative to IRSL. In contrast to IRSL, IRPL allows the direct non-destructive probing of trapped electrons with IR light, which excites the trapped electrons. Subsequent radiative relaxation of the electron from an excited state to the ground state of am electron trap results in the emission of IR photons. Besides its intended purpose as a new luminescence dating technique (Prasad et al., 2017), IRPL excitation and emission spectroscopy enables site-selective probing of the electron trap in feldspars (Kumar et al., 2020), and can thus provide further information on the characteristics of the electron trap in different feldspars. Additionally, IRPL has only recently been developed, and despite its promising start, further investigation of the characteristics of this novel technique and of potential sample-to-sample variations are necessary to improve its application in retrospective dosimetry.

The variety seen in feldspar IRSL and the novelty of IRPL require further investigations, particularly regarding the influence of the complex structural and chemical differences of members of the feldspar group. A combination of established spectroscopic methods and novel techniques will help to improve the

understanding of luminescence production in feldspars. This thesis explores the luminescence behaviour of structurally and chemically different feldspars and aims to contribute to the growing body of knowledge on luminescence production in feldspar, particularly in IRSL and IRPL, by answering a series of research questions outlined below:

IRSL is dependent on the evictions of electrons from electron traps and subsequent recombination with luminescence centres (e.g. Jain and Ankjærgaard, 2011). Thus, IRSL is influenced by the properties of electron trapping centres and recombination centres. IRPL, in contrast, is controlled by the properties of electron trapping centres and their environment (Kumar et al., 2018; 2020). Subsequently, for both methods, IRSL and IRPL, it is important to get further details into the properties of electron trapping centres:

Q.1.1: Where in the feldspar crystal are the defects functioning as electron trapping centres located?

Q.1.2: What are the physical properties of electron trapping centres? More particular: What are the energies of the ground and excited state of the type electron trap investigated and do they vary between samples? If these energies vary between samples, what are the driving forces for changes in energy level?

Q.1.3: IRPL as the result of radiative relaxation within electron trapping centres has been shown to result in emissions at ∼1.3 eV and at ∼1.4 eV. Are both emissions present in all types of structurally and chemically different feldspars, or are these emissions related to specific properties of the material?

Poolton et al. (2002a; 2009) have shown the presence of band-tail states in feldspars. These band-tail states play an important role in electron-hole recombination processes in feldspars (Poolton et al., 2009).

Q.2: How far do the band-tail states extend below the conduction band (band-tail states width) and does the width vary between chemically and structurally different feldspars?

The blue luminescence emission (∼410 nm) is the emission most commonly

used in luminescence dating of feldspars, however, variations in signal intensity have been found between samples (e.g. Smedley et al., 2012). Previous studies have tried to link the blue luminescence signal intensity and the measured dose stored within the crystal with the K-content in alkali feldspars (e.g. Smedley et al., 2012; Buylaert et al., 2018). However, no correlation has been found. It has been suggested that the blue emission originates from a hole centre located on Al-bridging O ions (Finch and Klein, 1999). Subsequently, the association of characteristics of the blue luminescence emission with chemical or structural properties of the samples might be more complex than a comparison of the K-content and the blue luminescence intensity.

Q.3: In which chemical and structural feldspars is the blue luminescence present and what controls the intensity of this emission?

Another interesting aspect of the blue luminescence emission, used in feldspar IRSL dating, is a loss of the trapped charge over time, referred to as anomalous fading (e.g. Wintle, 1973; Visocekas, 1985). Fading can be quantified in the laboratory (Huntley and Lamothe, 2001; Auclair et al., 2003) and obtained fading rates are known to vary between samples (e.g. Spooner, 1992, 1994; Huntley and Lian, 2006; Valla et al., 2016). Increased fading has been associated with volcanic feldspars and disorder of Al^{3+} and Si^{4+} ions on the alkali feldspar framework (Visocekas and Zink, 1995). However, not all fading feldspars used in luminescence dating are of volcanic origin (e.g. Valla et al., 2016; King et al., 2016a; Jenkins et al., 2018). Thus the questions to arise here are:

Q.4.1: Is anomalous fading ubiquitous for the blue luminescence emission in all feldspars?

Q.4.2: Can the fading rate be linked to properties of the sample, e.g. the sample chemistry or the structural state?

By exploring and aiming to answer these questions throughout this PhD thesis, it is hoped to establish a better understanding of luminescence production in feldspars, especially regarding variability seen in the IRSL signal and also in regard to the recently developed method of IRPL.

1.2 Feldspar luminescence

1.2.1 Feldspar as a natural dosimeter

The natural abundance and variations in chemistry and mineralogical properties of members of the feldspar group have led to a wide range of applications in Earth sciences, including luminescence dating. In luminescence dating, feldspar functions as a natural dosimeter and chronometer, storing energy in crystal defects over geological time scales. The stored energy can be released as light and the emitted light intensity is somewhat proportional to the stored energy and can thus give information on the time since the sample′s last exposure to heat (e.g. Aitken, 1985) or light (e.g. Huntley et al., 1985) or on the time elapsed since a certain temperature was passed during the cooling of bedrock (termed closure temperature; e.g. Guralnik et al., 2015; King et al., 2016b; Biswas et al., 2018).

During burial, mineral grains, such as feldspar, are exposed to environmental radioactivity. This radioactivity arises from cosmic radiation and from radioactive nuclides of elements, such as uranium (U), thorium (Th) and potassium (K) within the sediment (e.g. Aitken, 1985, p. 61-64). During radioactive decay, particles of different type and energy are emitted (alpha and beta particles, gamma rays), which interact with material, for example sediment. The energy released due to the radioactive decay of radionuclides and due to cosmic radiation can be summed as the *dose rate* and is expressed in Gy ka^{-1}, where 1 Gray (Gy) equals 1 J kg^{-1} and ka is the time span of 1,000 years. The energy absorbed by the mineral grain, which is exposed to the radioactivity, is termed *dose* and is expressed in Gy. The absorbed energy results in the excitation of charge that is stored in crystal defects and impurities in the mineral grain and can be released using thermal or optical stimulation, which can result in the emission of light, termed luminescence (e.g. Aitken, 1985, p. 1-2; Aitken, 1998, p. xi, 6-8; Huntley et al., 1985). The emitted luminescence signal intensity has some proportionality to the trapped charge within the defects in the crystal. Once the emitted luminescence is calibrated against known laboratory doses, an *equivalent dose* (in Gy) can be calculated. This equivalent dose is thought to be equivalent to the energy absorbed during burial of the grain. By dividing the equivalent dose by the dose rate a luminescence age is calculated (equation 1.1, Aitken, 1985, p. 9; Aitken, 1998, p. 7).

$$Luminescence\ age(ka) = \frac{Equivalent\ dose(Gy)}{Dose\ rate(Gy\ ka^{-1})} \tag{1.1}$$

Feldspars have been used in a wide range of luminescence dating applications in archaeological (e.g. Guo et al., 2016; Schaarschmidt et al., 2019; and Roberts et al., 2015, for a review) and geomorphological contexts, for example to date fluvial (Wallinga et al., 2001; Colarossi et al., 2015; and Wallinga, 2002, for a review on luminescence dating of fluvial deposits), aeolian (e.g. Wang et al., 2018; Buckland et al., 2019; and Roberts, 2008, for a review on luminescence dating of loess deposits), glacial (e.g. Klasen et al., 2007; Smedley et al., 2016; and Fuchs and Owen, 2008, for a review on luminescence dating of glacial deposits) and coastal deposits (Madsen et al., 2011; Reimann and Tsukamoto, 2012; Brill et al., 2018; Riedesel et al., 2018). Due to the late luminescence signal saturation and the brightness of the luminescence signal, feldspars are attractive as a luminescence chronometer, particularly when dating older (>100,000 years) sediment deposits (Duller, 2008; Preusser et al., 2008). However, despite this routine use of feldspars as chronometers in luminescence dating, their use and application is challenging and many questions regarding the physical processes behind the feldspar luminescence signal are still open. This thesis will address some of these challenges and open questions. A particular focus will be on constraining physical parameters governing electron trapping, re-trapping and electron-hole recombination in feldspar. Additionally, the major challenge in feldspar luminescence dating, an anomalous signal loss over time termed *anomalous fading* (Wintle, 1973), which leads to age underestimation is investigated. Potential sources of anomalous fading are further explored in this thesis.

1.2.2 Brief overview of feldspar crystal structure

Feldspars form an important part of igneous rocks, both plutonic and volcanic. Due to their abundance in the crust, weathering results in feldspars being common constituents of sedimentary rocks (Deer et al., 2013, p. 248). Feldspars are framework silicates with the general formula MT_4O_8. The framework comprises of interlinked Si,Al-tetrahedra on tetrahedral sites (T sites), which are connected by shared oxygen ions (O). Large cations occupy M sites in cavities of the framework, and the three main M site-occupying cations, K^+, Na^+ and Ca^{2+} define the end members of the feldspar group: K-feldspar ($KAlSi_3O_8$), Na-feldspar ($NaAlSi_3O_8$)

and Ca-feldspar ($CaAl_2Si_2O_8$). T sites are occupied by Si^{4+} or Al^{3+}, with a Si:Al ratio of 3:1 in K- and Na-feldspar and a ratio of 2:2 in Ca-feldspar, due to the difference in charge of the cation on the M sites (Na^+ and K^+, but Ca^{2+}; Deer et al., 2013, p. 248-249). At high temperatures (>1000 °C) feldspars are present as solid solutions. The solid solution between K- and Na-feldspar gives rise to alkali feldspar and between Na- and Ca-feldspar to plagioclase. At low temperatures (<1000 °C) only limited solid solution exists and is restricted to compositions close to the end members (Deer et al., 2013, p. 249).

Differences in ionic radii of K^+ (0.151 nm) and Na^+ (0.118 nm) result in an expansion of the Si,Al-framework in K-feldspar, compared to Na-feldspar and exsolution of K- and Na-feldspar phases takes place during cooling of the magma (Deer et al., 2013, p. 262). Exsolution refers to the formation of intergrowths of K-feldspar and Na-feldspar lamellae in alkali feldspar crystals upon cooling; the resulting feldspar is referred to as perthite. At low temperatures, all alkali feldspars, except the K- and Na-end members, occur as perthites (Deer et al., 2013, p. 262).

Another effect of cooling is a change in the T site occupancy of Si^{4+} and Al^{3+}, which is particularly important in alkali feldspar. At high temperatures (>1000 °C), Si^{4+} and Al^{3+} are randomly distributed across all four tetrahedral sites, resulting in a 25 % probability of finding an Al^{3+} ion on any T site. This is the case in the high temperature structural state of K-feldspar, referred to as sanidine. During cooling, ordering of Si^{4+} and Al^{3+} takes place and Al^{3+} migrates into one of two T site types (termed T_1 sites). A further decrease in temperature results in the migration of Al^{3+} to one tetrahedral site ($T_1(0)$ site); this causes a break in the symmetry and results in a change in the crystal system from monoclinic to triclinic (Deer et al., 2013, p. 256-257).

Changes in the order of Si^{4+} and Al^{3+}, the formation of intergrowths, vacancies and potential exchange of ions in the crystal with external ions (e.g. Fe^{3+} for Al^{3+}, Telfer and Walker, 1978; Prasad and Jain, 2018a) can create impurities and imperfections in the crystal. These imperfections can function as defects storing charge within the crystal over time and allow the use of feldspars as a natural dosimeter. Further details regarding potential defects in feldspars and their role in luminescence are presented in Chapter 3.

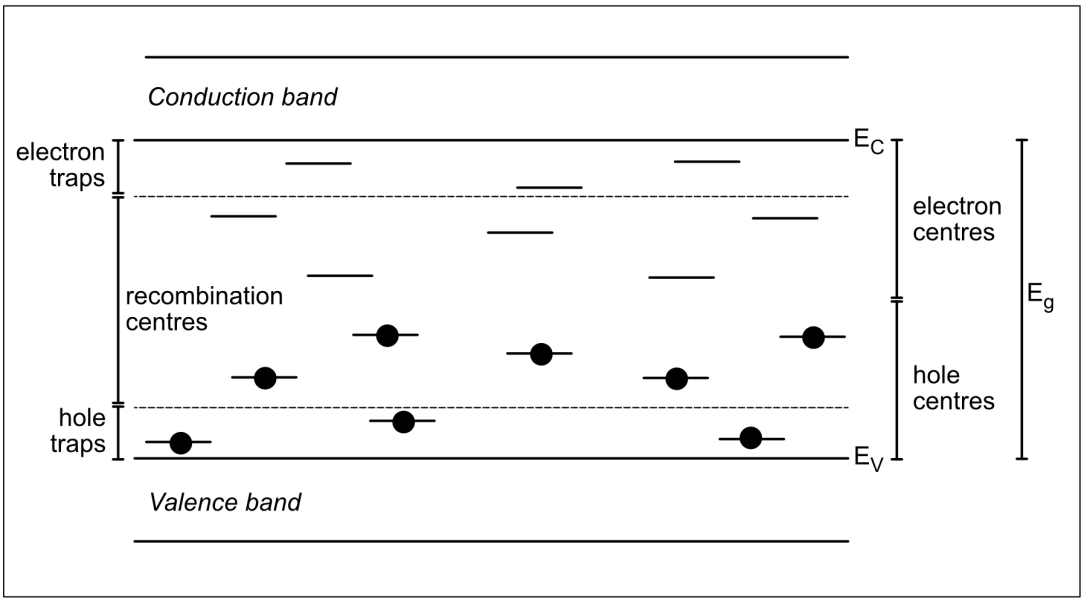

Figure 1.1: *Band diagram of an insulator with the two delocalised bands, the valence and conduction band. The edge of each band is denoted with E_v and E_c, respectively. Defects are shown within the band gap (E_g). In this example, all hole centres are filled with electrons, whereas all electron centres are empty. Centres close to the conduction band are likely to function as electron traps, centres close to the valence band are likely to be hole traps. Centres in the middle part of the band gap are likely to be recombination centres. The figure is based on McKeever 1985, p. 23; Yukihara and McKeever, 2011, p. 22.*

1.2.3 Energy band model and luminescence processes in feldspar

The energy band model of solids can be applied to feldspar. It is a simplified model, which can be used to explain electron trapping and recombination processes in solids and is used to visualise charge transport processes, which lead to luminescence phenomena. The energy band model of solids shows different allowed energy states of electrons, also referred to as bands, the valence band and the conduction band, separated by a forbidden gap, or band gap (Fig. 1.1; McKeever, 1985, p. 20). The difference in energy between the valence band and the conduction band defines the conductivity of the material, with the valence and the conduction band overlapping in conductors. Insulators, in contrast, have a wide band gap (of several eV) between the valence band and the conduction band (McKeever, 1985, p. 21). Feldspars have a band gap energy of ∼7.7 eV (Fig. 1.2; Malins et al., 2004), and are referred to as wide band gap materials. To allow charge transport within the solid, the energy given to the solid has to be large enough to allow electrons to move into the conduction band. In natural materials, impurities within a crystal will enable electrons to possess energies,

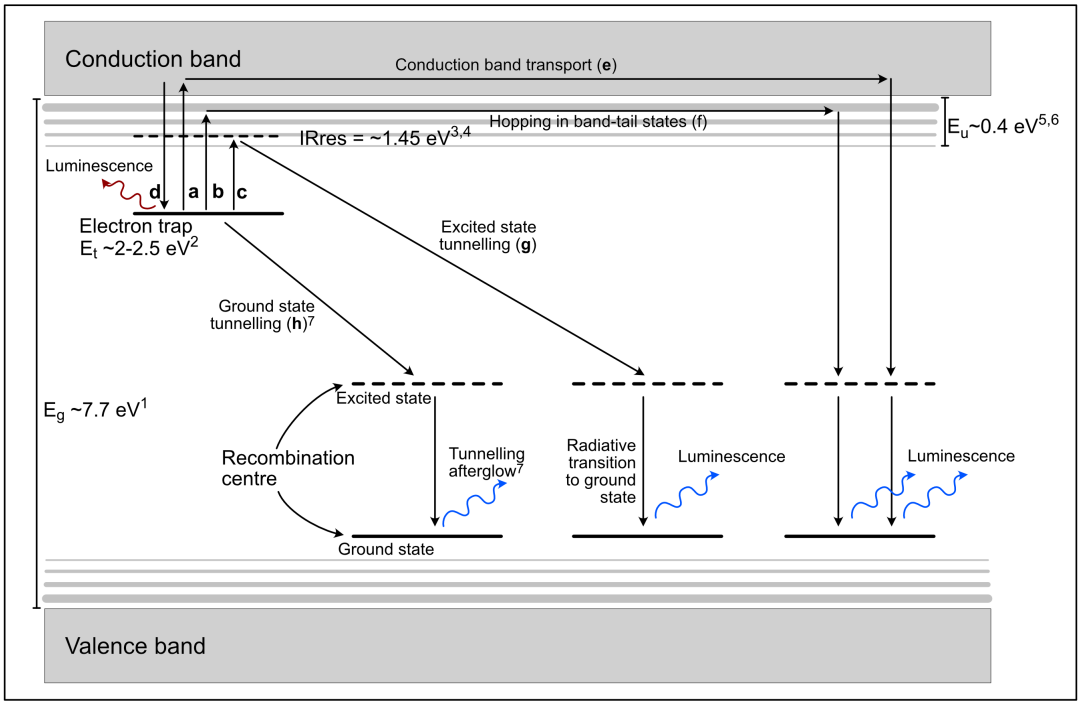

Figure 1.2: *Energy band model of feldspars and potential recombination pathways assuming one electron trap for simplicity; three recombination centres are drawn for the purpose of a better illustration of the different recombination routes and radiative recombination processes within the recombination centre. The letters refer to the following recombination routes, which are further explained in the text. a) Excitation to the conduction band, b) Excitation into the band-tail states, c) excitation to the excited state of the electron trap, d) re-trapping, e) transport via the conduction band, f) band-tail state hopping, g) excited state tunnelling, h) ground state tunnelling. References to numerical values within the figure are given here.* [1]*Malins et al. (2004),* [2]*Kars et al. (2013),* [3]*Clark and Sanderson (1994),* [4]*Baril and Huntley (2003),* [5]*Poolton et al. (2009),* [6]*Prasad and Jain (2018b),* [7]*Visocekas (1985).*

which are forbidden in a perfect crystalline structure. These impurities will allow electrons to occupy states within the forbidden gap (McKeever, 1985, p. 21). Dependent on the type of defect within the crystal, electron centres and hole centres will form within the band gap. Electron centres are located below the conduction band and are characterised by a net positive charge (Fig. 1.1). In contrast, hole centres are located above the valence band and are characterised by a net negative charge (Fig. 1.1; Aitken, 1985, p. 42; McKeever, 1985, p 23). Electron and hole centres can function as recombination centres or as electron and hole traps (Fig. 1.1). A recombination centre will first capture a hole from the valence band and then an electron from the conduction band, which will then recombine with the captured hole at the defect. Whether an electron centre or a hole centre is a recombination centre or a trap depends on the probability of charge trapped at the centre being stimulated into the valence or conduction band, or charge of the opposite sign being trapped at the same centre. In a recombination centre it is

more likely that charge of the opposite sign is also trapped at the centre, than the trapped charge being stimulated into either of the two delocalised bands. The opposite is the case for traps (Yukihara and McKeever, 2011, p. 23).

Ionising radiation, as the results of radioactive decay, can cause the ionisation of valence electrons. The ionised electron will leave its position in the valence band and will potentially, dependent on the ionising energy received, surmount the energy gap of the forbidden gap and will enter the conduction band. Within the conduction band, the electron is free to move within the crystal. Eventually, the electron will lose energy and will either become trapped within an electron trap below the conduction band, or will recombine with a hole. The ionisation of an electron from the valence band into the conduction band will result in a hole in the valence band. The hole will move into a hole trap, where it is available for recombination with an electron (McKeever, 1985, p. 26).

Electrons trapped in electron traps can be released through excitation with an energy which covers the transition from the electron trap to the conduction band, for example due to thermal or optical excitation. It has been debated whether there is only one type of electron trap in feldspars (e.g. Hütt and Jaek, 1989; Baril and Huntley, 2003), multiple distinctly different traps (e.g. Clark and Sanderson, 1994) or a distribution of traps (e.g. Strickertsson, 1985). The depth of one type of electron trap in feldspars has been constrained as $\sim$2 to 2.5 eV below the conduction band edge (Fig. 1.2; Hütt et al., 1988; Kars et al., 2013). Further details regarding different measurement techniques and the transition energy of electrons from the ground state of electron trapping centres to the conduction band in feldspars are given in Chapters 4 and 5. Once excited into the conduction band, the electron can either be re-trapped in an electron trap or it can move through the crystal until it finds a hole to recombine with. There is also the possibility for the electrons to recombine within the valence band (McKeever, 1985, p. 26; Jain and Ankjærgaard, 2011).

A variety of recombination pathways is available for excited electrons in feldspars (Jain and Ankjærgaard, 2011; Fig. 1.2). One reason for greater options in recombination pathways in feldspars is the presence of band-tail states (e.g. Monroe, 1985), which expand below the conduction band and above the valence band. The sub-conduction band-tail states play a role in recombination of electrons with holes in feldspars (Poolton et al., 2002a, 2009). Since these band-tail states extend below the conduction band, they lower the energy required to excite an electron out of an electron trap. The width of the sub-conduction band

tail states has been constrained as ∼0.4 eV (Fig. 1.2; Poolton et al., 2009; Prasad and Jain, 2018b). Although the mobility of electrons within the band-tail states is lower than in the conduction band, it still allows movements of the excited electron. Mobility of electrons within the band-tail states is thought to occur via tunnelling or hopping from tail to tail (Monroe, 1985; Poolton et al., 2009; Morthekai et al., 2012). Chapter 4 presents the results of measurements of the width of the sub-conduction band tail states in different feldspar samples.

Another recombination route in feldspars is excited state tunnelling (Fig. 1.2, transition g). Within an electron trap, excited states occur. These excited states might allow recombination of excited electrons from the excited state to a recombination hole centre, when the electron wavefunctions of the excited state and the hole trap overlap (Poolton et al., 2002b). In feldspar, electrons can also tunnel directly from the ground state of the electron trap to a nearby recombination centre (Fig. 1.2, transition h), when the wavefunctions of the electron trap and the hole trap overlap (Poolton et al., 2002b). This process is described as quantum mechanical tunnelling (Visocekas, 1985). It is the major drawback in the use of feldspars as a natural dosimeter, because it leads to a loss of charge from the electron traps over time and gives rise to the process referred to as anomalous fading (Wintle, 1973). This process is termed *anomalous* fading, because the loss of charge occurs over time scales, much shorter than the lifetimes predicted for the charge to be stable at (e.g. Aitken, 1985, p. 269-282). Fading will result in the underestimation of the luminescence age, if uncorrected. Correction methods for anomalous fading in feldspar have been proposed (Huntley and Lamothe, 2001; Kars et al., 2008), but these can result in large uncertainties on the corrected luminescence age. Thus, research has focussed on the development of measurement procedures, which isolate a stable, non-fading, luminescence signal of feldspar (e.g. Thomsen et al., 2008; Li and Li, 2011; Thiel et al., 2011; Buylaert et al., 2012). Chapter 6 explores potential sources of variations in fading rates of chemically and structurally different feldspar samples.

Upon recombination of an electron with a hole or during re-trapping of an electron, energy is released. If this energy is released as light it is referred to as luminescence. The wavelength of the emitted light is dependent on the energy transition within the trap during re-trapping or during recombination with a recombination centre. Chapter 6 discusses variations in luminescence emissions of a variety of feldspar samples, with a focus on the blue luminescence emission.

1.3 Outline of this PhD thesis

This thesis consists of seven chapters, out of which four are written as stand-alone scientific articles, some of which have been submitted to, or have been published by, scientific journals. Of these chapters one is a review (Chapter 3) and three are data-oriented research articles (Chapters 4, 5 and 6). At the time of submission of this thesis, Chapter 3 is a manuscript intended to be submitted, chapter 4 has been published, Chapter 5 is intended to be submitted and Chapter 6 is published. Furthermore this thesis contains prefaces to Chapters 4, 5 and 6, which introduce each chapter and its context within the thesis. Chapter 2 introduces the samples and instruments used and methods applied in this thesis.

Chapter 3

Chapter 3 is a manuscript, which is currently in preparation for submission to the journal *Earth Science Reviews* as:

Riedesel, S., Roberts, H.M., Duller, G.A.T., Pearce, N.J.G, in preparation. *Excitation and emission spectroscopy of feldspars — Insights into luminescence production in feldspars.*

Contributions: SR wrote the manuscript, HMR, GATD and NJGP read the manuscript and gave feedback.

This chapter summarises and discusses the current state of knowledge regarding excitation and emission spectroscopy of feldspars. The focus of this chapter lies on presenting excitation spectroscopy as a powerful tool used to constrain the energies for the band gap, the ground and the excited state of electron trapping centres in feldspars, and of applications of emission spectroscopy to gain information on different luminescence centres, but also more recent applications to constrain the width of sub-conduction band-tail states.

Chapter 4

This chapter is published in *Radiation Measurements* as:

Riedesel, S., King, G.E., Prasad, A.K., Kumar, R., Finch, A.A., Jain, M., 2019. *Optical determination of the width of the band-tail states, and the excited and ground state energies of the principal dosimetric trap in feldspar.* Radiation Measurements 125, 40-51.

Contributions: SR performed the measurements and wrote the manuscript. SR, GEK and MJ designed the study and discussed the results. AKP and RK provided help with the operation of the instrument. AAF provided sample material and was involved in data discussion. All authors read and commented on the manuscript.

This paper presents the results of excitation and emission spectroscopy, used to constrain the width of the sub-conduction band-tail states and the energies of the ground and excited state of an electron trap in feldspar and thus answers aspects of questions **Q.1.1**, **Q.1.2** and **Q.2**. The samples used in this study allow a comparison of the constrained parameters and the sample chemistry, particularly the K content.

Chapter 5

This chapter is a manuscript intended to be submitted to the *Journal of Luminescence* as:

Riedesel, S., Kumar, R., Duller, G.A.T., Roberts, H.M., Bell, A.M.T., Jain, M., in preparation for submission to the Journal of Luminescence. *Site-selective characterisation of electron trapping centres in relation to chemistry, structural state and phases present in single-crystal alkali feldspars.*

Contributions: SR performed luminescence experiments. AMTB performed XRF and XRD measurements. RK assisted with spectroscopy. SR, RK, MJ, GATD and HMR designed the study. SR wrote the manuscript. All authors read and commented on the manuscript.

To further explore the hypothesis, raised in Chapter 4, of electron trapping centres being located on the Si,Al-framework, this chapter uses low temperature excitation spectroscopy with the emission recorded at 880 and 955 nm on selected

alkali feldspar samples and their end members. Thereby, this chapter addresses aspects of questions **Q.1.1**, **Q.1.2**, and **Q.1.3**. Whilst Chapter 4 focussed on the K content of the sample as a potential driver of changes in trap depth and excited state, this chapter explores whether the structural state of the sample or the number of phases present in the crystal influence the trap depth in the samples.

Chapter 6

This chapter is published in *Radiation Measurements* as:

Riedesel, S., Bell, A.M.T., Duller, G.A.T., Finch, A.A., Jain, M., King, G.E., Pearce, N.J.G, Roberts, H.M., in revision. *Exploring sources of variation in thermoluminescence emissions and anomalous fading in alkali feldspars.* Radiation Measurements 141, 106541.

Contributions: SR performed all luminescence measurements and wrote the manuscript. AMTB performed XRF and XRD measurements. SR, GATD, GEK, NJGP and HMR designed the study and discussed the results. NJGP provided sample material. AAF provided sample material and helped with the interpretation of the results. MJ assisted with the spectroscopy. All authors read and commented on the manuscript.

Whilst Chapters 4 and 5 focussed on electron trapping centres and parameters, which influence electron trapping and detrapping, Chapter 6 focuses on the recombination side in luminescence processes. The research presented in this chapter answers research questions **Q.3** and **Q.4.1** and **Q.4.2**, therefore thermoluminescence emissions and the rate of fading of samples, which were already used in Chapters 4 and 5, are explored. This chapter explores potential effects of the variations in the sample chemistry, its structural state and the number of phases present in the sample on wavelength and temperature resolved luminescence emissions and on the rate of anomalous fading of the blue emission.

Chapter 7 summarises the results presented in Chapter 3 to Chapter 6, presents a conclusion on the work presented in this PhD thesis and in outlook towards potential future research.

References

Aitken, M.J., 1985. Thermoluminescence Dating. Academic Press, London, United Kingdom.

Aitken, M.J., 1998. An Introduction to Optical Dating. The dating of Quaternary sediments by the use of photon-stimulated luminescence. Oxford University Press, Oxford, United Kingdom.

Auclair, M., Lamothe, M., Huot, S., 2003. Measurement of anomalous fading for feldspar IRSL using SAR. Radiation Measurements 37, 487-492.

Baril, M.R., Huntley, D.J., 2003. Optical excitation spectra of trapped electrons in irradiated feldspars. Journal of Physics: Condensed Matter 15, 8011-8027.

Biswas, R.H., Herman, F., King, G.E., Braun, J., 2018. Thermoluminescence of feldspar as a multi-thermochronometer to constrain the temporal variation of rock exhumation in the recent past. Earth and Planetary Science Letters 495, 56-68.

Brill, D., Reimann, T., Wallinga, J., May, S.M., Engel, M., Riedesel, S., Brückner, H., 2018. Testing the accuracy of feldspar single grains to date late Holocene cyclone and tsunami deposits. Quaternary Geochronology 48, 91-103.

Buckland, C.E., Bailey, R.M., Thomas, D.S.G., 2019. Using post-IR IRSL and OSL to date young (<200yrs) dryland aeolian dune deposits. Radiation Measurements 126, 106-131.

Buylaert, J.-P., Jain, M., Murray, A.S., Thomsen, K.J., Thiel, C., Sohbati, R., 2012. A robust feldspar luminescence dating method for Middle and Late Pleistocene sediments. Boreas 41, 435-451.

Buylaert, J.-P., Ujavri, G., Murray, A.S., Smedley, R.K., Kook, M., 2018. On the relationship between K concentration, grain size and dose in feldspar. Radiation Measurements 120, 181-187.

Clark, R.J., Sanderson, D.C.W., 1994. Photostimulated luminescence excitation spectroscopy of feldspars and mica. Radiation Measurements 23, 641-646.

Colarossi, D., Duller, G.A.T., Roberts, H.M., Tooth, S., Lyons, R., 2015. Comparison of paired quartz OSL and feldspar post-IR IRSL dose distributions in poorly bleached fluvial sediments from South Africa. Quaternary Geochronology 30, 233-238.

Deer, W.A., Howie, R.A., Zussman, J., 2013. An introduction to rock-forming minerals (3rd Edition). Mineralogical Society, London, United Kingdom.

Duller, G.A.T., 2008. Luminescence Dating. Guidelines on using luminescence dating in archaeology. English Heritage.

Finch, A.A., Klein, J., 1999. The causes and petrological significance of cathodoluminescence emissions from alkali feldspars. Contributions to Mineralogy and Petrology 135, 234-243.

Fuchs, M., Owen, L.A., 2008. Luminescence dating of glacial and associated sediments: review, recommendations and future directions. Boreas 37, 636-695.

Guo, Y.-J., Li, B., Zhang, J.-F., Yuan, B.-Y., Xie, F., Roberts, R.G., 2016. Luminescence ages for three "Middle Palaeolithic" sites in the Nihewan Basin, northern China, and their archaeological and palaeoenvironmental implications. Quaternary Research 85, 456-470.

Guralnik, B., Jain, M., Herman, F., Ankjærgaard, C., Murray, A.S., Valla, P.G., Preusser, F., King, G.E., Chen, R., Lowick, S.E., Kook, M., Rhodes, E.J., 2015. OSL-thermochronometry of feldspar from the KTB borehole, Germany. Earth and Planetary Science Letters 423, 232-243.

Hütt, G., Jaek, I., Tchonka, J., 1988. Optical dating: K-feldspars optical response stimulation spectra. Quaternary Science Reviews 7, 381-385.

Huntley, D.J., Godfrey-Smith, D.I., Thewalt, M.L.W., 1985. Optical dating of sediments. Nature 313, 105-107.

Huntley, D.J., Lamothe, M., 2001. Ubiquity of anomalous fading in K-feldspars and the measurement and correction in optical dating. Canadian Journal of Earth Sciences 38, 1093-1106.

Huntley, D.J., Lian, O.B., 2006. Some observations on tunnelling of trapped electrons in feldspars and their implications for optical dating. Quaternary Science Reviews 25, 2503-2512.

Jain, M., Ankjærgaard, C., 2011. Towards a non-fading signal in feldspar: Insight into charge transport and tunnelling from time-resolved optically stimulated luminescence. Radiation Measurements 46, 292-309.

Jenkins, G.T.H., Duller, G.A.T., Roberts, H.M., Chiverrell, R.C., Glasser, N.F., 2018. A new approach for luminescence dating glaciofluvial deposits – High precision optical dating of cobbles. Quaternary Science Reviews 192, 263-273.

Kars, R.H., Wallinga, J., Cohen, K.M., 2008. A new approach towards anomalous fading correction for feldspar IRSL dating – tests on samples in field saturation. Radiation Measurements 43, 786-790.

Kars, R.H., Poolton, N.R.J., Jain, M., Ankjærgaard, C., Dorenbos, P., Wallinga J., 2013. On the trap depth of the IR-sensitive trap in Na- and K-feldspar. Radiation Measurements 59, 103-113.

King, G.E., Herman, F., Guralnik, B., 2016a. Northward migration of the eastern Himalayan syntaxis revealed by OSL thermochronometry. Science 353, 800-804.

King, G.E., Guralnik, B., Valla, P.G., Herman, F., 2016b. Trapped-charge thermochronometry and thermometry: A status review. Chemical Geology 446, 3-17.

Klasen, N., Fiebig, M., Preusser, F., Reitner, J.M., Radtke, U., 2007. Luminescence dating of proglacial sediments from the Eastern Alps. Quaternary International 164-165, 21-32.

Kumar, R., Kook, M., Murray, A.S., Jain, M., 2018. Towards direct measurement

of electrons in metastable states in K-feldspar: Do infrared-photoluminescence and radioluminescence probe the same trap? Radiation Measurements 120, 7-13.

Kumar, R., Kook, M., Jain, M., 2020. Understanding the metastable states in K-Na aluminosilicates using novel site-selective excitation-emission spectroscopy. Journal of Physics D: Applied Physics 53, 465301.

Li, B., Li, S.-H., 2011. Luminescence dating of K-feldspar from sediments: a protocol without anomalous fading correction. Quaternary Geochronology 6, 468-479.

Madsen, A.T., Buyleart, J.-P., Murray, A.S., 2011. Luminescence dating of young coastal deposits from New Zealand using feldspar. Geochronometria 38, 378-390.

Malins, A.E.R., Poolton, N.R.J., Quinn, F.M., Johnsen, O., Denby, P.M., 2004. Luminescence excitation characteristics of Ca, Na, and K-aluminosilicates (feldspars) in the stimulation range 5-40 eV: determination of the band-gap energies. Journal of Physics D: Applied Physics 37, 1439-1450.

Mondroe, D., 1985. Hopping in exponential band tails. Physical Review Letters 54, 146-149.

McKeever, S.W.S., 1985. Thermoluminescence of solids. Cambridge University Press, Cambridge, United Kingdom.

Morthekai, P., Thomas, J., Pandian, M.S., Balaram, V., Singvhi, A.K., 2012. Variable range hopping mechanism in band-tail states of feldspars: A time-resolved IRSL study. Radiation Measurements 47, 857-863.

Neudorf, C.M., Roberts, R.G., Jacobs, Z., 2012. Sources of overdispersion in a K-rich feldspar sample from north-central India: Insights from De, K content and IRSL age distributions for individual grains. Radiation Measurements 47, 696-702.

Poolton, N.R.J., Ozanyan, K.B., Wallinga, J., Murray, A.S., Bøtter-Jensen, L., 2002a. Electrons in feldspar II: a consideration of the influence of conduction

band-tail states on luminescence processes. Physics and Chemistry of Minerals 29, 217-225.

Poolton, N.R.J., Wallinga, J., Murray, A.S., Bulur, E., Bøtter-Jensen, L., 2002b. Electrons in feldspar I: on the wavefunction of electrons trapped at simple lattice defects. Physics and Chemistry of Minerals 29, 210-216.

Poolton, N.R.J., Kars, R.H., Wallinga, J., Bos, A.J.J., 2009. Direct evidence for the participation of band-tails and excited-state tunnelling in the luminescence of irradiated feldspars. Journal of Physics: Condensed Matter 21, 485–505.

Prasad, A.K., Poolton, N.R.J., Kook, M., Jain, M., 2017. Optical dating in a new light: A direct, non-destructive probe of trapped electrons. Scientific Reports 7, 12097.

Prasad, A.K., Jain, M., 2018a. Dynamics of the deep red Fe3+ photoluminescence emission in feldspar. Journal of Luminescence 196, 462-469.

Prasad, A.K., Jain, M., 2018b. Breakdown of Kasha's Rule in a ubiquitous, naturally occurring, wide bandgap aluminosilicate (feldspar). Scientific Reports 8, 810.

Preusser, F., Degering, D., Fuchs, M., Hilgers, A., Kadereit, A., Klasen, N., Krbetschek, M., Richter, D., Spencer, J.Q.G., 2008. Luminescence dating: basics, methods and applications. Eiszeitalter und Gegenwart – Quaternary Science Journal 57, 95-149.

Reimann, T., Tsukamoto, S., 2012. Dating the recent past (<500 years) by post-IR IRSL feldspar – Examples from the North Sea and Baltic Sea coast. Quaternary Geochronology 10, 180-187.

Reimann, T., Thomsen, K.J., Jain, M., Murray, A.S., Frechen, M., 2012. Single-grain dating of young sediments using the pIRIR signal from feldspar. Quaternary Geochronology 11, 28-41.

Riedesel, S., Brill, D., Roberts, H.M., Duller, G.A.T., Garrett, E., Zander, A.M.,

King, G.E., Tamura, T., Burow, C., Cunningham, A., Seeliger, M., De Batist, M., Heyvaert, V.M.A., Fujiwara, O., Brückner, H. and the QuakeRecNankai Team, 2018. Single-grain luminescence chronology of historical extreme-wave event deposits recorded in a coastal lowlands, Pacific coast of central Japan. Quaternary Geochronology 45, 37–49.

Roberts, H.M., 2008. The development and application of luminescence dating to loess deposits: a perspective on the past, present and future. Boreas 37, 483-507.

Roberts, R.G., Jacobs, Z., Li, B., Jankowski, N., Cunningham, A.C., Rosenfeld, A.B., 2015. Optical dating in archaeology: thirty years in retrospect and grand challenges for the future. Journal of Archaeological Science 56, 41-60.

Schaarschmidt, M, Fu, X., Li, B., Marwick, B., Khaing, K., Douka, K., Roberts, R.G., 2019. pIRIR and IR-RF dating of archaeological deposits at Badahlin and Gu Myaung Caves – First luminescence ages for Myanmar. Quaternary Geochronology 49, 262-270.

Smedley, R.K., Duller, G.A.T., Pearce, N.J., Roberts, H.M., 2012. Determining the K-content of single-grains of feldspar for luminescence dating. Radiation Measurements 47, 790-796.

Smedley, R.K., Glasser, N.F., Duller, G.A.T., 2016. Luminescence dating of glacial advances at Lago Buenos Aires (∼46°S), Patagonia. Quaternary Science Reviews 134, 59-73.

Spooner, N.A., 1992. Optical dating: Preliminary results on the anomalous fading of luminescence from feldspars. Quaternary Science Reviews 11, 139-145.

Spooner, N.A., 1994. The anomalous fading of infrared-stimulated luminescence from feldspars. Radiation Measurements 23, 625-632.

Telfer, D.J., Walker, G., 1978. Ligand field bands of Mn^{2+} and Fe^{3+} luminescence centres and their site occupancy in plagioclase feldspars. Modern Geology 6, 199-210.

Thiel, C., Buylaert, J.-P., Murray, A.S., Terhorst, B., Hofer, I., Tsukamoto, S., Frechen, M., 2011. Luminescence dating of the Stratzing loess profile (Austria) – Testing the potential of an elevated temperature post-IR IRSL protocol. Quaternary International 234, 23-31.

Thomsen, K.J., Murray, A.D., Jain, M., Bøtter-Jensen, L., 2008. Laboratory fading rates of various luminescence signals from feldspar-rich sediment extracts. Radiation Measurements 43, 1474-1486.

Trauerstein, M., Lowick, S., Preusser, F., Rufer, D., Schlunegger, F., 2012. Exploring fading in single grain feldspar IRSL. Quaternary Geochronology 10, 327-333.

Tsukamoto, S., Jain, M., Murray, A.S., Thiel, C., Schmidt, E., Wacha, L., Dohrmann, R., Frechen, M., 2012. A comparative study of the luminescence characteristics of polymineral fine grains and coarse-grained K- and Na-rich feldspars. Radiation Measurements 47, 903-908.

Valla, P.G., Lowick, S.E., Herman, F., Champagnac, J.-D., Steer, P., Guralnik, B., 2016. Exploring $IRSL_{50}$ fading variability in bedrock feldspars and implications for OSL thermochronometry. Quaternary Geochronology 36, 55-66.

Visocekas, R., 1985. Tunnelling radiative recombination in labradorite: Its association with anomalous fading of thermoluminescence. Nuclear Tracks and Radiation Measurements 10, 521-529.

Visocekas, R., Zink, A., 1995. Tunneling afterglow and point defects in feldspars. Radiation Effects and Defects in Solids 134, 265-272.

Wallinga, J., Murray, A.S., Duller, G.A.T., Törnqvist, T.E., 2001. Testing optically stimulated luminescence dating of sand-sized quartz and feldspar from fluvial deposits. Earth and Planetary Science Letters 193, 617-630.

Wallinga, J., 2002. Optically stimulated luminescence dating of fluvial deposits: a review. Boreas 31, 303-322.

Wang, Y., Chen, T., E, C., An, F., Lai, Z., Zhao, L., Liu, X.-J., 2018. Quartz OSL and K-feldspar post-IR IRSL dating of loess in the Huangshui river valley, northeastern Tibetan plateau. Aeolian Research 33, 23-32.

Wintle, A.G., 1973. Anomalous fading of thermoluminescence in Mineral Samples. Nature 245, 143-144.

Yukihara, E., McKeever, S.W.S., 2011. Optically stimulated luminescence. Fundamentals and Applications. Wiley, Chichester, United Kingdom.

Two

Materials and methods

2.1 Chemical and mineralogical methods

For the chemical and mineralogical analyses of the samples in this thesis, X-ray fluorescence (XRF) and X-ray powder diffraction (XRD) were performed. Details regarding the principles behind the methods and the instruments used are given in the following sections for both methods.

2.1.1 X-ray fluorescence

XRF is the result of the interaction of excitation radiation with a sample (Fig. 2.1A). Incident radiation with energy greater than the binding energy of electrons

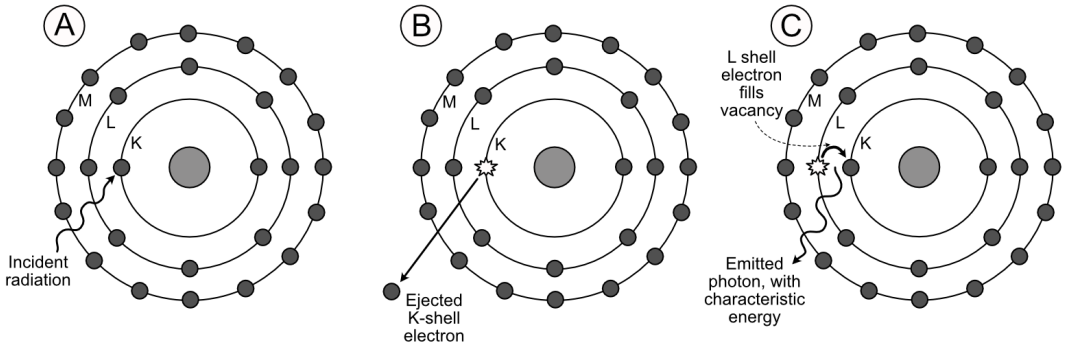

Figure 2.1: *Principle of X-ray fluorescence (modified from Margui and Van Grieken, 2013, p. 2). (A) Incident radiation with energy larger than the binding energy of an electron in an inner orbital causes absorption of this incoming energy. (B) Ionisation of the atom takes place by the ejection of the electron from an inner orbital (here K-shell electron). (C) The structure of the atom becomes unstable due to the ejection of the inner orbital electron. To restore stability, an electron from an outer orbital "falls" into the position of the previously ejected electron. During this transition, energy is emitted, which is characteristic for the energy difference of the two orbitals involved and gives information on the atom.*

in an inner atomic orbital/shell, causes ionisation of an atom by removal of an inner orbital electron from its position (Fig. 2.1B). The vacancy thus produced in the inner orbital causes instability of the atom. To restore stability, an electron from an outer orbital will "fall" into the vacant position. During this process energy is emitted as a photon. The energy of this photon is equal to the energy difference of the two orbitals involved. (Fig. 2.1C; Margui and Van Grieken, 2013, p. 1-3). XRF is widely used for element identification (qualitative XRF analysis) and calculation of the concentration of the respective element or oxide (semi-quantitative and quantitative XRF analysis) and has been applied in various contexts, including geological, geomorphological and archaeological studies (e.g. Shackley, 2010; Stevens et al., 2018).

In this thesis XRF measurements were performed using two different instruments: the chemical composition of samples used in Chapter 4 was determined using an XRF attachment to a Risø TL/OSL reader at the Department of Physics at the Technical University of Denmark and the chemical composition of samples used in Chapters 5 and 6 was determined using a PANalytical MagiX PRO XRF spectrometer at Sheffield Hallam University.

The XRF attachment to a Risø TL OSL reader consists of an Amptek Inc. Mini-X X-ray tube with an Au target operating at a tube power of 50 kV and 200 μA and an Amptek Inc. X123SDD X-ray spectrometer. The spectrometer is based on a silicon drift detector and has a resolution ranging from 125 eV to 140 eV. The XRF attachment operates under vacuum and the angle between incident radiation and characteristic X-ray fluorescence to the detector is 45° (M. Kook, personal communication). The operation of the instrument is achieved using the Sequence Editor software. For measurements, sample material was mounted as grains or crystal shards on Mo cups without silicone spray.

To enable a semi-quantification of the feldspar sample composition, a range of artificial calibration samples and certified reference material was measured using the XRF attachment to the Risø TL/OSL reader and on the basis of these results software (XRF analyse) was written by Dr Myungho Kook at the Department of Physics, Technical University of Denmark, which calculates the relative contributions of quartz, K-, Na- and Ca-feldspar of the samples using stoichiometry. This software was used for the semi-quantitative analyses of the samples used for the research in Chapter 4 and the results are given in Table 2.1.

XRF measurements of the samples presented in Chapters 5 and 6 were performed by Dr Anthony M.T. Bell (Materials and Research Engineering Institute,

Sheffield Hallam University) using a PANalytical MagiX PRO XRF spectrometer. For XRF and XRD measurements 1 g of sample material was finely ground in a mortar and pestle until the material did not feel gritty anymore, such that the grain size is expected to be ≤ 5 μm. For these XRF measurements 2 g of cellulose binder was placed into an Al sample boat. A subsample of the powdered sample (0.1 g) was then mixed with cellulose binder (0.1 g) and this mixture was spread on top of the cellulose binder in the Al sample boat. Each boat was then pressed at 20 t (using a Retsch RS200 press) into pellets for XRF measurements using a PANalytical MagiX PRO XRF spectrometer equipped with an Rh anode X-ray source. The spectra were collected over ten different energy ranges and then analysed to obtain semi-quantitative results. Elements could be detected over the range from F (Z = 9) to Am (Z = 95); it was not possible to detect elements lighter than F with this instrument as the X-ray energies for these lighter elements are too low in energy. F can be detected to ∼5 %, Na to ∼1 % and for the other detected elements the detection limit decreases with increasing atomic number. For the analyses, it was assumed that all elements, except for Cl, were present as oxides. The semi-quantitative XRF analyses were performed using the PANalytical IQ+ software and matrix absorption corrections were made. Individual sample compositions were calculated to give the molecular formula of the feldspar based on eight oxygen, following stoichiometry. To determine the feldspar compositions of the individual samples the following calculations were made:

Step 1: The wt% concentration of the measured oxide was divided by the molecular mass of the oxide; this was done for each oxide and the results are summed.

Step 2: The result of step 1 was subsequently used to scale it for the eight oxygen atoms, which are present in stoichiometric feldspar.

Step 3: The factor obtained in step 2 is needed to allow the calculation of the atoms needed per eight oxygen atoms in a feldspar, by multiplying the wt% of the oxide with the factor obtained in step 2 and dividing this by the molecular mass of the oxide.

Step 4: The triangular coordinates for the feldspar sample were calculated by

dividing the result of step 3 for Ca, Na and K individually, by the sum of these three atoms, i.e. to obtain the relative content of K-feldspar within a sample the K atoms per eight oxygen were divided by the sum of Ca, Na and K atoms per eight oxygen.

2.1.2 X-ray powder diffraction

X-ray powder diffraction (XRD) is used for the determination of the mineralogical composition of sediments and for phase-analysis of minerals, as well as for the determination of structural parameters of mineral samples (e.g. Hovis, 1989; Tucker, 1996, p. 177). Samples are powdered and consist of a large number of very small single crystals. In XRD, monochromatic X-rays are emitted from an anode onto a fine-grained sample (Fig. 2.2A). The sample is fixed on a sample holder, which rotates within the X-ray beam at a constant speed during measurement. The incident beam will get scattered from electrons in atoms within the sample material (Fig. 2.2A). Since the atoms in the crystal are arranged in a periodic array they are able to diffract X-rays (Fig. 2.2B). Diffraction only occurs when radiation with a wavelength of comparable lengths to the atomic spacing within a crystal is scattered (termed constructive interference). The diffracted X-rays can be detected and produce powder diffraction patterns, which are characteristic for the sample material. An example for X-ray diffraction patterns of sample FSM-13 is shown in Figure 2.3.

The method of X-ray diffraction is based on Bragg's law, which describes the condition for the angle of the incoming beam (θ) to the lattice plane to reflect back with the same angle of scattering. It also states that constructive interference will occur, because the wavelength of the incident beam λ is an integer n of the spacing between the lattice planes d.

$$n\lambda = 2d\,sin\theta \tag{2.1}$$

If two parallel beams of identical wavelength interfere with a crystal, then the lower beam will have to travel further than the upper beam until it becomes reflected from a lattice plane (Fig. 2.2B). The difference in distance between the upper and the lower beam gives information on the spacing between the lattice planes according to equation 2.1 (e.g. Tucker, 1996, p. 179-181; Allmann, 2003, p. 7-8). Diffractograms of powdered sample material are expressed as intensity (in counts) on the ordinate and 2θ on the abscissa. Whilst θ describes

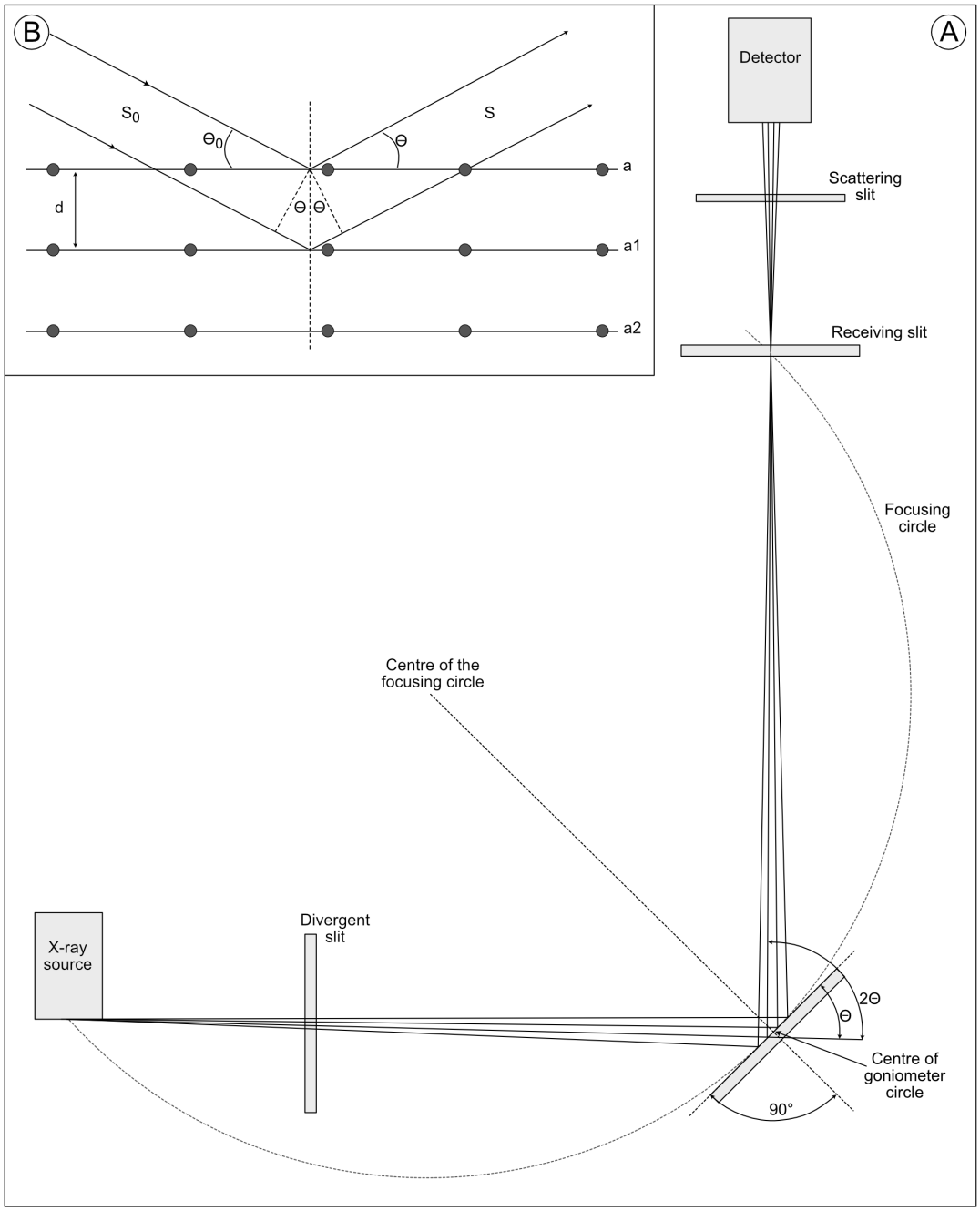

Figure 2.2: *(A) Schematic drawing of an X-ray diffractometer with Bragg-Brentano Geometry, routinely used for X-ray powder diffraction, and also used in this thesis (modified after Tucker, 1996, p. 180). (B) Principle of X-ray diffraction. a, a1 and a2 are lattice planes with atoms. d is the distance between the lattice planes, θ_0 the incoming beam and θ the diffracted beam (modified from Tucker, 1996, p. 181, and Allmann, 2003, p. 8).*

the angle between the incoming beam and the lattice plane, 2θ refers to the angle between the transmitted beam and the diffracted beam. Since XRD analyses the relationship between the wavelength of the incoming beam and the spacing of the lattice plane (Tucker, 1996, p. 179-181; Allmann, 2003, p. 7-8), XRD will only give information on properties inherent to the crystal which span multiple unit cells. Information on short range parameters, such as lattice disorder within one unit cell, cannot be obtained when using XRD. This should be kept in mind when assessing results.

For this thesis XRD was applied to determine the mineral phases present within single crystal samples and within a mixture of grains extracted from sediment and bedrock. The measurements were performed by Dr Anthony M.T. Bell at the Materials and Research Engineering Institute at Sheffield Hallam University (United Kingdom). The measurements were carried out using a PANalytical X'Pert MPD powder diffractometer operating with Cu Kα X-rays and a PIXCEL-1D area detector. Beta filters are placed between the sample and the detector, which remove 99 % of K-β lines, so that only K-α1 and K-α2 lines are detected. Please note that all 2θ mentioned in this chapter refer to 2θ recorded using Cu Kα X-rays. For these measurements 0.1 g of the powdered sample material (taken as a fresh aliquot from the powdered 1 g of sample material) was mounted on a low-background silicon XRD sample holder using acetone. Data were collected over the range of 5-100 degrees 2θ and each scan took just over 1 hour. Semi-quantitative phase-analyses were achieved using the PANalytical HighScore Plus software. The results of semi-quantitative phase analyses for samples used in Chapters 5 and 6 are given in Table 2.2 and 2.3 for single-crystal and grain mixtures, respectively.

For semi-quantitative phase analyses the diffractogram (see a diffractogram of sample FSM-13 in Fig. 2.3 as an example) was first compared to diffractograms of known phases (often referred to as powder diffraction file (PDF; International centre for diffraction data, https://www.icdd.com/), to identify the phases present in the sample by peak matching (intensity and d values) of diffraction peaks. Afterwards, the weight fractions of the phases present were determined semi-quantitatively by comparing the integrated intensities of the diffraction peaks of each of the phases present within the sample. Some diffraction peaks are not only indicators for the phases present within a sample, but also of crystallographic properties of the material, such as the structural state (e.g. Wright, 1968; Hovis, 1989). Diffraction peaks are denoted using the Miller indices (hkl),

which describe the orientation of a plane of atoms in a crystal. The three indices (hkl) are calculated based on the interceptions of the crystallographic planes with the axes of the unit cell (e.g. Allmann, 2003, p. 42-45). In feldspars there is a number of particularly important diffraction peaks, some of which are listed here and marked on the diffractogram in Figure 2.3. The $(\bar{2}01)$ peak occurs at a 2θ value between 20.95° and 22.05°, this peak helps in identifying the chemical composition of the sample and occurs at lower 2θ values for more K-rich feldspars, compared to more Na-rich feldspars (Hovis, 1989). Goldsmith and Laves (1954) and Garcia-Guinea et al. (1999) suggested to use the difference in spacing of the (131) and $(1\bar{3}1)$ diffraction peaks to evaluate the relative degree of disorder of Al^{3+} and Si^{4+} on the framework, since the difference in 2θ between these two peaks describes the triclinicity of the feldspar. An ordered triclinic feldspar would show both of these diffraction peaks. In a disordered monoclinic sanidine these two peaks would merge to a single peak. Another possibility to identify the type of feldspar one is examining was suggested by Wright (1968). According to Wright (1968) by creating a plot comparing the positions of the $(\bar{2}04)$ and (060) diffraction peaks, the structural state of the feldspars can be determined.

Another possibility used to obtain more information on the crystal structure, for instance to define the tetrahedral site occupancy, is a method termed Rietveld refinement (Rietveld, 1969). This method requires a starting crystal structure which is reasonably close to the actual structure of the material. From this known structure model theoretical diffraction pattern are calculated. A least-squares refinement process is then used to minimise the differences between the calculated and the measured diffraction pattern. The results can then be used to obtain information on e.g. phase quantities, site occupancy or unit cell parameters (e.g. Allmann, 2003, p. 217-219). This method was tried on some of the measured samples, however, due to the strong preferred orientation of the powdered sample material, this did not give good matches between the observed and calculated crystal structures therefore this method was not applicable.

2.2 Samples

In this thesis single crystal feldspar specimens and grain mixtures of feldspars extracted from sediment and bedrock (using density separation) were used. The samples explored in Chapter 4 are mainly grain mixtures, but also three single crystal specimen and one feldspar sample, which had been used in an inter-

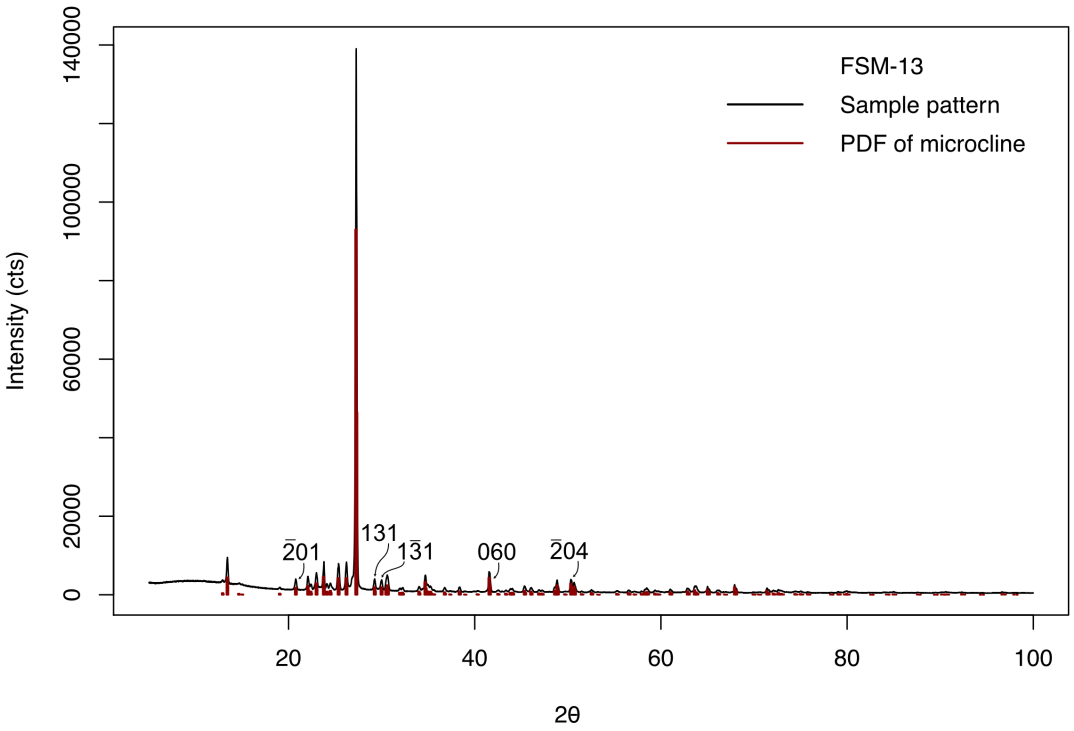

Figure 2.3: *X-ray diffraction pattern of sample FSM-13 and of the matched reference powder diffraction file (PDF) of microcline.*

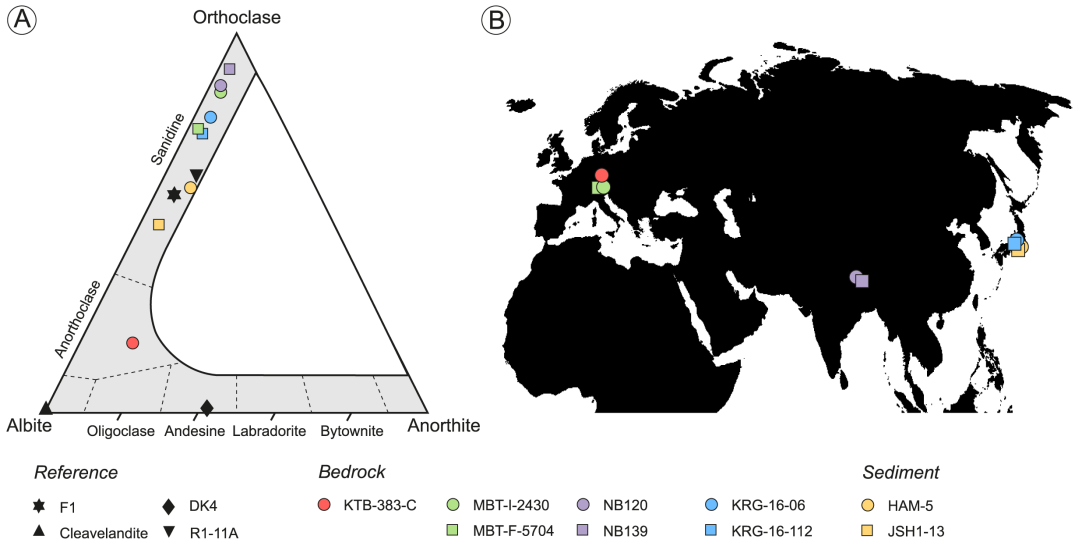

Figure 2.4: *Feldspar ternary diagram of the chemical composition of samples used in Chapter 4 and a simplified map that shows the geographical location of the sampling site (Figure from Chapter 4). Please note that the term orthoclase in this figure refers to the K-feldspar end member, albite to the Na-feldspar end member and anorthite to the Ca-feldspar end member.*

Table 2.1: *List of samples used in Chapter 4, their chemical composition determined using the Risø XRF OSL/TL reader attachment, (Kook et al., 2012) and geological origin. Reference cited in this table correspond to literature in which the samples have been used previously in luminescence studies. The table is already published in Riedesel et al. (2019, see Chapter 4).*

ID	Type[a]	Origin	Chemical composition[b] (FS %[c]) Or	Ab	An	Quartz (%)	Geological age	Reference
NB139	Bedrock	Migmatitic gneiss, Namche Barwa, Nepal	89.3	9.4	1.4	4.2	Proterozoic (Burg et al., 1997)	King et al. (2016)
NB120	Bedrock	Migmatitic gneiss, Namche Barwa, Nepal	86.2	11.0	2.9	5.0	Proterozoic (Burg et al., 1997)	King et al. (2016)
MBT-I-2530	Bedrock	Calc-alkaline granite, Mont Blanc Tunnel, Italy	86.7	12.0	1.3	4.2	∼300 Ma (Bussy et al., 1989; Bussy and Von Raumer, 1993)	Lambert,2018)
MBT-F-5704	Bedrock	Calc-alkaline granite, Mont Blanc Tunnel, Italy	76.3	22.5	1.2	4.6	∼300 Ma (Bussy et al., 1989; Bussy and Von Raumer, 1993)	Lambert,2018
KRG-16-06	Bedrock	Kurobegawa granite, Japanese Alps, Japan	79.4	17.3	3.2	3.1	<10 Ma (Ito et al., 2013)	
KRG-16-112	Bedrock	Kurobegawa granite, Japanese Alps, Japan	75.2	21.3	3.5	3.4	<10 Ma (Ito et al., 2013)	
R1-11A	Museum	Rapakivi Granite, Southern Greenland	68.0	22.0	10.0	0.0	c. 1750 Ma (Finch and Klein, 1999)	Harrison et al. (1990), Finch and Klein (1999)
F1	IAEA AQCS Ref. Feldspar	NA	61.3	33.4	5.4	0.3	NA	IAEA (1999), Sanderson and Clark (1994), Clark and Sanderson (1994)
JSH1-13	Sediment	Shirasuka lowlands, Japan	50.4	37.6	12.1	38.1	NA	Riedesel et al. (2018)
HAM-5	Sediment	Lake Hamana, Japan	64.9	31.1	4.0	19.3	NA	
KTB-383-C	Bedrock	KTB borehole, Germany	18.2	67.6	14.4	52.8	NA	Guralnik et al. (2015)
Cleavelandite	Museum	Golonca District, Minas Gerais, Brazil	0.5	99.3	0.2	3.9	650-450 Ma (Cassedanne and Roditi, 1996)	NA
DK4	Museum	Klokken intrusion, South Greenland	5.0	36.0	59.0	0.0	1.18 Ma)	NA

[a]Museum specimen are single crystals, the IAEA reference feldspar, feldspars extracted from bedrock and sediment samples were mounted as coarse multiple-grain aliquots

[b]Determined by XRF measurements

[c]Assuming 100 % feldspar.

Table 2.2: *Details regarding the origin, chemical composition, phases and size of perthite lamella for samples investigated in Chapter 5 and 6. The chemical composition in % feldspars, was done using stoichiometric conversion of the semi-quantitative XRF data. Chemical composition and present phases of R1-11A was taken from Harrison et al. (1990). The presence of particular phases is based on semi-quantitative XRD analyses at Sheffield Hallam University.*

Sample ID	Origin	Chemical composition (FS %)			Phases						Perthite development	Reference
		K-FS	Na-FS	Ca-FS	Microcline	Orthoclase	Sanidine	Albite	Anorthite	Other		
FSM-13	Brazil	98.5	1.5	0.0	100	-	-	-	-	-	None	-
FSM-13LH	Brazil	98.5	1.5	0.0	100	-	-	-	-	-	None	-
FSM-3	Granite pegmatite, Toe Head, South Harris, Scotland, UK (Cunningham, 1981)	82.5	17.2	0.3	78.0	-	-	22.0	-	-	Sub-optical scale	-
R1-11A	Rapakivi Granite, South Greenland	81.0	19.0	1.0	Microcline and albite (Harrison et al., 1990)						Cryptoperthite	Harrison et al., 1990; Finch and Klein, 1999
FSM-15	Quebec, Canada	80.4	19.6	0.0	82.0	-	-	18.0	-	-	Sub-optical scale	-
FSM-14	Iveland, Southern Norway	78.3	21.2	0.5	54.0	-	-	46.0	-	-	Sub-optical scale	-
FSM-8	Norway	77.1	22.6	0.3	68.0	-	-	32.0	-	-	Sub-optical scale	-
FSM-7	Unknown	76.8	22.0	1.2	48.0	-	-	51.0	-	1.0	Sub-optical scale	-
FSM-5	Unknown	74.8	25.2	0.0	57.0	-	-	43.0	-	1.0	Macroperthite	-
FSM-6	Granite pegamite, Trezaise Quarry, Cornwall, UK (see Ussher et al., 1909)	74.4	25.3	0.3	-	38.0	-	62.0	-	1.0	Sub-optical scale	-
FSM-6LH	Granite pegamite, Trezaise Quarry, Cornwall, UK (see Ussher et al., 1909)	74.4	25.3	0.3	-	-	100.0	-	-	-	None	-
FSM-11	Perth, Canada	65.2	34.8	0.0	62.0	-	-	38.0	-	1.0	Macroperthite	-
Al-I	Pinzele, Trente, Italy	1.0	97.0	2.0	-	-	-	95.0	-	5.0	None	-
CLBR	Pegmatite, Golonca District, Minas Gerais, Brazil	0.5	99.3	0.2	-	-	-	100.0	-	-	None	Rendell and Clarke (1997); Garcia-Guinea et al., 1999

Table 2.3: *Details on feldspar extracted from sediment and bedrock samples used in Chapter 6. The chemical composition in % feldspars, was done using stoichiometric conversion of the semi-quantitative XRF data. Present phases are based on semi-quantitative XRD analyses.*

Sample ID	Origin	Chemical composition (FS %)			Phases						Perthite development	Reference
		K-FS	Na-FS	Ca-FS	Microcline	Orthoclase	Sanidine	Albite	Anorthite	Other		
MBT-I-2430	Mont Blanc, Italy	86.1	13.4	0.6	85.0	-	-	15.0	-	-	-	Lambert,2018
HAM-5	Lake Hamana, Japan	70.4	27.2	2.4	-	30.0	-	27.0	-	43.0	-	
WHB-7	Channelled Scablands, Washington State, USA	63.9	31.5	4.6	37.0	-	-	30.0	-	33.0	-	-

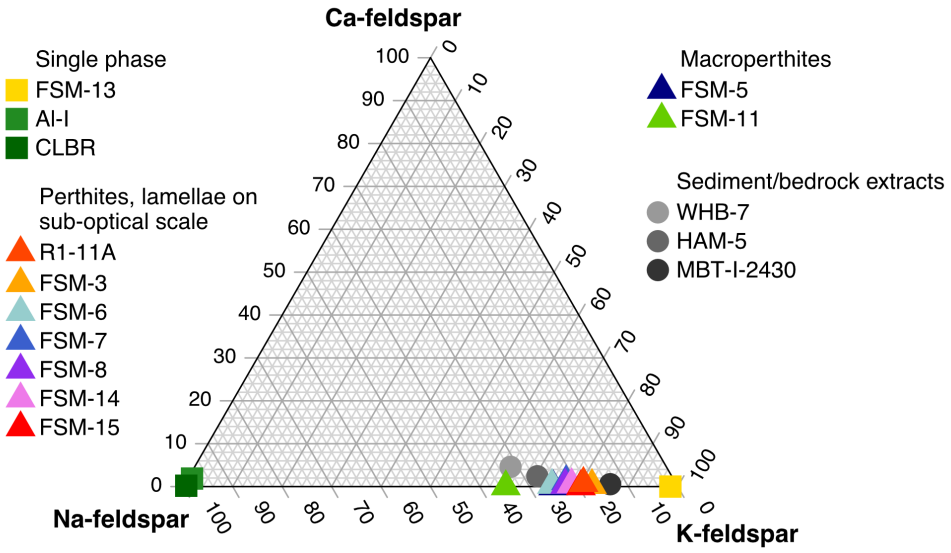

Figure 2.5: *Feldspar ternary diagram of samples used in chapter 6, some of these samples were also used in Chapter 5. The position of the samples on the feldspar ternary is based on XRF results and a conversion of K_2O, Na_2O and CaO contents using stoichiometry. Single-phase feldspars are displayed as squares, perthites as triangles and samples used for optical dating of sediments and thermochronometry as circles.*

laboratory comparison by the International Atomic Energy Agency (IAEA, sample: F1), were used. The samples were selected to represent a wide range of chemical compositions, and it was important that the samples represented material commonly used in luminescence dating studies. In contrast samples used in the research presented in Chapters 5 and 6, were mainly single crystal specimens. The grain mixtures used in Chapter 4 contained not only feldspar grains, but also other minerals which were not completely removed by density separation, mainly quartz. The purity of these samples was checked under a microscope and most of the unwanted minerals were removed by handpicking individual non-feldspar grains. The use of single crystal specimens enabled the analysis of luminescence properties of pure feldspar samples and also allowed investigations into the mineralogical properties of the samples, such as the phases present in a single crystal, the size of perthite lamellae and the relative degree of disorder of Al^{3+} on the framework.

The samples studied in this thesis are described below. Some of the samples were kindly provided by supervisors (Prof G.A.T. Duller, Prof N.J. Pearce) and collaborators (Prof Adrian A. Finch, Dr. Benny Guralnik, Prof Georgina E. King, Dr Renske Lambert, Prof D.C.W. Sanderson). Others were purchased for this thesis from commercial suppliers (Edmonton Mineral Fair, Canada, and A Bijoux

Minerals, France). The relative proportions of K-, Na- and Ca-feldspar are given for each sample in common notation and are described as the relative proportions of each feldspar as determined using XRF, and denoted as Or for Orthoclase or K-feldspar, Ab for albite or Na-feldspar and An for anorthite or Ca-feldspar (Figs. 2.4 and 2.5). In the literature the pure K alkali feldspar end member is termed K-feldspar or orthoclase. The term orthoclase is also used as a term for the structural state of a specific type of feldspar. To avoid any confusion, the alkali feldspar end member is referred to as K-feldspar in this thesis, and orthoclase is used as for the structural state of an alkali feldspar with monoclinic symmetry, but where the tetrahedral site occupancy is not fully disordered. Since Chapter 4 is already published and here the term orthoclase was used for the pure K alkali feldspar end member, this terminology was kept in Chapter 4.

Additionally, it should be mentioned prior to the presentation of the samples, that the relative proportions of K-, Na- and Ca-feldspar, determined using XRF, and the results of the semi-quantitative phase-analysis using XRD might seem to indicate different results (Table 2.2 and 2.3). For example perthite sample FSM-6 has been defined as $Or_{74.4}Ab_{25.3}An_{0.3}$, but according to the phase analysis this sample consist of 38 % microcline and 62 % albite. These differences occur, because the two methods (XRF and XRD) used are complimentary methods. XRF detects elements, and it can also detect elements present in amorphous materials. In contrast, XRD can only detect crystalline components; no amorphous material can be detected, and neither can elements or oxides, which are not included in the mineral phases present. The elements detected by XRF are assumed to be present as oxides for feldspar analysis. The oxides detected using XRF are then used for the phase identification using XRD. However, only the oxides present, not their content is used for the phase identification. As an example: when searching the XRD library for potential matching phases, it is included that the phase may contain Al_2O_3, but not that it contains a certain percentage of given oxide. Additionally, during qualitative phase analysis, it is assumed that the phases present have exactly the same stoichiometry as is given on the powder diffraction file (PDF, see chapter 2.1.2) for the phase. Therefore the allocation of a sample regarding its relative proportions of K-, Na- and Ca-feldspar (Table 2.1, 2.2 and 2.3; Fig. 2.5 and 2.6) is based on their chemical composition determined using XRF. The semi-quantitative phase analyses performed using XRD are complementary results, which are used to define the phases present in the sample, but not for the chemical allocation of the sample on ternary diagrams

such as in Figure 2.5 and 2.6 (see Loubser and Verryn, 2008, for further details regarding the complementary use of XRF and XRD analyses of minerals).

Sample DK4 ($Or_{0.5}Ab_{36.0}An_{59.0}$ is a plagioclase, only presented in Chapter 4) was taken from the Klokken Intrusion in South Greenland.

CLBR ($Or_{0.5}Ab_{99.3}An_{0.2}$), is a single-phase albite from a pegmatite in the Golonca District, Minas Gerais, Brazil. This sample is termed Cleavelandite in Chapter 4. CLBR has previously been studied for its luminescence properties by Rendell and Clarke (1997) and Garcia-Guinea et al. (1999). The other albite sample explored here is Al-I ($Or_{1.0}Ab_{97.0}An_{2.0}$). This sample originates from Pinzele, Trente, Italy and contains 5 % quartz, based on semi-quantitative phase analysis using XRD (Table 2.2).

FSM-13 is a single-phase microcline ($Or_{98.5}Ab_{1.5}An_{0.0}$) from Brazil (Table 2.2); the exact sampling location is unknown.

In total nine perthites were studied, this includes crypto-/micro- and macroperthites with K-feldspar end-member contents ranging from 82.5 mol % to 74.4 mol %. The perthites were examined visually, using a hand lens. If the perthite lamellae were visible with the naked eye or by using the hand lens then the samples were classified as macroperthites. If the lamellae were not visible by eye, but the XRD results described the samples as two-phase feldspars, then they were classified as perthites with lamellae on the sub-optical scale, which includes micro- and cryptoperthites. Most of the perthites consist of microcline and albite as the two mineral phases present, only FSM-6 ($Or_{74.4}Ab_{25.3}An_{0.3}$, originating from a granite pegmatite, Trezaise Quarry, Cornwall, United Kingdom) consists of orthoclase and albite, and is thus expected to be slightly more disordered on tetrahedral sites than perthites that consist of microcline and albite. The only perthite of this collection previously studied regarding its luminescence behaviour is R1-11A ($Or_{81.0}Ab_{19.0}An_{1.0}$, Rapakivi Granite, South Greenland). Finch and Klein (1999) used this sample for cathodoluminescence studies, combined with electron paramagnetic resonance (EPR). Detailed chemical analyses of this sample were performed by Harrison et al. (1990). Based to the results by Harrison et al. (1990), R1-11A can be classified as a cryptoperthite. Other perthites with lamellae on the sub-optical scale studied in this thesis are FSM-3 ($Or_{82.5}Ab_{17.2}An_{0.3}$, Toe Head, South Harris, Scotland, United Kingdom), FSM-15 ($Or_{80.4}Ab_{19.6}An_{0.0}$, Quebec, Canada), FSM-14 ($Or_{78.3}Ab_{21.2}An_{0.5}$, Iveland, South Norway), FSM-8 ($Or_{77.1}Ab_{22.6}A_{0.3}$, Norway, exact location unknown) and FSM-7 ($Or_{76.8}Ab_{22.0}An_{1.2}$, location unknown). Macroperthites studied are FSM-

5 ($Or_{74.8}Ab_{25.2}An_{0.0}$, unknown origin) and FSM-11 ($Or_{65.2}Ab_{34.8}An_{0.0}$, Perth, Canada).

Sample F1 ($Or_{61.3}Ab_{33.4}An_{5.4}$) is an International Atomic Energy Agency (IAEA) reference feldspar. No XRD was performed on this sample, but according to the findings by Alexander (2007, p. 127, p. 174) it can be described as a patch microperthite. Its luminescence has been studied previously by Clark and Sanderson (1994), Sanderson and Clark (1994) and Alexander (2007).

In Chapter 4 and 6 a total of ten grain mixtures extracted from sediment and bedrock were used. The sediment samples (HAM-5, JSH1-13 and WHB-7) were prepared in the laboratory prior to any luminescence measurements. The sample material of HAM-5 ($Or7_{70.4}Ab_{27.2}An_{2.4}$) and JSH1-13 ($Or_{50.4}Ab_{37.6}An_{12.1}$) was treated using hydrochloric acid (HCl; 10 %), hydrogen peroxide (H_2O_2; 10 %) and sodium oxalate ($Na_2C_2O_4$; 0.01N) to remove carbonates, organic matter and to disperse the particles. Samples were dry sieved to separate the 100 μm to 200 μm fraction that was then density separated using sodium polytungstate to isolate alkali-feldspar fractions ($\rho < 2.58$ g cm^{-3}). For WHB-7 ($Or_{63.9}Ab_{31.5}An_{4.6}$) the chemical pre-treatment was identical to the other two sediment extracts, but for WHB-7 the material was sieved to 180-212 μm and density separated to 2.53 g cm^{-3} $< \rho <$ 2.58 g cm^{-3}. The bedrock extracts were obtained by crushing the rock; subsequently the material was sieved to isolate the fraction of 180-212 μm. This fraction was then treated with 10 % HCl and 20 vols of H_2O_2 to remove carbonates and organic material, respectively. The K-feldspar fraction was isolated using sodium polytungstate at a density of 2.58 g cm^{-3}. The density separated sample material of KTB-383-C ($Or_{18.2}Ab_{67.6}An_{14.4}$) was also etched in 10 % HF for 40 min and subsequently washed in 10 % HCl, aiming at the removal of fluorides which might have formed during HF etching (see supplementary material of Guralnik et al., 2015 for details regarding the sample preparation procedure of KTB-383-C). Some of the samples extracted from crushed bedrock and sediments were used previously in luminescence dating studies: JSH1-13 has been collected from a tsunami deposit identified within a sediment core from the Pacific coast of central Japan and has been dated by Riedesel et al. (2018). NB120 ($Or_{86.2}Ab_{11.0}An_{2.9}$) and NB139 ($Or_{98.3}Ab_{9.4}An_{1.4}$) are thermochronometry samples from Namche Barwa in the Himalaya (King et al., 2016). KTB-383-C was taken from the KTB-borehole in south-east Germany and was used for thermochronometry by Guralnik et al. (2015). MBT-I-2403 ($Or_{86.7}Ab_{12.0}An_{1.3}$) and MBT-F-5704 ($Or_{76.3}Ab_{22.5}An_{1.2}$) are also thermochronometry samples (Lambert,

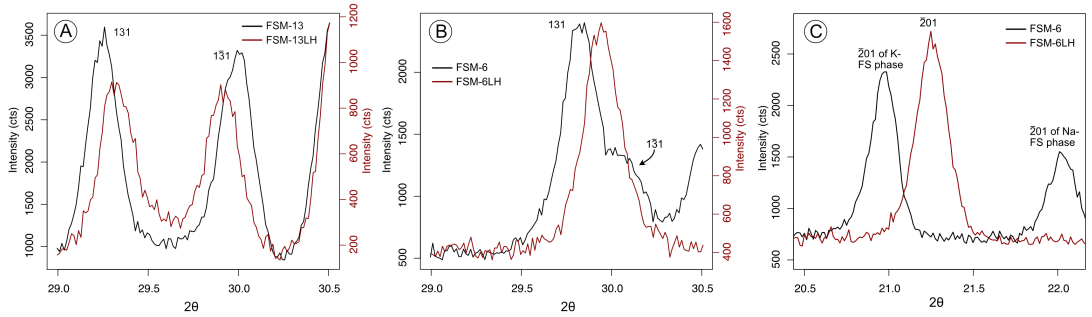

Figure 2.6: *X-ray diffraction pattern of feldspar samples FSM-13 and heated material FSM-13LH (A), as well as FSM-6 and heated material FSM-6LH (B). The figures show the comparison of the (131) and (1$\bar{3}$1) diffraction peaks of all four samples. One would expect one defined peak in a disordered sanidine sample, and two individual peaks ((131) and (1$\bar{3}$1)) in an ordered microcline (cf. Garcia-Guinea et al., 1999). In both samples, subtle changes to the two diffraction peaks are visible. In (A) the diffraction peaks move closer together due to the heating and rapidly cooling of the sample. Nevertheless, still two individual peaks are visible. In the case of FSM-6 and FSM-6LH (B), only a single peak is visible after the heating experiment, and the remainder of the (1$\bar{3}$1) peak, visible as a shoulder in FSM-6, disappears. C) Comparison of the $\bar{2}$01 diffraction peak in perthite FSM-6 and in sanidine FSM-6LH. The heating experiment caused a homogenisation of the distribution of K^+ and Na^+ ions within the crystal. Whilst FSM-6 shows two $\bar{2}$01 diffraction peaks (on for each phase), FSM-6LH only shows a single diffraction peak, reflecting the homogeneous distribution of the cations.*

2018) and they originate from the Mont Blanc Massif in Italy and France. KRG-16-06 ($Or_{79.4}Ab_{17.3}An_{3.2}$) and KRG-16-112 ($Or_{75.2}Ab_{21.3}An_{3.5}$) originate from the Kurobegawa granite in the Japanese Alps. HAM-5 originates from a tsunami deposit within the sedimentary record of coastal Lake Hamana (Pacific coast of central Japan) and WHB-7 was taken from glacial lake outburst flood deposits at the White Bluffs site in the Channelled Scablands (Washington State, United States of America).

In addition to these samples, which reflect a variety of chemically and mineralogically different feldspars, two samples, single-phase microcline FSM-13 and perthite FSM-6, were selected for a laboratory heating experiment. The heating experiment was designed to artificially disorder the tetrahedral site occupancy of Al^{3+} ions. To explore the effect of Si and Al disorder on luminescence properties, 0.5 g of powdered sample material of samples FSM-6 and FSM-13 (referred to as FSM-6LH and FSM-13LH after heating) were placed in acid cleaned Pt crucibles and heated to 105 °C overnight to remove any potential liquid present in the sample material. The Pt crucibles with the sample material were then placed in a preheated furnace at 1050 °C and covered with fitted Pt lids. The temperature was controlled by the furnace temperature control. To retain the disordered structure, the samples were rapidly cooled to room temperature within less than 1 min by placing the Pt crucibles in cooled sample holders. FSM-6 and FSM-13

were heated for different durations: 10 days for FSM-6LH compared to 5 days for FSM-13LH. This is due to the different degree of framework disorder achieved during this experiment. Since FSM-13 did not reveal any changes in Al^{3+} order after 5 days of heating. A new aliquot was heated, this time for 10 days. This longer heating procedure resulted in a change in Al^{3+} order, as visible in Figure 2.6A. To evaluate the success of the experiment, X-ray diffraction pattern of the unheated and heated material of the two samples was compared (Fig. 2.6A, B). X-ray diffraction patterns of the unheated and heated material of both sample pairs reveal differences linked to states of Al-Si order (Fig. 2.6A, B). The method described by Garcia-Guinea et al. (1999), which qualitatively evaluates the triclinicity of the sample material by comparing the positions and shapes of the (131) and ($1\bar{3}1$) diffraction peaks (see Chapter 2.1.2 for further details), was chosen to evaluate the success of the heating experiment. From Figure 2.6 it becomes apparent that the two starting materials of FSM-13 and FSM-6 already showed different diffraction patterns: Whilst FSM-13 shows two fully defined diffraction peaks between 29° and 32° 2θ, FSM-6 shows a single peak at 29.8° 2θ with a minor peak around 30° 2θ. This was expected since the qualitative phase analyses of FSM-13 revealed microcline as the mineral phase present, whereas FSM-6 consists of albite and orthoclase (Table 2.2). Orthoclase is more disordered than microcline, and whilst orthoclase has a monoclinic structure, microcline has a triclinic structure (see Chapter 3.2 for further details). As a result of the heating experiment the two individual peaks in the diffractogram of FSM-13 (Fig. 2.6A) move closer together (see red line) and the shoulder in the diffraction pattern of FSM-6 (Fig. 2.6B) disappears and only a single diffraction peak around 30° 2θ is visible in the diffractogram of FSM-6LH (Fig. 2.6B, red line). This shows that the heating experiment is successful for both samples, but that the heated material of FSM-6LH is more disordered compared to FSM-13LH.

In addition to changes of the tetrahedral site occupancy by Al^{3+}, prolonged heating is expected to influence the distribution of K^+ and Na^+ ions within the perthitic sample FSM-6. Whilst semi-quantitative phase analyses of the unheated sample FSM-6 characterised it as two-phase, consisting of albite and orthoclase, the heated sample FSM-6LH is characterised as sanidine. In sanidine Na^+ and K^+ ions are distributed evenly throughout the crystal and not separated in perthite lamellae of K- and Na-feldspar. This is particularly visible when comparing the position of the ($\bar{2}01$) diffraction peak (Deer et al., 2013, p. 260). In perthitic sample FSM-6 are two ($\bar{2}01$) peaks, one for each phase (at 20.98° 2θ for the

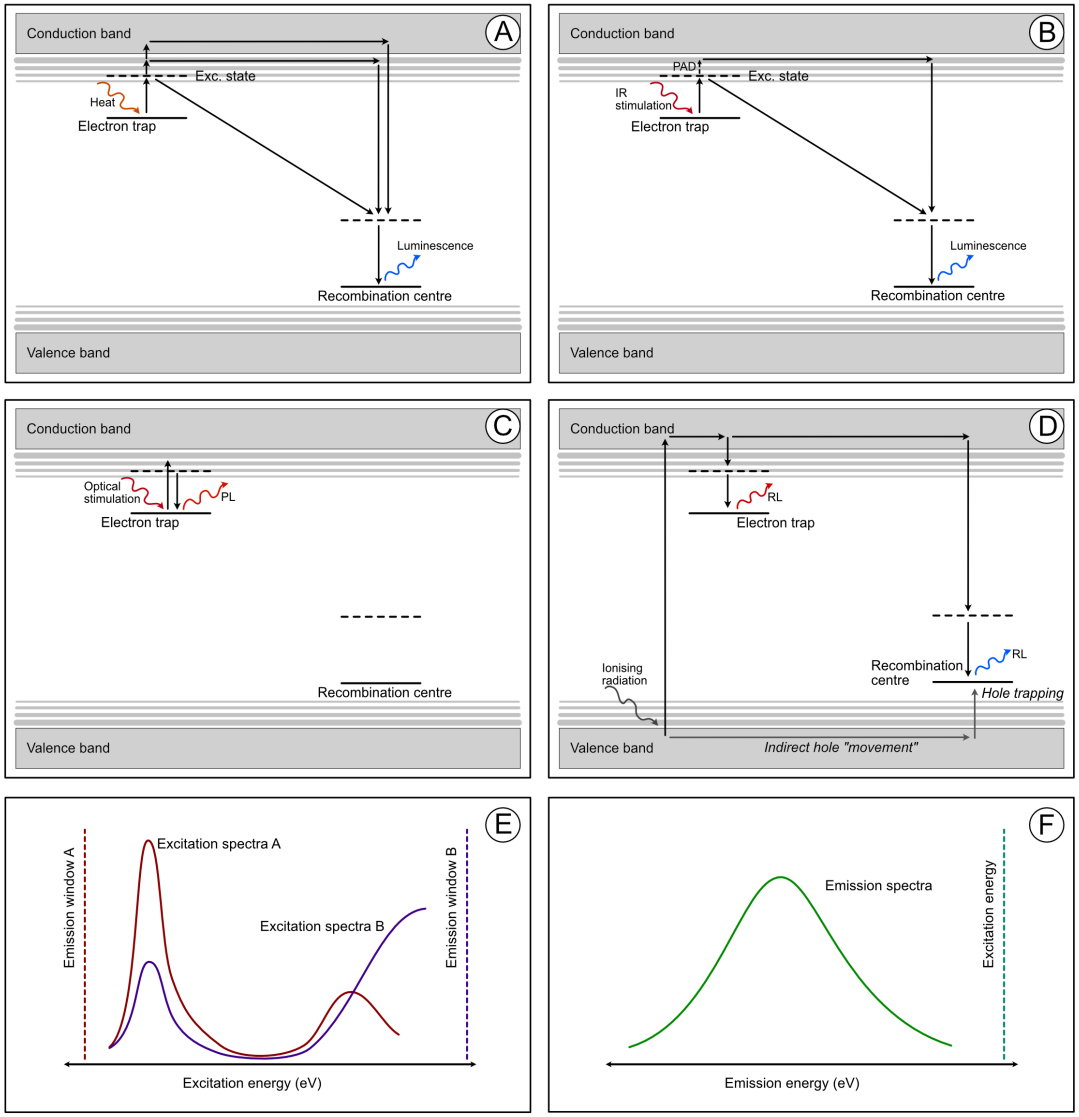

Figure 2.7: *(A) Thermoluminescence, (B) Infrared stimulated luminescence (IRSL), PAD refers to phonon assisted diffusion, (C) Photoluminescence, (D) Radioluminescence, (E) Excitation spectrum, (F) Emission spectrum.*

microcline phase, at 22.01° 2θ for the albite phase). In contrast, there is only a single $(\bar{2}01)$ diffraction peak in FSM-6LH at 21.25° 2θ (Fig. 2.6C).

2.3 Luminescence methods used in this thesis

To probe trapped charge in solids, e.g. feldspars, a variety of luminescence methods have been developed. In this PhD thesis a range of these luminescence methods are used to constrain physical parameters governing electron trapping, and electron-hole recombination in feldspar. The methods used during the course of the PhD are explained in this chapter.

2.3.1 Thermoluminescence

Thermoluminescence (TL) describes the phenomena of light emitted due to radiative recombination of electrons, which were thermally excited from their trap, with luminescence centres (Fig. 2.7A). As the temperature is increased linearly, the intensity of the emitted light varies and may form one or more peaks (Aitken, 1985, p. 47-48). It has been under debate, whether the different peaks in TL curves observed in feldspar reflect a distribution of electron traps (e.g. Strickertsson, 1985; Kirsh et al., 1987) or an underlying distribution of distances between electron trap and hole trap (Pagonis and Brown, 2019). These TL peaks not only occur at different temperatures, but also in different wavelengths, dependent on the crystal defect, which gives rise to the specific coloured emission (e.g. Krbetschek et al., 1997). Thermoluminescence has been used as a dating method, particularly to date heated material, e.g. pottery and flint, in archaeological contexts (e.g. Aitken, 1985). In Chapter 5 of this thesis, thermoluminescence emission spectra of a variety of feldspars are presented and analysed with a focus on potential variations in TL emissions caused by the chemical composition or the structural state of the feldspar sample.

2.3.2 Optically stimulated luminescence and infrared stimulated luminescence

Optically stimulated luminescence (OSL) is the result of electron-hole recombination following optical excitation of electrons from electron traps (Fig. 2.7B). Optically stimulated luminescence is a broad term for this phenomenon and is widely used to describe the process when using blue (∼470 nm) or green (∼530 nm) optical stimulation, for instance when dating quartz (e.g. Huntley et al., 1985; Murray and Wintle, 2000). Since feldspars are routinely stimulated using infrared (typically ∼830 to ∼880 nm) photons (e.g. Hütt et al., 1988; Wallinga et al., 2000), the method is referred to as infrared stimulated luminescence (IRSL). The use of infrared photons to stimulate trapped electrons in feldspar is based on the discovery of an IR resonance peak in excitation spectra of K-feldspar (Hütt et al., 1988). The optical stimulation using IR photons enables the excitation of the electron from the ground state of the electron trap to the excited state. Thermo-optical processes, so the combination of optical stimulation and heating, enables further excitation of the electron (Hütt et al., 1988). The presence of sub-conduction band-tail states in feldspars (e.g. Poolton et al., 2009) enable

hopping of the excited electron and thus allow further mobility (e.g. Morthekai et al., 2012). Phonon-assisted diffusion enables electron mobility in high band-tail states (Jain and Ankjærgaard, 2011). IR photons as a stimulation source enable the recording of a wide range of emissions. Usually OSL and IRSL are used as anti-Stokes processes it means that the emission wavelength recorded has a shorter wavelength than the stimulation light. In IRSL, the emission is routinely recorded in the blue (∼410 nm) (e.g. Thomsen et al., 2008; Buylaert et al., 2012), but other signals have also been explored (e.g. Krause et al., 1997; Sohbati et al., 2013). Since the energy of the excitation light is smaller than the trap depth of the electron trap in feldspar, the band-tail states play an important role in charge recombination processes in IRSL (Poolton et al., 2009). Additionally, measurements at elevated temperatures enable phonon assisted diffusion (PAD), which enables electron mobility in higher band-tail states (Jain and Ankjærgaard, 2011). In Chapter 6 fading of the IRSL signal is measured for selected alkali feldspars and their end members, with the aim of understanding the drivers behind differences in IRSL fading rates of chemically and structurally different feldspar.

2.3.3 Photoluminescence

Photoluminescence (PL) describes the light emitted, due to radiative relaxation of an electron, which was stimulated with photons (Waychunas, 2014; Fig. 2.7C). Whilst OSL describes the light emitted due to electron-hole recombination, PL is associated with the excitation and subsequent relaxation of an electron within one defect. In this thesis PL experiments are conducted on feldspars: In Chapter 4 a type defect with emission in the green is probed by excitation in the green (with excitation light being 20 nm shorter than the shortest wavelength of the emission) to give information on the width of the sub-conduction band-tail states. In Chapter 5, PL with excitation and emission in the infrared (IRPL) is used to gain further knowledge on electron trapping centres in feldspars.

2.3.4 Radioluminescence

Radioluminescence (RL, Fig. 2.7D) occurs due to the trapping of electrons in electron traps during exposure to ionising radiation. The electron is ionised from the valence band and moved into the conduction band, from where it may becomes trapped in an electron trap below the conduction band (Fig. 2.7D). If

the transition from the excited state of the trap to the ground state is radiative then the emission is termed radioluminescence (Trautmann et al., 1999; Kumar et al., 2018). RL upon X-ray irradiation is sometimes referred to as XEOL (X-ray excited optical luminescence). Since RL reflects a trap filling process, the intensity of the emitted light decreases with increasing irradiation time as the trap becomes filled, which is in contrast to TL and OSL/IRSL methods, where an increase in irradiation dose results in an increase in luminescence intensity. In Chapter 5, the radioluminescence of feldspars with emissions in the infrared is explored.

2.3.5 Excitation spectroscopy

Excitation spectra show the change in emitted light intensity of a single wavelength or emission window as a function of the excitation wavelength (Fig. 2.7E, Hamilton et al., 1978, p. 154). High intensities in an excitation spectrum indicate that the electrons trapped in crystal defects are particularly sensitive to optical stimulation at that specific wavelength, which results in the excitation of such electrons due to the absorption of the incident photons. Subsequent radiative relaxation within the same defect or in another defect (due to recombination) results in intense emissions. Thus, excitation spectra give information on electronic transitions, which result in the emission of photons (Waychunas, 2014), e.g. the transition from the ground state of the defect to various excited states or even to the conduction band and subsequent relaxation. Chapter 3 presents a variety of studies, which have used excitation spectroscopy to investigate physical properties of feldspar. Excitation spectra of feldspar are recorded with emissions in the UV (Chapter 4) and in the infrared (Chapter 5) in this thesis and are used to constrain the trap depth of the electron in feldspar, as well as the position of the characteristic infrared resonance.

2.3.6 Emission spectroscopy

Emission spectra are recorded using either a broad-band excitation (e.g. heat in thermoluminescence emission spectra or infrared light in infrared stimulated luminescence emission spectra) or a single excitation wavelength (e.g. by using a laser or a monochromatic beam of light extracted from a white light source using a grating system); the emission of the sample is recorded at a range of wavelengths (Fig. 2.7F, Hamilton et al., 1978, p. 156). Chapter 3 highlights studies

Table 2.4: *Specifications of luminescence readers used during the course of the PhD at the Aberystwyth Luminescence Research Lab (ALRL, United Kingdom) and the Risø National Laboratory (Denmark). All readers are equipped with blue and IR LEDs for stimulation and UV sensitive PMTs.*

Details	Risø4	Risø5	Risø8	Reader A	Reader U
Manufacturer	Risø	Risø	Risø	Risø	Risø
Model	DA20	DA20	DA20	XX	DA20
Laboratory	ALRL	ALRL	ALRL	Risø	Risø
Beta source	^{90}Sr/^{90}Y, ∼0.03 Gy/s	^{90}Sr/^{90}Y, ∼0.07 Gy/s	^{90}Sr/^{90}Y, ∼0.1 Gy/s	^{90}Sr/^{90}Y, ∼0.1 Gy/s	^{90}Sr/^{90}Y, ∼0.1 Gy/s
DASH head	No	No	Yes	Yes	Yes
XY box for SG measurements	Yes	Yes	No	No	No
Other attachements	NA	Sample camera	EMCCD camera	Risø spectrometer	Risø spectrometer

which have used emission spectroscopy to investigate different luminescence centres in feldspar. Chapter 4 in this thesis presents results from photoluminescence emission spectra with a focus on the green emission. RL and PL emission spectra in the infrared are presented in Chapter 5 of this thesis. Three-dimensional TL emission spectra are shown in Chapter 6.

2.4 Instruments used in this study

2.4.1 Risø TL/OSL reader

Risø TL/OSL readers are widely used as instruments in retrospective dosimetry (e.g. Bøtter-Jensen et al., 2000, 2003, 2010). All the luminescence readers used in this thesis are equipped with a ^{90}Sr/^{90}Y beta source for irradiation, a stimulation head including blue and infrared LEDs and a UV-sensitive photo multiplier tube (PMT) used for luminescence signal collection. Figure 2.8 shows a schematic drawing of the Risø TL/OSL reader. For the experiments presented in this thesis, different instruments were used and their specifications are summarised in Table 2.4. Details regarding the experimental setup, including the stimulation light source and detection unit setup, are described in detail in Chapter 6, where a Risø reader is used to perform fading measurements and to record TL emission spectra.

2.4.2 Risø TL/OSL spectrometer

The Risø reader emission spectrometer attachment (Prasad, 2017) consists of a single-photon EMCCD-based spectrograph system attached to the DASH (De-

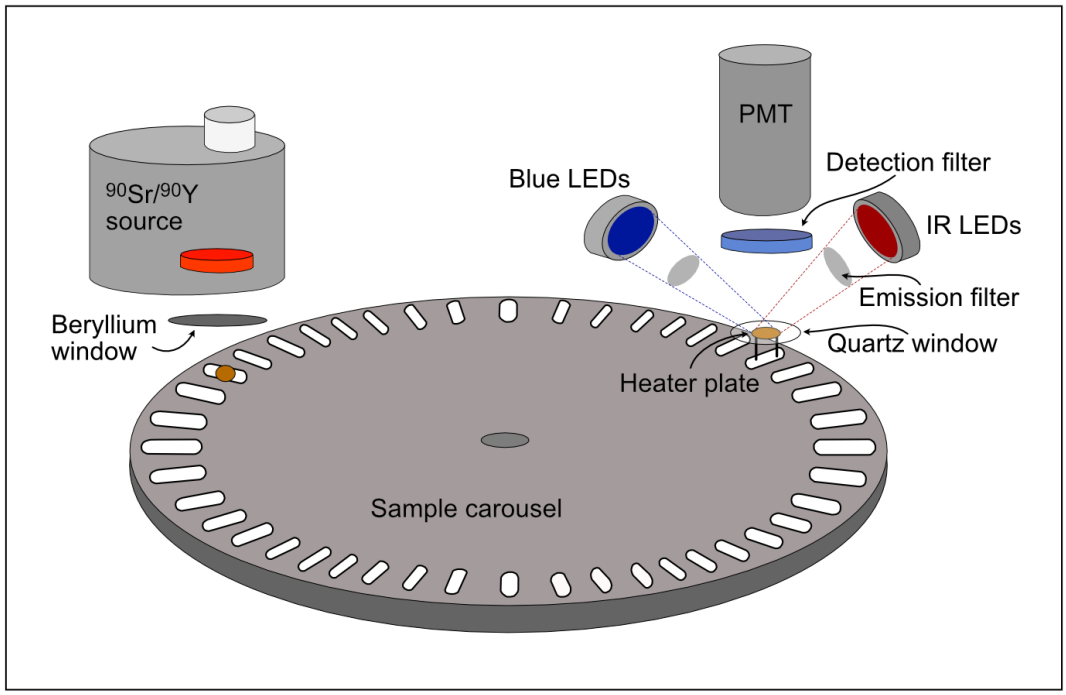

Figure 2.8: *Schematic drawing of the Risø TL/OSL reader, as used in luminescence experiments in this thesis (modified from Guide to the Risø TL/OSL reader, 2017).*

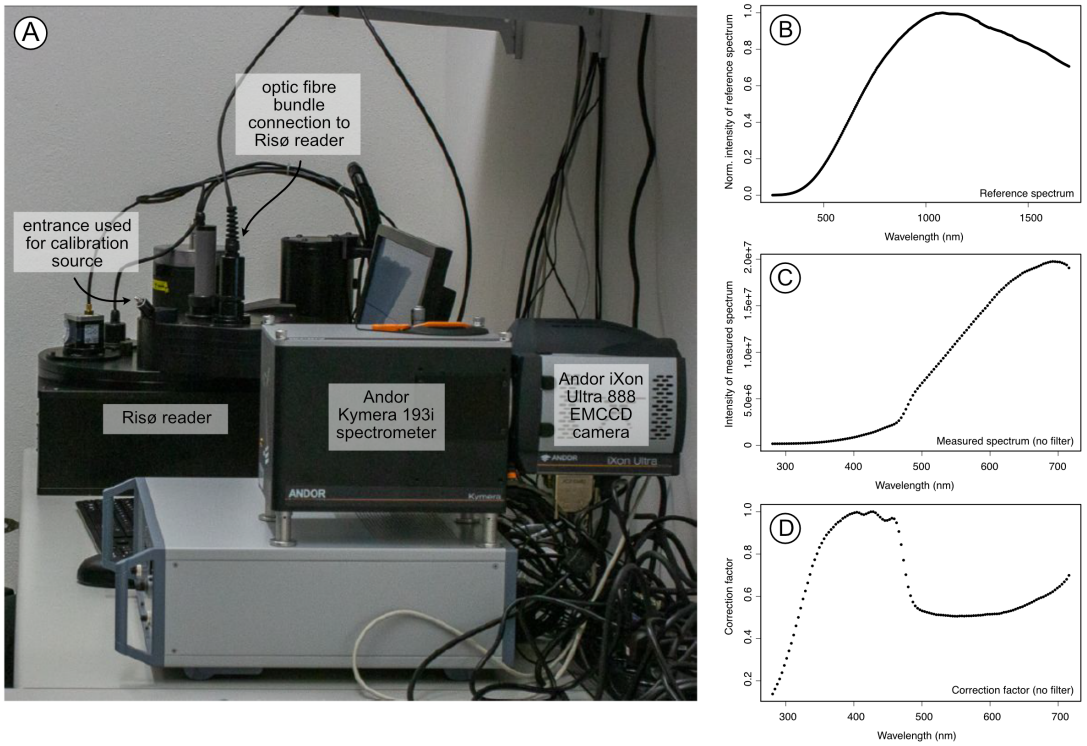

Figure 2.9: *(A) Risø reader A with the emission spectrometer attachment consisting of an Andor Kymera 193i spectrometer and an Andor iXon Ultra 888 EMCCD camera (Photo: Risø). (B) Reference spectrum provided by the manufacturer (Oxford Instrumnents – Andor). (C) Spectrum of the calibration source, measured for this specific spectrometer. (D) Correction factor for efficiency correction calculated based on the difference between the reference and the measured spectra.*

tection And Stimulation Head) of a Risø DA20 TL/OSL reader using a fibre optic bundle cable. The spectrograph is an Andor Kymera SR193 Czerny-Turner spectrograph, which is attached to a thermoelectrically cooled EMCCD camera (Andor iXon Ultra 888, Fig. 2.9). The EMCCD camera has a 1024 x 1024 sensor format and a 13 µm pixel size. The spectrometer is controlled using the Sequence Editor software. This allows the user to choose between different gratings and different centre wavelengths. For this PhD work a centre wavelength of 500 nm and a grating of 150 lines/mm and 500 blaze was used to measure the wavelength range from 280 nm to 720 nm. It would have been possible to choose other centre wavelengths, as well as different gratings (300 lines/mm and 500 blaze). However, for the study presented in Chapter 5, it was important to record a wide range of wavelength including the UV and the red emission. This was achieved using a centre wavelength of 500 nm and the rather coarse grating (150 lines/nm compared to 300 lines/nm). The electron multiplying (EM) gain of the EMCCD was altered between samples, to enable optimal signal to noise ratios. An efficiency correction was necessary for all performed measurements, since the spectrometer does not have the same efficiency over the entire wavelength range. Wavelength calibration was performed by Karsten Brach Nielsen (Risø) following the approach described in Prasad (2017, p. 42) using an Ocean Optics Mercury Argon calibration source. For calibration the peaks at 435.8 nm and 763.5 nm were used after the dispersed light spectrum had been focussed on the CCD chip. The spectrum of the calibration source was measured and the resulting spectrum (Fig. 2.9C) was divided by the by the reference spectrum for the calibration source provided by Ocean Optics (Fig. 2.9B) (Prasad, 2017, p. 42). The correction factors for each wavelength were thus calculated and are displayed in Figure 2.9D, for the case that no filter was used for the signal collection, as is the case for all thermoluminescence spectra shown in this thesis. Further details regarding the experiments in which this spectrometer is used can be found in Chapter 6.

2.4.3 COLUR - Risø station for CryOgenic LUminescence Research

The Risø Station for CryOgenic LUminescence Research (COLUR, Fig. 2.10A) is a custom-built spectrometer stationed at the Risø Campus, DTU Physics (Roskilde, Denmark). COLUR is based on a modified Horiba Spectrofluorome-

ter (Fluorolog–3), including a modified sample chamber, which allows measurements to be conducted at temperatures ranging from 7 to 295 K (temperature of the cold-finger on which the sample is mounted), and multiple attachments for excitation-emission spectroscopy and luminescence decay measurements in the wavelength range from 200 to 1050 nm (Prasad, 2017). The ability of COLUR to perform luminescence measurements at cryogenic temperatures and at room temperature enables the assessment of the impact of thermal assistance or the effect of band-tail states on luminescence measurements. Dependent on the research question, the appropriate temperature needs to be selected. Whilst measurements at cryogenic temperatures enable luminescence measurements without the influence of thermal assistance to be recorded, these measurements are more time consuming than room temperature measurements. For low temperature measurements a vacuum has to be established prior to cooling of the sample. Establishing a vacuum and cooling the sample to 7 K requires ∼3 hours. After the measurements have been performed, COLUR needs to warm up to room temperature overnight, before the vacuum can be released. Due to this time consuming procedure and limited time on the instrument, the advantages and disadvantages of low temperature measurements have to be evaluated in context of the research question prior to performing the measurements.

COLUR also has the possibility to attach an X-ray source, which can be placed on top of the sample chamber. The X-ray source used is a filament-based X-ray tube with a copper anode. The source was operated at 40 kV and 100 μA (Kumar, 2019). The X-ray source delivers a dose rate of ∼0.05 Gy at the sample position. The dose rate was determined by dosing a sample in COLUR using the attached X-ray source and then treating this given dose as an unknown dose in a single aliquot regenerative (SAR) dose protocol performed on a Risø TL/OSL reader (A. K. Prasad, personal communication). It should be noted that the doses in the SAR protocol were administered by a ^{90}Sr/^{90}Y beta source. Thus potential differences in luminescence sensitivity in response to beta or X-ray source irradiation might occur (e.g. Jain et al., 2007; Guérin et al., 2018).

Samples are mounted on a copper sample-finger using carbon tape. The sample holder is attached to a closed-loop liquid He cryostat. COLUR is used for excitation and emission spectroscopy in this thesis and details of the individual experiments as well as the exact instrumental setup for each experiment can be found in Chapters 4 and 5. Below an overview is given on the different excitation light sources and emission-detection setups used.

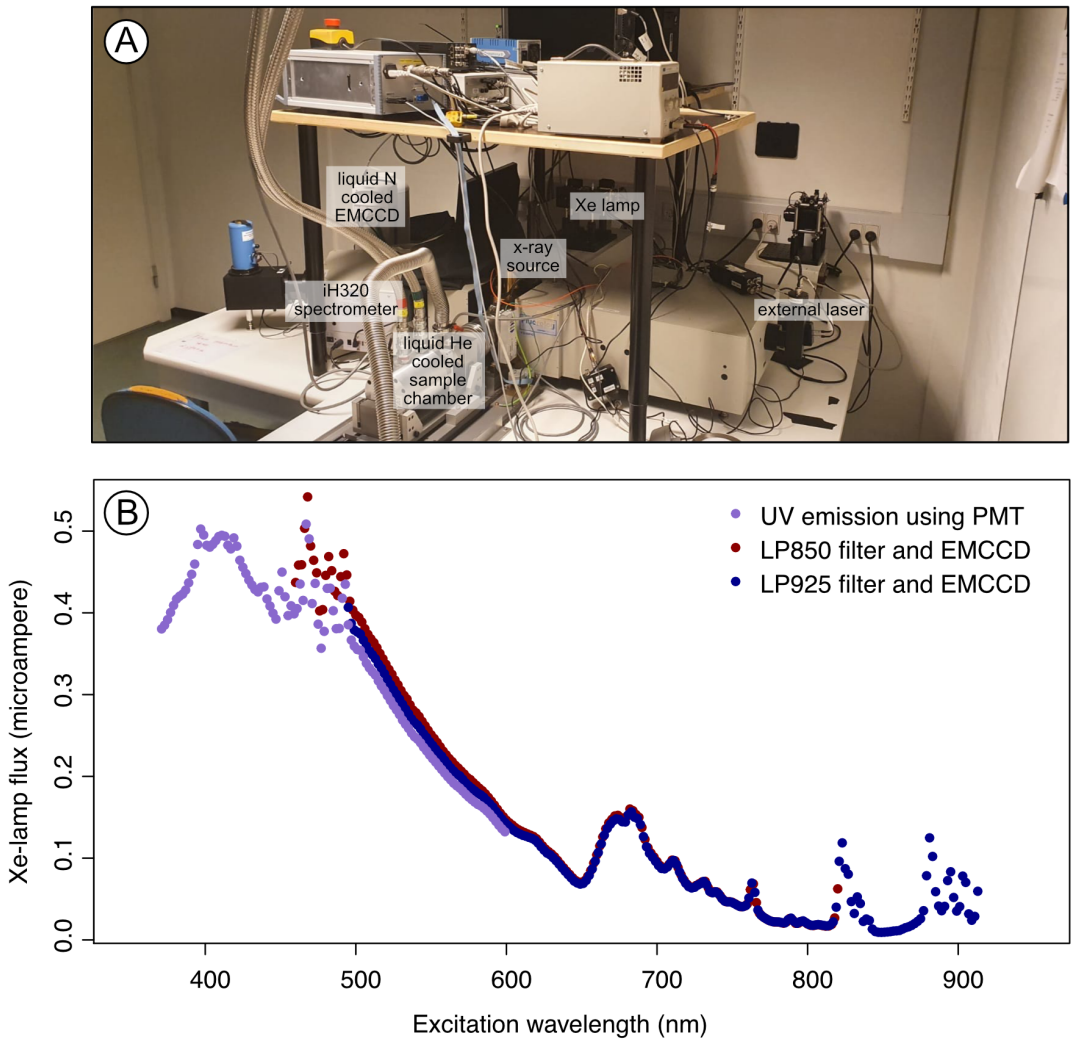

Figure 2.10: *The Risø station for CryOgenic Luminescence Research. (B) The Xe-lamp intensity is usually given in irradiance, radiant flux or power received by a surface per unit area ($W\ m^{-2}$). Irradiance differs for difference wavelengths from a light source (i.e. Xe-lamp). In this spectrometer the change in Xe-lamp flux is measured in terms of current (μA) by an inbuilt photodiode (which acts as the reference detector R1) (R. Kumar, personal communication). The flux is measured directly and it does not pass through any filter, which is why all three curves in B are similar.*

Excitation light sources

In this thesis, excitation is achieved using two different excitation light sources: (i) A continuous wave 450 W Xenon source attached to an excitation monochromator (Czerny-Turner double grating spectrometer, Shafer et al., 1964) and (ii) an external 830 nm continuous-wave laser.

Emission-detection setup

External PMT

An external photo-multiplier tube (Hamamatsu R-928P) can be placed on top of the sample chamber (instead of the X-ray source). The Hamamatsu R-928P has a detection range from 200 nm to 900 nm (Hamamatsu, 2016), but a correction is only available from 290 nm to 850 nm (Kumar, 2019). The quantum efficiency of the PMT drops rapidly below 2 % at wavelengths longer than ∼820 nm (Hamamatsu, 2016). The PMT was used for UV signal detection and a 5 mm thick U340 filter was placed in front of the PMT. The U340 filter transmits from 260 nm (0.2 %) to 390 nm (0.2 %), with a maximum transmission of 75.9 % at 340 nm. A secondary transmission window lies between 680 and 770 nm, where the maximum transmission is 2.1 % (Hoya, 2020).

Horiba iHR320 spectrometer and liquid Nitrogen cooled CCD camera

The iHR320 spectrograph contains a Czerny-Turner spectrograph, which offers three different gratings to be selected: (1) 500 nm blaze and 300 lines/mm, (2) 500 nm blaze and 1200 lines/mm and (3) 750 nm blaze and 1200 lines/mm. In this thesis a 500 nm blaze and 300 lines/mm have been used, as this combination allowed the detection of a wider wavelength range, compared to the 1200 lines/mm grating. The CCD (Horiba Symphony II) has a detection window from 200 to 1050 nm, with correction only available from 290 to 1050 nm (Kumar, 2019). This range of detection wavelength and correction limits the range of emissions to be detected. However, for this thesis, the wavelengths of interest are within this range. Using the spectrometer and the coupled CCD, it is possible to record 2D (intensity vs. excitation or emission wavelength, see Chapter 4) and 3D spectra (intensity vs. excitation and emission wavelength, Chapter 5).

Filters

Optical filters were used to isolate the desired emission wavelength and to protect the emission-detection unit. A 5 mm thick U340 filter was used in combination with the external PMT to isolate the UV emission of the sample. If the detection was achieved using the Horiba iHR320 spectrometer and liquid Nitrogen cooled CCD camera two longpass filters (LP850 and LP925) were placed in the sample chamber in front of the spectrometer to isolate the IR emission of the sample.

System operation and data processing

COLUR is operated using the FluorEssence v3.5 software by Horiba. All measured spectra (T) are corrected (Tc) for the instrumental background (dark counts) and a correction factor is applied, which takes care of variations in the efficiency (e.g. grating, which differs for different wavelengths) by calculating Tc = (T - dark counts) * correction factor. The corrected spectrum (Tc) is then corrected for the Xe-lamp light flux (Fig. 2.10B). The efficiency correction was supplied by Horiba and wavelength calibrations were done frequently in-house by Risø staff (R. Kumar, personal communication). Depending on the experiment and the brightness of the sample, a wide range of settings for the integration time and slit width (excitation and emission) were used and are listed in Chapters 4 and 5 for the individual experiments.

References

Aitken, M.J., 1985. Thermoluminescence Dating. Academic Press, London, United Kingdom.

Alexander, S.A., 2007. The stability of the remnant luminescence emissions of alkali feldspar. PhD thesis, Univeristy of Glasgow, United Kingdom, 362 p.

Allmann, R., 2003. Röntgenpulverdiffraktometrie. Springer, Heidelberg, Germany.

Bøtter-Jensen, L., Bulur, E., Duller, G.A.T., Murray, A.S., 2000. Advances in luminescence instrument systems. Radiation Measurements 32, 523-528.

Bøtter-Jensen, L., Andersen, C.E., Duller, G.A.T., Murray, A.S., 2003. Developments in radiation, stimulation and observation facilities in luminescence measurements. Radiation Measurements 37, 535-541.

Bøtter-Jensen, L., Thomsen, K.J., Jain, M., 2010. Review of optically stimulated luminescence (OSL) instrumental developments for retrospective dosimetry. Radiation Measurements 45, 253-257.

Burg, J.-P., Davy, P., Nievergelt, P., Oberli, F., Seward, D., Diao, Z., Meier, M., 1997. Exhumation during crustal folding in the Namche-Barwa syntaxis. Terra Nova 9, 53-56.

Bussy, F., Schaeltegger, U., Marro, C., 1989. The age of the Mont Blanc granite (western Apls): A heterogeneous isotopic system dated by Rb-Sr whole rock determination on its microgranular enclaves. Schweiz. Mineral. Petror. Mitt. 69, 3-13.

Bussy, F., Von Raumer, J. F., 1993. U-Pb dating of Palaeozoic events in the Mont-Blanc crystalline massif, western Alps. Terra Nova Abstracts 5, 382.

Buylaert, J.-P., Jain, M., Murray, A.S., Thomsen, K.J., Thiel, C., Sohbati, R., 2012. A robust feldspar luminescence dating method for Middle and Late Pleis-

tocene sediments. Boreas 41, 435-451.

Cassedanna, J. P., Roditi, M., 1996. The location, geology and mineralogy of gem tourmalines in Brazil. J. Gemm. 25, 263-298.

Clark, R.J., Sanderson, D.C.W., 1994. Photostimulated luminescence excitation of spectroscopy of feldspars and micas. Radiat. Meas. 23, 641–646.

Cunningham, G.J., 1981. Petrology and geochemistry of Lewisian pegmatites and granites, N.W., Scotland. PhD thesis, Imperial College London, United Kingdom.

Finch, A.A., Klein, J., 1999. The causes and petrological significance of cathodoluminescence emissions from alkali feldspars. Contributions to Mineralogy and Petrology 135, 234-243.

Garcia-Guinea, J., Townsend, P.D., Sanchez-Muños, Rojo, J.M., 1999. Ultraviolet-blue ionic luminescence of alkali feldspars from bulk and interfaces. Physics and Chemistry of Minerals 26, 658- 667.

Goldsmith, J.R., Laves, F., 1954. The microcline-sanidine stability relations. Geochemica et Cosmochemica Acta 5, 1-19.

Guérin, G., Mihailescu, L.-C., Jain, M., 2018. Photon energy (8-250 keV) response of optically stimulated luminescence: Implications for luminescence geochronology. Journal of Luminescence 204, 135-144.

Guralnik, B., Jain, M., Herman, F., Ankjærgaard, C., Murray, A. S., Valla, P. G., Preusser, F., King, G. E., Chen, R., Lowick, S. E., Kook, M., Rhodes, E. J., 2015. OSL-thermochronometry of feldspar from the KTB borehole, Germany. Earth and Planetary Science Letters 423, 232-243.

Hamamatsu Photonics K.K., 2016. Hamamatsu Photomultiplier tubes R928, R928P, R955, R955P, manual.

Hamilton, T.D.S., Munro, I.H., Walker, G., 1978. Luminescence instrumentation.

In Lumb, M.D. (Ed.). Luminescence spectroscopy. Academic Press, London.

Harrison, T.N., Parsons, I., Brown, P.E., 1990. Mineralogical evolution of fayalite-bearing rapakivi granites from the Prins Christians Sund pluton, South Greenland. Mineralogical Magazine 54, 57–66.

Hovis, G.I., 1989. Effect of Al-Si distribution on the powder-diffraction maxima of alkali feldspars and an easy method to determine T1 and T2 site occupancies. Canadian Mineralogist 27, 107-118.

Hoya, 2020. U340 data sheet.

Huntley, D.J., Godfrey-Smith, D.I., Thewalt, M.L.W., 1985. Optical dating of sediments. Nature 313, 105-107.

Hütt, G., Jaek, I., Tchonka, J., 1988. Optical dating: K-feldspars optical response stimulation spectra. Quaternary Science Reviews 7, 381-385.

International Atomic Energy Agency, Analytical Quality Control Services, Seibersdorf (Austria) (1999). IAEA AQCS catalogue for reference materials and intercomparison exercises 1998/1999 (INIS-XA–131). International Atomic Energy Agency (IAEA)

International Centre for Diffraction Data (ICDD), Newtown Square (Pennsylvania, USA). https://www.icdd.com.

Ito, H., Yamada, R., Tamura, A., Arai, S., Horei, K., Hokada, T., 2013. Earth's youngest exposed granite and its tectonic implications: the 10-0.8 Ma Kurobegawa Granite. Scientific Reports 3, 1306.

Jain, M., Ankjærgaard, C., 2011. Towards a non-fading signal in feldspar: Insight into charge transport and tunnelling from time-resolved optically stimulated luminescence. Radiation Measurements 46, 292-309.

Jain, M., Bøtter-Jensen, L., Thomsen, K.J., 2007. High local ionization density effects in r-ray excitations deduced from optical stimulation of trapped charge in

Al_2O_3:C. Journal of Physics: Condensed Matter 19, 116201.

King, G. E., Herman, F., Guralnik, B., 2016. Northward migration of the eastern Himalayan syntaxis revealed by OSL thermochronometry. Science 353 (6301), 800-804.

Kook, M.H., Lapp, T., Murray, A.S., Thiel, C., 2012. A Risø XRF Attachment for Major Element Analysis of Aliquots of Quartz and Feldspar Separates. UK Luminescence and ESR Meeting, Aberystwyth, pp. 37 September 2012 (abstract).

Kirsh, Y., Shoval, S., Townsend, P.D., 1987. Kinetics and emission spectra of thermoluminescence in the feldspars albite and microcline. Physica Status Solidi 101, 253-262.

Krause, W.E., Krbetschek, M.R., Stolz, W., 1997. Dating of quaternary lake sediments from the Schirmacher Oasis (East Antarctica) by infra-red stimulated luminescence (IRSL) detected at the wavelength of 560 nm. Quaternary Science Reviews (Quaternary Geochronology) 16, 387-392.

Krbetschek, M.R., Götze, J., Dietrich, A., Trautmann, T., 1997. Spectral information from minerals relevant for luminescence dating. Radiation Measurements 27, 695-748.

Kumar, R., Kook, M., Murray, A.S., Jain, M., 2018. Towards direct measurement of electrons in metastable states in K-feldspar: Do infrared-photoluminescence and radioluminescence probe the same trap? Radiation Measurements 120, 7-13.

Kumar, R., 2019. A new understanding of luminescence processes in feldspar using novel site-selective spectroscopy techniques. PhD thesis, Technical University of Denmark.

Lambert, R., 2018. Investigating Thermal Decay in K-Feldspar for the Application of IRSL Thermochronometry on the Mont Blanc massif. University of Lausanne, pp. 139.

Loubser, M., Verryn, S., 2008. Combining XRF and XRD analyses and sample preparation to solve mineralogical problems. South African Journal of Geology 111, 229-238.

Margui, E., Van Grieken, R., 2013. X-ray fluorescence spectrometry and related techniques. An Introduction. Momentum Press, New York, United States of America.

Morthekai, P., Thomas, J., Pandian, M.S., Balaram, V., Singhvi, A.K., 2012. Variable range hopping mechanism in band-tail states of feldspars: A time-resolved IRSL study. Radiation Measurements 47, 857-863.

Murray, A.S., Wintle, A.G., 2000. Luminescence dating of quartz using an improved single-aliquot regenerative-dose protocol. Radiation Measurements 32, 57-73.

Pagonis, V., Brown, N., 2019. On the unchanging shape of thermoluminescence peaks in preheated feldspars: Implications for temperature sensing and thermochronometry. Radiation Measurements 124, 19-28.

Poolton, N.R.J., Kars, R.H., Wallinga, J., Bos, A.J.J., 2009. Direct evidence for the participation of band-tails and excited-state tunneling in the luminescence of irradiated feldspars. Journal of Physics: Condensed Matter 21, 1-10.

Prasad, A.K., 2017. Understanding defect related luminescence processes in wide bandgap materials using low temperature multi-spectroscopic techniques. PhD thesis, Technical University of Denmark.

Rendell, H.M., Clarke, M.L., 1997. Thermoluminescence, radioluminescence and cathodoluminescence spectra of alkali feldspars. Radiation Measurements 27, 263-272.

Riedesel, S., Brill, D., Roberts, H.M., Duller, G.A.T., Garrett, E., Zander, A.M., King, G.E., Tamura, T., Burow, C., Cunningham, A., Seeliger, M., De Batist, M., Heyvaert, V.M.A., Fujiwara, O., Brückner, H. and the QuakeRecNankai Team, 2018. Single-grain luminescence chronology of historical extreme-wave event de-

posits recorded in a coastal lowland, Pacific coast of central Japan. Quaternary Geochronology 45, 37–49.

Rietveld, H.M., 1969. A Profile Refinement method for Nuclear and Magnetic structures. Journal of Applied Crystallography 2, 65-71.

Risø Manual "Guide to the Risø TL/OSL Reader", 2017. DTU Nutech, Technical University of Denmark, Denmark.

Sanderson, D.C.W., Clark, R.J., 1994. Pulsed photostimulated luminescence of alkali feldspars. Radiation Measurements 23, 633-639.

Shackley, M. S., 2010. An Introduction to X-ray Fluorescence (XRF) analysis in Archaeology. Springer, berlin, Germany.

Shafer, A.B., Megill, L.R., Droppleman, L., 1964. Optimization of the Czerny-Turner Spectrometer. Journal of the Optical Society of America 54, 879-887.

Sohbati, R., Murray, A.S., Jain, M., Thomsen, K.J., Hong, S.-C., Yi, K., Choi, J.-H., 2013. Na-rich feldspar as a luminescence dosimeter in infrared stimulated luminescence (IRSL) dating. Radiation Measurements 51-52, 67-82.

Stevens, T., Buylaert, J.-P., Thiel, C., Ujvári, G., Yi, S., Murray, A.S., Frechen, M., Lu, H., 2018. Ice-volume-forced erosion of the Chinese Loess Plateau global Quaternary stratotype site. Nature Communications 9, 983.

Strickertsson, K., 1985. The thermoluminescence of potassium feldspars – glow curve characteristics and initial rise measurements. Nuclear Tracks 10, 613-617.

Thomsen, K.J., Murray, A.D., Jain, M., Bøtter-Jensen, L., 2008. Laboratory fading rates of various luminescence signals from feldspar-rich sediment extracts. Radiation Measurements 43, 1474-1486.

Trautmann, T., Krbetschek, M.R., Dietrich, A., Stolz, W., 1999. Feldspar radioluminescence: a new dating method and its physical background. Journal of Luminescence 82, 45-58.

Tucker, M., 1996. Methoden der Sedimentologie. Enke, Stuttgart, Germany.

Ussher, W.A.E., Barrow, G., McAlister, D.A., 1909. The Geology of the country around Bodmin and St. Austell. Memoirs of the Geological Survey England and Wales – Explanation of Sheet 347.

Wallinga, J., Murray, A.S., Wintle, A.G., 2000. The single-aliquot regenerative-dose (SAR) protocol applied to coarse-grain feldspar. Radiation Measurements 32, 529-53.

Waychunas, G.A., 2014. Luminescence Spectroscopy. Reviews in Mineralogy and Geochemistry 78, 175-217.

Wright, T.L., 1968. X-ray and optical study of alkali feldspar II. An x-ray method for determining the composition and structural state from measurements of 2θ values for the three reflections. American Mineralogist 53, 88-104.

Three

Excitation and emission spectroscopy of feldspars — Insights into luminescence production in feldspars

This chapter is in preparation for submission to *Earth Science Reviews* as

Riedesel, S., Roberts, H.M., Duller, G.A.T., Pearce, N.J. *Excitation and emission spectroscopy of feldspars — Insights into luminescence production in feldspars.*

Abstract

Despite the routine use of feldspars as a natural dosimeter in luminescence dating studies, many questions remain regarding the crystal defects and physical processes involved in luminescence production in feldspars. This chapter reviews the current knowledge on the use of excitation and emission spectroscopy of feldspars, and shows open questions, which require answers to enable a better understanding of luminescence production in feldspars, which will enable an improved use of these minerals as natural dosimeters.

In this review it is shown that excitation spectroscopy is a powerful tool to constrain defect related parameters, e.g. trap depth and optical resonances associated with electron traps and hole traps and the band gap energy of feldspars. Emission spectroscopy of feldspar gives insights into potential relationships between different emissions and chemical and crystallographic properties of the sample and can thus help to identify defects within the crystal that give rise to respective emissions. From the reviewed literature it becomes apparent that further research is necessary, to enable links to be drawn between chemical and structural properties of various feldspars and luminescence emissions. Particularly interesting will be the detailed understanding of crystallographic sources of the blue luminescence emission and related anomalous fading processes, as well as understanding the defects giving rise to the UV and green-yellow emission. Whilst the crystallographic defect giving rise to the red emission has been identified, the physical process leading to this emission is still under debate. Additionally, the defects acting as electron trapping centres in feldspars are still unknown, but the promising new technique of infrared photoluminescence might offer the potential to get further insights into relationships between the electron traps and chemical and structural properties of feldspars.

3.1 Introduction

Feldspars are the most common minerals in the Earth's crust and are used in a wide range of Earth Science research including luminescence dating. Measurements of luminescence from feldspars extracted from bedrock, rock and sediment can be used to constrain the rock's or sediment's last exposure to heat (e.g. Aitken, 1985), or light (e.g. Huntley et al., 1985), or the cooling history of bedrock (e.g. Guralnik et al., 2015, King et al., 2016). Despite the wide use of feldspars as luminescence chronometers in retrospective dosimetry, the physical processes behind luminescence production in these minerals as well as the crystallographic defects giving rise to luminescence are not fully understood. This limits further improvements of the use of feldspars in luminescence dating. This review aims at presenting the knowledge on various luminescence emissions, covering the spectral range from the ultraviolet (UV) to the infrared (IR), and on the crystallographic defects taking part in the luminescence production in feldspars.

In 1997, Krbetschek et al. presented an extensive review on spectral information gained from quartz and feldspar, the two minerals most commonly used in luminescence dating. More than 20 years have past and further information has been gathered on different emissions in feldspars and related crystallographic defects. Additionally, the use of feldspars as a luminescence dosimeters have long been limited, due to a loss of charge over time, termed anomalous fading (e.g. Wintle, 1973). However, in the past 20 years, improvements have been made in order to correct for fading (e.g. Huntley and Lamothe, 2001; Kars et al., 2008), or to circumvent fading, by adjusting measurement procedures (e.g. Thomsen et al., 2008; Thiel et al., 2011; Buylaert et al., 2012). Thus, feldspars have become more and more attractive in luminescence dating studies, which makes a re-evaluation of the state-of-the-art knowledge on luminescence production and potential knowledge gaps particularly relevant.

Important methods used to understand luminescence production in minerals have been excitation and emission spectroscopy, as these two methods enable probing the crystal defects acting as the electron trapping centres and recombination centres. This review presents the knowledge on luminescence production and participating defects in feldspar gained using excitation and emission spectroscopy. This review will give a brief overview of alkali feldspars and plagioclase feldspars, describing their chemistry and different structural states (section 2) as well as a broad overview of the energy band model that is often used to ex-

plain luminescence processes in solids (section 3). Section 4 presents studies, which use excitation spectroscopy. Here the focus is mainly on defining the electron trapping site in feldspars, presenting findings regarding the band gap energy (section 4.1), constraining the ground (section 4.2) and excited state energies (section 4.3) and discussing band-tail states (section 4.4). Section 5 is focussed on emission spectroscopy, the different emission centres in feldspars, and related defects. Section 5 is separated into sections on the different emissions, including the UV (section 5.1), blue (section 5.2), green-yellow (section 5.3), red and deep red (section 5.4) and IR (section 5.5). In these sections studies are reviewed that identified these emissions in various chemically and structurally different feldspars. For each emission, an overview on potential crystallographic defects giving rise to these emissions is presented. Additionally, challenges which have been identified for some emissions, such as the thermolability of the UV emission (section 5.1.2), anomalous fading of the blue emission (section 5.2.3) and thermal quenching of the red and deep red emission (section 5.4.3) and their potential sources are discussed. All presented findings are discussed in section 6, with a focus on combining all information to develop a better understanding of luminescence production in feldspars and to identify potential knowledge gaps.

3.2 Structures of alkali feldspars and plagioclases

Feldspars are the most abundant mineral group in the Earth crust, where they are important constituents of igneous rocks of various chemical compositions, they are also present in metamorphic rocks, such as gneisses and schists, regionally and thermally metamorphosed rocks (Deer et al., 2013, p. 248). Feldspars are framework silicates, and the feldspar group consists of three end members, between which solid solutions are formed. The three end members are defined by the alkali cation that occupies cavities in the crystal lattice, the three end members are: $NaAlSi_3O_8$ (albite [Ab], Na-feldspar), $KAlSi_3O_8$ (orthoclase [Or], K-feldspar) and $CaAl_2Si_2O_8$ (anorthite [An], Ca-feldspar). The solid solution between Na- and Ca-feldspar is termed plagioclase, and between K- and Na-feldspar it is termed alkali feldspar. There is only limited solid solution between K- and Ca-feldspar (<10 %). At high temperatures, alkali feldspars exist as a complete solid solution and may be preserved by very rapid cooling (e.g. volcanic erup-

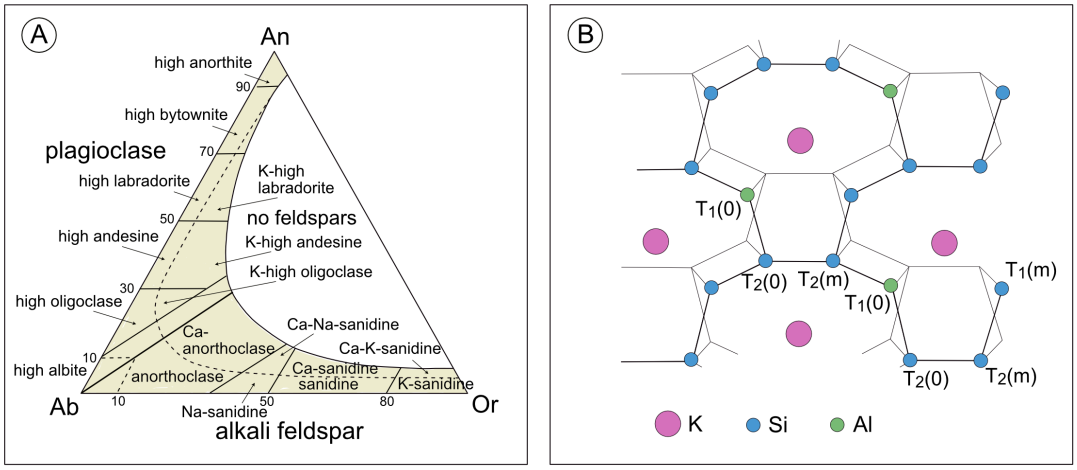

Figure 3.1: *(A) Feldspar composition ternary diagram showing the maximum extent of solid solutions at $T > 1000\,^{\circ}C$ (modified from Deer et al., 2013, p. 249). (B) Structure of sanidine viewed on (001). M and T sites are shown, but oxygen atoms forming the tetrahedra with Si and Al are not shown. In the case of sanidine the Si:Al ratio is 3:1, with, Al randomly occupying all tetrahedral sites. Tetrahedral sites are labelled (modified from Deer et al., 2013, p. 257).*

tion). At low temperatures and high pressure (>0.5 GPa), such as slowly cooled (intrusive) rocks, solid solution between the two end-members is very limited, and these occur as low albite (Na-feldspar end member) and low microcline (K-feldspar end member). In any other intermediate environment, feldspars form intergrowths (Deer et al., 2013, p. 248-250). Figure 3.1A presents the feldspar composition ternary diagram, showing the maximum extent of solid solutions at 1000 °C.

The framework in feldspars consists of corner sharing (Si, Al)-O tetrahedra (Fig. 3.1B). Si^{4+} and Al^{3+} occupy four-fold coordinated tetrahedral sites (T sites) in the lattice and form the framework. Cations are placed, charge balancing, in the spaces in between the tetrahedra on M sites in the crystal lattice. In alkali feldspars, M sites are filled with eight-fold coordinated K^+ and Na^+, which are homogeneously distributed in the lattice at high temperatures. The exsolution of K^+ and Na^+, i.e. the separation of Na^+ from K^+ as the lattice contracts during cooling of the rock, forms the perthitic structure of most alkali feldspars, which is caused by the large difference in ionic radii of $^{[8]}K^+$ (0.151 nm) and $^{[8]}Na^+$ (0.118 nm) (Deer et al., 2013, p. 250). In plagioclases, with $^{[8]}Na^+$ and $^{[8]}Ca^{2+}$ having similar ionic radii (0.118 nm compared to 0.112 nm, respectively), the size of the cation is not a significant driver of changes in the crystal lattice. Here, the difference in charge of Na^+ and Ca^{2+} influences the crystal structure, with the coupled substitution of

$$Ca^{2+} + Al^{3+} \rightleftharpoons Na^{+} + Si^{4+} \tag{3.1}$$

maintaining charge balance (equation 3.1). This results in a Si:Al ratio of 2:2 in Ca^{2+}-rich plagioclases, compared to a Si:Al ratio of 3:1 in albite (Deer et al., 2013, p. 294). In alkali feldspars, Si^{4+} and Al^{3+} can alternate between the four tetrahedral sites, referred to as $T_1(0)$, $T_1(m)$, $T_2(0)$ and $T_2(m)$ (Fig. 3.1B). Dependent on the state of order of the alkali feldspar, Al^{3+} can be found on different T sites. The most disordered alkali feldspar exists at high temperatures (>1000 °C). Here the distribution of Al^{3+} and Si^{4+} amongst the tetrahedral sites is random. This is the case in monoclinic high sanidine and it results in a 1-in-4 chance of finding an Al^{3+} ion on any given T site. Disordered sanidine can be found in volcanic rocks, due to rapid cooling, during which this disordered structure is retained. During slow cooling Si^{4+} and Al^{3+} become arranged in tetrahedral sites, with T_1 sites being more energetically favoured by Al^{3+}. The difference between T_1 and T_2 sites is that T_2 sites are closer together and have a different relationship to M sites (Deer et al. 2013, p. 257). In this step Al^{3+} becomes concentrated in T_1 sites, but stays randomly distributed in these, which maintains the symmetry in the crystal and the monoclinic structure in low sanidine/orthoclase. During extended slow cooling of the magma, or during cooling of thermally and regionally metamorphosed rocks, Al^{3+} becomes concentrated in $T_1(0)$ sites, which changes the crystal structure to triclinic and results in microcline, where the symmetry is broken (Deer et al., 2013, p. 257).

3.3 Electron and hole centres in feldspars

A simplified energy band model of solids can be applied to feldspars and can then be used to explain charge transport processes within feldspar. The energy band model of solids shows different allowed energy states of electrons, or bands. The valence band and the conduction band are separated by a forbidden gap, or band gap (McKeever, 1985, p. 20). The size of the band gap defines the conductivity of the material, with conductors having the narrowest band gap, and insulators having the widest band gap. Semi-conductors have band gap energies between those of conductors and insulators (McKeever, 1985, p. 21). Defects within a crystal are located within the forbidden gap between the valence and the conduction band. A defect within a crystal represents deficit of charge and thus locally the crystal does not have charge electroneutrality. Defects can

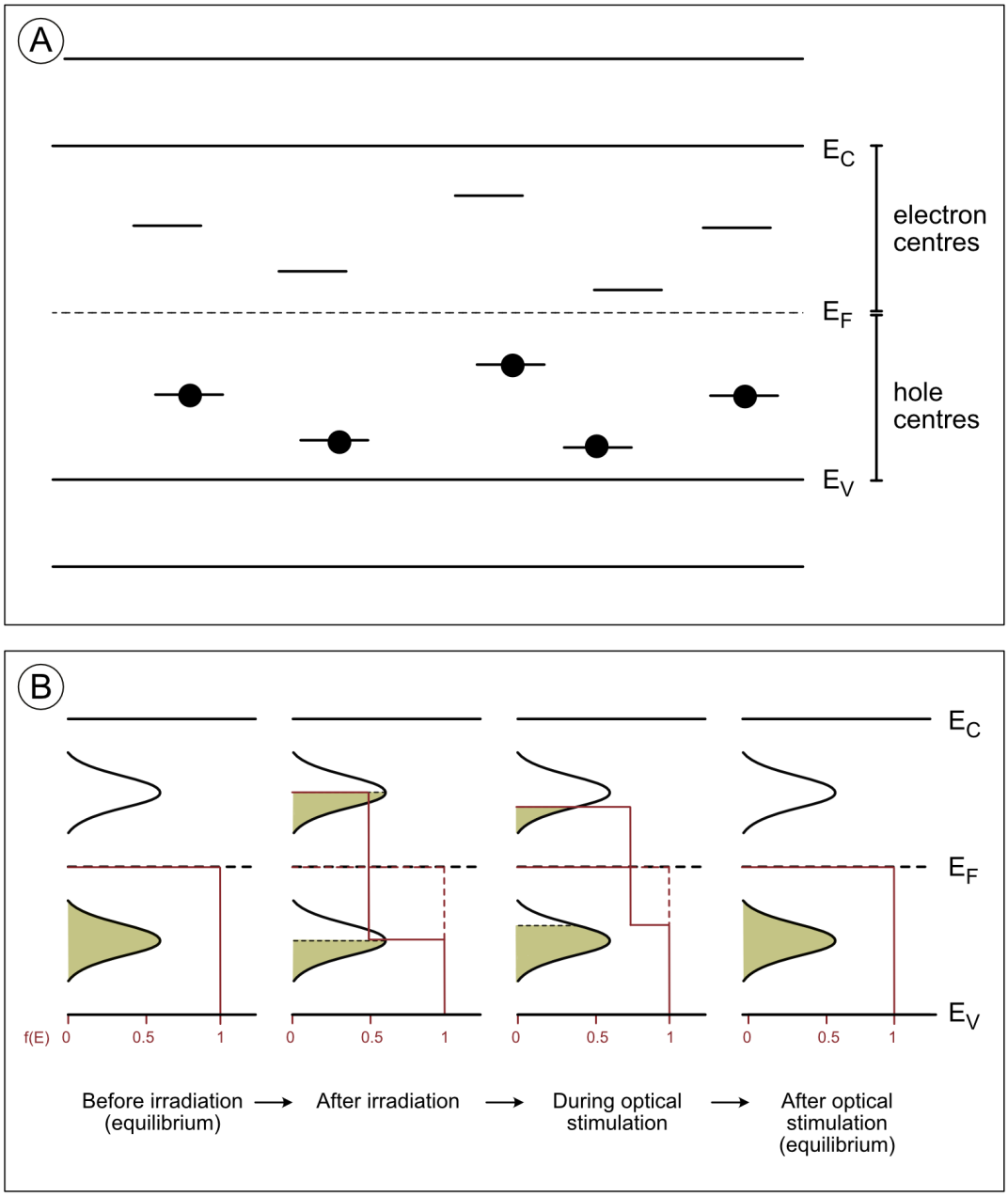

Figure 3.2: *A) Energy levels in an insulator at equilibrium state (at 0 K). In this case all hole centres below the Fermi level (E_F) are filled with electrons. All centres above the Fermi level are empty. E_c and E_v refer to the bottom of the conduction band and the top of the valence band, respectively. B) Occupancies of states in the forbidden gap at 0 K (modified from Bøtter-Jensen et al., 2003). Before irradiation, all states below the Fermi level are filled with electrons (as also in A), due to subsequent irradiation, some states above the Fermi level are filled. Optical stimulation empties those again and thus fills states below the Fermi level due to recombination. After optical stimulation the equilibrium is restored. f(E) describes the occupancy, with f(E) = 1 in the original equilibrium occupancies with all states below the Fermi level filled. In this case f(E) = 0 for the states above the Fermi level. The figure is modified from McKeever (1985, p. 23).*

either function as electron centres or as hole centres in luminescence processes, depending on their net charge. A deficiency of negative charge results in a hole centre, whereas a deficiency of positive charge in an electron centre. The location of either centre within the forbidden gap of an insulator is defined by the energy required to free an electron. Thus, hole centres are located below the Fermi-level, an equilibrium level beneath which the energy levels are completely full, and above which the energy levels are completely empty, at a temperature of 0 K. In comparison, electron centres have an energy level above the Fermi-level. This means that they are potential electron traps, as this level is free of electrons (Marfunin, 1979, p. 244; McKeever, 1985, p. 21-23; Fig. 3.2A).

In the case of equilibrium, all states below the Fermi level are filled with electrons, and all states above the Fermi level are empty (McKeever, 1985, p. 20; Fig. 3.2B). Interaction of a solid with ionising radiation causes ionisation of electrons from the valence band into the conduction band, where they are free to move through the crystal lattice. The ionised electrons might become trapped in an electron trap below the conduction band (Fig. 3.2B). The hole, left by the ionised electron, will indirectly move (termed hole diffusion) and will eventually become trapped in a hole trap above the valence band. The trapped electrons may be released by optical or thermal excitation (Fig. 3.2B) e.g. McKeever, 1985, p. 26; Bøtter-Jensen et al., 2003, p. 1). Once freed, electrons are able to move within the crystal and recombine with a trapped hole; this process resulting in the emission of photons, if radiative, is called luminescence. Non-radiative transitions result in the emission of phonons, which are vibrations of the crystal lattice (e.g. McKeever, 1985, p. 32-34).

A defect within the crystal lattice refers to any position within the lattice where the actual structure violates the symmetry described by the symmetry space group of the crystal (Marfunin, 1979, p. 244). These defects are referred to as point defects. Different types of point defects can occur: vacancies of either anions or cations, impurity ions (inclusion of ions not natural to the lattice), interstitial atoms or molecules (atoms or molecules occupying spaces within the lattice, which do not belong to the regular lattice structure) and atoms in disorder solid solution (Marfunin, 1979, p. 244). After irradiation these point defects may function as metastable or unstable defects and may then serve as electron or hole traps (e.g. Marfunin, 1979, p. 244; McKeever, 1985, p. 21-23).

In feldspars different types of defects have been found. An example for a defect resulting from disorder in solid solution is the substitution of Si^{4+} ions by

Al^{3+} ions. This disorder can then cause an electron deficiency due to irradiation where the hole moves to an oxygen ion, which is a neighbour of Al^{3+}, resulting in the formation of Al^{3+}-O^{-}-Al^{3+} bridges (Speit and Lehmann, 1982). Impurity related defects have been found in feldspars. These impurity defects can either be substitutional centres or interstitial ions (e.g. Götze et al., 1999; Jones et al., 2004; Preusser et al., 2009). Different substitutions of M site cations by minor and trace elements (mainly Sr, Rb, Ca, Pb and Eu or other rare earth elements) have been found in feldspars (e.g. Ribbe, 1983, p. 1; Smith, 1983, p. 282). On tetrahedral sites substitutions by, for example, Fe^{3+} and Ti^{4+} have been found (Ribbe, 1983, p. 1; Smith, 1983, p. 281). Some of these substitutions are the source of colour in feldspars (e.g. Hofmeister and Rossman, 1983, p. 271-280; Smith, 1983, p. 295). If the substituting ions have a different valence as the ion they are substituting for, charge imbalance is introduced. As described above, deficiency of an electron can result in a potential electron trap and deficiency of a hole can result in a potential hole trap. Besides variations in valence, substitutions, vacancies and also exsolution may cause stress and strain to the lattice (e.g. Brown and Parsons, 1984), which is mainly compensated by twinning in feldspars (e.g. Parsons et al., 2015).

Luminescence can be activated by different types of impurities or vacancies, which allow charge to be carried by electrons and holes (e.g. Telfer and Walker, 1978; Finch and Klein, 1999; Götze et al., 1999). Additionally, luminescence can be caused by ion motion (e.g. Kirsh, 1992), for example by motion of Na atoms through phase-interfaces in perthites (e.g. Garcia-Guinea et al., 1999).

For feldspars, a variety of hole centres have been identified (Speit and Lehmann, 1976; Speit and Lehmann, 1982). Using Electron Paramagnetic Resonance (EPR), Speit and Lehmann (1982) could only identify one type of electron centre (Ti^{3+} substituting for Al^{3+} on a tetrahedral site) in sanidine and labradorite samples. Matyash et al. (1982) defined another electron trapping centre in feldspar by using EPR. The authors locate the trapped electrons at a bridging oxygen ion, which links two SiO_4^{4-} tetrahedra. Based on infrared radioluminescence measurements of feldspar and lead doped potassium chloride (KCl:Pb), Erfurt and Krbetschek (2003) suggest that Pb^{2+}, reduced to Pb^{+} due to ionising radiation, could function as an electron trap, when substituting for K^{+} on M sites. However, KCl:Pb has a cubic lattice, whilst feldspars are framework silicates, so a comparison could encounter difficulties. Short (2004) inferred from polarisation effects of optical transitions in an orthoclase sample that the defect responsible

for an electron trap in feldspar is associated with the T_1 tetrahedral site on the framework. However, Short (2004) does not attempt to describe a particular type of defect occupying the T_1 site in feldspars.

Further research has tried to identify the specific crystal defects in feldspars related to electron and hole trapping which produce luminescence. Excitation spectroscopy has enabled the physical properties of the electron-trapping site in feldspars to be constrained and further details are discussed in section 4 of this paper. Additionally, the newly developed method of infrared photoluminescence (IRPL, Prasad et al., 2017) opens potentials to further explore the nature of the electron trapping centres in feldspars. Whilst the crystal defects related to the electron trapping centres in feldspars is still unknown, further progress has been made in defining different recombination centres. Here excitation (section 4) and emission spectroscopy (section 5) have been used and allowed correlation of different luminescence emissions with defects in the crystal. Research about the different emissions of feldspars is discussed in section 5.

3.4 Excitation spectroscopy of feldspars

In excitation spectroscopy, the excitation energy is varied, whilst the recorded emission window remains unchanged. In such measurements, excitation peaks at particular wavelengths may become apparent and can then be used for further interpretation regarding associated defects within the crystal or physical properties of the host lattice (Waychunas, 2014). The following section will give an overview on how excitation spectroscopy has been used to constrain the band gap energies (section 4.1), the ground and excited state energies of the IR sensitive trap(s) in feldspar (section 4.2 and 4.3), and the width of the sub-conduction band-tail states (section 4.4).

3.4.1 Band gap energy

The first to present an estimation of the optical band gap energy of feldspars were Jaek et al. (1997a, b), who used excitation spectra to prove that laboratory doping of feldspar with various elements (Eu, Cu, Ti, Ga and In) results in specific excitation peaks. Although the success of the experiment is difficult to judge, as the authors do not present any excitation spectra of non-doped material, the obtained spectra are useful regarding constraints of the band gap

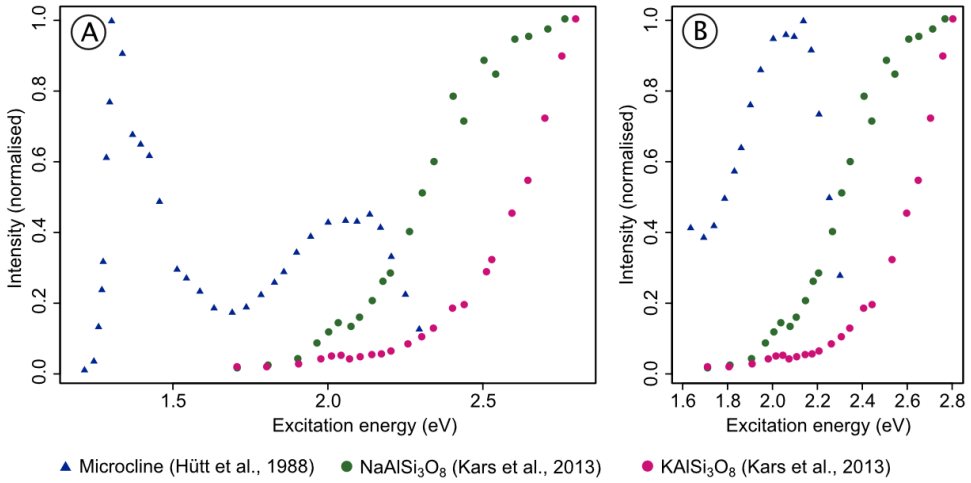

Figure 3.3: *(A) Example excitation spectra of different feldspar samples by Hütt et al. (1988) and Kars et al. (2013) and. Note that the decrease in the intensity in the spectrum of Hütt et al. (1988) above an excitation energy of 2.25 eV is due to instrumental limitations. (B) A close-up of the excitation energy range from 1.6 to 2.8 eV. This energy range was used by Kars et al. (2013) for fitting using equation 3.2 to obtain the trap depth.*

energy of feldspars. Since Jaek et al. (1997a, b) find excitation peaks up to excitation energies of 8 eV, they suggest the band gap in feldspar to be greater than 8 eV. This energy value for the optical band gap is later adjusted by Malins et al. (2004), who used low temperature (8 K) synchrotron-based excitation spectroscopy and determined the band gap of feldspar to be ∼7.7 eV, with small variations between the K-, Na- and Ca-feldspar end members (7.70, 7.86 and 7.62 eV, respectively). This band gap is narrower than in quartz (by ∼1 eV, Malins et al., 2004), which will possibly have an effect on the stability of electron and hole traps within it (see section 5.1). The band gap energy of 7.7 eV is later independently confirmed by Poolton et al. (2006), who used photo-transferred-OSL (PT-OSL) excitation spectroscopy on $KAlSi_3O_8$ and $NaAlSi_3O_8$ specimens.

3.4.2 Trap depth

The trap depth (in eV) defines the energy difference of the ground state of the trap to the conduction band edge and is an important parameter in luminescence dating, as the trap depth will influence the stability of trapped electrons over geological time scales (e.g. Aitken, 1985, p. 269-273; Strickertsson, 1985). In terms of trap depth, this section will only consider the optical trap depth, since this can be determined using optical excitation spectra. The term trap depth is also used in relation to a thermal trap depth (e.g. Strickertsson, 1985; Brown and Rhodes, 2017), however, these findings will not be discussed here. Excitation

spectroscopy has also been used to determine whether the commonly used IRSL arises from a single type of trap or multiple distinctly different traps and whether TL and IRSL arise from the same defect types.

Hütt et al. (1988) and Hütt and Jeak (1989) used excitation spectroscopy combined with thermo-optical bleaching experiments and suggested that the electron trapping centres involved in IRSL are located ∼2.25 eV below the conduction band and that IR stimulation (∼1.43 eV) results in a thermo-optical release of the electrons from said trapping centres via excited states of the trapping centres. In addition, Hütt and Jaek (1989) link TL and IRSL to the same type of crystal defect that functions as electron trapping centres in feldspars.

Whilst Hütt et al. (1989) and Hütt and Jeak (1989) proposed a model for IRSL which is based on a single type of electron trapping centre, Clark and Sanderson (1994) presented a model which includes two different types of electron trapping centres. Their spectroscopic pulse annealing studies revealed a stable component in their excitation spectrum between ∼500 and ∼540 nm even after 30 s of annealing the samples at 400 °C. Based on this observation Clark and Sanderson (1994) proposed two mechanisms: (i) one type of electron trap with a trap depth of 2.5 eV and two excited states and (ii) a second type of electron trap with a depth of 2.9 to 3.3 eV and one excited state, with both mechanisms controlling optically stimulated luminescence processes in feldspars. However, the less thermally stable component, which is related to the shallower trap, according to Clark and Sanderson (1994), is much more intense than the thermally stable component related to the type of trap with a depth between 2.9 eV and 3.3 eV. This lead these authors to suggest that thermo-optical emptying of the trapped electrons is the dominant process.

In 2003 Baril and Huntley test the luminescence response due to different excitation energies ranging from 1.24 eV to 2.54 eV and found that the increase in luminescence intensity is proportional to the increase in excitation energy up to ∼2.5 eV. Baril and Huntley (2003) also show that the excitation spectra are similar when recorded in the violet, green-yellow and UV. Based on these results Baril and Huntley (2003) propose that only one type of electron trap plays a role in these luminescence processes.

Andersen et al. (2012) measured excitation spectra with a focus on the IR resonance peak after different heat and IR stimulation pre-treatments. The authors observed a decrease in signal intensity with increasing preheat temperatures, but no change in IR resonance peak shape was observed. Thus, Andersen et al. (2012)

inferred that the IRSL signal of feldspars originates from either a single type of deep electron trap or multiple types of deep electron traps, but these authors exclude the participation of shallow traps in the IRSL process. To further explore whether one or multiple deep electron traps are the source of the IRSL signal of feldspars, Andersen et al. (2012) measured dose response curves of the IRSL and post-IR IRSL signals. Dose response curves measured using different excitation wavelengths show identical shapes. These observations support the hypothesis of a single type of electron trap being responsible for the IRSL and post-IR-IRSL signal. Andersen et al. (2012) observed differences in the thermal stability of the IRSL and post-IR IRSL signal, and also differences in the shape of the dose response curve for the two signals, however, they explain this with the different access to different luminescence centres in a distribution of such centres, dependent on the measurement temperature. Thus, Andersen et al. (2012) concluded that the infrared stimulated luminescence signal of feldspars arises from a single type of electron trap.

The first to hypothesise a trap depth for an electron trap in feldspar were Hütt et al. (1988). Using excitation spectroscopy and theoretical considerations, Hütt et al. (1988) suggested the optical trap depth to be ∼2.5 eV (Fig. 3.3). Kars et al. (2013) performed similar experiments to Hütt et al. (1988), but at cryogenic temperatures (10 K) with excitation energies ranging from 1.7 eV to 2.8 eV (Fig. 3.3). Here the emission was recorded in the UV (290-360 nm). Using equation 3.2 for the photo-ionisation cross-section (Bøtter-Jensen et al., 2003, p. 22), Kars et al. (2013) fitted the high-energy part of the non-resonant rising continuum to obtain the optical trap depth E_t.

$$\sigma(E, E_t) \propto \frac{(E - E_t)^{3/2}}{E(E - E_t(1 - m_0/m^*))} \tag{3.2}$$

In equation 3.2 σ is the photo-ionisation cross-section, E_t is the trap depth, m_0 the electron rest mass, m^* the effective electron mass (fixed at $m^* = 0.79\ m_0$, Poolton et al., 2001; Kars et al., 2013) and E the excitation energies used. Kars et al. (2013) thus constrained E_t for a K- and Na-feldspar specimen and obtained trap depths of $> \sim$2.5 and ∼2.1 eV, respectively.

3.4.3 IR resonance peak

Hütt et al. (1988) showed the presence of two IR excitation peaks. Other authors further investigated the position and shape of the IR resonance peak. Clark

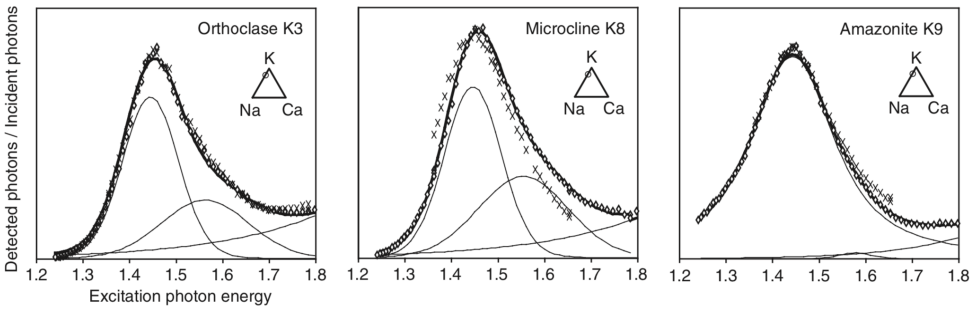

Figure 3.4: *Measured IR resonance peaks for three different samples for the violet emission (open diamonds), green-yellow emission (crosses for K8 and K9), and UV emission (crosses for K3). The bold line is the fit to the violet emission data using a Voigt profile, a Gaussian and an exponential function. The figure has been taken from Baril and Huntley (2003).*

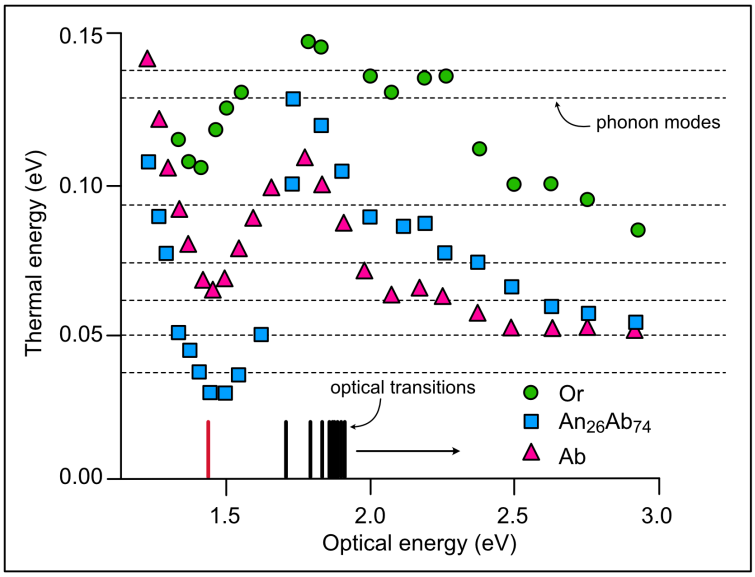

Figure 3.5: *Thermal activation energy dependent on the optical excitation energy of three different feldspar samples. The IR resonance is clearly visible due to the low thermal activation energy needed in the excitation process of trapped electrons in that optical excitation energy range (∼1.45 eV). With all optical transitions being allowable at optical excitation energies >1.896 eV, the thermal energies decrease. Possible optical transitions in the Bohr hydrogen model of a donor defect in albite are shown, with the arrow indicating that all transitions above 1.896 eV are allowable. The horizontal dashed lines represent thermal energies at which main lattice vibrational modes occur. Modified from Poolton et al. (1995b).*

and Sanderson (1994) compared excitation spectra of a K-rich feldspar sample (F1) measured with excitation from a Xe-lamp and a tungsten halogen lamp and observed that the spectrum measured using the halogen lamp, as well as a power-normalised spectrum using the Xe-lamp, revealed only a single IR resonance peak, in contrast to their and Hütt et al.'s (1988) Xe-lamp excited spectra. Thus, the two excitation peaks in the IR are artificial artefacts caused by the Xe-lamp used as excitation light source. By comparing the IR resonance peak position measured in excitation spectra of K-, Na- and Ca-rich single crystal feldspars with theoretical calculations assuming a Bohr hydrogen model to be valid for feldspars, Poolton et al. (1995a) inferred that the IR resonance peak reflects the first excited state of an electron trap in feldspars.

Bailiff and Barnett (1994) explored variations in IR resonance peak position with different measurement temperatures for a microcline microperthite. These authors found that the peak position shifted by 0.022 eV, from 1.455 eV at room temperature to 1.477 eV at 145 K; this is accompanied by a narrowing of the peak width (decrease in FWHM of 0.01 eV). Godfrey-Smith and Cada (1996) measured the IR resonance peak position of chemically different feldspars and found excitation peak positions between 840 nm and 845 nm (1.476 and 1.467 eV) for all alkali and plagioclase feldspar samples investigated, which suggests only little variations in the first excited state between samples. Baril and Huntley (2003) recorded excitation spectra of different feldspars, with a particular focus on the IR resonance peak, with emissions recorded in the blue, UV and yellow-green region (Fig. 3.4 for examples from Baril and Huntley, 2003). All samples showed an IR resonance peak at ∼1.44 eV, and no significant differences were observed for the different emissions, except in the excitation spectra of one sample, a microcline perthite (K8). For this sample, Baril and Huntley (2003), saw differences between the excitation peak recorded in the blue and green-yellow bands (Fig. 3.4), which led the authors to suggest that the differences arise due to the two different mineral phases present in the sample. Although, the position of the peak maxima does not change between samples, the general shape of the peak does, so that Baril and Huntley (2003) used different fits (Gaussian, Lorentzian and Voigt) to describe them. These authors tried to relate differences in the fit with physical properties of the samples, but were not able to draw any conclusions. However, based on the fitting, Baril and Huntley (2003) described the peak as three resonances, located at 1.32, 1.44 and 1.56 eV. Measurements at temperatures ranging from 290 K to 490 K indicated that the excitation peak broadens

with increasing temperature, but fitting of the excitation spectra measured at different temperatures suggested that the 1.44 eV resonance width remains unchanged, leading the authors to conclude that no phonon interactions are involved in the peak broadening of the 1.44 eV resonance.

Clark and Sanderson (1994) showed that thermal assistance increased the luminescence emission across the entire excitation spectrum investigated. From excitation spectra measured at different temperatures, Clark and Sanderson (1994) calculated thermal activation energies for different excitation wavelengths (0.2 eV at 910 nm, 0.17 eV at 624 nm and 0.15 eV at 500 nm). These findings were adjusted by Poolton et al. (1995b), who used an Arrhenius relationship of the temperature dependence of the luminescence intensity. The thermal activation energies calculated for different optical excitation energies are presented in Figure 3.5, for orthoclase, albite and a plagioclase sample. The data by Poolton et al. (1995b) shows the effect of the IR resonance peak on the thermal activation energy needed, in addition to optical excitation, to evict charge from the electron trap. For the plagioclase sample ($An_{26}Ab_{74}$, Fig. 3.5) it is evident from Figure 3.5 that the additional thermal activation energy required to evict charge from an electron trap is lowest around 1.45 eV. For the two alkali feldspar samples (referred to as Or and Ab in Fig. 3.5), the thermal activation energies are not at the lowest value of the entire excitation energies measured, but the data in Figure 3.5 does show a definite decrease in thermal activation energy needed for trapped charge eviction around the energy of the IR resonance peak.

3.4.4 Band-tail states

In 1994, Poolton et al. proposed the presence of band-tail states in feldspars. They explain this with large variations in bonding angles within the crystal and the high ionicity of feldspars. This will form band-tail states below the conduction and above the valence band, which allow charge to move through the crystal, either by hopping or via tunnelling (Poolton et al., 1994). To assess the influence of thermal assistance and the presence of band-tail states in feldspars, Poolton et al. (1994, and in more detail in 1995b) measured optical excitation spectra at temperatures ranging from room temperature to 500 °C and calculated thermal activation energies for the different optical excitations. The results of Poolton et al. (1995b) are shown in Figure 3.5 for orthoclase, albite and a plagioclase sample ($An_{26}Ab_{74}$). From these measurements, and measurements of thermal

dependence of photoconductivity, Poolton et al. (1994) hypothesised the presence of band-tail states below the conduction band of feldspars. This was later confirmed by Poolton et al. (2002a, b) and Malins et al. (2004).

Although the presence of such band-tails had been confirmed, the actual width and their role in luminescence processes needed further attention. Poolton et al. (2009) gave further information regarding the nature of the band-tail states and their role in luminescence processes in feldspars. These authors measured excitation spectra from 1 eV to 1.95 eV at 300, 200, 100 and 10 K of X-ray irradiated K- and Na-feldspar specimens (emission recorded in the range of 300nm to 380 nm). The excitation spectra show the expected IR resonance peak at ∼1.44 eV and a non-resonant rising continuum, which Poolton et al. (2009) fit with Equation 3.3 to obtain ΔE, the width of the band-tail states accessible from the ground state of the trap.

$$OSL(E) \propto exp(\frac{E - E_t}{\Delta E}) \tag{3.3}$$

In equation 3.3, E_t is the trap depth (in eV) of the defect, and E the different excitation energies used (in eV). By fitting the non-resonant rising continuum obtained in the measurements at different temperatures, Poolton et al. (2009) observed a rapid change in ΔE with decreasing temperature from 300 to 100 K, reaching a plateau for measurements below 100 K. This change in ΔE arises due to changes in charge transport through the band-tail states at different temperatures. Poolton et al. (2009) gave the explanation that, at room temperature, charge transport occurs due to a thermally activated hopping processes. At low temperatures, such hopping is not possible anymore, and charge will now only move via tunnelling from tail to tail, which is non-thermal. At room temperature, ΔE was measured as 0.3 eV and 0.12 eV for K- and Na-feldspars, respectively. Kars et al. (2013) used the same approach and were able to support these findings, by obtaining ΔE values of 0.23 eV and 0.18 eV for K- and Na-feldspar, respectively.

In addition to the constraints of ΔE, Poolton et al. (2009) also determined E_u (the full band-tail width, also termed Urbach width). Using photo-transferred OSL (synchrotron photons of energies of 5.5 eV to 9.0 eV) E_u was measured as 0.67 eV and 0.28 eV for K- and Na-feldspar at 10 K, respectively. In a third experiment, which involved fitting of energy-resolved stimulation spectra (after X-ray irradiation), E_u was measured as 0.54 eV and 0.32 eV, for the two samples,

respectively. As an average of these different measurements, Poolton et al. (2009) present 0.4 eV. Using an excitation energy dependent emission (EDE) of the green photoluminescence emission Prasad and Jain (2018a) measured the width of the sub-conduction band-tail states to be ∼0.6 eV, which is in agreement with the findings by Poolton et al. (2009). The results of the width of the band-tail states are particularly important as they suggests that on the basis of an electron trap depth of 2.25 eV (Hütt et al., 1988; Kars et al., 2013), the IR resonance peak, possibly reflecting the first excited state of the electron trap, potentially lies within these band-tail states. If this is the case, it will result in charge in the trap being less stable compared to a hypothetical case where band-tail states are not present.

3.5 Luminescence emissions and associated defects

In contrast to excitation spectroscopy, emission spectra are recorded using either a broad-band excitation (e.g. heat in TL emission spectra or IR LEDs in IRSL emission spectra) or a single excitation wavelength (e.g. by using a laser or a monochromatic beam of light extracted from a white light source using a grating system); the emission of the sample is recorded either by scanning a range of wavelengths (Hamilton et al., 1978, p. 156) or using polychromatic spectrometers such as a CCD detector. The following section will discuss different emissions from the ultraviolet (UV) to the infrared (IR), looking at their properties and the defects that they may be related to. Figure 3.6 presents results from various emission spectroscopic studies of different feldspars and gives an overview of observed emission bands and might help to understand possible dependencies of emissions on the feldspar type.

3.5.1 UV emission

Presence and sources of the UV emission (∼290 nm)

The emission in the UV, centred around ∼290 nm, has been found in a variety of feldspar samples, in alkali feldspar and plagioclase, with varying intensities (e.g. Prescott and Fox, 1993; Prescott et al., 1994; Rendell et al., 1995; Garcia-Guinea et al., 1996). Prescott and Fox (1993) found that the UV (275 nm) emission

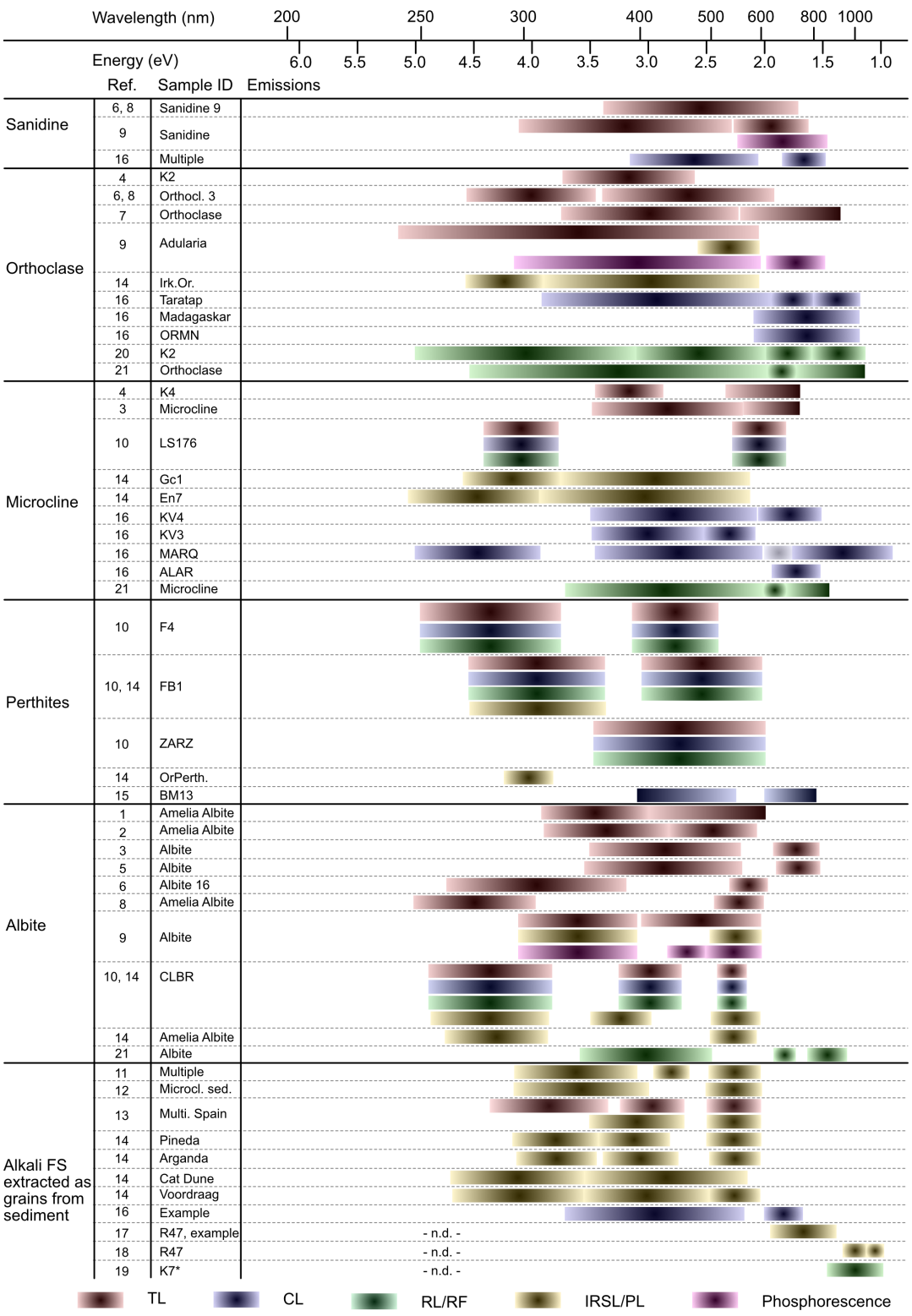

Figure 3.6: *Emissions recorded for various alkali feldspars. Details regarding the indexed studies can be found in the caption of Fig. 3.6 (continued).*

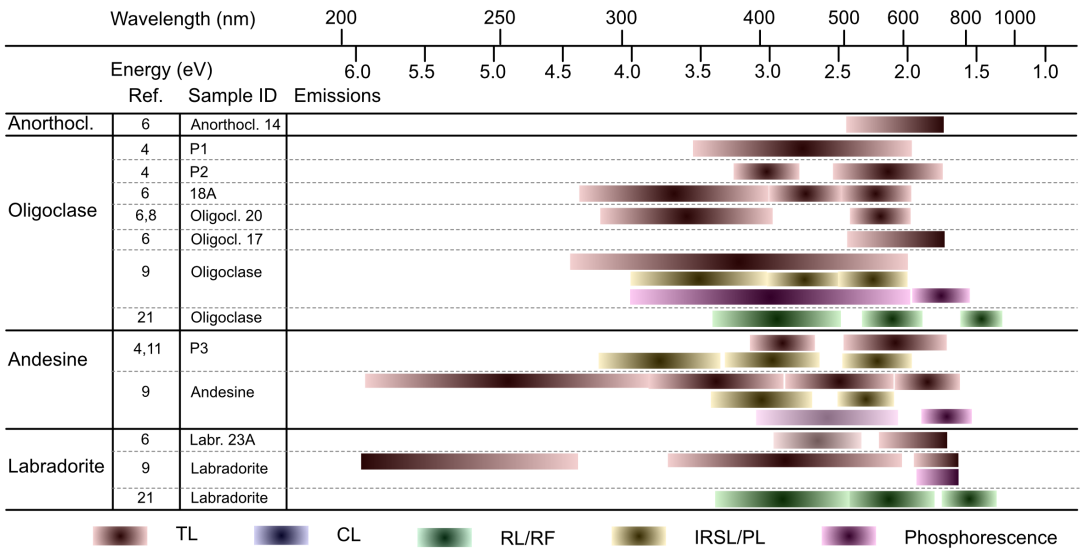

Figure 3.6 (continued): *Emissions recorded for various plagioclase feldspars. The different intensities of the coloured bars reflect the intensity of the emission, with the darker part of the bars representing the peak of the emission. When analysing this figure, it should be noted that the emissions were recorded on different instruments and that some spectra were not corrected for the instrumental response. Some spectra presented in the literature showed intense emission in the long wavelength range, which might arise due to black body radiation. In such cases, these emissions are not shown in the figure. The reader is referred to the individual publications listed here. References:* [1]*Levy (1979),* [2]*Akber and Prescott (1985),* [3]*Kirsh et al. (1987),* [4]*Huntley et al. (1988),* [5]*Kirsh and Townsend (1988),* [6]*Prescott and Fox (1993),* [7]*Dalal et al. (1988),* [8]*Prescott et al. (1994),* [9]*Krbetschek and Rieser (1995),* [10]*Rendell and Clarke (1997),* [11]*Huntley et al. (1991),* [12]*Rieser et al. (1997),* [13]*Rendell et al. (1995),* [14]*Clarke and Rendell (1997),* [15]*Finch and Klein (1999),* [16]*Visocekas et al. (2014),* [17]*Prasad and Jain (2018b),* [18]*Kumar et al. (2018),* [19]*Erfurt and Krbetschek (2003),* [20]*Erfurt (2003),* [21]*Trautmann et al. (1998).*

is weaker in alkali feldspars, compared to their plagioclase with more than 75 mole % albite (their Amelia albite and oligoclase sample). Rendell et al. (1995) observed that the UV emission (∼290 nm) is only present in TL spectra, not in IRSL spectra of feldspar extracted from sand-sized sediment (density 2.58 g cm^{-3}; see spectra for reference 13 in Fig. 3.6). By comparing TL spectra before and after IR stimulation, Rendell et al. (1995) found that the UV emission in TL is considerably reduced by IR stimulation. These authors hypothesise that IRSL stimulation may remove charge from the defect associated with the UV emission, or might even destroy the defect. As a hypothetical example, Rendell et al. (1995) mention defect sites, which could have an —H or —OH group attached. These groups could be released during IR stimulation, which would result in destruction of the associated defect. Garcia-Guinea et al. (1996) only saw the UV emission (∼290 nm) in samples with exsolution features in perthites, and in albite. Thus, Garcia-Guinea et al. (1996, 1999) associated the UV emission (∼290 nm) with either Na-feldspar phases or the interfaces in perthites and link the emission to

Na self-diffusion through interfaces, and the occurrence of Na-O bonds. This is particularly interesting, as luminescence phenomena are mostly associated with electron and hole recombination. The findings by Garcia-Guinea et al. (1996, 1999) are supported by the experimental results of Rendell and Clarke (1997). They observed a UV emission around ∼290 nm for their orthoclase sample, which contained 2.77 % Na_2O but showed exsolution features (emission spectrum for samples LS176 for reference 10 in Fig. 3.6), while a sanidine sample containing 4.3 % Na_2O, but which did not exhibit exsolution features, did not have a UV emission.

Instability of the UV emission (∼290 nm)

The UV emission (∼290 nm) has been found to be unstable over time and sensitive to optical and thermal treatment. Prescott et al. (1994) show that the UV emission is rapidly reset by sunlight bleaching. Clarke and Rendell (1997) observe that the UV emission is only present in IRSL spectra after artificial irradiation, and not in sample material which contain their natural dose, and they link this to instability of the signal over time. Experiments by Clarke and Rendell (1997) confirmed this hypothesis, with a preheat at 220 °C for 5 min removing the 290 nm UV emission completely, and room temperature storage of 17 h and 20 h resulted in the decrease of the 290 nm emissions in two albite samples investigated. The low stability of the UV emission is supported by findings of Garcia-Guinea et al. (1999), who observed a loss of the UV emission in IRSL spectra of their single-phase albite (CLBR) due to preheating at temperatures ranging from 80 °C to 200 °C. The greatest loss of UV signal is recorded for the highest preheat temperature. Another effect of preheating on the UV emission (∼290 nm) is a displacement of the emission peak in IRSL spectra (Garcia-Guinea et al., 1999). Larger displacements of the UV emission peak are observed for samples with a higher degree of Al-Si disorder on the framework, exsolution features and higher Na contents. The fully disordered sanidine sample did not show any UV emission (Garcia-Guinea et al., 1999).

By calculating the energy difference between the conduction band edge and the recombination centre responsible for the UV emission, Malins et al. (2004) give a possible explanation for the low stability of this emission. Based on results of low temperature synchrotron excitation spectroscopy Malins et al. (2004) infer a band gap of ∼7.7 eV in feldspars. This band gap is about ∼1 eV smaller than the band gap of quartz. This slightly narrower band gap will have an influence on

the presence of stable electron and hole traps for geological dating purposes. Due to their small trap depth (∼2 eV) from the valence band, recombination centres with emission wavelengths shorter than 300 nm will be unstable (Malins et al., 2004). This would thus relate to the observed unstable UV emission in feldspars and would mean that the defect is located in close proximity of the valence band, which will cause its low stability.

Additional (near-) UV emissions and their relationships to each other

Other emissions in the near-UV region have been found in different feldspars: Bailiff and Poolton (1991) observed an emission band around 360 nm in a sanidine sample and Huntley et al. (1991) observe an emission between 300 and 350 nm for plagioclase feldspar. Krbetschek and Rieser (1995) detect the emission in albite and oligoclase, but not in andesine and in any of the alkali feldspars investigated. In contrast Garcia-Guinea et al. (1999) found the near-UV emission band around ∼340 nm in microcline samples from plutonic and metamorphic rocks. The emission is absent in sanidine samples. Garcia-Guinea et al. (1999) thus associated the presence of the 340 nm emission band with cross-hatch twinning, which characterises the microcline samples; no twinning is apparent in the sanidine samples.

Clarke and Rendell (1997) and Garcia-Guinea et al. (1999) investigated possible relationships between the 290 nm and 340 nm emission bands in feldspars using the same albite sample (CLBR, a single crystal albite specimen from Brazil). Both groups of authors collected IRSL spectra of the sample after different preheat temperatures and found that the emission band around ∼290 nm decreased with increasing preheat temperature. Clarke and Rendell (1997) found that simultaneously the emissions around ∼380 nm and around ∼570 nm increased, and described this as charge transfer from the ∼290 nm emission band into the other bands in the albite sample CLBR. Garcia-Guinea et al. (1999) observed similar results, especially for the violet (∼390 nm) and the blue emission (∼420 nm). Garcia-Guinea et al. (1999) associated this with either ionic motion or charge tunnelling. Garcia-Guinea et al. (1999) investigated potential relationships between the emissions around 290 nm and 340 nm and found two trends: For K-feldspars the intensity of both emissions increases proportionally to each other, in comparison for sodium-perthites the intensity of the 340 nm emission band increases with decreasing 290 nm band emission intensity. The authors did not explain the physical processes behind these trends, but point out that

these relationships could be used to further investigate the nature of the defects associated with the two emission bands in feldspars.

3.5.2 Blue emission

The blue emission (∼410 nm) is a common feature across the whole feldspar group and has been observed in radioluminescence (RL), cathodoluminescence (CL), TL and IRSL spectra in a variety of feldspars (e.g. Sippel and Spencer, 1970; Kirsh et al., 1987; Huntley et al., 1988; Huntley et al., 1991; Garcia-Guinea et al., 1996). Exemplary emission spectra showing the presence of the blue emission in a variety of samples measured by Kirsh et al. (1987) and Huntley et al. (1988, 1991) are presented in Figure 3.6. The blue emission centred at ∼410 nm is commonly used in IRSL dating of feldspar and is thus of particular interest. Although the emission centred at ∼410 nm is commonly referred to in luminescence dating studies of feldspars, the isolation of this emission is often achieved using different filter combinations. These filter combinations have transmission windows that result in the transmission of not only the 410 nm emission, but rather a wide range stretching from ∼360 nm to ∼460 nm (e.g. when using a filter combination of a Schott BG39 and Schott BG3) and will thus potentially include emissions arising from different emissions.

Blue emission upon different excitations and in relationship to other emissions

Sippel and Spencer (1970) measured luminescence emission spectra upon electron beam excitation of 47 terrestrial feldspars and found the blue emission (∼450 nm) in 45 of these samples, with the exception of two alkali feldspars. The authors observed a specimen-dependent shift of the blue emission band, but the shift is not relatable to the sample composition and the cause is unknown. The authors suggested that multiple emission centres could cause the blue emission. Dalal et al. (1988) investigated TL emissions from an orthoclase sample immediately after X-ray irradiation (see Fig. 3.6, reference 7 for the freshly irradiated TL emission spectrum), and after 23 hours of storage. The sample shows broad emissions with emission peak intensities in the blue and red wavelength region. The authors observed a shift in emission peak energy towards higher temperatures when storing the sample prior to the measurement; additionally the overall luminescence intensity decreases due to storage. Prescott and Fox (1993) found the 400 nm TL

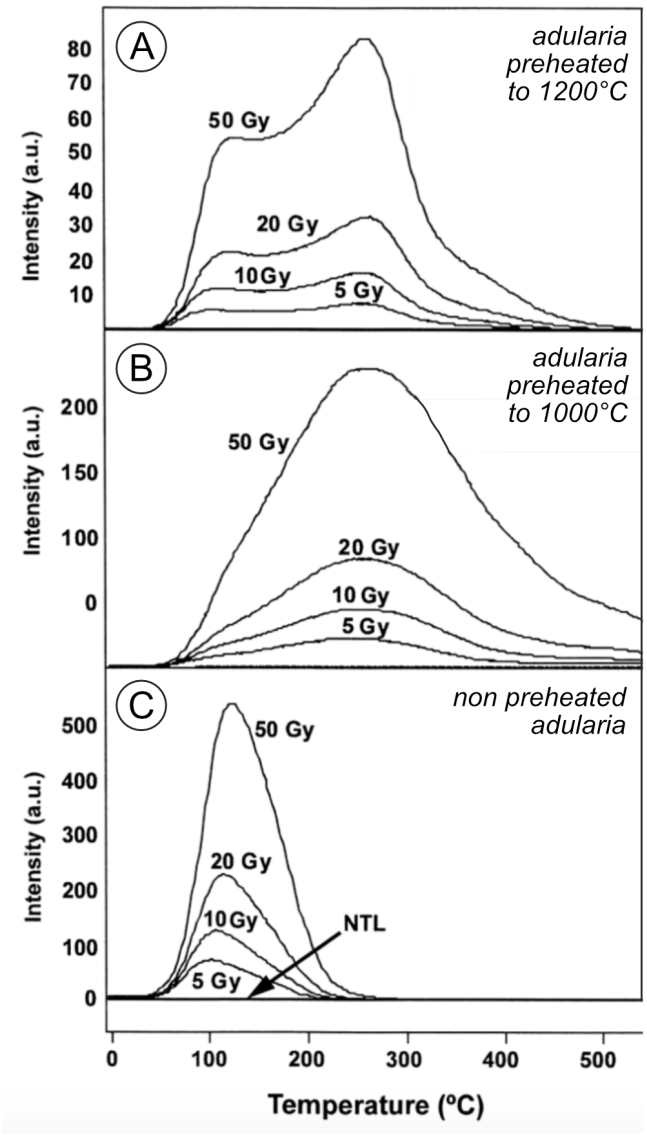

Figure 3.7: *Comparison of TL curves of the non-heated (C) adularia feldspar, the same sample heated to 1000 °C for 24 hours (B) and the adularia heated to 1200 °C for 240 hours (A) (Figure modified from Correcher et al., 2000).*

emission band to be the dominant emission in alkali feldspars with a K-feldspar content of more than 80 % (see TL emission band in Fig. 3.6 for sanidine 9). The emission is also present, but weaker, in alkali feldspar with smaller K-feldspar content and in some of the plagioclases investigated. Additionally, Prescott et al. (1994) describe a broad blue emission band centred around ∼480 nm, with a tail towards the UV (see emission bands for Orthoclase 3 in Fig. 3.6). The temperature at which the 480 nm emission band occurs varies between natural and artificially irradiated samples, with the emission occurring at lower temperatures for artificial TL (Prescott and Fox, 1993). Krbetschek and Rieser (1995) compare TL and IRSL spectra of orthoclase and show that the blue emission (∼420 nm)

is only present in TL, but not in IRSL spectra (Fig. 3.6, Adularia sample of reference 9. Rendell and Clarke (1997) observed a shift of the blue emission peak due to different excitation modes, when comparing CL, RL and TL. For CL the emission occurs at slightly longer wavelength compared to RL and TL (cf. TL, RL and CL for samples of reference 10 in Fig. 3.6).

Potential defects giving rise to the blue emission

The blue emission is thought to arise from a hole centre located on an Al-bridging O, as determined by EPR studies (Speit and Lehmann, 1982; Finch and Klein, 1999). Speit and Lehmann (1982) used EPR on eight feldspar samples and found electron-hole centres located on Al-bridging O ions in a variety of alkali feldspars, and in albite, oligoclase and labradorite. These hole centres occur in ordered (microcline) and disordered (sanidine) K-feldspars; however, only in sanidine are they present prior to artificial irradiation. Finch and Klein (1999) showed that the hyperfine structures in EPR, related to this hole centre, are only present in grains emitting blue CL, but not in grains which only show red CL. These hole centres were detected at low temperatures (e.g. 4 K and 77 K in Speit and Lehmann, 1982; at 50 K and 77 K in Finch and Klein, 1999), but are not detectable at higher temperatures (e.g. room temperature). The absence of the hyperfine structures in room temperature EPR measurements is likely due to rapid exchange of the hole between nearby oxygen ions (Speit and Lehmann, 1982). This is only possible in a cluster situation of three Al ions (one structural Al and two impurity Al ions, substituting for Si^{4+}). Thus, these hole centres associated with Al-O-Al bridges also indicate a certain degree of disordering (Speit and Lehmann, 1982; Finch and Klein, 1999): Al-O-Al bridges cannot exist in fully ordered feldspars, as slight disorder stabilises these bridges.

Short (2004) evaluated the response of the 3.1 eV (400 nm) emission of an orthoclase feldspar sample due to different polarisation of the excitation light (1.45 eV). It was found that the emission intensity depends on the polarisation of the excitation light, and additionally the emission was also polarised. Based on the excitation and emission results and the observed polarisation, Short (2004) inferred that a pair of dipole directions is aligned to the symmetry directions of the T1 sites and the four associated oxygen ions. Since this was found to be the case for the excitation at 1.45 eV and the emission at 3.1 eV, Short (2004) hypothesised that the defects responsible for the IR-sensitive electron trap and the defect associated with the blue emission are associated with transitions in defects

on T_1 sites. Short (2004) independently validates his hypothesis by investigating the potential defect location for Fe^{3+}, which is known to occupy T_1 sites on the framework of feldspars (see more details in section 5.4).

Garcia-Guinea et al. (1999) showed that the blue emission in alkali feldspars could be increased in intensity by high temperature annealing plus short wavelength irradiation (e.g. UV, gamma or X-ray). The lattice is sensitised by heating, and the short wavelength irradiation then activates the emission centre. The authors explained this by thermal leakage of various ions and molecules (e.g. Na^+, K^+, OH^-, H^+ and H_2O), especially along twin-interfaces in single-phase feldspars, and inferred that a similar process could occur along interfaces in perthites. The broadness of the blue emission (∼350–500 nm) arises due to thermal treatments, which modify distances between Na^+ and O^{2-} ions and result in an increase in thermal vibration of Na atoms. Especially thermal treatments around 700-800 °C cause irreversible changes to the lattice and cause the very broad blue emission (Garcia-Guinea et al., 1999). Correcher et al. (2000) made similar observations for adularia feldspar ($KAlSi_3O_8$). The authors observed an increase in blue luminescence intensity with high temperature (prolonged 1000 °C and 1200 °C) pre-treatments. Additionally, a TL curve measured for the blue emission changed its shape, from a low temperature TL peak (∼100 °C) towards a broader peak, with a maximum at ∼300 °C (Fig. 3.7). Correcher et al. (2000) explained the signal increase and the shift in emission temperature with movement and a reduction of ionic charge compensators, such as H^+, Na^+ and K^+ and subsequent creation of hole centres associated with AlO_4 on the framework (note that the oxygen ions are shared between Al- and Si- tetrahedra, so that the hole centre on AlO_4 balances the net negative charge). Heating at temperatures between 400 and 700 °C increases the luminescence intensity of emissions between 420 to 500 nm of the adularia feldspar. Correcher et al. (2000) associated this with alkali ion diffusion causing homogenisation of K- and Na-feldspar phases. For luminescence dating it should be noted that heat treatments at temperatures as low as 400 °C can influence the blue luminescence signal, which could result in changes in sensitivity of the signal.

In contrast to the proposed hole centre on an Al-bridging O ion being responsible for the blue emission in alkali feldspars, a different defect has been proposed for the blue emission in plagioclase. Mariano and Ring (1975) and Götze et al. (1999) observed a blue emission centred around ∼420 nm in Eu^{2+}-doped synthetic anorthite and natural plagioclase and link the emission to Eu^{2+} substi-

tuting for Mn^{2+} on M sites. Decay time measurements performed by Finch and Klein (1999) of blue CL indicated that Eu^{2+} cannot be responsible for the blue luminescence in alkali feldspar, since a short half-life (6 μs) determined for the blue CL in alkali feldspar is characteristic for an intrinsic defect, and not of an extrinsic defect such as Eu^{2+} substituting on M sites. These observations suggest that the source of the blue emission differs in alkali feldspars and plagioclases.

Despite these differences in potential crystal defects associated with the blue emission in alkali feldspars and plagioclases, similar energies for an excitation feature linked to the blue luminescence were observed from photo-transferred OSL excitation spectra (Poolton et al., 2006). These excitation peaks, observed at 4.3 eV and 4.5 eV for Na- and K-feldspar, respectively, indicate that the defect giving rise to the blue emission in these end members is located about 4.4 eV below the conduction band edge (Poolton et al., 2006).

Fading of the blue luminescence

It has been found that the luminescence signals of feldspars are not stable over time. In 1973 Wintle attempted to date feldspars from lava flows using thermoluminescence and observed TL ages which underestimated the known ages of the lava flows by up to a magnitude. Wintle (1973) referred to this loss of charge as anomalous fading. Fading has been observed to occur in TL (e.g. Wintle, 1973; Visocekas, 1985) and IRSL (e.g. Thomsen et al., 2008) and of different emissions (e.g. Krause et al., 1997; Zink and Visocekas, 1997; Thomsen et al., 2008). This loss of charge over time will results in age underestimation, if uncorrected. Thus, overcoming fading has been the main aim of research studying feldspar luminescence and considerable improvements have been made regarding the stability of the luminescence signal used for dating (e.g. Thomsen et al., 2011; Li and Li, 2011; Buylaert et al., 2012) and in developing methods which correct for anomalous fading (Huntley and Lamothe, 2001; Kars et al., 2008). Despite these improvements, many questions remain especially regarding the fundamental processes and the crystallographic defects influencing anomalous fading in feldspars require further investigation, particularly of the blue emission.

Quantum mechanical tunnelling (Visocekas et al., 1976; Visocekas, 1985) is generally accepted as the process behind this anomalous signal loss over time, though other processes have been proposed: Wintle (1977) discussed the possibilities of defect diffusion, direct transfer from an electron trap to a luminescence centre and a decay of effective luminescence centres; Templer (1986) proposed a

localised transition model for anomalous fading in different minerals; and Chen et al. (2000) suggested competition with non-radiative recombination centres as an additional process to quantum mechanical tunnelling. Visocekas (1979) reported a logarithmic decay for fading. This logarithmic decay has later been used in models describing anomalous fading and in proposed correction methods (Huntley and Lamothe, 2001; Huntley, 2006; Kars et al., 2008). Huntley (2006) linked the rate of anomalous fading with the density of available recombination centres, and showed that an increase in the number of recombination centres would result in higher fading rates. In response to the presented tunnelling (or proximity) models, which form the basis of Huntley's (2006) model, Sanderson (1988) considered hypothetical defect concentrations based on luminescence signal intensities and found that in order to make a tunnelling model work (so that an empty hole trap is actually within tunnelling distance of an electron trap) much higher defect densities would be required, which in turn would result in much higher luminescence signal intensities, as those observed and considered by Sanderson (1988). Significant differences in anomalous fading rates have been observed in single-crystal feldspars (e.g. Spooner, 1992, 1994; Huntley and Lian, 2006) and in feldspar (single) grains extracted from sediments and bedrock (e.g. Neudorf et al., 2012; Trauerstein et al., 2012; Valla et al., 2016).

Spooner (1992, 1994) compared feldspar IRSL signal intensities of the emission ranging from ∼360 to ∼620 nm of chemically different feldspars before and after storage (up to 15 months) at 10 °C and 100 °C and observed different stabilities of the IRSL signal, dependent on the sample and the storage temperature. Spooner (1994) measured stable IRSL signals for an orthoclase, a microcline and an albite sample. However, two further microcline feldspars in his study faded. Visocekas and Zink (1995) proposed that the volcanic origin of samples and the associated disorder of Al^{3+} and Si^{4+} on the framework, in addition to Fe^{3+} ions substituting for Al^{3+}, increase fading in feldspars. Visocekas and Zink (1995) suggested that ordered feldspars should thus not suffer from fading. However, this suggestion contradicts the mixed observations by Spooner (1994), and also by Huntley and Lian (2006) who measured IRSL fading rates of the ∼360 to ∼620 nm emission up to 12 % (over a time period of up to 600 days) in their, as microcline described, feldspars. Huntley and Lian (2006) compared fading rates of a total of 27 feldspars, including alkali feldspar, plagioclase and feldspars extracted from rocks and sediments. A comparison of measured laboratory fading rates and concentrations of K, Na, Ca, Fe and Mg (%) showed no correlation with

any of the parameters in the case of alkali feldspar. For plagioclases, Huntley and Lian (2006) reported a slight trend of increasing fading rate with increasing Ca-concentration, although even samples with the same Ca-concentration showed large differences in fading rates (%/decade). Valla et al. (2016) extracted feldspars from bedrock samples by crushing them and isolating material less than 2.58 g.cm^{-3} and material from 2.58-2.70 g.cm^{-3}. They then measured fading using an IRSL signal measured at 50°C with delays up to 55 hours. For the samples where material less than 2.58 g.cm^{-3} occurred, they observed fading rates between 3 and 11 %/decade. However, for samples where no material in this density occurred, they analysed material from 2.58-2.70 g.cm^{-3} and assumed that the IRSL signal arose from Na and/or Ca rich feldspars – these yielded high fading rates (up to 41.3 %/decade) and showed significant variability between samples (0.5 to 41.3 %/dec). In agreement with Huntley and Lian (2006), Valla et al. (2016) observed a pattern of increasing fading with increasing Ca-content of the samples.

Beside the association of increased fading with increased framework disorder (e.g. Visocekas and Zink, 1995) and the observed pattern of increasing fading with increasing content of Ca^{2+} ions (Huntley and Lian, 2006; Valla et al., 2015), no clear model has been proposed, which explains the role of crystal defects and anomalous fading rate of the blue emission in feldspars. However, a potential problem of in assigning a source to fading in feldspars is that fading measurements have been performed under different conditions, for instance using different preheat and IR stimulation temperatures or different delay durations (cf. Spooner, 1992; Huntley and Lian, 2006; Valla et al., 2016) or even the use of different protocols, i.e. protocols from the pre-single aliquot regenerative dose protocol time (e.g. Spooner, 1992), or different duration of IR probing of the trapped charge (i.e. short shine protocols or protocols using multiple irradiation and read out steps, cf. Auclair et al., 2003; e.g. Valla et al., 2016). A second problem could be the chemical and mineralogical identification of the feldspars used in fading experiments. Often feldspars are further described mineralogically (i.e. they are referred to as microcline, sanidine etc.), however, no experimental data is provided in the publications, which allows the reader to assess the mineralogical description of the samples (e.g. see Huntley and Lian, 2006; see also the discussion in Alexander, 2007, p. 228).

3.5.3 Green-yellow emission

Dependency on physical sample properties and measurement conditions

The green-yellow emission (∼550 nm to ∼580 nm) has been found in different feldspars. In some cases, it overlaps with the previously described blue emission, as visible from examples given in Figure 3.6. Kirsh et al. (1987) observed the emission in albite and microcline. Huntley et al. (1988) described the green-yellow emission (∼580 nm) as a key feature of the plagioclase feldspars that they studied, with the exception of an oligoclase sample. This oligoclase sample shows a broad emission from 380 nm to 620 nm, but it does not show the strong peak centred around ∼580 nm. In contrast, Prescott and Fox (1993) find the green-yellow emission in all plagioclase feldspars investigated with more than 75 mole % albite, thus also in oligoclase. Garcia-Guinea et al. (1996) observed the green-yellow emission (550–570 nm) in albite (CLBR) and, additionally, in one of the two investigated intermediate microcline samples. Clarke and Rendell (1997) confirmed these observations and described an independency of the green-yellow emission band position in albite CLBR and microcline LS176 on the excitation mode used (RL, CL, TL, see Figure 3.6 and emission bands for references 10 and 14). Krbetschek and Rieser (1995) observed a green emission at slightly shorter wavelength (∼510 nm) for orthoclase in TL and IRSL spectra.

Levy (1979) performed heating experiments of an Amelia albite sample and found that the peak wavelength of the emission band at ∼550 nm shifts with the duration of heating at 1050 °C. The maximum shift, from 2.22 eV (∼558 nm) to 2.18 eV (∼268 nm), was observed after 500 hours of heating. Levy (1979) suggested that disordering the crystal lattice during the experiment might have caused this shift in the peak position. By comparing TL emission spectra of albite, oligoclase and labradorite, Akber and Prescott (1985) found that the emission band around ∼530 nm decreases from albite to oligoclase to only a shoulder of the blue emission band in labradorite. The authors assumed that this is related to changes in the crystal structure of plagioclase, based on different Al:Si ratios and relative contents of Na^+ and Ca^{2+}.

Potential defects related to the green-yellow emission

Geake et al. (1971) measured emission spectra of lunar and terrestrial plagioclase samples with 60 keV proton excitation. The authors observed a strong green-

yellow emission in the plagioclase samples. To examine the origin of the green-yellow emission (∼560 nm), a terrestrial labradorite was doped with 0.1 % Mn during heating to 1050 °C for 30 min, which increased the green emission. Based on the doping experiment and crystal field theory, the authors conclude that Mn^{2+} substitutes for Ca^{2+} on M sites in the crystal. The resulting emission occurs between 550 and 600 nm, with a slight variation in peak position due to the co-ordination of the ion or a distortion of the octahedral symmetry (Geake et al., 1971). However, the authors did not mention if the actual heating could have caused these changes or if solely the doping is responsible for the larger intensity of the green emission after the experiment. Garlick et al. (1971) found that doping plagioclase with Mn results in brighter TL emission, without changing the shape of the TL curve, leading to the hypothesis that electron traps giving rise to TL are not closely associated with the green emission centres. Telfer and Walker (1978) used excitation spectroscopy and ligand field parameter calculations to investigate the site occupancy of Fe^{3+} and Mn^{2+} in plagioclase feldspars, by doping synthetic feldspar with Mn^{2+} and Fe^{3+}. The authors were able to show that there is a correlation of emission intensity in the green and the mole% of Mn^{2+} in synthetic feldspars. In excitation spectra overlapping peaks are observed, which cannot be distinguished, and open the possibility of Mn^{2+} potentially occupying two different sites in plagioclases. Based on calculations, taking bond distances and ionic radii into account, it is more likely for Mn^{2+} to occupy M sites, than T sites, but Telfer and Walker (1978) do not rule out the possibility of Mn^{2+} substituting for Al^{3+} in tetrahedral sites. However, room temperature decay times for yellow-green CL emission assigned to Mn^{2+} are ∼3 ms, which is three times longer than for the red emission of Fe^{3+}, which is thought to occupy T sites, by substituting for Al^{3+} (Telfer and Walker, 1978). Clark and Bailiff (1998) performed fast time-resolved IR-stimulated luminescence measurements of chemically and structurally different feldspars and fast decay lifetimes on the sub-ms to even ns scale for the green-yellow emission. Based on their results, Clark and Bailiff (1998) infer that these short lifetimes cannot result from the spin-forbidden transition of Mn^{2+} ions located on M sites. Instead, Clark and Bailiff (1998) consider the by Telfer and Walker (1978) and Kirsh et al. (1987) proposed T site occupancy of Mn^{2+} as a potential explanation of the fast lifetimes observed. Prasad et al. (2016) measured phosphorescence decay and found a dominant lifetime of the yellow-green emission band of the order of hundreds of microseconds to less than a millisecond. As Clark and Bailiff (1998) before, Praad et al. (2016) highlight

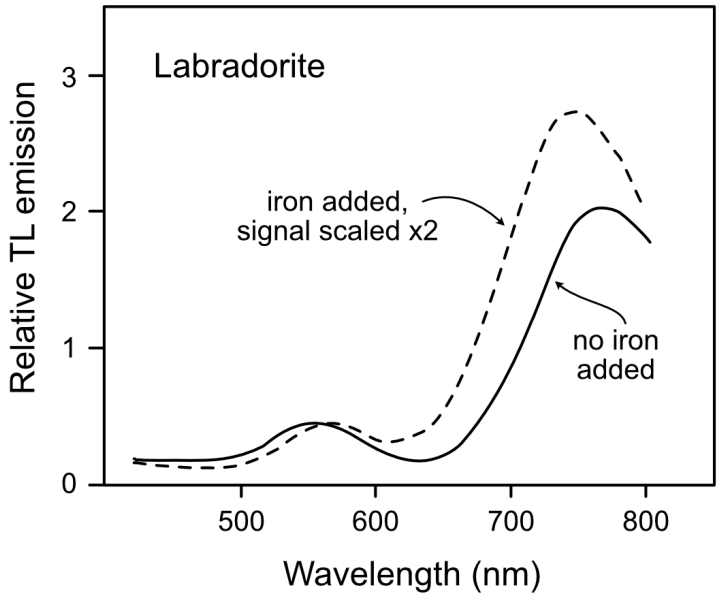

Figure 3.8: *Geake et al. (1972) doped a labradorite feldspar with Fe by heating the feldspar to 1200 °C in air and adding ferrous sulphate. The heated curve has been scaled b a factor of 2. Thus, the overall luminescence signal decreases due to the doping procedure with iron, but the smallest reduction is found for the red emission band. The figure has been modified from Geake et al. (1972).*

that these short lifetimes suggest that Mn^{2+} cannot be the activator for this emission band, as the spin and partially forbidden $^4T_1 \rightarrow {}^6A_1$ transition named for Mn^{2+} would result in much longer lifetimes (Prasad et al., 2016).

Beside lifetime measurements, Prasad et al. (2016) reveal an excitation energy dependent shift of the green emission whilst conducting emission spectroscopy. Integrating the area under the photoluminescence peak measured using different excitation energies for each emission spectra, reveals an exponential change of this area with excitation energy. Prasad and Jain (2018a) interpret this exponential shift to reveal information on the sub conduction band-tail states, with the slope being related to the width of these tails.

3.5.4 Red and deep red emissions

The red emission of feldspars has been under investigation for half a century, and is probably one of the best-studied and well-constrained emissions. This section describes this red emission (which extends into the deep red) and related crystallographic defects.

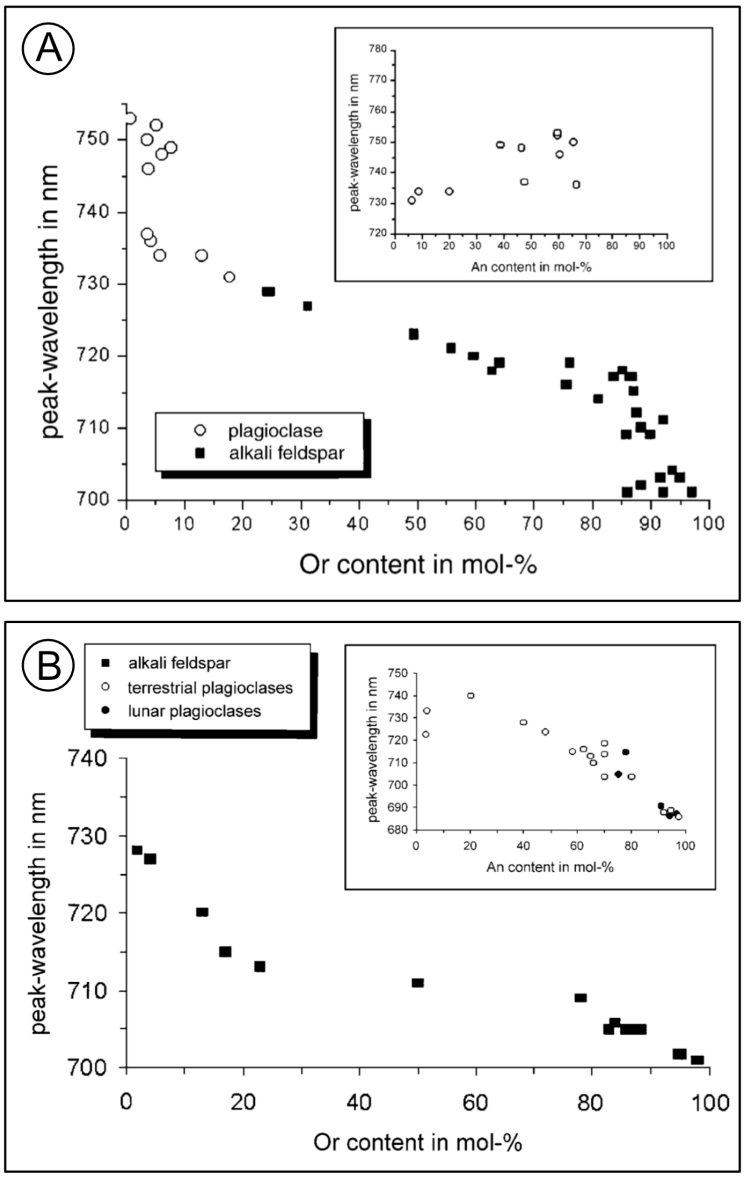

Figure 3.9: *(A) The by Krbetschek et al. (2002) observed shift of the red emission in radiophosphorescence spectra with Or and An content in mol-%. (B) The shift of the red emission observed in cathodoluminescence measurements observed by Krbetschek et al. (2002). The figure is modified from Krbetschek et al. (2002).*

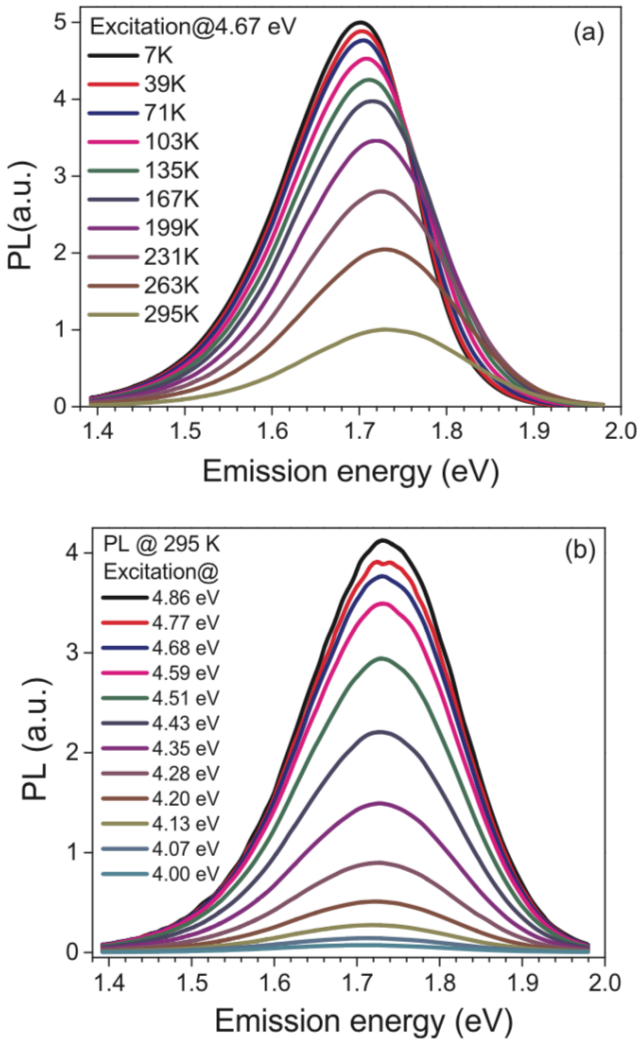

Figure 3.10: *(A) PL emission spectra of R56, an alkali feldspar, at different measurement temperatures, excited using 4.67 eV excitation. B) PL emission spectrum of the same sample measured at room temperature using different excitation energies. Figure is taken from Prasad and Jain (2018b).*

Occurrence of the red and deep red emission in feldspars

An emission in the red and deep-red has been found in a variety of feldspar samples. Sippel and Spencer (1970) found the deep red emission commonly present in terrestrial plagioclase, but not in plagioclase from lunar rocks. Krbetschek and Rieser (1995) identified the red emission (∼750 nm) in TL of orthoclase as the strongest emission, and in sanidine, where the red emission is weaker than blue and UV emissions. The red TL is not present in TL emission spectra of albite, and only weakly present in oligoclase feldspar Krbetschek and Rieser, 1995). However, the red emission (∼750 nm) dominates the phosphorescence spectra for orthoclase, sanidine and albite, andesine and labradorite and is also present in

phosphorescence spectra of oligoclase (Krbetschek and Rieser, 1995). Prescott and Fox (1993) described the red emission with peak wavelength of ∼730 nm for their Na-rich alkali feldspars and for plagioclases.

Defects associated with the red and deep red emissions in feldspars

In 1972, Geake et al. investigated the source of the emission around ∼770 nm by electron excitation and for this purpose doped a labradorite sample with Fe during heating to 1200 °C in air, to include Fe as Fe^{3+} in the crystal. Doping the sample with Fe resulted in an overall reduction in luminescence intensity, but the smallest reduction is observed for the deep red emission (Fig. 3.8). This could either be caused by the inclusion of Fe as Fe^{2+}, instead of the desired Fe^{3+}, which is a known luminescence quencher, or by differential quenching of Fe (Geake et al., 1972). Geake et al. (1972) tend to the latter explanation, based on results of decay time measurements, and hypothesise that Fe^{3+} and Mn^{2+} would substitute for Ca^{2+} on M sites in the crystal. The luminescence transitions are similar between both ions: both are spin forbidden and have a d_5 electron configuration. The only difference lies in the crystal field splitting parameter (Δ), with Δ being larger for Fe^{3+}, compared to Mn^{2+}, resulting in a longer emission wavelength for Fe^{3+}. Further work by Geake et al. (1973) showed that doping a synthetic anorthite with 1000 ppm Fe^{3+} results in a prominent emission peak around ∼700 nm. Additionally Geake et al. (1973) showed that Fe^{3+} in γ-Al_2O_3 results in IR emission (∼800 nm), which is in agreement with Pott and McNicol (1971). This would suggest that Fe^{3+} substitutes for Al^{3+} on T sites, rather than for Ca^{2+} on M sites (Geake et al., 1973). This is in agreement with the findings by Marfunin et al. (1967), who used EPR measurements and the comparison of the orientation of the measured g-factors and the principal directions of electric field gradients and concluded that Fe^{3+} will be included in the crystal lattice of oligoclase, sanidine and microcline on the T_10 site by substituting for Al^{3+}.

Smith (1974) compared microcline and microcline-perthite and was able to show a change in EPR spectra of Fe^{3+} when comparing the samples before and after heating to 1050 °C (24 hours). After heating, the measured spectra showed lower resolution, which Smith (1974) interpreted as a sign of disorder. Smith (1974) suggested that Fe^{3+} preferentially enters T_10 sites in microcline, but when the feldspar is disordered Fe^{3+} will be able to enter T_1 and T_2 sites. EPR spectra of albite show large signal intensities, which Smith (1974) suggested to indicate that in low albite, which is ordered, Fe^{3+} occupies T_1 site similar to Fe^{3+} in

microcline. These results are supported by the analysis of polarization effects of the excitation and emission of Fe^{3+} in feldspars (Short, 2005). Short (2005) found that a pair of crystal field symmetry directions obtained from polarisation data for different optical transitions aligned with the symmetry axis of the four anions around the T_1 site in an orthoclase sample.

Telfer and Walker (1978) used excitation spectroscopy and ligand field parameter calculations to investigate the site occupancy of Fe^{3+} and Mn^{2+} in plagioclase feldspars. Mn^{2+} and Fe^{3+} were added to synthetic feldspar samples. The measured excitation spectra show that Fe^{3+} occupies T-sites, but Telfer and Walker (1978) observed differences in the spectra of the plagioclase feldspars investigated, which they relate to degrees of distortion due to ordering processes in feldspars, and the chemistry of the samples. The decay time for CL of Fe^{3+} at room temperature was determined as ∼1 ms, which is three times shorter than for the green-yellow emission. White et al. (1986) used UV and electron beam excitation to examine the deep red emission in terrestrial and lunar feldspars in excitation spectra and show that the emission is due to the transition of $^4T_1 \rightarrow {}^6A_1$ of Fe^{3+} in Al^{3+} sites.

Finch and Klein (1999) examined red and blue CL in patch perthites and microperthites. Generally, the authors found red CL in turbid feldspars, but not in pristine cryptoperthites. Finch and Klein (1999) linked the wavelength of the red/IR emission in feldspar to the crystallisation history and state of order of the crystals. Red CL is thought to arise from highly ordered tetrahedral Fe^{3+}. Based on EPR measurements and the thus defined state of Fe^{3+} tetrahedral order, Finch and Klein (1999) conclude that Fe^{3+} occupying T_1 sites results in red CL. In contrast, if Fe^{3+} occupies T_2 sites (which are smaller than T_1 sites) it will give rise to CL at longer wavelength, in the IR region of the spectrum. Finch and Klein (1999) concluded that fluid-rock interaction influences the state of order of Fe^{3+} in feldspar, increasing the ordering and thus resulting in visible red CL. Additionally, ordering will remove blue CL, as holes related to Al-O-Al bridges are related to at least partially disordered feldspars. Interactions with fluids intensify the IR emission, and/or shift it to the more visible spectrum for IR to red. Finch and Klein (1999) also fit the red CL decay profile using a sum of two exponential functions, which indicates that the red CL emission is a combination of superimposed, but different emissions. Half-lives obtained for the fit were 165 μs and 770 μs.

Brooks et al. (2002) measured CL and RL spectra from 30 K to 270 K and

see a temperature dependence the two observed red emission peaks in a highly ordered, perfectly exsolved patch perthite. The emission occurs at shorter wavelength during room temperature measurements, compared to low temperature measurements. The change in wavelength dependence on the measurement temperature is explained by changes to Fe-O bond lengths due to contraction of the cell during cooling along the unit cell parameter a. In agreement with Götze et al. (2000), Brooks et al. (2002) relate the two red emissions to albite and microcline phases in the sample, with the shorter wavelength (∼702 nm) being related to orthoclase and the longer wavelength (∼729 nm) being related to albite (Götze et al., 2000). This is supported by earlier data by Dütsch and Krbetschek (1997) and by Krbetschek et al. (2002), who showed an increase in red radio-phosphorescence emission wavelength with decreasing K-feldspar content (in mole-%). Additionally, Krbetschek et al. (2002) could not find any correlation with the red RL peak and the structural state of the K-feldspar, triclinic and monoclinic varieties emit in the same wavelength. For plagioclase feldspar these authors observed a peak shift of the red emission in RL measurements towards longer wavelength, with increasing Ca-feldspar content (Fig. 3.9A). Using CL, Krbetschek et al. (2002) found that, in contrast to the RL results, the red emission in plagioclases shifts to shorter wavelengths with increasing Ca-feldspar content (Fig. 3.9B). However, for alkali feldspar, a trend, similar to the one observed in radio-phosphoresence experiments is found for CL: decreasing peak wavelengths with increasing K-feldspar content (Fig. 3.9A, B). Thus, the authors concluded that the emission peak wavelength is dependent on the mode of excitation and the composition of the feldspar sample. A possible explanation could be different site occupancies and differences in Fe-O bond distances (Krbetschek et al., 2002).

Using different excitation energies (ranging from 4.00 eV to 4.86 eV) and different measurement temperatures (7 K to 295 K), Prasad and Jain (2018b) were able to show that the deep red emission is strongly influenced by phonons, causing a red shift and a narrowing of the PL emission (Fig. 3.10). The authors also observed that the excitation energy influences the emission wavelength (termed: excitation-energy dependent emission, EDE) and the thermal quenching behaviour. By comparing a perthitic feldspar to a non-perthitic K-feldspar end member, Prasad and Jain (2018b) related the EDE to changes in the emission due to Fe^{3+} occupying two different types of lattice sites in the crystal and conclude that the shifting peak is the sum of two different emissions. The largest shift in EDE and thus the most separate probing of the two different sites occu-

pied by Fe^{3+} is achieved at 7 K, as at low temperatures the phonon interactions are minimised. Lifetime determinations using time-resolved photoluminescence of the Fe^{3+} emission reveal long decay lifetimes (∼4 ms for resonant excitation) and a decrease in lifetime with increasing temperature (from 5.07 to 0.90 ms for non resonant excitation at 7 K and 295 K, respectively; from 4.76 ms to 3.32 ms for resonant excitation at 7 K and 295 K, respectively), indicating thermal quenching. These observations are in agreement with previous studies (e.g. White et al., 1986; Poolton et al., 1995c; Zink and Visocekas, 1997; Visocekas et al., 2014). Time-resolved measurements also strengthen the hypothesis of Fe^{3+} occupying two different types of sites in the crystal lattice, as the data reveals two different decays dependent on whether they have been measured at 7 K or at room temperature. Comparing lifetimes obtained by fitting the time-resolved data for resonant and non-resonant excitation results in similar (long, ms scale) lifetimes, which the authors relate to the radiative transition from $^4T_1$ (G) → $^6A_1$ (S), from the lowest excited state to the ground state.

Although the general source of the deep red luminescence has been assigned to Fe^{3+} occupying tetrahedral sites by substituting for Al^{3+}, a debate arose on the physical process behind this emission band. Kirsh et al. (1987) further investigated the source of the TL emission in the infrared (∼730 nm) and explained the emission as a secondary emission, caused by blue photons being absorbed by Fe^{3+} ions and then re-emitted as infrared light. Later, Kirsh and Townsend (1988) proposed two different explanations for the luminescence resulting from Fe^{3+} (substituting for Al^{3+} on the framework): (i) X-ray irradiation reduces some of the Fe^{3+} to Fe^{2+} and additionally creates holes. The electrons are trapped at Fe, the holes likely at different hole centres, e.g. O^{2-}. Heating results in thermal release of the trapped holes, which would then result in recombination of such holes with electrons trapped at Fe^{2+}, creating Fe^{3+}, under the emission of light. (ii) The other option proposed by Kirsh and Townsend (1988) refers to the excitation of Fe^{3+} due to electron-hole recombination elsewhere. In this model, the red emission would be a secondary emission due to absorption of photons by Fe^{3+}, which would subsequently result in the emission of red photons. Visocekas et al. (2014) observed lower fading rates for the deep red emission, compared to the blue emission and associated this with the lower mobility of holes compared to electrons. Subsequently, Visocekas et al. (2014) proposed the following process for the deep red emission, which is based on a previous consideration by Kirsh and Townsend (1988). According to Visocekas et al. (2014) the red luminescence

emission can be explained as (eq. 3.4 and 3.5): During irradiation:

$$Fe^{3+} + e^{-} + hole \rightarrow Fe^{2+} + trapped\ hole \tag{3.4}$$

During subsequent heating, Fe^{2+} and a detrapped hole will result in the excited state of Fe^{3+} (referred to as $(Fe^{3+})^*$), subsequent radiative relaxation results in Fe^{3+} and the emission of a deep red photon (eq. 3.5):

$$Fe^{2+} + detrapped\ hole^{+} \rightarrow (Fe^{3+})^{*} + photon \tag{3.5}$$

In contrast, Jain et al. (2015) suggested that the emission arises due to the capture of a free electron, reducing Fe^{4+} to Fe^{3+} during thermal or optical excitation (eq. 3.6):

$$Fe^{4+} + e^{-} \rightarrow (Fe^{3+})^{*} \rightarrow Fe^{3+} + photon \tag{3.6}$$

No agreement has yet been reached, and further experiments are necessary to be able to fully explain the source of the deep red emission in feldspars. However, it should be mentioned that Fe^{4+} rarely occurs in natural settings (e.g. Illbert and Bonnofoy, 2013), compared to Fe^{2+} and Fe^{3+}, which are the most common forms of iron in minerals (Albarède, 2009, p. 295-298) and is thus an unlikely candidate as source for the deep red emission.

Thermal quenching of the red luminescence

The reduction in emitted light (loss of luminescence efficiency) with increasing temperature is termed thermal quenching. This process arises due to the increased probability of non-radiative transitions within a defect at elevated temperatures (e.g. Wintle, 1975 for quartz; Poolton et al., 1995c for feldspar; Aitken, 1985 and Bøtter-Jensen et al. 2003, p. 44, for general thermal quenching in TL).

Thermal quenching can be described by equation 3.7:

$$I(T) = \frac{1}{1 + Cexp^{\frac{-W}{k_B T}}} \tag{3.7}$$

Where C is a constant, W the activation energy (eV) for thermal quenching, k_B the Boltzmann constant (in eV K^{-1}) and T the temperature in K.

Thermal quenching has been investigated for different emissions in feldspars (e.g. White et al., 1986; Poolton et al., 1995c; Zink and Visocekas, 1997; Visocekas et al., 2014; Kumar et al., 2018), but has been found to be strongest for

the red/deep-red emission (e.g. Poolton et al., 1995c; Visocekas et al., 2014). Poolton et al. (1995c) explored thermal quenching in different feldspars and its effect on PL, TL and IRSL in different emission wavelengths. In agreement with previous research (e.g. White et al., 1986), Poolton et al. (1995b) observed strong thermal quenching of the red to deep red emission of Fe^{3+} in PL, TL and IRSL measurements. This quenching behaviour of the red emission has been confirmed by other studies in more recent years (e.g. Zink and Visocekas, 1997, Visocekas et al., 2014; Prasad and Jain, 2018b). The value for the quenching energy W obtained by Poolton et al. (1995c) is 0.34 eV for an alkali feldspar for the deep red emission (Fe^{3+}) and was associated with internal vibrational modes of the Fe^{3+} ion. This is in contrast to 0.054 eV, obtained by White et al. (1986) for thermal quenching of the Fe^{3+} emission of an orthoclase. Poolton et al. (1995c) explained these differences by vibrational energies of the ion and the host lattice for the two very different values, respectively.

The relative stability of the deep red emission compared to the UV to visible emissions

Whilst the UV to blue emission has often been referred to as resulting in unstable luminescence signals and thus showing high fading rates, the deep red emission was found to exhibit little to no fading in laboratory fading experiments (e.g. Visocekas and Zink, 1999; Fattahi and Stokes, 2003; Visocekas et al., 2014). Visocekas (1985) investigated tunnelling radiative recombination and fading rates in a labradorite feldspar and showed that the sample exhibited a luminescence emission in the deep red, which the author associated with radiative recombination of electrons and holes as a result of quantum mechanical tunnelling. Visocekas (1985) referred to this emission as tunnelling afterglow. Interestingly, Visocekas (1985) found that tunnelling afterglow would primarily occur in the deep red wavelength region, although the visible wavelength region (termed "blue emission" by Visocekas and Zink, 1999) would show greater fading compared to the deep red emission (Visocekas and Zink, 1999). Visocekas and Zink (1999) hypothesised that one potential explanation for the little loss of deep red TL could be due to most of the charge recombining non-radiatively in the case of this emission. These authors then suggested that for the blue emission generally more charge recombines radiatively, and thus the loss of signal is more prominent. However, this does not explain why tunnelling afterglow occurs in the deep red wavelength region, but not in the visible (or "blue") wavelength region. In response, Hunt-

ley et al. (2007) highlighted that the results from e.g. Visocekas (1985) and Visocekas and Zink (1995) might be erroneous, as no preheating was applied in their work to empty any shallow traps, thus the observed signal, referred to as tunnelling afterglow by Visocekas (1985), might just be phosphorescence.

3.5.5 Occurrence of and potential defect related to the IR emission in feldspar

Exploring emissions in the infrared are of particular interest, since a type of electron trap in feldspars is sensitive to IR stimulation. Radiative relaxation within the defect can result in the emission of infrared light, which then offers potential to explore the crystal defect functioning as electron trap in feldspars.

Trautmann et al. (1998) measured radioluminescence emission spectra of irradiated and non-irradiated feldspars, including microcline, orthoclase, albite, oligoclase and labradorite. The spectra show typical emissions of feldspars, with peaks in the red, blue and UV region of the spectrum. Additionally, the K-feldspar end members, orthoclase and microcline, show an intense RL peak at ∼1.5 eV. Due to instrumental limitations, this peak was only partially recorded. One year later, Trautmann et al. (1999) presented further investigations on this emission peak in radioluminescence. They found that the emission peak in the infrared, centred around ∼865 nm (∼1.43 eV), decreases with increasing irradiation dose, which is in contrast to other emission bands, where irradiation causes an increase in intensity (e.g. the blue emission during IRSL measurements). Sunlight bleaching results in an increase in IR radioluminescence intensity (Trautmann et al., 1999). Trautmann et al. (1999) interpret the different behaviour of the IR emission during irradiation as trap filling of the IR-sensitive electron trap in feldspars.

Erfurt and Krbetschek (2003) measured radio-fluorescence (RF) and radio-phosphorescence (RP) spectra of feldspars in the infrared. Using peak fitting, Erfurt and Krbetschek (2003) showed that the RF and RP emission shows two overlapping peaks, one centred at ∼1.36 eV and the second one at ∼1.43 eV (Fig. 3.11). By comparing IR-RL and IR (as emission)-UV (as excitation)-photoluminescence (henceforth UV-IRPL) in Pb-rich $KAlSi_3O_8$ (Amazonite, microcline variety) and KCl:Pb, Erfurt (2003) proposed a potential defect type functioning as IR-sensitive electron trapping centres in feldspars. Erfurt (2003) first made observations on the cubic KCl:Pb using RL emission and UV-IRPL,

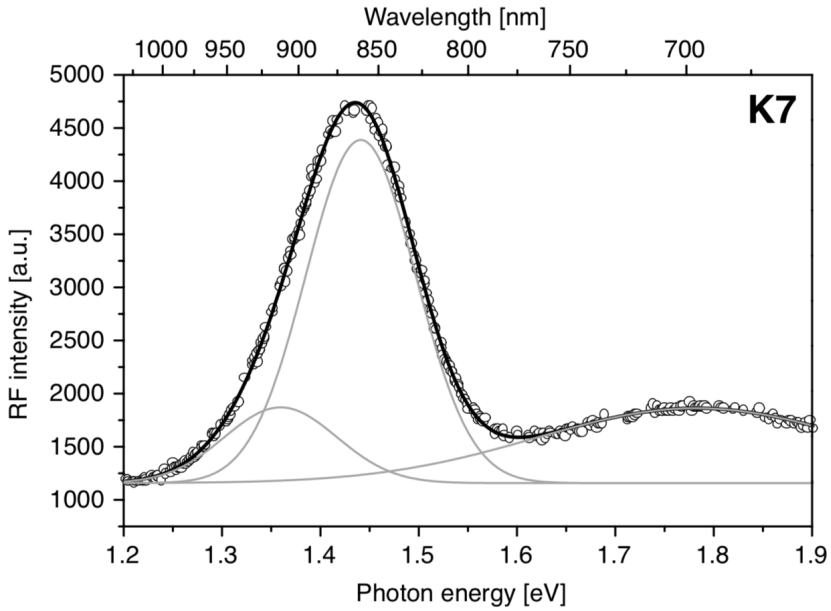

Figure 3.11: *Radiofluorescence (RF) emission spectrum of a rock-forming alkali feldspar sample, which shows two emission peaks revealed by peak fitting with Gaussian functions at 1.36 eV and at 1.43 eV. The spectrum is taken from Erfurt and Krbetschek (2003).*

before then comparing the results to the luminescence of the Pb-rich microcline and an orthoclase sample with lower Pb content. Erfurt (2003) observed similar behaviour for these different substrates regarding the IR emission peak around ∼855 nm. Based on his findings, Erfurt (2003) proposed that during irradiation an extrinsic defect, namely Pb^{2+}, located on M sites in the crystal, and substituting for K^+, will capture an electron. This reduces Pb^{2+} to Pb^+ and results in the emission of infrared photons, during relaxation of excited Pb^+ to its ground state. Continuously decreasing the Pb^{2+} concentration thus results in a decrease of IR-RL with irradiation dose (Erfurt, 2003). Based on these findings, Erfurt (2003) and Erfurt and Krbetschek (2003) proposed IR-RL as a potential dating method.

Further investigating the infrared emission of feldspars, Prasad et al. (2017) proposed a new, non-destructive dating method of feldspar. Whilst usual IRSL measurements are based on anti-Stokes emissions (excitation energy < emission energy), the signal discovered by Prasad et al. (2017) relies on a Stokes emission (excitation energy > emission energy). Using an infrared laser (885 nm, 1.4 eV), Prasad et al. (2017) excited different irradiated feldspars, and subsequently measured their emission spectrum at room temperature and at 7 K and 77 K. They observed a Stokes emission peak around ∼1.3 eV (955 nm), which they interpreted as the emission arising from relaxation of electrons from the excited

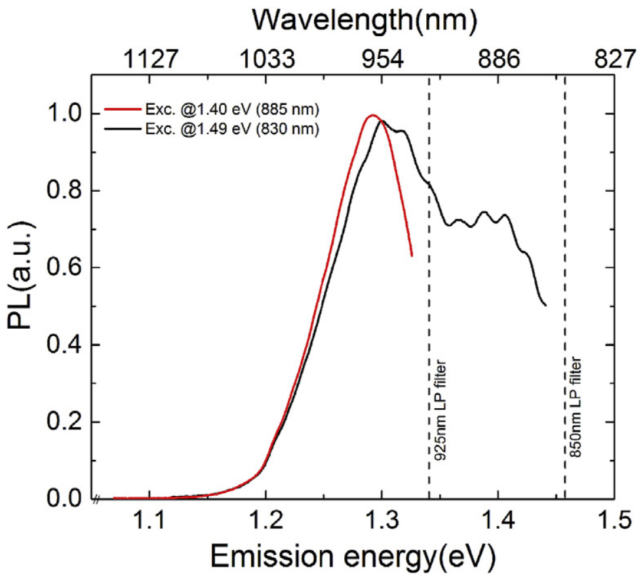

Figure 3.12: *IRPL emission spectra recorded by Kumar et al. (2018) using 1.40 eV (red curve) and 1.49 eV (black curve) laser excitation. The emission spectrum recorded during 1.49 eV excitation reveals two emission peaks in the infrared: one at ∼1.3 eV and a second peak at ∼1.4 eV. The Figure has been taken from Kumar et al. (2018).*

state to the ground state of IR-sensitive electron trapping centres in feldspars. This signal is termed infrared photoluminescence (IRPL). Other observations by Prasad et al. (2017) are an increase in signal intensity with increasing irradiation dose and with decreasing temperature. The increase in signal with decreasing temperature is in contrast to the behaviour of the IRSL emission, which leads the authors to the conclusion that at cryogenic temperatures, no transport via the band-tail states is possible, which results in a larger probability of electrons getting re-trapped in the electron trap (and hence generating IRPL) rather than recombining with a hole (and hence generating IRSL). An initial decrease in signal intensity of the IRPL signal is observed under IR laser stimulation at room temperature over a period of ∼30 minutes at room temperature and this is interpreted as a loss of trapped electrons due to recombination. However, Prasad et al. (2017) suggested that there is a stable component of electrons in the electron trap, which emit in the IR upon optical excitation with an IR laser and can thus be used as a non-destructive, stable, dose-dependent signal for optical dating.

Kumar et al. (2018) compared IRPL and IR-RL, to investigate if the two signals are associated with the same type of electron trap in feldspar. Kumar et al. (2018) measured IRPL using 885 nm laser excitation and obtained a similar emission peak at 1.3 eV (∼955 nm) as already described by Prasad et al.

(2017). However, since this emission was interpreted as a radiative relaxation process from the lowest excited state to the ground state, Kumar et al. (2018) tried excitation of the sample using 830 nm, whilst measuring the emission spectra. Using this second approach, they observed two different emission peaks (see Fig. 3.12), the known peak around ∼955 nm (∼1.3 eV) and a second, new peak around ∼880 nm (1.41 eV). This coincides with the findings of two radio-phosphorescence emission peaks presented by Erfurt and Krbetschek (2003) and two radio-luminescence peaks, reported by Erfurt (2003). Further comparing the two IRPL and IR-RL peaks, Kumar et al. (2018) found that the emissions occur at the same wavelength, but that their intensities and curve shapes vary. Whilst the IR-RL peaks show an increase in signal with increasing measurement temperature, IRPL shows a decrease in intensity at higher temperatures, with the longer wavelength peak suffering more from thermal quenching. When increasing the temperature from 7 K to room temperature, for both methods, the two peaks merge to one broad peak, from about 220 K upwards. Dosing of the sample has different effects on the IRPL and IR-RL signal intensities: Whilst IR-RL decreases with increasing dose, due to filling of the electron traps, IRPL increases with dose. Additionally, Kumar et al. (2018, 2020) show differences in the intensity of the two IRPL emissions at 1.3 and at 1.41 eV in different samples investigated. Kumar et al. (2018) show that the IRPL emission centred around 1.3 eV is stronger in an alkali feldspar compared to the emission at ∼1.41 eV when measured at 7 K. The opposite is the case at room temperature measurement of the same sample. An additional alkali feldspar sample in Kumar et al. (2018) and in three further alkali feldspars investigated by Kumar et al. (2020) the IRPL emission at ∼1.41 eV is brighter than the lower energy emission. It is unclear whether the relative intensities of these two IRPL emissions are related to the measurement temperatures or the mineralogical characteristics of the samples investigated. Based on their experiments, Kumar et al. (2018) concluded that the same type of crystal defect is responsible for IRPL and IR-RL. Whilst Erfurt (2003) suggested that the two IR-RL emission peaks arise due to probing of different excited states of a single type of defect, Kumar et al. (2018) hypothesised that the same excited state of the same type of defect, but at different crystal lattice sites is probed (e.g. different lattice environment, Kumar et al., 2018; Kumar et al., 2020). However, the exact type of crystal defect or their locations are still unknown.

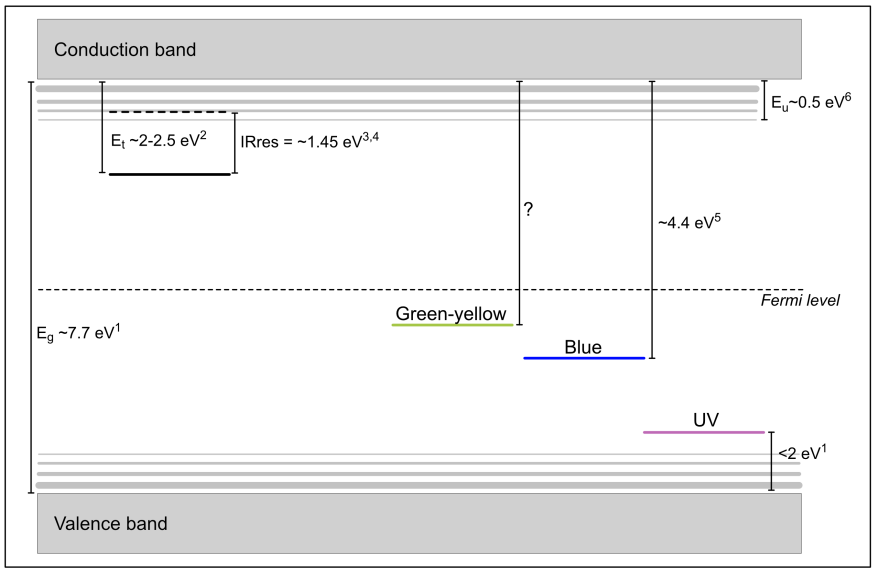

Figure 3.13: *Band model of feldspars with known electron and hole traps and depth of the defects from conduction and valence band, the band gap energy (E_g), and the width of the sub-conduction band-tail states (E_u). The distances between the electron trap and the hole traps are not indicative of actual differences in the lattice. Since the mechanism that gives rise to red and deep red luminescence is still under debate (Visocekas et al., 2014; Jain et al., 2015), the defect is not shown in the figure. References given in the figure: 1 Malins et al. (2004), 2 Kars et al. (2013), 3 Clark and Sanderson (1994), 4 Baril and Huntley (2003), 5 Poolton et al. (2006), 6 Poolton et al. (2009).*

3.6 Discussion and conclusions

This paper presented results from published literature on the use of excitation and emission spectroscopy to gain insights into the luminescence production in feldspars. It is shown that excitation spectroscopy is a powerful tool to constrain defect related parameters, e.g. trap depth and optical resonances associated with electron traps and hole traps and the band gap energy of feldspar. A model based on the results is summarised in Figure 3.13 for a situation where a singly type of electron trap (represented by one trap in the figure) and three different types of hole centres giving rise to the green-yellow, blue and UV emissions in feldspars are assumed. Excitation spectra and excitation energy dependent emission spectra were used to show the presence and characteristics of band-tail states (E_u, e.g. Poolton et al., 2009; Kars et al., 2013; Prasad and Jain, 2018a). Band-tail states, expanding below the conduction band, have implications for charge mobility within the crystal. Besides electron-hole recombination via the conduction band and electron trap to hole trap tunnelling, charge can also hop or tunnel via the band-tail states to recombine (e.g. Morthekai et al., 2012). It has been under debate whether luminescence in feldspars is connected to the eviction of electrons

from a single type of electron trap (e.g. Hütt et al., 1988; Jain and Ankjærgaard, 2011; Andersen et al., 2012) or from different types of electron traps (e.g. Clark and Sanderson, 1994). The depth of a type of electron trap (E_t), which has been associated with the IRSL signal of feldspars, was constrained by fitting of a non-resonant continuum observed at higher excitation energies in excitation spectra as ∼2 to 2.5 eV (Kars et al., 2013). Using IR stimulation, the electron eviction from the trap is a thermally assisted process, with high luminescence efficiency (e.g. Poolton et al., 1995b), which enables the detection of a wide range of emission wavelengths in the infrared/near infrared to UV range (Fig. 3.13).

Various emissions were recorded for feldspars using different excitation methods (e.g. TL, RL, CL, IRSL, PL, or by monitoring phosphorescence; see Fig. 3.6). However, not all emissions have been associated with crystallographic defects. The best constrained emission is the red-deep red emission band, which has been associated with Fe^{3+} substituting for Al^{3+} on T_1 sites on the framework of feldspars (e.g. Telfer and Walker, 1978; Short, 2005). Although the point defect is known, the physical process that gives rise to the red to deep red emission (hole capture vs. electron capture) is still under debate (Visocekas et al., 2014; Jain et al., 2015).

The green-yellow emission has mostly been explained by Mn^{2+} substituting for Ca^{2+} on M sites, or even for Al^{3+} on T sites (Telfer and Walker, 1978). Doping experiments were used to explore the impact of Mn on the intensity of this emission band (Garlick et al., 1971), but since the doping procedure involves prolonged heating of the sample material to 1050 °C, it is unknown whether any increase in signal observed is related to the doping or the potential disordering of the framework due to the heating. Additionally, the lifetimes measured for the green-yellow emission by Clark and Bailiff (1998) and Prasad et al. (2016) are too short to explain the spin forbidden electron transition, which was proposed for Mn^{2+} as an activator on M sites. Thus, there is the need of further experimental evidence to conclusively assign this emission band to specific defects and their lattice environments.

The most likely defect assigned to the blue emission is a hole on an Al-bridging oxygen (resulting in Al^{3+}-O^{1-}-Al^{3+}, e.g. Finch and Klein, 1999). This defect is of particular importance for luminescence dating, since the blue emission is commonly used in such applications. The presence of this defect is associated with a certain degree of element disorder within the crystal, allowing the possibility of having two neighbouring Al^{3+} ions. Disorder of the framework occurs due to

rapid cooling (e.g. associated with a volcanic origin). If such crystals have a higher density of these defects, then this could explain the commonly reported high fading rates of volcanic feldspars. In addition to framework disorder, the blue luminescence has also been linked to the twin interfaces in feldspar, where heating of the material could cause the movement of alkali ions and the subsequent creation of hole centres (Garcia-Guinea et al., 1999; Correcher et al., 2000) and to Eu^{2+} ions substituting for Ca^{2+} ions on M sites in plagioclase feldspars (Götze et al., 1999). The source of the blue luminescence emission requires further investigation as it is unclear if all of the three proposed mechanisms (Al-O-Al bridge, twin interfaces and Eu^{2+} substituting for Ca^{2+}), an interplay of them, only one of them, or potentially a very different mechanism causes the blue emission in chemically and structurally different feldspars. Additionally, despite high fading rates being linked to Al^{3+} disorder on the framework (e.g. Visocekas and Zink, 1995), fading has also reported for feldspars of plutonic origin (e.g. Valla et al., 2016; Jenkins et al., 2018). Thus, other mineralogical properties of the sample, other than framework disorder, will have an influence on the fading rate. However, these potential sources have not been considered so far.

For the UV emission, no defect has yet been proposed, however, the low stability (high fading rate and thermolability) of this emission can be explained by the narrower band gap of feldspar, as this would result in the emission centre being in relatively close proximity to the valence band (Malins et al., 2004). Additionally, the UV emission has been linked to Na-phases in feldspars with exsolution features (Garcia-Guinea et a., 1996). Metastable accumulation of Na at the interfaces and the presence of other mobile compounds (e.g. water or hydroxide) could cause the instability of the emission. Self-diffusion of Na from the twin-interfaces and phase-interfaces throughout the crystal and loss of the associated mobile compounds would thus be the explanation (Garcia-Guinea et al., 1999).

In addition to unknown defects or debatable defect-associations for emissions in the UV, blue, green-yellow and red, further investigations into the nature of electron trapping centres in feldspars are necessary. Here the recently developed method of infrared photoluminescence (IRPL, Prasad et al., 2017; Kumar et al., 2018, 2020) offers potential insights into variations in the electron trap in chemically and structurally different feldspars. Questions to arise here are for example, which crystal defects function as electron trapping centres in feldspars and which properties inherent to the sample drive the variations seen in IRPL

emission spectra.

Despite the presence of different emissions, studies investigating the applicability of emissions other than blue to optical dating (e.g. observing the response of other emissions to optical resetting, fading measurements, and their performance in dating protocols) are rare and this might have lead to the potential of some of these emissions not being exploited. Within the feldspar groups, large differences in sample chemistry and crystallographic parameters (e.g. symmetry, ordering, impurity ions) are present, which can cause a large variability in their luminescence behaviour, if this is associated to the sample characteristics. More research into the crystal defects in feldspars and the relationship between mineralogical parameters and luminescence behaviour is needed to improve the understanding of luminescence production in feldspars. Maybe the variety within the feldspar group is not a limitation, but a potential, which needs exploring as a means to understanding feldspars as natural dosimeters.

Acknowledgements

SR's PhD research is funded through an AberDoc PhD scholarship (Aberystwyth University).

References

Aitken, M.J., 1985. Thermoluminescence Dating. Academic Press, London, United Kingdom.

Akber, R.A., Prescott, J.R., 1982. Thermoluminescence in some feldspars: Early results from studies of spectra. Nuclear Tracks and Radiation Measurements 10, 575-580.

Albarède, F., 2009. Geochemistry – An Introduction. Cambridge University Press, Cambridge, United Kingdom.

Alexander, S., 2007. The stability of the remnant luminescence emissions of alkali feldspar. PhD thesis, University of Glasgow, 362 p.

Andersen, M.T., Jain, M., Tidemand-Lichtenberg, P., 2012. Re-IR stimulated luminescence in K-feldspar: single or multiple trap origin? Journal of Applied Physics 112, 043507.

Auclair, M., Lamothe, M., Huot, S., 2003. Measurement of anomalous fading for feldspar IRSL using SAR. Radiation Measurements 37, 487-492.

Bailiff, I.K., Poolton, N.R.J., 1991. Studies of charge transfer mechanisms in feldspars. Nuclear Tracks and Radiation Measurements 18, 111-118.

Bailiff, I.K., Barnett, S.M., 1994. Characteristics of infrared-stimulated luminescence from a feldspar at low temperatures. Radiation Measurements 23, 541-545.

Baril, M.R., Huntley, D.J., 2003. Optical excitation spectra of trapped electrons in irradiated feldspars. Journal of Physics: Condensed Matter 15, 8011-8027.

Bøtter-Jensen, L., McKeever, S.W.S., Wintle, A.G., 2003. Optically stimulated luminescence dosimetry. Elsevier, Amsterdam.

Brooks, R.J., Finch, A.A., Hole, D.E., Townsend, P.D., Wu, Z.-L., 2002. The red to near infrared luminescence in alkali feldspars. Contributions to Mineralogy

and Petrology 143, 484-494.

Brown, W.L., Parsons, I., 1984. The nature of potassium feldspar, exsolution microtextures and development of dislocations as a function of composition in perthitic feldspars. Contributions to Mineralogy and Petrology 86, 335-341.

Brown, N.D., Rhodes, E.J., 2017. Thermoluminescence measurements of trap depth in alkali feldspars extracted from bedrock. Radiation Measurements 96, 53-61.

Buylaert, J.-P., Jain, M., Murray, A.S., Thomsen, K.J., Thiel, C., Sohbati, R., 2012. A robust feldspar luminescence dating method for Middle and Late Pleistocene sediments. Boreas 41, 435-451.

Chen, R., Leung, P.L., Stokes, M.J., 2000. Apparent anomalous fading of thermoluminescence associated with competition with radiationless transitions. Radiation Measurements 32, 505-511.

Clark, R.J., Sanderson, D.C.W., 1994. Photostimulated luminescence excitation spectroscopy of feldspars and micas. Radiation Measurements 23, 641-646.

Clark, R.J., Bailiff, I.K., 1998. Fast time-resolved luminescence emission spectroscopy in some feldspars. Radiation Measurements 29, 553-560.

Clarke, M.L., Rendell, H.M., 1997. Infra-red stimulated luminescence spectra of alkali feldspars. Radiation Measurements 27, 221-236.

Correcher, V., Garcia-Guinea, J., Delgado, A., 2000. Influence of preheating treatment on the luminescence properties of adularia feldspar (KAlSi3O8). Radiation measurements 32, 709-715.

Dalal, M.L., Kirsh, Y., Rendell, H.M., Townsend, P.D., 1988. TL emission spectra of natural feldspar. Nuclear Tracks and Radiation Measurements 14, 57-62.

Deer, W.A., Howie, R.A., Zussman, J., 2013. In introduction to rock-forming minerals (3rd Edition). Mineralogical Society, London, United Kingdom.

Dütsch, C., Krbetschek, M.R., 1997. New methods for a better internal 40K dose rate determination. Radiation Measurements 27, 377-381.

Duller, G.A.T., Bøtter-Jensen, L., Poolton, N.R.J., 1995. Stimulation of mineral-specific luminescence from multi-mineral samples. Radiation Measurements 24, 87-93.

Erfurt, G., 2003. Infrared luminescence of Pb^+ centres in potassium-rich feldspars. Physica Status Solidi 200, 429-438.

Erfurt, G., Krbetschek, M.R., 2003. Studies on the physics of the infrared radioluminescence of potassium feldspar and on the methodology of its application to sediment dating. Radiation Measurements 37, 505-510.

Fattahi, M., Stokes, S., 2003. Red luminescence from potassium feldspar for dating applications: a study of some properties relevant for dating. Radiation Measurements 37, 647-660.

Finch, A.A., Klein, J., 1999. The causes and petrological significance of cathodoluminescence emissions from alkali feldspars. Contributions to Mineralogy and Petrology 135, 234-243.

Garcia-Guinea, J., Rendell, H.M., Sanchez-Munoz, L., 1996. Luminescence spectra of alkali feldspars: some relationships between structural features and luminescence emission. Radiation Protection Dosimetry 66, 395-398.

Garcia-Guinea, J., Townsend, P.D., Sanchez-Munoz, L., Rojo, J.M., 1999. Ultraviolet-blue ionic luminescence of alkali feldspars from bulk and interfaces. Physics and Chemistry of Minerals 26, 658-667.

Garlick, G.F.J., Lamb, W.E., Steigmann, G.A., Geake, J.E., 1971. Thermoluminescence of lunar samples and terrestrial plagioclases. Proceedings of the Second Lunar Science Conference 3, 2277-2283.

Geake, J.E., Walker, G., Mills, A.A., Garlick, G.F.J., 1971. Luminescence of

Apollo lunar samples. Proceedings of the Second Lunar Science Conference 3, 2265-2275.

Geake, J.E., Walker, G., Mills, A.A., Garlick, G.F.J., 1972. Luminescence of lunar material excited by electrons. Proceedings of the third Lunar Science Conference 3, 2971-2979.

Geake, J.E., Walker, G., Telfer, D.J., Mills, A.A., Garlick, G.F.J., 1973. Luminescence of lunar, terrestrial, and synthesized plagioclase, caused by Mn^{2+} and Fe^{3+}. Proceedings of the fourth Lunar Science Conference 3, 3181-3189.

Götze, J., Habermann, D., Neuser, R.D., Richter, D.K., 1999. High-resolution spectrometric analysis of rare earth elements-activated cathodoluminescence in feldspar minerals. Chemical Geology 153, 81-91.

Götze, J., Krbetschek, M.R., habermann, D., Wolf, D., 2000. High-Resolution Cathodoluminescence Studies of Feldspar Minerals. In: Pagel M., Barbin V., Blanc P., Ohnenstetter D. (eds) Cathodoluminescence in Geosciences. Springer, Berlin, Heidelberg.

Godfrey-Smith, D.I., Cada, M., 1996. IR stimulation spectroscopy of plagioclase and potassium feldspars, and quartz. Radiation Protection Dosimetry 66, 379-385.

Guralnik, B., Jain, M., Herman, F., Ankjærgaard, C., Murray, A.S., Valla, P.G., Preusser, F., King, G.E., Chen, R., Lowick, S.E., Kook, M., Rhodes, E.J., 2015. OSL-thermochronometry of feldspar from the KTB borehole, Germany. Earth and Planetary Science Letters 423, 232-243.

Hamilton, T.D.S., Munro, I.H., Walker, G., 1978. Luminescence instrumentation. In Lumb, M.D. (Ed.). Luminescence spectroscopy. Academic Press, London.

Hofmeister, A.M., Rossman, G.R., 1983. Color in feldspars. . In: Ribbe, P.H. (ed.). Feldspar Mineralogy (second edition). Reviews in Mineraology 2, 271-280.

Hütt, G., Jaek, I., Tchonka, J., 1988. Optical dating: K-feldspars optical re-

sponse stimulation spectra. Quaternary Science Reviews 7, 381-385.

Huntley, D.J., Godfrey-Smith, D.I., Thewalt, M.L.W., 1985. Optical dating of sediments. Nature 313, 105-107.

Huntley, D.J., Godfrey-Smith, D.I., Thewalt, M.L.W., Berger, G.W., 1988. Thermoluminescence spectra of some mineral samples relevant to thermoluminescence dating. Journal of Luminescence 39, 123-136.

Huntley, D.J., Godfrey-Smith, D.I., Haskell, E.H., 1991. Light induced emission spectra from some quartz and feldspars. Nuclear Tracks and Radiation Measurements 18, 127-131.

Huntley, D.J., Lamothe, M., 2001. Ubiquity of anomalous fading in K-feldspars and the measurement and correction for it in optical dating. Canadian Journal of Earth Sciences 38, 1093-1106.

Huntley, D. J., 2006. An explanation of the power-law decay of luminescence. Journal of Physics: Condensed Matter 18, 1359-1368.

Huntley, D.J., Lian, O.B., 2006. Some observations on tunnelling of trapped electrons in feldspars and their implications for optical dating. Quaternary Sciences Reviews 25, 2503-2512.

Huntley, D.J., Baril, M.R., Haidar, S., 2007. Tunnelling in plagioclase feldspars. Journal of Physics D: Applied Physics 40, 900-906.

Illbert, M., Bonnefoy, V., 2013. Insights into the evolution of the iron oxidation pathways. Biochimica et Biophysica Acta – Bioenergetis 1827, 161-175.

Jaek, I., Hütt, G., Vasilchenko, E., Nagirnyi, V., Zazubovich, S., Seeman, V., 1997a. Luminescence and microstructure of Ga, In and Ti centres inlaboratory-doped natural feldspars. Journal of Luminescence 72-74, 681-683.

Jaek, I., Hütt, G., Vassiltchenko, I., 1997b. Luminescence study of Eu- and Cu-

doped natural alkali feldspars and quartz and some problems of palaeodosimetry. Radiation Measurements 27, 473-477.

Jain, M., Ankjærgaard, C., 2011. Towards a non-fading signal in feldspar: Insight into charge transport and tunnelling from time-resolved optically stimulated luminescence. Radiation Measurements 46, 292-309.

Jain, M., Sohbati, R., Guralnik, B., Murray, A.S., Kook, M., Lapp, T., Prasad, A.K., 2015. Kinetics of infrared stimulated luminescence from feldspars. Radiation Measurements 81, 242-250.

Jenkins, G.T.H., Duller, G.A.T., Roberts, H.M., Chiverrell, R.C., Glasser, N.F., 2018. A new approach for luminescence dating glaciofluvial deposits – High precision optical dating of cobbles. Quaternary Science Reviews 192, 263-273.

Jones, A., Islam, M.S., Mortimer, M., Palmer, D., 2004. Alkali ion migration in albite and K-feldspar. Physics and Chemistry of Minerals 31, 313-320.

Kars, R.H., Wallinga, J., Cohen, K.M., 2008. A new approach towards anomalous fading correction for feldspar IRSL dating – tests on samples in field saturation. Radiation Measurements 43, 786-790.

Kars, R.H., Poolton, N.R.J., Jain, M., Ankjærgaard, C., Dorenbos, P., Wallinga, J., 2013. On the trap depth of the IR-sensitive trap in Na- and K-feldspar, Radiation Measurements 59, 103-113.

King, G.E., Guralnik, B., Valla, P.G., Herman, F., 2016. Trapped-charge thermochronometry and thermometry: A status review. Chemical Geology 446, 3-17.

Kirsh, Y., 1992. Kinetic analysis of thermoluminescence. Physica Status Solidi 129, 15-48.

Kirsh, Y., Shoval, S., Townsend, P.D., 1987. Kinetics and emission spectra of thermoluminescence in the feldspars albite and microcline. Physica Status Solidi 101, 253-262.

Kirsh, Y., Townsend, P.D., 1988. Speculations on the blue and red bands in the TL emission spectrum of albite and microcline. Nuclear Tracks and Radiation Measurements 14, 43-49.

Krause, W.E., Krbetschek, M.R., Stolz, W., 1997. Dating of quaternary lake sediments from the Schirmacher Oasis (east Antarctica) by infra-red stimulated luminescence (IRSL) detected at the wavelength of 560 nm. Quaternary Science Reviews 16, 387-392.

Krbetschek, M.R., Rieser, U., 1995. Luminescence spectra of alkalifeldspars and plagioclases. Radiation Measurements 24, 473-477.

Krbetschek, M.R., Götzetze, J., Dietrich, A. and Trautmann, T., 1997. Spectral information from minerals relevant for luminescence dating. Radiation Measurements 27: 695-748.

Krbetschek, M.R., Götze, J., Irmer, G., Rieser, U., Trautmann, T., 2002. The red luminescence emission of feldspar and its wavelength dependence on K, Na, Ca – composition. Mineralogy and Petrology 76, 167-177.

Kumar, R., Kook, M., Murray, A.S., Jain, M., 2018. Towards direct measurement of electrons in metastable states in K-feldspar: Do infrared-photoluminescence and radioluminescence probe the same trap? Radiation Measurements 120, 7-13.

Kumar, R., Kook, M., Jain, M., 2020. Understanding the metastable states in K-Na aluminosilicates using novel site-selective excitation-emission spectroscopy. Journal of Physics D: Applied Physics 53, 465301.

Levy, P.W., 1979. Thermoluminescence studies having applications to geology and archaeometry. Pact 3, 466-480.

Li, B., Li, S.-H., 2011. Thermal stability of infrared stimulated luminescence of sedimentary K-feldspar. Radiation Measurements 46, 29-36.

Malins, A.E.R., Poolton, N.R.J., Quinn, F.M., Johnsen, O., Denby, P.M., 2004. Luminescence excitation characteristics of Ca, Na and K-aluminosilicates (feldspars)

in the stimulation range 5-40 eV: determination of the band gap energies. Journal of Physics D: Applied Physics 37, 1439-1450.

Marfunin, A.S., 1979. Spectroscopy, Luminescence and Radiation Centres in Minerals. Springer, Berlin.

Marfunin, A.S., Bershov, L.V., Meilman, M.L., Michoulier, J., 1967. Paramagnetic Resonance of Fe^{3+} in some feldspars. Schweizer mineralogische und petrographische Mitteilungen 47, 13-19.

Mariano, A.N., Ring, P.J., 1975. Europium-activated cathodoluminescence in minerals. Geochimica et Cosmochimica Acta 39, 649-660.

Matyash, I.V., Bagmut, N.N., Litovchenko, A.S., Proshko, V.Y., 1982. Electron paramagnetic resonance study of new paramagnetic centers in microcline-perthites from pegmatites. Physics and Chemistry of Minerals 8, 149-152.

McKeever, S.W.S., 1985. Thermoluminescence of solids. Cambridge University Press, Cambridge.

Morthekai, P., Thomas, J., Pandian, M.S., Balaram, V., Singhvi, A.K., 2012. Variable range hopping mechanism in band-tail states of feldspars: A time-resolved IRSL study. Radiation Measurements 47, 857-863.

Neudorf, C.M., Roberts, R.G., Jacobs, Z., 2012. Sources of overdispersion in a K-rich feldspar sample from north-central India: Insights from De K content and IRSL age distributions for individual grains. Radiation Measurements 47, 696-702.

Parsons, I., Fitz Gerald, J.D., Lee, M.R., 2015. Routine characterisation and interpretation of complex alkali feldspar intergrowths. American Mineralogist 100, 1277-1303.

Poolton, N.R.J., Bøtter-Jensen, L., Ympa, P.J.M., Johnsen, O., 1994. Influence of crystal structure on the optically stimulated luminescence properties of feldspars. Radiation Measurements 23, 551-554.

Poolton, N.R.J., Bøtter-Jensen, L., Johnsen, O., 1995a. Influence on donor electron energies of the chemical compositions of K, Na and Ca aluminosilicates. Journal of Physics: Condensed Matter 7, 4751-4762.

Poolton, N.R.J., Bøtter-Jensen, L., Johnsen, O., 1995b. Thermo-optical properties of optically stimulated luminescence in feldspars. Radiation Measurements 24, 531-534.

Poolton, N.R.J., Bøtter-Jensen, L., Duller, G.A.T., 1995c. Thermal quenching of luminescence processes in feldspars. Radiation Measurements 24, 57-66.

Poolton, N.R.J., Wallinga, J., Murray, A.S., Bulur, E., Bøtter-Jensen, L., 2002a. Electrons in feldspar I: on the wavefunction of electrons trapped at simple lattice defects. Physics and Chemistry of Minerals 29, 210-216.

Poolton, N.R.J., Ozanyan, K.B., Wallinga, J., Murray, A.S., Bøtter-Jensen, L., 2002b. Electrons in feldspar II: a consideration of the influence of conduction band-tail states on luminescence processes. Physics and Chemistry of Minerals 29, 217-225.

Poolton, N.R.J., Mauz, B., Lang, A., Jain, M., Malins, A.E.R., 2006. Optical excitation processes in the near band-edge region of $KAlSi_3O_8$ and $NaAlSi_3O_8$ feldspar. Radiation Measurements 41, 542-548.

Poolton, N.R.J., Kars, R.H., Wallinga, J., Bos, A.J.J., 2009. Direct evidence for the participation of band-tails and excited state tunnelling in the luminescence of irradiated feldspars. Journal of Physics: Condensed Matter 21, 1-10.

Pott, G.T., McNicol, B.D., 1971. Spectroscopic study of the coordination and valence of Fe and Mn ions in and on the surface of aluminas and silicas. Discussions of the Faraday Society 52, 121-131.

Prasad, A.K., Lapp, T., Kook, M., Jain, M., 2016. Probing luminescence centers in Na rich feldspar. Radiation measurements 90, 292-297.

Prasad, A.K., Poolton, N.R.J., Kook, M., Jain, M., 2017. Optical dating in a new light: A direct, non-destructive probe of trapped electrons. Scientific Reports 7, 12097.

Prasad, A. K., Jain, M., 2018a. Breakdown of Kasha's Rule in a ubiquitous, naturally occurring, wide bandgap aluminosilicate (feldspar). Scientific Reports 8:810.

Prasad, A.K., Jain, M., 2018b. Dynamics of the deep red Fe^{3+} photoluminescence emission in feldspar. Journal of Luminescence 196, 462-469.

Prescott, J.R., Fox, P.J., 1993. Three-dimensional thermoluminescence spectra of feldspars. Journal of Physics D: Applied Physics 26, 2245-2254.

Prescott, J.R., Fox, P.J., Robertson, G.B., Hutton, J.T., 1994. Three-dimensionless spectral studies of the bleaching of the thermoluminescence of feldspars. Radiation Measurements 23, 367-375.

Preusser, F., Chitambo, M.L., Götte, T., Martini, M., Ramseyer, K., Sendezera, E.J., Susino, G.J., Wintle, A.G., 2009. Quartz as a natural luminescence dosimeter. Earth-Science Reviews 97, 184-214,

Rendell, H.M., Townsend, P.D., Wood, R.A., 1995. TL and IRSL emission spectra of detrital feldspars. New Experimental Data. Physica Status Solidi 190, 321-330.

Rendell, H.M., Clarke, M.L., 1997. Thermoluminescence, radioluminescence and cathodoluminescence spectra of alkali feldspars. Radiation Measurements 27, 263-272.

Ribbe, P.H., 1983. Chemistry, structure and nomenclature of feldspars. In: Ribbe, P.H. (ed.). Feldspar Mineralogy (second edition). Reviews in Mineraology 2, 1-20

Rieser, U., Hütt, G., Krbetschek, M.R., Stolz, W., 1997. Feldspar IRSL emission spectra at high and low temperatures. Radiation Measurements 27, 273-278.

Sanderson, D.C.W., 1988. Fading of thermoluminescence in feldspars: Characteristics and corrections. Nuclear Tracks and Radiation Measurements 14, 155-161.

Short, M.A., 2004. Determining the possible lattice sites of two unknown defects in orthoclase from the polarization effects in their optical transitions. Journal of Physics: Condensed Matter 16, 7405-7417.

Short, M.A., 2005. Polarization effects in the excitation and emission of Fe^{3+} in orthoclase and their relevance to the determination of lattice sites of unknown defects. Journal of Physics: Condensed Matter 17, 205-220.

Sippel, R.F., Spencer, A.B., 1970. Luminescence petrography and properties of lunar crystalline rocks and breccias. Proceedings of the Apollo 11 Lunar Science Conference 3, 24113-2426.

Smith, J.V., 1974. Feldspar Minerals. Springer, Heidelberg.

Smith, J.V., 1983. Some chemical properties of feldspars. In: Ribbe, P.H. (ed.). Feldspar Mineralogy (second edition). Reviews in Mineraology 2, 281-296.

Speit, B., Lehmann, G., 1976. Hole centers in the feldspar sanidine. Physica Status Solidi 36, 471-481.

Speit, B., Lehmann, G., 1982. Radiation Defects in Feldspars. Physics and Chemistry of Minerals 8, 77-82.

Spooner, N.A., 1992. Optical dating: Preliminary results on the anomalous fading of luminescence from feldspars. Quaternary Science Reviews 11, 139-145.

Spooner, N.A., 1994. The anomalous fading of infrared-stimulated luminescence from feldspars. Radiation Measurements 23, 625-632.

Street, R.A., 1976. Luminescence in amorphus semiconductors. Advances in physics 25, 397-454.

Strickertsson, K., 1985. The thermoluminescence of potassium feldspars – glow curve characteristics and initial rise measurements. Nuclear Tracks 10, 613-617.

Telfer, D.J., Walker, G., 1978. Ligand field bands of Mn^{2+} and Fe^{3+} luminescence centres and their site occupancy in plagioclase feldspars. Modern geology 6, 199-210.

Templer, R.H., 1986. The localised transition model of anomalous fading. Radiation Protection Dosimetry 17, 493-497.

Thiel, C., Buylaert, J.-P., Murray, A.S., Terhorst, B., Hofer, I., Tsukamoto, S., Frechen, M., 2011. Luminescence dating of the Stratzing loess profile (Austria) – Testing the potential of an elevated temperature post-IR IRSL protocol. Quaternary International 234, 23-31.

Thomsen, K.J., Murray, A.S., Jain, M., Bøtter-Jensen, L., 2008. Laboratory fading rates of various luminescence signals from feldspar-rich sediment extracts. Radiation Measurements 43, 1474-1486.

Thomsen, K.J., Murray, A.S., Jain, M., 2011. Stability of IRSL signals from sedimentary K-feldspar samples. Geochronometria 38, 1-13.

Trauerstein, M., Lowick, S., Preusser, F., Rufer, D., Schlunegger, F., 2012. Exploring fading in single grain feldspar IRSL. Quaternary Geochronology 10, 327-333.

Trautmann, T., Krbetschek, M.R., Dietrich, A., Stolz, W., 1998. Investigations of feldspar radioluminescence: Potential for a new dating technique. Radiation Measurements 29, 421-425.

Trautmann, T., Krbetschek, M.R., Dietrich, A., Stolz, W., 1999. Feldspar radioluminescence: a new dating method and its physical background. Journal of Luminescence 82, 45-58.

Valla, P.G., Lowick, S.E., Herman, F., Champagnac, J.-D., Steer, P., Gurlanik, B., 2016. Exploring IRSL50 fading rates variability in bedrock feldspars and im-

plications for OSL thermochronometry. Quaternary Geochronology 36, 55-66.

Visocekas, R., Ceva, T., Marti, C., Lefaucheux, F., Robert, M.C., 1976. Tunneling processes in afterglow of Calcite. Physica status solidi 35, 315-327.

Visocekas, R., 1979. Miscellaneous aspects of artificial TL of calcite: emission spectra, athermal detrapping and anomalous fading. PACT 3, 258-265.

Visocekas, R., 1985. Tunneling radiative recombination in labradorite: its association with anomalous fading of thermoluminescence. Nuclear Tracks 10, 521-529.

Visocekas, R., Zink, A., 1995. Tunneling afterglow and point defects in feldspars. Radiation Effects and Defect in Solids 134, 1-4.

Visocekas, R., Zink, R., 1999. Use of the far red TL emission band of alkali feldspars for dosimetry and dating. Quaternary Geochronology 18, 271-278.

Visocekas, R., Barthou, C., Blanc, P., 2014. Thermal quenching of far-red Fe^{3+} thermoluminescence of volcanic K-feldspars. Radiation Measurements 61, 52-73.

Waychunas, G.A., 2014. Luminescence Spectroscopy. Reviews in Mineralogy and Geochemistry 78, 175-217.

White, W.B., Matsumura, M., Linnehan, D.G., Furukawa, T., Chandrasekhar, B.K., 1986. Absorption and luminescence of Fe^{3+} in single crystal orthoclase. American Mineralogist 71, 1415-1419.

Wintle, A.G., 1973. Anomalous fading of thermoluminescence in mineral samples. Nature 245, 143-144.

Wintle, A.G., 1975. Thermal quenching of thermoluminescence in quartz. Geophysical Journal of the Royal Astronomical Society 41, 107-113.

Wintle, A.G., 1977. Detailed study of a thermoluminescent material exhibiting anomalous fading. Journal of luminescence 15, 385-393.

Zink, A.J.C., Visocekas, R., 1997. Datability of sanidine feldspars using the near-infrared TL emission. Radiation Measurements 27, 251-261.

Preface to Chapter 4

The review in Chapter 3 (*Excitation and emission spectroscopy of feldspars – Insights into luminescence production in feldspars*) has not only presented state-of-the-art knowledge, but has also revealed potential challenges and gaps in the knowledge of feldspar as natural luminescence dosimeters. The following chapters aim at filling parts of these gaps, in particular (i) regarding the crystal defects hosting electron trapping centres in feldspars and their properties and (ii) regarding potential sample-to-sample variations in the blue (∼410 nm) IRSL signal intensity and its fading rate. To gain further insights into electron trapping and recombination processes in feldspars the following chapters explore a range of chemically and structurally different feldspars.

Chapters 4 and 5 explore variations in electron trapping centres, their ground and excited state energies, in chemically and structurally different feldspars. This is anticipated to help further isolate potential crystal environments which host the defects acting as electron trapping centres in feldspars. Additionally, Chapter 4 investigates the width of the sub-conduction band-tail states in chemically different feldspars.

Chapter 6 focusses on the recombination site by exploring sources of variations in the blue luminescence signal intensity and the rate of anomalous fading of this emission. The results expected for Chapter 6 are hoped to further understand the relationship between mineralogical properties inherent to the sample and characteristics of the blue IRSL signal commonly used in luminescence dating studies.

Four

Optical determination of the width of the band-tail states, and the excited and ground state energies of the principal dosimetric trap in feldspar

This chapter is published in *Radiation Measurements* as

Riedesel, S., King, G.E., Prasad, A.K., Kumar, R., Finch, A.A., Jain, M., 2019. *Optical determination of the width of the band-tail states, and the excited and ground state energies of the principal dosimetric trap in feldspar*. Radiation Measurements 125, 40-51.

Abstract

We constrain parameters that determine thermal stability of the infrared stimulated luminescence (IRSL) signal in a suite of 13 compositionally different feldspar samples by optical probing. We focus specifically on the excited and ground state of the principal trap and the width of the sub-conduction band-tail states. Excitation spectra measured at room temperature result in approximate trap depth of about 2.04 eV and the excited state energy at 1.44 ± 0.02 eV, irrespective of feldspar composition for the sample's measured here. Fitting the non-resonant rising continuum of the excitation spectra suggests that the width of the band-tail states accessible from the ground state of the trap (ΔE) ranges from 0.21 to 0.47 eV at room temperature between the different samples. Photoluminescence measurements are used to constrain the full sub-conduction band-tail width (Urbach width, E_u) using the excitation-energy-dependent emission (EDE), resulting in values ranging from 0.26 to 0.81 eV. While the depth of the principal trap and its main excited state seem to be independent of feldspar composition, the difference between ΔE and E_u seems to be related to sample K-content.

4.1 Introduction

Feldspar is widely used as a chronometer in luminescence dating. The development of post-infrared infrared-stimulated luminescence (post-IR IRSL) protocols (Thomsen et al., 2008; Thiel et al., 2011; Buylaert et al., 2012), which reduce the effects of athermal signal loss (anomalous fading, Wintle, 1973) have increased the use of feldspar in many luminescence studies. Whilst anomalous fading still poses a challenge for some samples, the infrared-stimulated luminescence (IRSL) of feldspar offers a number of advantages over quartz optically stimulated luminescence (OSL), including higher signal sensitivity and saturation dose. Furthermore, the newly developed infrared-photoluminescence (IR-PL) method (Prasad et al., 2017) can be used to date feldspar non-destructively, i.e. without depleting the trapped electron population, opening a range of new research opportunities. The recent methodological developments in feldspar luminescence dating have been paired with an increased understanding of luminescence recombination processes within feldspar minerals (e.g. Jain and Ankjærgaard, 2011) and several models have been developed to describe the thermal stability of feldspar IRSL (e.g. Jain et al., 2012; 2015; Li and Li, 2013; Guralnik et al., 2015; Lambert et al., In Review).

In luminescence dating applications, provided that the specific luminescence signal under investigation is sufficiently stable relative to the timescale being dated (Aitken, 1985), exact knowledge of the kinetic parameters that govern the signal's stability is not necessary. However, luminescence is increasingly being used to determine rock thermal histories (e.g. Guralnik et al., 2015; King et al., 2016) and such applications require accurate constraint of the parameters that govern thermal decay, in order to extrapolate the cooling history of bedrock over geological timescales. Such extrapolations potentially result in the introduction of large uncertainties on past rock temperatures (Yukihara et al., In Press). Requirement of specialised instrumentation has meant that comparatively few studies have sought to directly characterise the key physical parameters associated with feldspar lRSL thermal decay. The focus of this study is to use optical methods to determine (i) the trap depth and (ii) the excited state energy of the principal trap, and (iii) the width of the sub-conduction band-tail states, in a suite of feldspar samples of different chemical compositions. Analysing a range of different feldspars may provide insights into the cause of the differing thermal stability observed between feldspars that are chemically different (e.g. Tsukamoto

et al., 2012).

4.2 Previous investigations of luminescence kinetics of feldspar

Feldspars are wide band-gap (∼7.7 eV) alumino-silicates (Malins et al., 2004), and defects in their crystal lattice allow storage, transport and recombination of charge carriers (Fig. 4.1). Electrons get trapped in defects (trapping centres) following excitation by ionising radiation. These trapping centres are able to store electrons over geological time, making trapped-charge dating techniques (luminescence and electron spin resonance dating) possible (Krbetschek et al., 1997; Ikeya, 1993). Electrons can be released from a trap when they receive sufficient energy, either from optical and/or thermal excitation (e.g. Aitken, 1985; Huntley et al., 1985) and when the released electron recombines with a hole (luminescence centre), a luminescence signal is produced (Fig. 4.1). The thermal stability of a luminescence signal, and thus its validity as a chronometer is at least partly determined by the electron trap depth of the signal under investigation.

4.2.1 The ground and excited state of the IRSL (principal) trap

Constraining the depth of the principal trap in feldspar has been the subject of fundamental research since the mid-1980s (e.g. Strickertsson, 1985; Hütt et al., 1988) however the exact defect associated with feldspar IRSL remains unclear. Initial research focussed on defining optimal stimulation and emission-detection wavelengths for sediment dating applications (e.g. Hütt et al., 1988; Bailiff and Poolton, 1991; Krbetschek et al., 1996; summary given in Krbetschek et al., 1997) whilst more recent studies have sought to identify the trap depth using the relationship between thermoluminescence (TL) emission peaks and IRSL signals (e.g. Murray et al., 2009; Tsukamoto et al., 2012), or isothermal holding experiments coupled with numerical models (e.g. Guralnik et al., 2015). It has been widely debated whether the luminescence of feldspar is derived from a single trap or multiple traps (e.g. Clark and Sanderson, 1994; McKeever et al., 1997; Baril and Huntley, 2003; Murray et al., 2009; Jain and Ankjærgaard, 2011), although spectroscopic evidence suggests that the same electron trapping centre participates in IRSL and post-IR IRSL signals (Andersen et al., 2012).

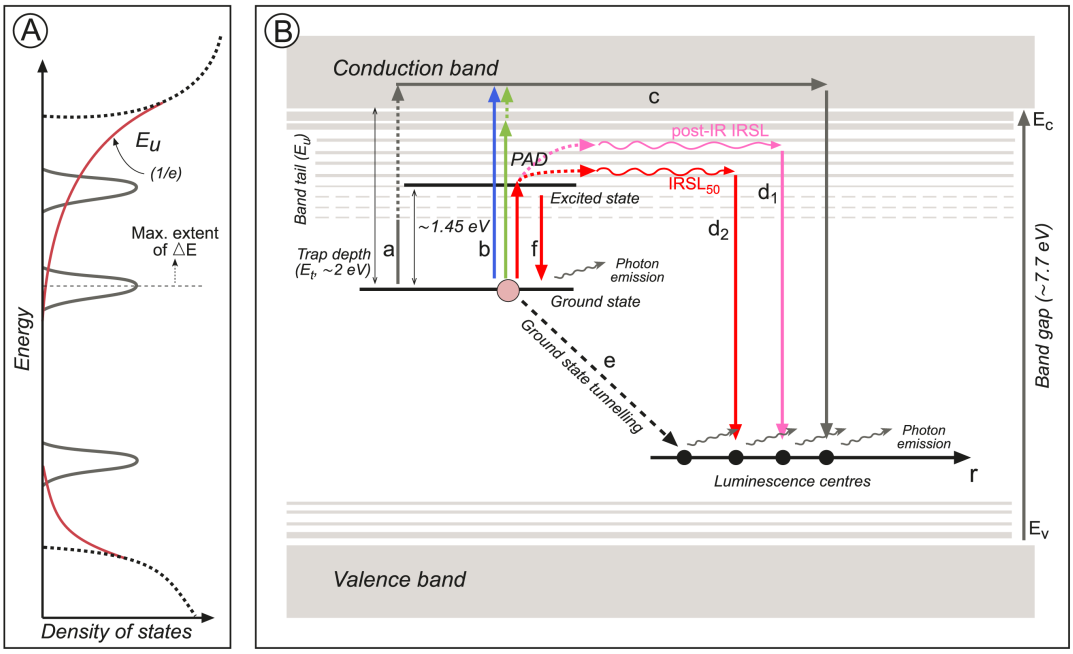

Figure 4.1: *Schematic energy band model with density of states, recombination processes and energy transitions of the principal trap in feldspar. A) Schematic distribution of the density of states, Gaussian distributions correspond to different energy states (e.g. the ground state and excited state of the IRSL (principal) trap in feldspar). While the density of sub-conduction band-tail states are thought to be exponentially distributed with energy below the conduction band edge, energy states in the conduction band follow a parabolic shape (modified from Poolton et al., 2002b; Jain and Ankjærgaard, 2011). The full sub-conduction band-tail width (i.e. the Urbach width) is referred to as E_u (as they are also called Urbach tail), and may extend below the ground state of the principal trap, whereas ΔE defines the band-tail states accessible form the ground state of the defect. B) Possible transitions from the ground state of the IRSL trap (modified from Jain and Ankjærgaard, 2011). a) Thermal excitation. b) Optical excitation by different wavelengths; whereas blue light stimulation allows immediate transition into the conduction band, green light results in a sub-conduction band transition and IR stimulation excites the electron to the excited state. c) Recombination through the conduction band. d) Recombination through the band-tail states. When the electron has been excited to the excited state of the trap by IR stimulation, phonon-assisted diffusion (PAD) allows transition through the band-tail states. e) Athermal signal loss due to quantum mechanical tunnelling from the ground state of the trap. f) Retrapping, which may result in a photon with the same energy as the absorbed photon.*

The trap depth (with respect to the edge of the conduction band) of a charge trapping centre is determined from the energy required to ionise it. The thermal activation energy required to evict charge from a trap is typically lower (e.g. Stickertsson, 1985; Hütt et al., 1988; Brown and Rhodes, 2017) than the optical energy (e.g. Kars et al., 2013). Hütt et al. (1988) initially constrained the optical activation energy required to release electrons from traps in feldspar, and thus the optical trap depth. They recorded a rising continuum (continuous increase in emission intensity with increasing excitation energy) in the excitation spectra of an irradiated microcline until ∼2.25 eV, where their curves peaked (note that the following decrease in signal intensity reported in that study is an instrumental artefact). Poolton et al. (2002a, b) estimated the optical trap depths of $NaAlSi_3O_8$ and $KAlSi_3O_8$ as 1.97 eV and 1.99 eV, respectively, assuming a hydrogenic model, and validated their results against the experimental data of Bailiff and Poolton (1991) and Spooner (1994). Based on the thermal dependence of time-resolved (TR) green-light stimulated luminescence, Jain and Ankjærgaard (2011) argued that the trap depth of their orthoclase sample was likely to be ≥2.4 eV (see green arrow in Fig. 4.1A). Most recently Kars et al. (2013) determined the optical trap depths of $NaAlSi_3O_8$ (2.1 eV) and $KAlSi_3O_8$ (≥2.5 eV) by fitting excitation spectra measured at 10 K following Bøtter-Jensen et al. (2003).

The excited state energy of the principal trap can also be inferred from excitation spectra. Feldspar show a resonance peak at ∼1.45 eV (e.g. Hütt et al., 1988; Baril and Huntley, 2003), with reported full width at half maximum (FWHM) values of 0.12 to 0.13 eV (Godfrey-Smith and Cada, 1996) and 0.11 to 0.21 eV (Baril and Huntley, 2003). Some studies have reported multiple IR excitation peaks (e.g. Hütt et al., 1988; Bailiff and Poolton, 1991; Clark and Sanderson, 1994) and Bøtter-Jensen et al. (1994) observed composition dependent variations in the shape and position of the resonance peak for plagioclase, albite and potassium-rich feldspar.

4.2.2 Sub-conduction band-tail states

Whilst IR (∼1.4 eV) stimulation excites electrons from the ground state to the excited state, it is insufficient for electrons to access the conduction band directly. Poolton et al. (2002a, b) suggested that sub-conduction band-tail states are present within feldspar (Fig. 4.1A, B), and that they play a key role in electron-hole recombination processes. Band-tail states arise due to imperfections and are

distributed in energy levels above the valence band and below the conduction band. Charge in the band-tail states can migrate by hopping (e.g. Morthekai et al. 2012).

Poolton et al. (2009) used photo-transferred OSL (synchrotron photons of energies of 5.5 to 9.0 eV) measured at 10 K to determine the full sub-conduction band-tail width (i.e. Urbach width, E_u) for a $NaAlSi_3O_8$ (R27) and $KAlSi_3O_8$ (R28) sample, obtaining values of 0.28 eV and 0.67 eV respectively. Fitting of energy-resolved stimulation spectra of the same samples (measured at 10 K), but after x-ray irradiation yielded values of 0.32 eV ($NaAlSi_3O_8$, R27) and 0.54 eV ($KAlSi_3O_8$, R28). Poolton et al. (2009) also determined the width of the band-tail states, which are accessible from the ground state of the defect (referred to as ΔE), by fitting the non-resonant rising continuum excitation spectrum of the same samples at 300, 200, 100 and 10 K. They found a decrease in ΔE at lower temperatures (from 0.12 to 0.09 eV for $NaAlSi_3O_8$ and from 0.30 to 0.16 eV for $KAlSi_3O_8$). Based on this, Poolton et al. (2009) identified two different, temperature dependent, processes governing IRSL in feldspar: (i) a thermally assisted hopping process at temperatures $\geq$100 K, and (ii) an athermal process, which disables hopping, although tunnelling remains possible (either via tail-to tail, or tail-to-recombination centre). Whilst at temperatures $\geq$100 K (i.e. with thermal assistance) a large proportion of band-tail states are accessed resulting in a large ΔE, at temperatures $\leq$100 K, ΔE is comparably small and invariant with temperature. Kars et al. (2013) used the same approach to determine ΔE for the same samples examined by Poolton et al. (2009) and calculated values of 0.18 (R27) and 0.23 eV (R28) for measurements made at 10 K.

More recently Prasad et al. (2016) developed a new method of determining the Urbach width (i.e. the width of the sub-conduction band-tail states, referred to as E_u). Using a photoluminescence (PL) emission in the green-orange, they observed an excitation-energy-dependent emission (EDE). The emission peak position shifted linearly, while the peak intensity varied exponentially with a change in the excitation energy; this effect was attributed to the exponentially distributed density of the sub-conduction band-tail states. High excitation energies are able to access band-tail states closer to the conduction band edge, where the density of states is highest and emission intensities are correspondingly larger. Further from the conduction band edge, the density of states is lower and excitation to this part of the band-tail (i.e. using a lower energy excitation) results in a lower emission intensity. Repeating the experiment at 7, 100 and 295 K yielded PL

emission spectra that were broadly similar, supporting the hypothesis that the emissions reflect a continuous distribution of the band-tail states. Using this approach, Prasad et al. (2016) obtained E_u of 0.32 eV for the oligoclase sample investigated. Prasad and Jain (2018) present and discuss a detailed model of the EDE and its application for measuring the band-tail width. Their measurements at 295 K resulted in E_u values of 0.29 to 0.51 eV. EDE at cryogenic temperatures (7 K) and room temperature (295 K) yielded similar results for their perthitic sample (R58) of 0.33 eV. However, R28 exhibited different band-tail widths at different measurement temperatures: 0.29 eV (295 K) compared to 0.41 eV (7 K). Prasad and Jain (2018) attribute these differences to an increase in retrapping efficiency, from the lower band-tail states at cryogenic temperatures, related to mobility, which is a function of the net density of states.

As is clear from the discussion above, while there are several articles characterising the excited state energy of the principal trap, only few studies have reported the trap depth and the band tail width. In this contribution, our focus is to characterise the ground and excited state energies of the principal trap and the width of the band tail states using optical methods, in feldspars of different chemical compositions. Specifically, we use excitation spectra to explore (i) the excited and ground state of the IRSL trap and (ii) use the approach of Poolton et al. (2009) and Kars et al. (2013) to fit the rising continuum of the same spectra to indirectly estimate the trap depth and the sub-conduction band-tail states accessible from the ground state of the trap (ΔE). Finally, (iii) following Prasad et al. (2016) and Prasad and Jain (2018), we use EDE to directly measure the width of the sub-conduction band-tail states (i.e. the Urbach width, E_u). Characterising the energy levels of the principal trap and the width of the band tail states is necessary for understanding the thermal stability of IRSL in different feldspar samples.

4.3 Materials and methods

4.3.1 Samples

The suite of feldspars selected for this study are summarised in Table 4.1 and Figure 4.2. Through characterising samples with different chemical compositions, we can contrast the kinetic parameters of different feldspar with chemical control. We investigated five museum specimens, two sediment samples from

Table 4.1: *List of samples with chemical composition (determined using the Risø XRF OSL/TL reader attachment, Kook et al., 2012) and geological origin.*

ID	Type[a]	Origin	Chemical composition[b] (FS %[c]) Or	Ab	An	Quartz (%)	Geological age	Reference
NB139	Bedrock	Migmatitic gneiss, Namche Barwa, Nepal	89.3	9.4	1.4	4.2	Proterozoic (Burg et al., 1997)	King et al. (2016)
NB120	Bedrock	Migmatitic gneiss, Namche Barwa, Nepal	86.2	11.0	2.9	5.0	Proterozoic (Burg et al., 1997)	King et al. (2016)
MBT-I-2530	Bedrock	Calc-alkaline granite, Mont Blanc Tunnel, Italy	86.7	12.0	1.3	4.2	∼300 Ma (Bussy et al., 1989; Bussy and Von Raumer, 1993)	Lambert et al. (in revision)
MBT-F-5704	Bedrock	Calc-alkaline granite, Mont Blanc Tunnel, Italy	76.3	22.5	1.2	4.6	∼300 Ma (Bussy et al., 1989; Bussy and Von Raumer, 1993)	Lambert et al. (in revision)
KRG-16-06	Bedrock	Kurobegawa granite, Japanese Alps, Japan	79.4	17.3	3.2	3.1	<10 Ma (Ito et al., 2013)	This study
KRG-16-112	Bedrock	Kurobegawa granite, Japanese Alps, Japan	75.2	21.3	3.5	3.4	<10 Ma (Ito et al., 2013)	This study
R1-11A	Museum	Rapakivi Granite, Southern Greenland	68.0	22.0	10.0	0.0	c. 1750 Ma (Finch and Klein, 1999)	Harrison et al. (1990), Finch and Klein (1999)
F1	IAEA AQCS Ref. Feldspar	NA	61.3	33.4	5.4	0.3	NA	IAEA (1999), Sanderson and Clark (1994), Clark and Sanderson (1994)
JSH1-13	Sediment	Shirasuka lowlands, Japan	50.4	37.6	12.1	38.1	NA	Riedesel et al. (2018)
HAM-5	Sediment	Lake Hamana, Japan	64.9	31.1	4.0	19.3	NA	This study
KTB-383-C	Bedrock	KTB borehole, Germany	18.2	67.6	14.4	52.8	NA	Guralnik et al. (2015)
Cleavelandite	Museum	Golonca District, Minas Gerais, Brazil	0.5	99.3	0.2	3.9	650-450 Ma (Cassedanne and Roditi, 1996)	NA
DK4	Museum	Klokken intrusion, South Greenland	5.0	36.0	59.0	0.0	1.18 Ma)	NA

[a]Museum specimen are single crystals, the IAEA reference feldspar, feldspars extracted from bedrock and sediment samples were mounted as coarse multiple-grain aliquots

[b]Determined by XRF measurements

[c]Assuming 100 % feldspar.

Japan (Riedesel et al., 2018, for JSH1-13), and seven bedrock samples from the KTB borehole in Germany, the Japanese Alps, Namche Barwa in the Himalaya, and the Mont Blanc massif, some of which have been studied previously (Guralnik et al., 2015; King et al., 2016; Lambert et al., In Review). The majority of the samples are part of the alkali feldspar solid solution, although one is an alkali feldspar end-member (Cleavelandite), one is a ternary feldspar (KTB-383-C) and one (DK4) is a plagioclase. Only phase-pure K-feldspar is stable at low (≤ 300°C) temperature and hence we assume that the alkali feldspars are perthites, comprising intergrowths of K-feldspar (either orthoclase or intermediate microcline) and intermediate albite. One sample, R1-11A, is a microcline cryptoperthite in which the K- and Na-feldspars are coherently intergrown on nm-scales and in which the interfaces between the two phases comprise a significant proportion of the volume of the mineral. F1 is an International Atomic Energy Agency (IAEA AQCS) secondary reference feldspar (IAEA, 1999).

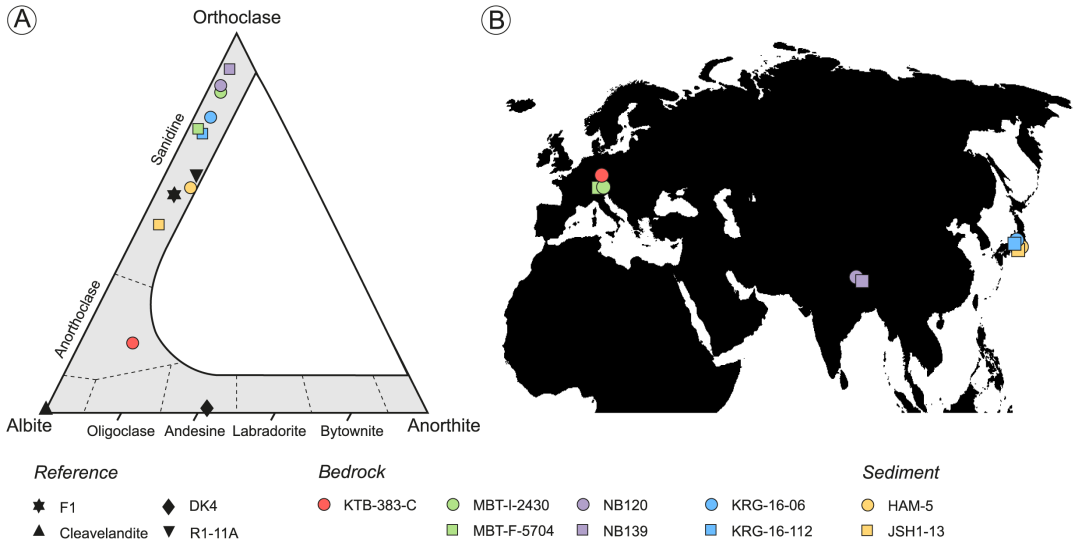

Figure 4.2: *Feldspar ternary of chemical composition and origin map for samples in this study.*

4.3.2 Instrumentation

Measurements were made using the Risø station for CryOgenic Luminescence Research (COLUR; Prasad et al., 2016, 2017), at the Centre for Nuclear Technology, Technical University of Denmark, Risø Campus, Roskilde, Denmark. The measurements were made using a Tungsten halogen lamp, for excitation between 500 and 1000 nm, and a CW Xenon lamp for excitation between 370 and 560

nm. Excitation wavelengths were selected using a double-grating Czerny-Turner monochromator and excitation spectra were recorded through a U340 filter with a UV-sensitive photomultiplier tube (PMT). Emission spectra were detected using the UV-sensitive PMT together with the monochromator. All spectra were corrected for excitation light flux and system response; excitation spectra were converted into photons/s/unit energy interval. Sample material was mounted on the sample holder within COLUR using carbon tape. The sample holder of COLUR comprises the cold finger of a closed loop He-cryostat that allows temperature dependent measurements to be performed. A blank aliquot of carbon tape was measured at 300 K to quantify any background signal.

4.3.3 Excitation spectra: Determining trap depth, band-tail width and the excited state of the IRSL (principal) trap

A large aliquot of sand-sized sample material or a single crystal (∼2 mm diameter, ≤1 mm thick, sample dependent, see Table 4.1) were beta irradiated to deposit 500 Gy using a Sr^{90}/Y^{90} beta source attached to a Risø TL/OSL Reader (TL-DA-20). Prior to mounting in the COLUR sample chamber, the samples were preheated for 60 s at 250°C to remove trapped charge which is thermally unstable over laboratory timescales. Excitation spectra were measured from 500 to 1000 nm, using a step size of 5 nm, a bandpass of 10 nm and an integration time of 1 s. We tested the effect of measurement temperature on selected sample F1, which was measured at 7 K and 300 K; all other measurements were made at 300 K.

4.3.4 Emission spectra: Determining the band-tail width using the excitation-energy-dependent emission (EDE)

The width of the full sub-conduction band-tail states (E_u) of the different samples were determined following Prasad et al. (2016), using fresh, non-irradiated large aliquots of sand-sized samples or single crystals (∼2 mm diameter). Samples were mounted on the sample holder in the measurement chamber and excited from 370 to 520 nm using 5, 10 or 20 nm steps, dependent on samples brightness. Emission spectra were recorded with a 1 nm wavelength-scanning interval in the range of 390 to 540 nm, using a 2 nm bandpass. The integration time was

either 1 or 10 s, depending on sample brightness. At least two measurements were repeated for each sample within each measurement cycle to confirm measurement reproducibility, and two samples (NB120 and MBT-I-2430) were measured twice. The results of these repeat measurements were consistent with each other.

4.4 Results

4.4.1 Excitation spectra: Determining trap depth, accessible band-tail width and the excited state of the IRSL trap

The carbon tape substrate (blank measurement) had no detectable emission at any excitation wavelength. The excitation spectrum of each sample showed two distinct features (see examples in Fig. 4.3B); a resonance peak centred at ∼1.45 eV in the low energy region (1.24 to 1.70 eV), followed by a monotonic rise to the maximum excitation energy of 2.48 eV measured here. These results are qualitatively consistent with previous studies (e.g., Baril and Huntley, 2003).

The luminescence intensities and the contrast between the two features vary between the different samples (Fig. 4.3A, B, Figs. S4.4-S4.7). Cleavelandite (albite) shows the brightest signal intensity whereas plagioclase sample DK4 has very dim luminescence. For all samples except Cleavelandite, F1 and KTB-383-C, the resonant luminescence emission intensity is stronger than that at the highest excitation energy. In addition to the IR resonance peak, MBT-I-2430 shows a broad absorption peak centred at ∼2.1 eV, which is superimposed on the rising continuum (Fig. 4.3B).

F1 was measured at 300 and 7 K (Fig. 4.3A), to investigate the effect of different measurement temperatures. The initial luminescence intensity in response to excitation of 2.25 eV is about an order of magnitude greater at room temperature, relative to measurement at 7 K, which is significant as some of our samples showed very weak luminescence. The IR resonance peak is absent in the 7 K excitation spectrum (Fig. 4.3A).

Trap depth

Following Kars et al. (2013) we fitted part of the rising continuum present in the excitation spectra of Cleavelandite, KTB-383-C, NB139, NB120, MBT-F-5704,

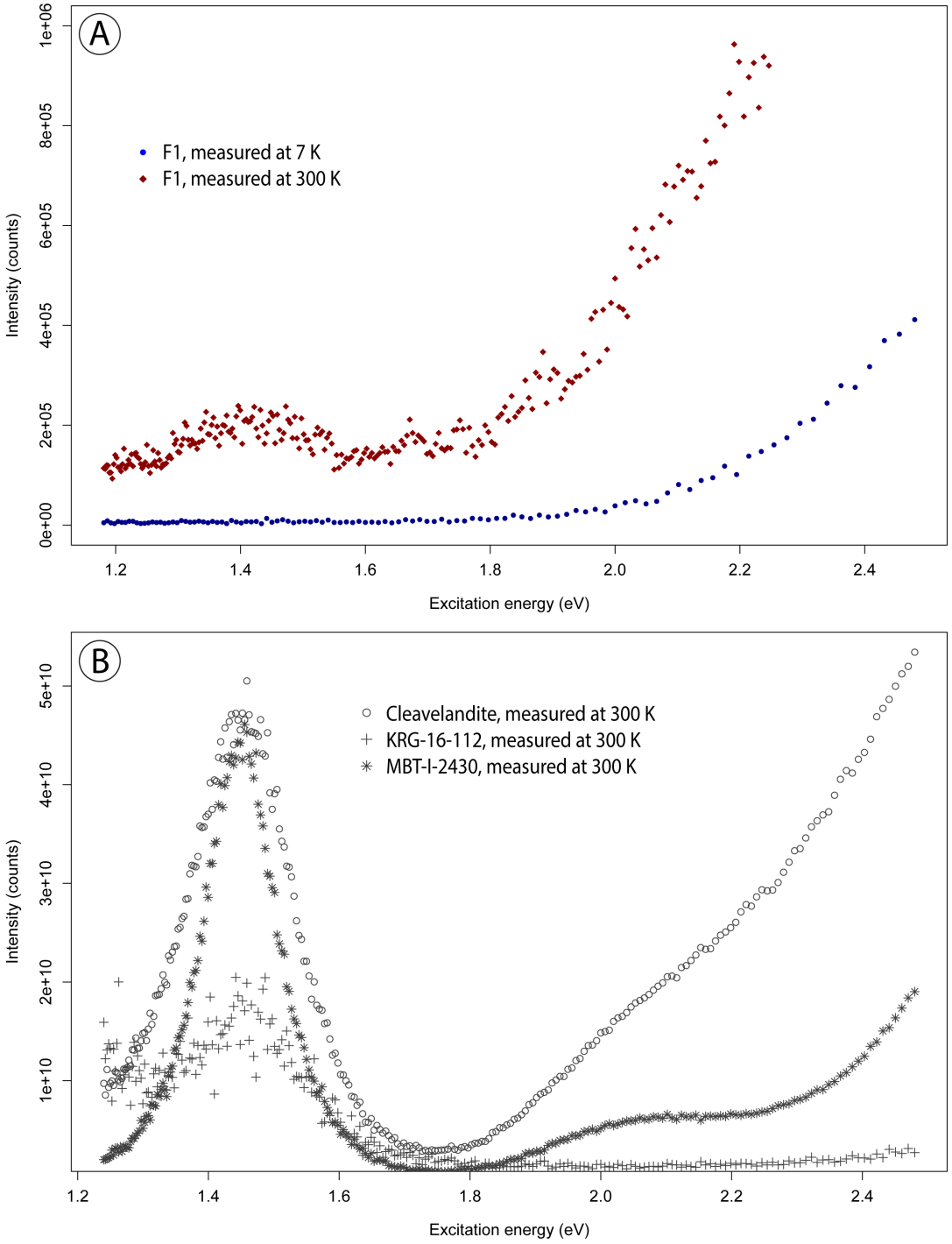

Figure 4.3: *Example excitation spectra: A) Rising continuum of F1, measured at 7 and 300 K; B) Excitation spectra of Cleavelandite, KRG-16-112 and MBT-I-2430. These spectra are representative for the range of sample brightness and the shape of the IR resonance peak and non-resonant rising continuum. In contrast to the other samples investigated, MBT-I-2430 also shows a peak centred at 2.10 eV superimposed on the rising continuum.*

MBT-I-2430, R1-11A, JSH1-13 and HAM-5 to estimate trap depth using equation 4.1 (Bøtter-Jensen et al., 2003); the excitation spectra of the other samples were

not sufficiently bright.

$$\sigma(E, E_t) \propto \frac{(E - E_t)^{3/2}}{E(E - E_t(1 - m0/m*))} \tag{4.1}$$

where σ is the photo-ionisation cross-section, E the excitation energy (eV), E_t the trap depth (eV), m* the effective electron mass (fixed at m* = 0.79 m0, Poolton et al., 2001; Kars et al., 2013) and m0 the electron rest mass. Data were fitted in MATLAB and following Kars et al. (2013), only a part of the rising continuum was fitted (Fig. 4.4, S4.1, S4.2 and S4.3), using equation 4.1 we fitted the luminescence emission intensity for each excitation energy (E). Kars et al. (2013) measured excitation spectra up to 2.80 eV, however due to instrumental limitations during the analytical period, the maximum excitation energy explored in this study was 2.48 eV. We tested the influence of fitting different excitation energy ranges on the obtained E_t to evaluate whether our spectra are sufficiently described (i.e. from 2.10 eV to 2.35 eV in 0.05 eV steps, Table S3.1). We recorded an average variance of 7 %, with a trend towards higher E_t values as the lowest fitted excitation energy increased.

We report values derived from fitting the emission intensity for excitation energies ranging from 2.30 to 2.48 eV and the mean optical trap depth is 2.04 ± 0.05 eV. Sample MBT-I-2430 exhibit the greatest trap depths of 2.15 ± 0.01 and Cleavelandite has the shallowest trap depth of 1.99 ± 0.01 eV (Table 4.2). Given that the high-energy plateau predicted by equation 4.1 is not observed in our experimental data, the model fits are mathematically poorly constrained and these trap depths should be considered as preliminary estimates.

Excited state of the IRSL trap

The IR resonance peak was fitted with a single Gaussian distribution (eq. 4.2) to characterise the excited state of the IRSL trap.

$$f(x) = k * exp(-\frac{1}{2} * \frac{(E - \mu)^2}{\sigma^2}) \tag{4.2}$$

where k is a pre-exponential factor, E the corresponding excitation energy, μ the mean energy of the Gaussian distribution and σ the standard deviation. All samples showed similar IR resonance with the Gaussian distribution centred between 1.41 and 1.46 eV (Fig. 4.3, Figs. S4.4 and S4.5). The FWHM varied from 0.16 to 0.40 eV; results are given in Table 4.2.

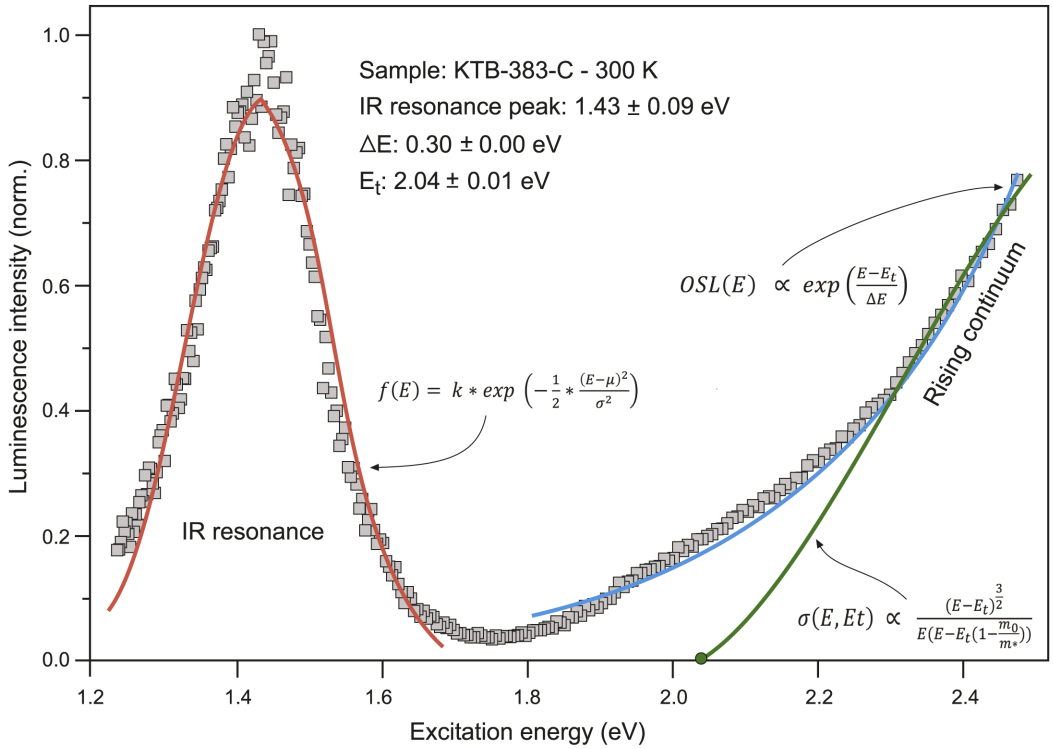

Figure 4.4: *Excitation spectrum of KTB-383-C showing model fits. The IR resonance peak was fitted with a single Gaussian distribution (eq. 4.2) and the rising continuum was fitted with equation 4.1 (Bøtter-Jensen et al., 2003) to estimate trap depth and equation 4.3 (Poolton et al., 2009) to obtain an estimate of the band-tail width accessible from the ground state of the trap (ΔE). Each part of the excitation spectrum was fitted separately.*

Estimation of band-tail width

To obtain the width of the band-tail states (ΔE) accessible from the ground state of the trap, following Kars et al. (2013) we fitted the rising continuum from 1.80 to 2.48 eV with equation 4.3 (Poolton et al., 2009).

$$OSL(E) \propto exp(\frac{E - E_t}{\Delta E}) \tag{4.3}$$

where E is the excitation energy, E_t the trap depth and ΔE the band-tail width accessible from the ground state of the trap. The broad absorption peak at ~2.1 eV superimposed on the rising continuum of sample MBT-I-2430 (Fig. 4.3B, Fig. S4.3C) was excluded from the fit of this sample, so that the final excitation energy range considered was limited to 2.22 to 2.48 eV.

The quality of fit varied between samples. It was not possible to calculate ΔE for KRG-16-112 or DK4, and some deviation between the fit and the measured data is recorded for Cleavelandite, JSH1-13, HAM-5 and KTB-383-C in the low excitation energy region (Figs S4.6 and S4.7). Calculated ΔE ranges from 0.22

eV (MBT-I-2430) to 0.47 eV (NB120). Compared to the overall range in ΔE, measurements of F1 at 300 K (0.29 eV) and 7 K (0.21 eV) yield similar values.

4.4.2 Estimation of band-tail width using the excitation-energy-dependent emission (EDE)

The PL emission spectra of the different samples were similar and are characterised by a single emission peak. Reducing the excitation energy systematically causes signal intensities to decrease and the emission peak to become narrower and to shift to lower emission energy. At ∼2.2 eV excitation, no detectable peak is observed. The area under the PL peak was integrated and an exponential relationship between the PL intensity (integrated PL peak area) and the corresponding excitation energy was observed (Fig. 4.5; Figs. S4.8, S4.9). Taking the natural logarithm of the integrated PL peak area enabled us to fit a linear regression between ln(PL) and the excitation energy (Fig. 4.5). The inverse of the slope of the fitted line represents the band-tail width. Based on this relationship and following the approach of Prasad et al. (2016) we estimated E_u for all samples by calculating the inverse of the slope. This resulted in band-tail width estimates ranging from 0.26 to 0.81 eV for plagioclase sample DK4 and ternary feldspar sample KTB-383-C respectively, full results are listed in Table 4.2. No shift in peak position was observed for sample R1-11A making it impossible to determine E_u for this sample.

4.5 Discussion

Previous studies have indicated that the thermal stability of different feldspars may vary (e.g. Tsukamoto et al., 2012). However, no dependence of either the energy of the trap depth or the excited state of the principal trap are apparent for the feldspars investigated here (Fig. 4.7). The IR resonance of our samples is in agreement with published values (Baril and Huntley, 2003; Poolton et al., 2009) and has an average peak position of 1.44 ± 0.02 eV and FWHM of 0.19 to 0.40 eV. Bøtter-Jensen et al. (1994) proposed that alkali-feldspar chemical composition influences the IR-resonance. However, no clear relationship between mode IR resonance or FWHM, and sample chemical composition, is apparent for our data (Fig. 4.7).

Table 4.2: *Optical kinetics of feldspar samples investigated in this study. The reported uncertainties account only for the fitting, no uncertainties resulting from the instrumentation are added.*

Sample[a]	Optical E_t (eV)[b]	Excited state (IR resonance peak)[c]			Band-tail width (ΔE, fitting using eq. 4.3)		Band-tail width (E_u, eV)
		Mode (eV)	Standard dev. (eV)	FWHM	ΔE (eV)	Fitted exc. energy range (eV)	
NB139	2.03 ± 0.02	1.46	0.09	0.21	0.39 ± 0.01	1.80 - 2.48	0.37 ± 0.01
NB120	2.03 ± 0.04	1.45	0.11	0.26	0.47 ± 0.02	1.80 - 2.48	0.42 ± 0.01
MBT-I-2430	2.15 ± 0.01	1.45	0.07	0.16	0.22 ± 0.01	2.22 - 2.48	0.32 ± 0.01
MBT-F-5704	2.05 ± 0.01	1.44	0.08	0.19	0.31 ± 0.01	1.80 - 2.48	0.30 ± 0.03
KRG-16-06	NA	1.44	0.14	0.33	0.46 ± 0.03	1.80 - 2.48	0.42 ± 0.01
KRG-16-112	NA	1.41	0.16	0.38	NA	NA	0.45 ± 0.01
R1-11A	2.02 ± 0.03	1.43	0.12	0.28	0.38 ± 0.01	1.80 - 2.48	no shift
F1	NA	1.45	0.10	0.24	0.29 ± 0.01	1.80 - 2.48	0.48 ± 0.03
F1 (7K)	2.10 ± 0.02	no peak	no peak	no peak	0.21 ± 0.00	1.80 - 2.48	no peak shift
JSH1-13	2.01 ± 0.01	1.43	0.10	0.24	0.36 ± 0.01	1.80-2.48	0.50 ± 0.01
HAM-5	2.03 ± 0.01	1.43	0.10	0.24	0.31 ± 0.00	1.80 - 2.48	0.42 ± 0.01
KTB-383-C	2.04 ± 0.01	1.43	0.09	0.21	0.30 ± 0.00	1.80 - 2.48	0.81 ± 0.03
Cleavelandite	1.99 ± 0.01	1.45	0.10	0.24	0.34 ± 0.01	1.80 - 2.48	0.33 ± 0.00
DK4	NA	1.41	0.17	0.40	NA	NA	0.26 ± 0.02

[a]Samples are sorted from high to low potassium content, DK4 is a plagioclase.
[b]Excitation energy range used for fitting with equation 1: 2.30 – 2.48 eV.
[c]The parameters refer to the fitted Gaussian distribution (eq. 4.2), not to the peak itself.

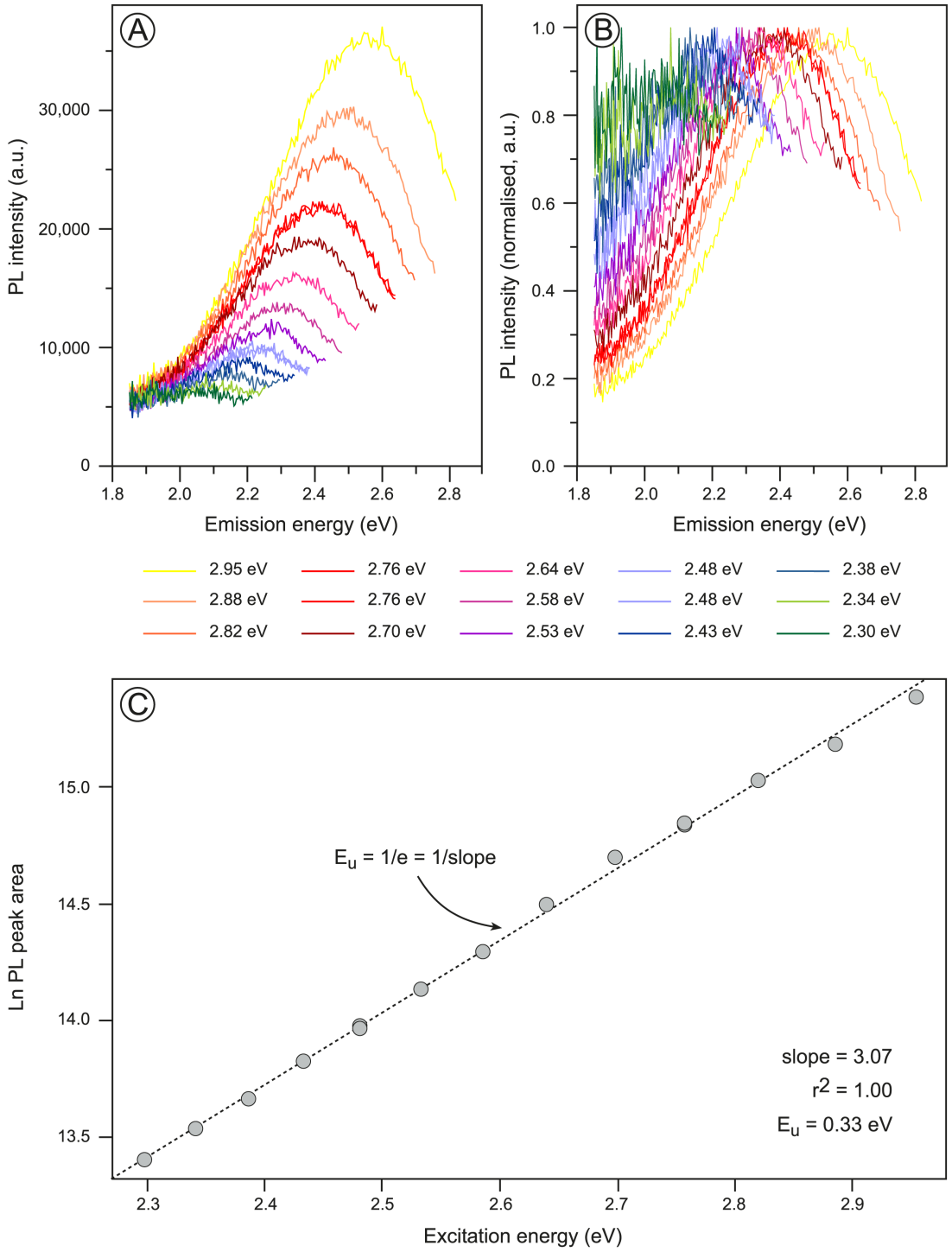

Figure 4.5: *Photoluminescence emission spectra of the excitation-energy-dependent emission (EDE) and the full band-tail width (E_u) calculation for Cleavelandite. (A) EDE spectra. (B) Normalised EDE spectra. (C) Exponential relationship between the integrated area under the emission spectrum and the corresponding excitation energy. The inverse of the slope (1/e) gives E_u.*

The similarity between the different feldspar variants indicates that the defect causing IR absorption is likely to be on the feldspar silicate framework, rather

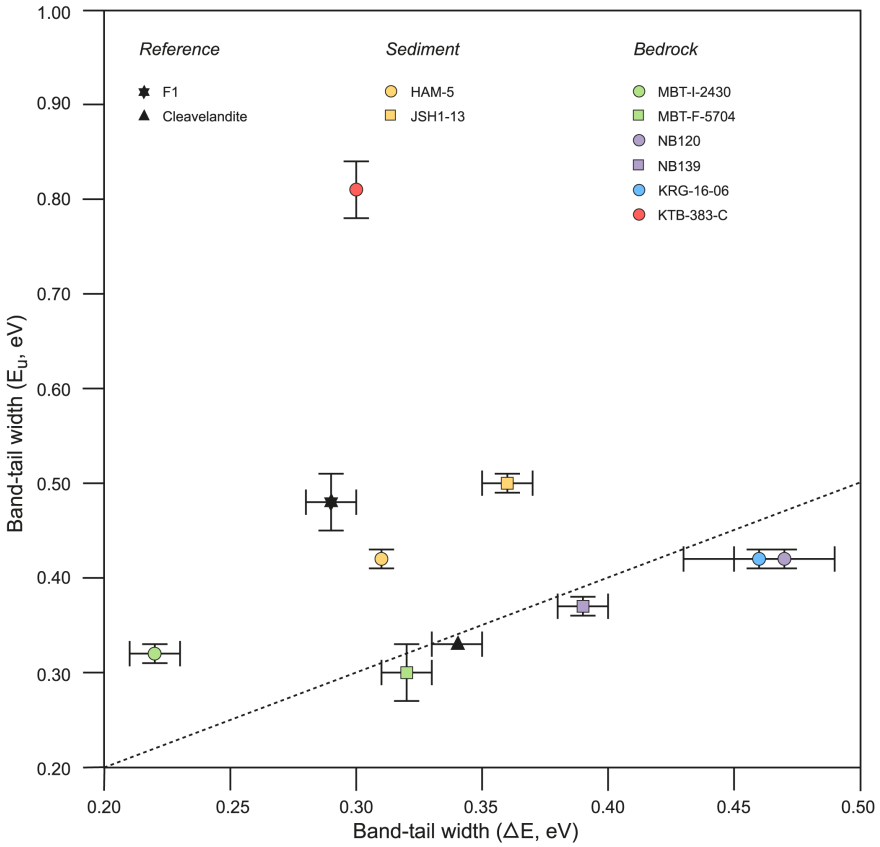

Figure 4.6: *Comparison of band-tail states accessible from the ground state of the trap (ΔE) and the full band-tail width (E_u) calculated from fitting the rising continuum with eq. 4.3 and by using EDE respectively. The dashed line indicates the 1:1 relationship.*

than a substitution or defect on the metal site (the compositions and symmetry of which changes substantially across the feldspar mineral group), which is in agreement with previous work (e.g. Short, 2004). However, a specific defect has not yet been associated with IR absorption in feldspar. The trap depth is a critical parameter for determining the thermal stability. To illustrate, assuming first order kinetic behaviour (which is rarely the case, cf. Guralnik et al., 2015), an E_t of 2.0 eV yields a lifetime at 50°C of 13 Ga whereas an E_t of 1.90 eV yields a lifetime of only 359 Ma assuming a lattice vibration frequency factor (s) of 3.9 x 10^{13} s^{-1}. In feldspar, the band-tail width also modifies thermal stability (e.g. Li and Li, 2013) and constraining the trap depth of feldspar is challenging because of the presence of the band-tail states (Poolton et al., 2009; Kars et al., 2013). However, despite this it is encouraging that all of our samples, irrespective of chemical composition, yield a nominal average optical trap depth of 2.04 eV with a relatively small standard deviation of 0.05 eV. Furthermore the individual estimates of trap depth are within uncertainties of one another (Fig. 4.7; Table 4.2). These preliminary data suggest that the defect or defects interrogated in the op-

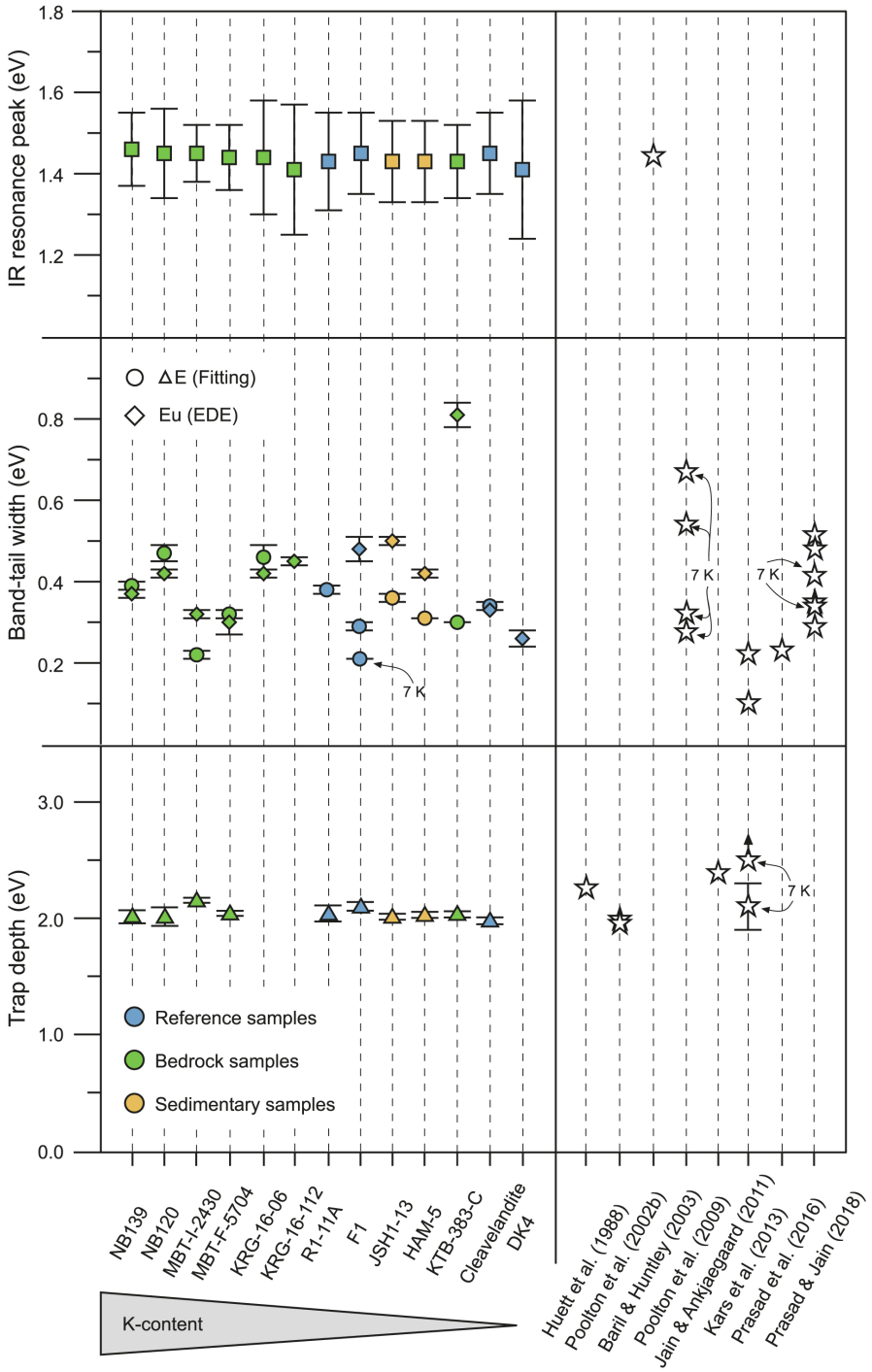

Figure 4.7: *Summary of trap depth, band-tail width and position of the IR resonance peak, obtained from optical measurements. Results of this study are compared to published research. Baril and Huntley (2003) investigated 19 samples, since all their samples show a main IR-resonance at 1.44 eV – 1.45 eV, just a single point represents their data.*

tical probing experiments presented here are part of the feldspar alumino-silicate framework, which is broadly consistent between all feldspar variants. In terms of trap depth calculations, a common value of E_t may be applicable to feldspar of different compositions, and further investigations using low temperature OSL

excitation spectra, and/or newly developed optical probing methods to directly characterise the IRSL trap depth without the effects of competing recombination processes (Prasad et al., 2017), will be useful to investigate this potential in the future.

Regarding the width of the sub-conduction band-tail states, both methods, viz. the excitation spectra measured at 300 K to determine ΔE (equation 4.3) and EDE (Prasad et al., 2016; Prasad and Jain, 2018) used to determine E_u yield broadly similar results for some samples (Fig. 4.6). ΔE ranged from 0.21 to 0.46 eV and E_u from 0.26 to 0.81 eV (Figs. 4.6, 4.7). These results are within the range of previously published values (Poolton et al., 2009; Prasad and Jain, 2018). The reference feldspars that we investigated (F1, Cleavelandite and DK4; listed from medium to low potassium content), exhibit a decrease in E_u with reducing K-content from 0.48 ± 0.03 eV (orthoclase content: 61.3 %) to 0.26 ± 0.02 eV (orthoclase component: 0.5 %). However, this trend is not apparent in the non-reference feldspar samples measured as large aliquots of sand-sized material, which may be a consequence of signal averaging across grains of different chemical composition. Single-phase feldspars are unlikely in this sand-sized material, and the feldspars under investigation are likely to comprise intergrowths of K-feldspar and Na-feldspar. Consequently the apparent consistency might be related to one phase dominating the response in these experiments.

The relationship between E_u and ΔE is also interesting (Fig. 4.6). Our results suggest that ΔE is either consistent with E_u (five samples) or smaller than E_u (five samples). This relationship confirms expectation because whereas E_u (the Urbach band-tail width) mainly maps the excitation efficiency, ΔE (the width of the band-tail accessible from the ground state of the trap) depends on both the excitation efficiency and the recombination efficiency, which in turn is a function of the energy of the band tail state (Jain and Ankjærgaard, 2011) and temperature. Interestingly four out of five samples with $\Delta E < E_u$ have relatively low K contents (F1, JSH1-13, HAM-5, KTB-383-C), potentially indicating reduced recombination efficiency with band-tail energy in K-poor feldspars. Poolton et al. (2009) and Kars et al. (2013) also found that ΔE is narrower in $NaAlSi_3O_8$ than in $KAlSi_3O_8$, providing support for this observation.

Whilst it is important to consider the absolute width of the band-tail states, the absolute density of band-tail states will also impact the thermal stability of luminescence signals in feldspars. This aspect has not been investigated in the present study but should be considered for assessing thermal stability of IRSL.

4.6 Conclusion

In this study we investigated the kinetic parameters of feldspar that are thought to determine thermal decay using optical probing, and attempted to relate these parameters to feldspar chemical composition. We obtained a nominal average estimate for the optical trap depth of 2.04 ± 0.05 eV and the energy of the excited state of the IRSL trap of 1.44 ± 0.02 eV, with FWHM ranging from 0.16 to 0.40 eV. Detailed analyses of both the full sub-conduction band-tail width (Eu) and the sub-conduction band-tail states accessible from the ground state of the trap (ΔE), revealed values ranging from 0.2 to 0.8 eV. All values are consistent with previous studies. Interestingly the difference between ΔE and E_u is greater for samples with low K-content, potentially indicating that recombination efficiency must vary more with band tail energy in K poor feldspars. Based on these findings we tentatively conclude that the defect or the defects leading to IRSL in feldspar are within the alumino-silicate framework of feldspar, which is almost the same for all alkali feldspars and would explain the similarity in our results. In contrast to the trap energy levels (ground and excited state), ΔE, E_u and the FWHM of the excited state exhibited larger variability between samples; combining these data with numerical models of feldspar thermal decay, and contrasting them with isothermal decay data in future work will provide further insights into which parameters are the key drivers of differences in the thermal stability of feldspars.

Acknowledgements

SR would like to acknowledge funding by the Deutschlandstipendium of the Bundesministerium for Bildung und Forschung - Stiftung Studium und Lehre (Ministry of Education and Research of the German government) and an AberDoc PhD Scholarship of Aberystwyth University. An Erasmus+ student mobility grant enabled SR's research stay at the Center for Nuclear Technologies, Technical University of Denmark, DTU Risø Campus, Roskilde, Denmark. GEK acknowledges support from SNSF grant number PZ00P2-167960.

Samples HAM-5 and JSH1-13 were taken in the framework of the QuakeRec-Nankai project, funded by the Belgian Science Policy Office (BELSPO BRAIN-be BR/121/A2). We thank Benny Guralnik for the provision of KTB-383-C, Renske Lambert for MBT-I-2430 and MBT-F-5704, Javier Garcia-Guinea for Cleavelandite and David Sanderson for F1.

We thank two anonymous reviewers for their constructive comments that helped to improve the manuscript.

References

Aitken, M. J., 1985. Thermoluminescence dating. Oxford, Academic Press, 385 p.

Andersen, M. T., Jain, M., Tidemand-Lichtenberg, P., 2012. Red-IR stimulated luminescence in K-feldspar: Single or multiple trap origin? Journal of Applied Physics 112, 1–11.

Bailiff, I. K., Poolton, N. R. J., 1991. Studies of charge transfer mechanisms in feldspars. Nuclear Tracks and Radiation Measurements 18, 111–118.

Baril, M. R., Huntley, D. J., 2003. Optical excitation spectra of trapped electrons in irradiated feldspars. Journal of Physics: Condensed Matter 15, 8011–8027.

Bøtter-Jensen, L., Duller, G. A. T., Poolton, N. R. J., 1994. Excitation and emission spectrometry of stimulated luminescence from quartz and feldspars. Radiation Measurements 23 (2/3), 613–616.

Bøtter-Jensen, L., McKeever, S. W. S., Wintle, A. G., 2003. Optically Stimulated Luminescence Dosimetry. Elsevier, Amsterdam, 375 p.

Brown, N. D., Rhodes, E. J., 2017. Thermoluminescence measurements of trap depth in alkali feldspars extracted from bedrock samples. Radiation Measurements 96, 53–61.

Burg, J.-P., Davy, P., Nievergelt, P., Oberli, F., Seward, D., Diao, Z., Meier, M., 1997. Exhumation during crustal folding in the Namche-Barwa syntaxis. Terra Nova 9, 53-56.

Bussy, F., Schaeltegger, U., Marro, C., 1989. The age of the Mont Blanc granite (western Apls): A heterogenous isotopic system dated by Rb-Sr whole rock determination on its microgranular enclaves. Schweizer Mineralogische und Petrologische. Mitteilungen 69, 3–13.

Bussy, F., Von Raumer, J. F., 1993. U-Pb dating of Palaeozoic events in the

Mont-Blanc crystalline massif, western Alps. Terra Nova Abstracts 5, 382.

Buylaert, J.-P., Jain, M., Murray, A. S., Thomsen, K. J. Thiel, C., Sohbati, R., 2012. A robust feldspar luminescence dating method for Middle and Late Pleistocene sediments. Boreas 41, 435–451.

Cassedanna, J. P., Roditi, M., 1996. The location, geology and mineralogy of gem tourmalines in Brazilian Journal of Gemmonology 25, 263–298.

Clark, R.J., Sanderson, D.C.W., 1994. Photostimulated luminescence excitation of spectroscopy of feldspars and micas. Radiation Measurements 23, 641–646.

Finch, A. A., Klein, J., 1999. The causes and petrological significance of cathodoluminescence emissions from alkali feldspars. Contribution to Mineralogy Petrology 135, 234–243.

Godfrey-Smith, D. I., Cada, M., 1996. IR stimulation spectroscopy of plagioclase and potassium feldspars, and quartz. Radiation Protection Dosismetry 66, 379–385.

Guralnik, B., Jain, M., Herman, F., Ankjærgaard, C., Murray, A. S., Valla, P. G., Preusser, F., King, G. E., Chen, R., Lowick, S. E., Kook, M., Rhodes, E. J., 2015. OSL-thermochronometry of feldspar from the KTB borehole, Germany. Earth and Planetary Science Letters 423, 232–243.

Harrison, T. N., Parsons, I., Brown, P. E., 1990. Mineralogical evolution of fayalite-bearing rapakivi granites from the Prins Christians Sund pluton, South Greenland. Mineralogical Magazine 54, 57–66.

Hütt, G., Jaek, I., Tchonka, J., 1988. Optical dating: K-feldspars optical response stimulation spectra. Quaternary Science Reviews 7, 381–385.

Huntley, D. J., Godfrey-Smith, D. I., Thewalt, M. L. W., 1985. Optical dating of sediments. Nature 313, 105–107.

Ikeya, M., 1993. New Applications of Electron Spin Resonance. World Scien-

tific. ISBN 978-981-4317-21-4.

International Atomic Energy Agency, Analytical Quality Control Services, Seibersdorf (Austria) (1999). IAEA AQCS catalogue for reference materials and intercomparison exercises 1998/1999 (INIS-XA–131). International Atomic Energy Agency (IAEA)

Ito, H., Yamada, R., Tamura, A., Arai, S., Horei, K., Hokada, T., 2013. Earth's youngest exposed granite and its tectonic implications: the 10-0.8 Ma Kurobegawa Granite. Scientific Reports 3, 1306.

Jain, M., Sohbati, R., Guralnik, B., Murray, A. S., Kook, M., Lapp, T., Prasad, A. K., Thomsen, K. J., Buylaert, J. P., 2015. Kinetics of infrared stimulated luminescence from feldspars. Radiation Measurements 81, 242–250.

Jain, M., Guralnik, B., Thalbitzer Andersen, M., 2012. Stimulation luminescence emission from localized recombination in randomly distributed defects. Journal of Physics: Condensed Matter 24, 1–12.

Jain, M., Ankjærgaard, C., 2011. Towards a non-fading signal in feldspar: Insight into charge transport and tunnelling from time-resolved optically stimulated luminescence. Radiation Measurements 46, 292–309.

Kars, R. H., Poolton, N.R.J., Jain, M., Ankjærgaard, C., Dorenbos, P., Wallinga, J., 2013. On the trap depth of the IR-sensitive trap in Na- and K-feldspar. Radiation Measurements 59, 103–113.

King, G. E., Herman, F., Guralnik, B., 2016. Northward migration of the eastern Himalayan syntaxis revealed by OSL thermochronometry. Science 353 (6301), 800–804.

Kook, M. H., Lapp, T., Murray, A. S., Thiel., C., 2012. A Risø XRF attachement for major element analysis of aliquots of quartz and feldspar separates. UK Luminescence and ESR Meeting, Aberystwyth, September 2012 (abstract), p. 37.

Krbetschek, M. R., Götze, J., Dietrich, A., Trautmann, T., 1997. Spectral infor-

mation from minerals relevant for luminescence dating. Radiation Measurements 27 , 695–748.

Krbetschek, M. R., Rieser, U., Stolz, W., 1996. Optical dating: Some luminescence properties of natural feldspars. Radiation Protection Dosimetry 66 (1-4), 407–412.

Lambert, R., King, G.E., Valla, P.G., Herman, F., In Review. Investigating thermal kinetic processes of feldspar for the application of luminescence thermochronometry. Radiation Measurements

Li, B., Li, S.-H., 2013. The effect of band-tail states on the thermal stability of the infrared stimulated luminescence from K-feldspar. Journal of Luminescence 136, 5–10.

Malins, A. E. R., Poolton, N. R. J., Quinn, F. M., Johnsen, O., Denby, P. M., 2004. Luminescence excitation characteristics of Ca, Na, and K-aluminosilicates (feldspars) in the stimulation range 5–40 eV: determination of the band-gap energies. Journal of Physics D: Applied Physics 37, 1439–1450.

McKeever, S. W. S., Bøtter-Jensen, L., Agersnap Larsen, N., Duller, G. A. T., 1997. Temperature dependence of OSL decay curves: Experimental and theoretical aspects. Radiation Measurements 27 (2), 161–170.

Morthekai, P., Thomas, J., Pandiam, M. S., Balaram, V., Singhvi, A. K., 2012. Variable range hopping mechanism in band-tail states of feldspars: A time-resolved IRSL study. Radiation Measurements 47, 857–863.

Murray, A. S., Buylaert, J. P., Thomsen, K. J., Jain, M., 2009. The effect of preheating on the IRSL signal from feldspar. Radiation Measurements 44, 554–559.

Poolton, N. R. J., Nicholls, J. E., Bøtter-Jensen, L., Smith, G. M., Riedi, P. C., 2001. Observation of free electron cyclotron resonance in $NaAlSi_3O_8$ feldspar: Direct determination of the effective electron mass. Physica status solidi 225 (2), 467–475.

Poolton, N. R. J., Wallinga, J., Murray, A. S., Bulur, E., Bøtter-Jensen, L., 2002a. Electrons in feldspar I: on the wavefunction of electrons trapped at simple lattice defects. Physics and Chemistry of Minerals 29, 210–216.

Poolton, N. R. J., Ozanyan, K. B., Wallinga, J., Murray, A. S., Bøtter-Jensen, L., 2002b. Electrons in feldspar II: a consideration of the influence of conduction band-tail states on luminescence processes. Physics and Chemistry of Minerals 29, 217–225.

Poolton, N.R.J., Kars, R.H., Wallinga, J., Bos, A.J.J., 2009. Direct evidence for the participation of band-tails and excited-state tunneling in the luminescence of irradiated feldspars. Journal of Physics: Condensed Matter 21, 1–10.

Prasad, A.K., Lapp, T., Kook, M., Jain, M., 2016. Probing luminescence centres in Na rich feldspar. Radiation Measurements 90, 292–297.

Prasad, A. K., Poolton, N. R. J., Kook, M., Jain, M., 2017. Optical dating in a new light: A direct, non-destructive probe of trapped electrons. Scientific Reports 7, 1–15.

Prasad, A. K., Jain, M., 2018. Breakdown of Kasha´s Rule in a Ubiquitous, Naturally Occuring, Wide Bandgap Aluminosilicate (Feldspar). Scientific Reports 8, 1–12.

Riedesel, S., Brill, D., Roberts, H.M., Duller, G.A.T., Garrett, E., Zander, A.M., King, G.E., Tamura, T., Burow, C., Cunningham, A., Seeliger, M., De Batist, M., Heyvaert, V.M.A., Fujiwara, O., Brückner, H. and the QuakeRecNankai Team, 2018. Single-grain luminescence chronology of historical extreme-wave event deposits recorded in a coastal lowland, Pacific coast of central Japan. Quaternary Geochronology 45, 37–49.

Sanderson, D.C.W., Clark, R.J., 1994. Pulsed photostimulated luminescence of alkali feldspars. Radiation Measurements 23, 633–639.

Short, M. A. (2004). Determining the possible lattice sites of two unknown

defects in orthoclase from the polarization effects in their optical transitions. Journal of Physics: Condensed Matter, 16(41), 7405.

Spooner, N. A., 1994. The anomalous fading of infrared-stimulated luminescence from feldspars. Radiation Measurements 23, 625–632.

Strickertsson, K., 1985. The thermoluminescence of potassium feldspars – glow curve characteristics and initial rise measurements. Nuclear Tracks 10, 613–617.

Thiel, C., Buylaert, J.-P., Murray, A., Terhorst, B., Hofer, I., Tsukamoto, S., Frechen, M., 2011. Luminescence dating of the Stratzig loess profile (Austria) – Testing the potential of an elevated temperature post-IR IRSL protocol. Quaternary International 234, 23–31.

Thomsen, K. J., Murray, A. S., Jain, M., Bøtter-Jensen, L. 2008: Laboratory fading rates of various luminescence signals from feldspar-rich sediment extracts. Radiation Measurements 43, 1474–1486.

Tsukamoto, S., Jain, M., Murray, A., Thiel, C., Schmidt, E., Wacha, L., Dohrmann, R., Frechen, M., 2012. A comparative study of the luminescence characteristics of polymineral fine grains and coarse-grained K- and Na-rich feldspars. Radiation Measurements 47, 903–908.

Wintle, A. G., 1973. Anomalous fading of thermoluminescence in mineral samples. Nature 245, 143–144.

Yukihara, E.G., Coleman, A.C., Biswas, R.H., Lambert, R., Herman, F., King, G.E., In Press. Thermoluminescence Analysis for Particle Temperature Sensing and Thermochronometry: Principles and Fundamental Challenges. Radiation Measurements.

Supplementary Material – Optical determination of the width of the band-tail states, and the excited and ground state energies of the principal dosimetric trap in feldspar

This chapter contains supplementary material to the article published in *Radiation Measurements* as

Riedesel, S., King, G.E., Prasad, A.K., Kumar, R., Finch, A.A., Jain, M., 2019. *Optical determination of the width of the band-tail states, and the excited and ground state energies of the principal dosimetric trap in feldspar*. Radiation Measurements 125, 40-51.

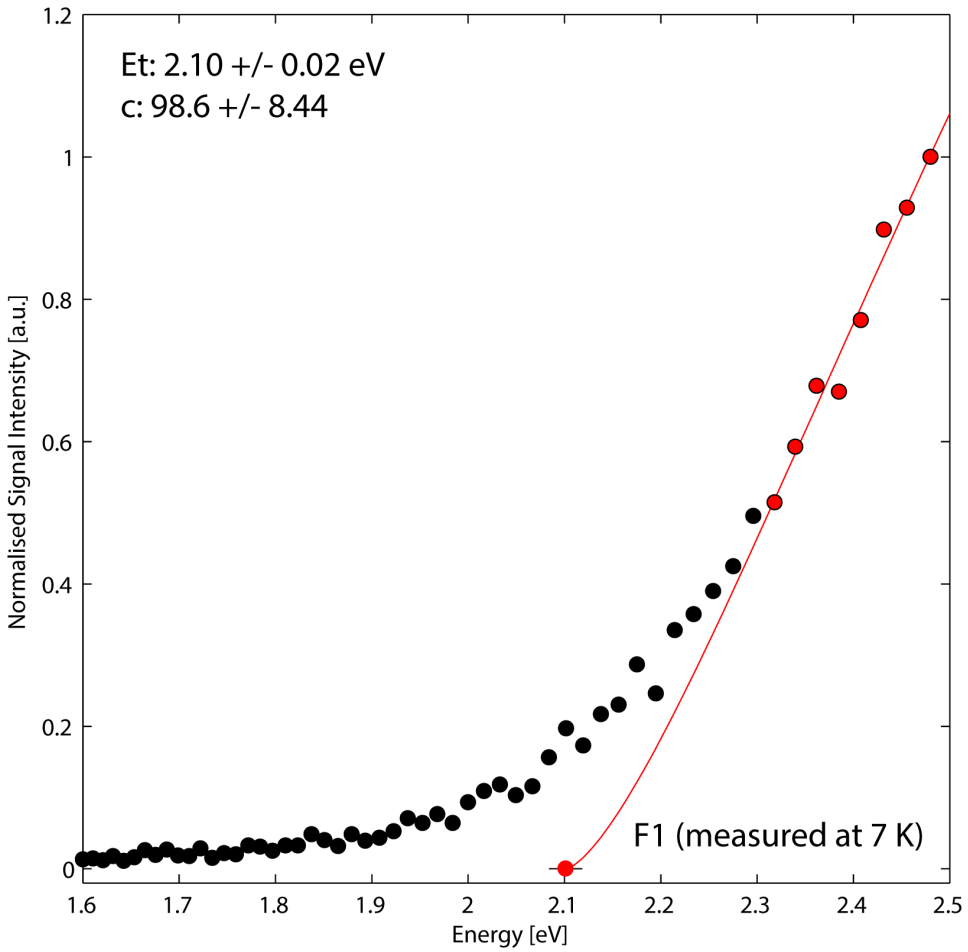

Figure S4.1: *Excitation spectra fitted using eq. 4.1 (Bøtter-Jensen et al., 2003) to determine trap-depth (E_t) for F1, which was measured at 7 K. The solid line shows the fit and the dashed line the extrapolated curve. The intersect of the curve with the x-axis gives the trap depth.*

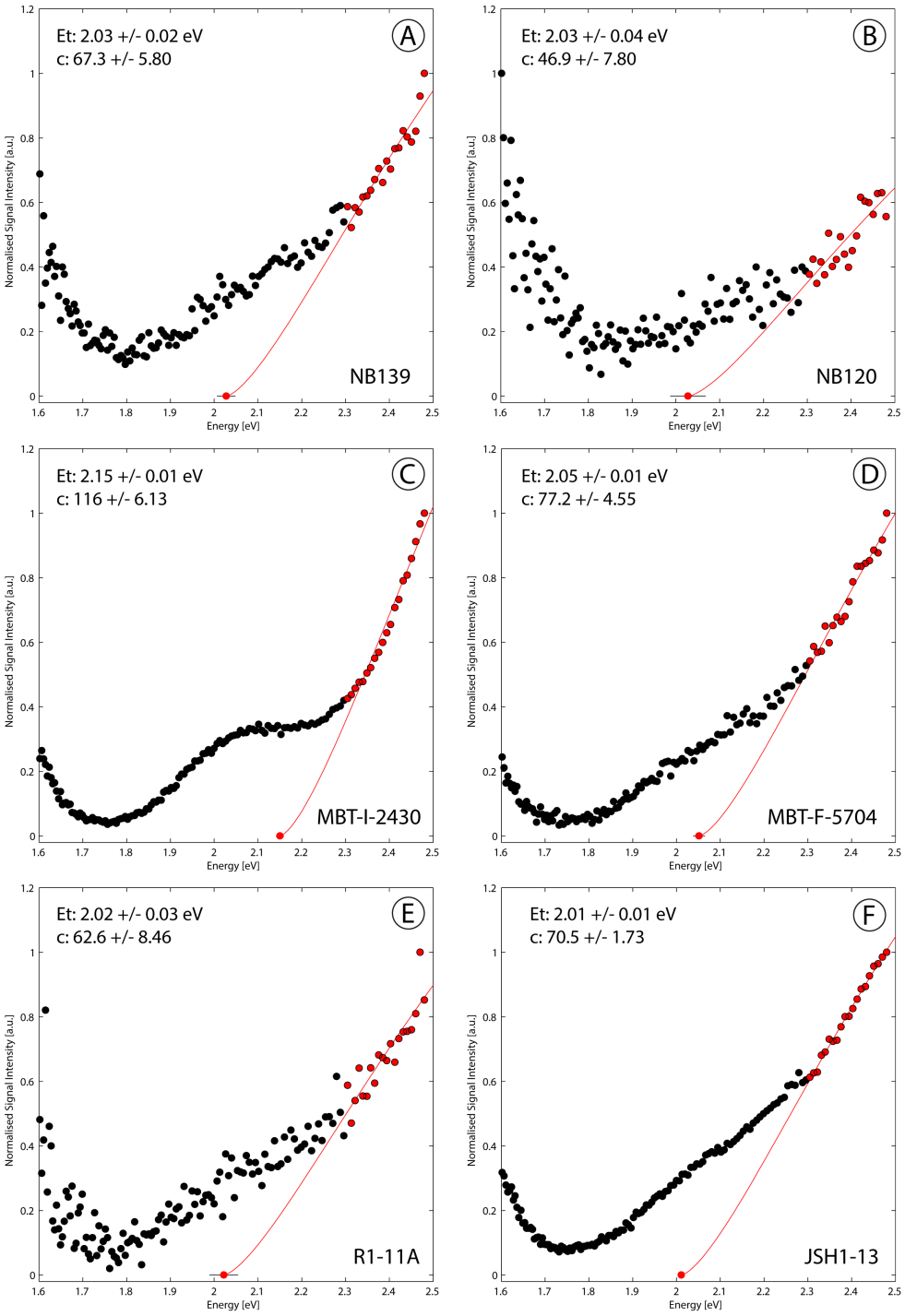

Figure S4.2: *Excitation spectra fitted using eq. 4.1 (Bøtter-Jensen et al., 2003) to determine trap-depth (E_t) for samples NB139, NB120, MBT-I-2430, MBT-F-5704, R1-11A and JSH1-13, all measured at 300 K. The solid line shows the fit and the line the extrapolated curve. The intersect of the dashed curve with the x-axis gives the trap depth.*

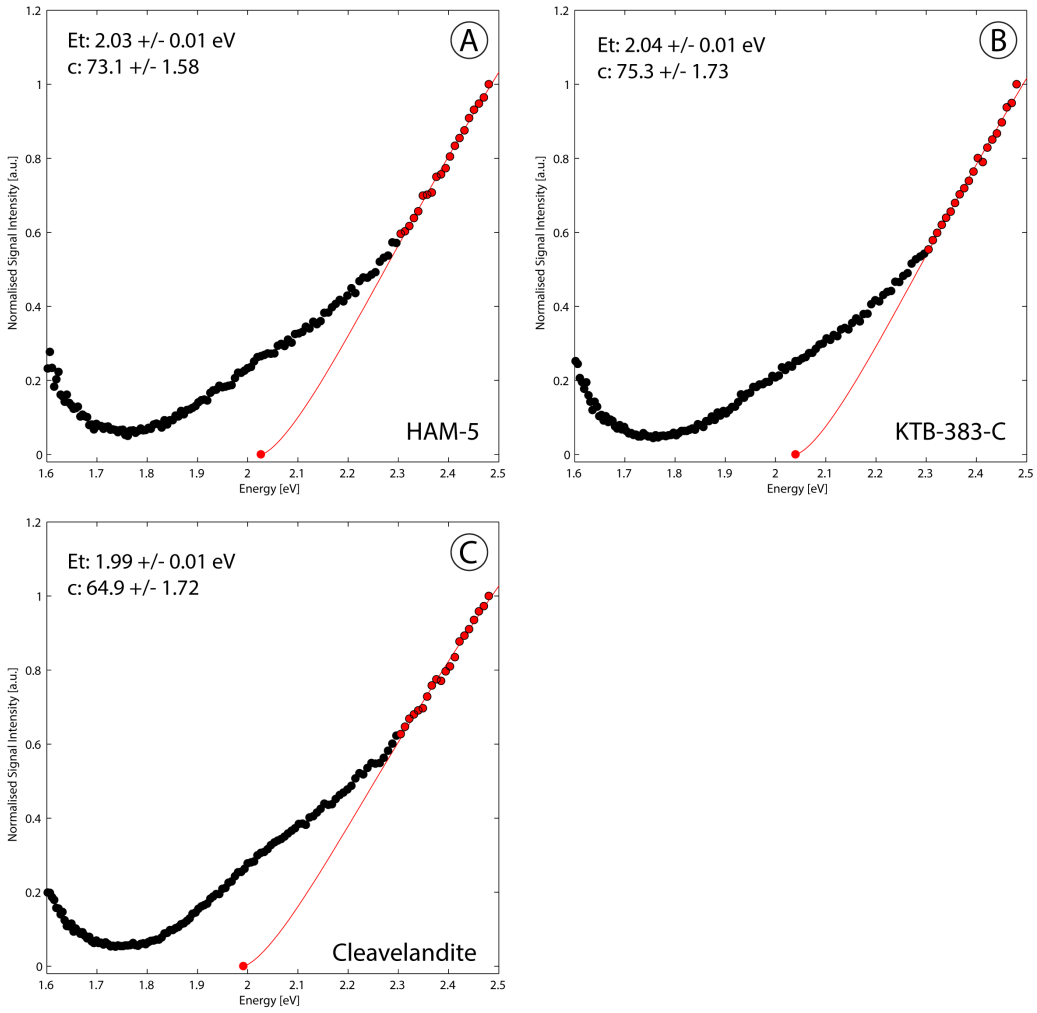

Figure S4.3: *Excitation spectra fitted using eq. 4.1 (Bøtter-Jensen et al., 2003) to determine trap-depth (E_t) for samples HAM-5, KTB-383-C and Cleavelandite, all measured at 300 K. The solid line shows the fit and the dashed line the extrapolated curve. The intersect of the curve with the x-axis gives the trap depth.*

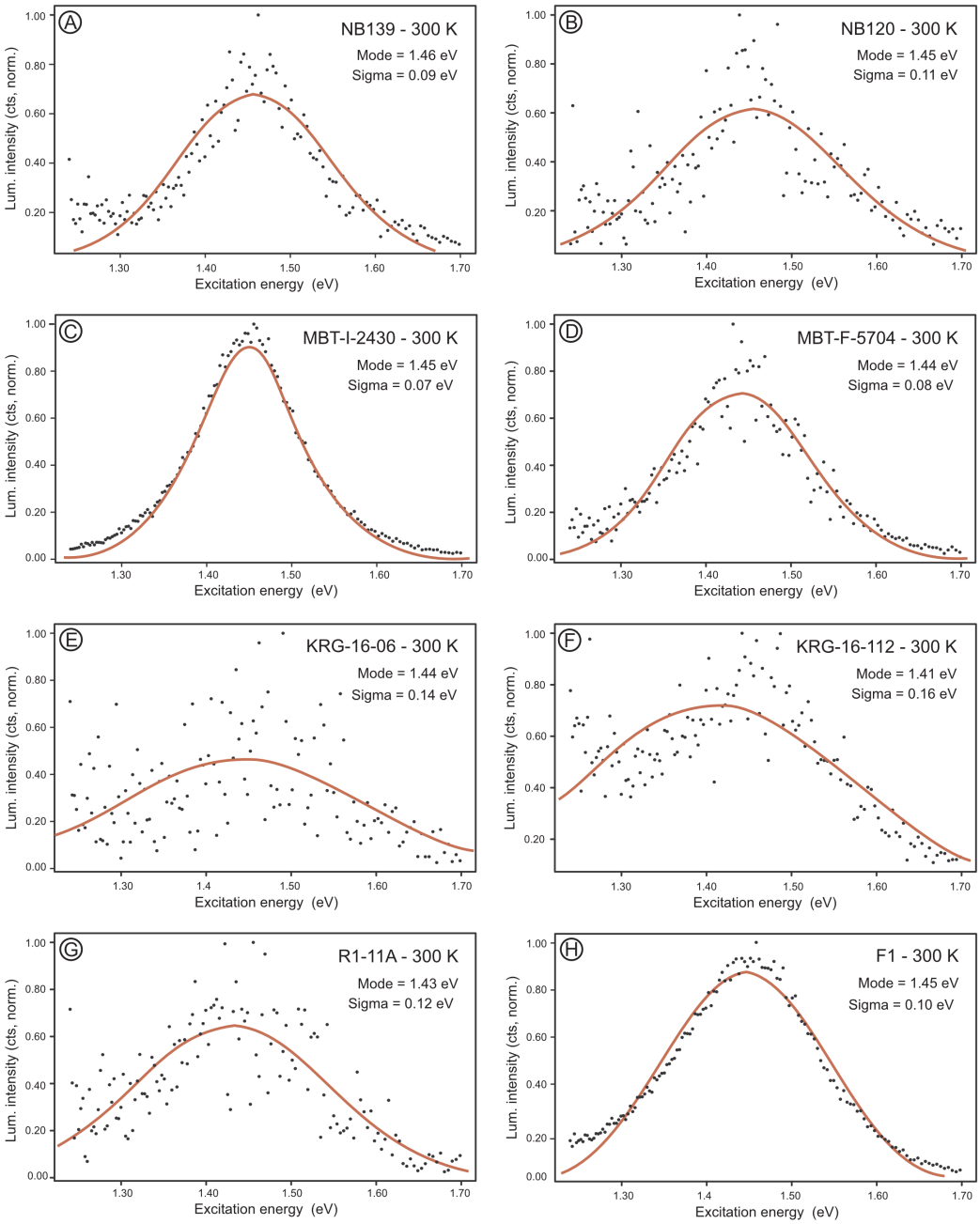

Figure S4.4: *Excitation spectra showing the fit of the IR resonance peak of samples NB139, NB120, MBT-I-2430, MBT-F-5704, KGR-16-06, KRG-16-112, R1-11A and F1 with a single Gaussian distribution (eq. 4.2).*

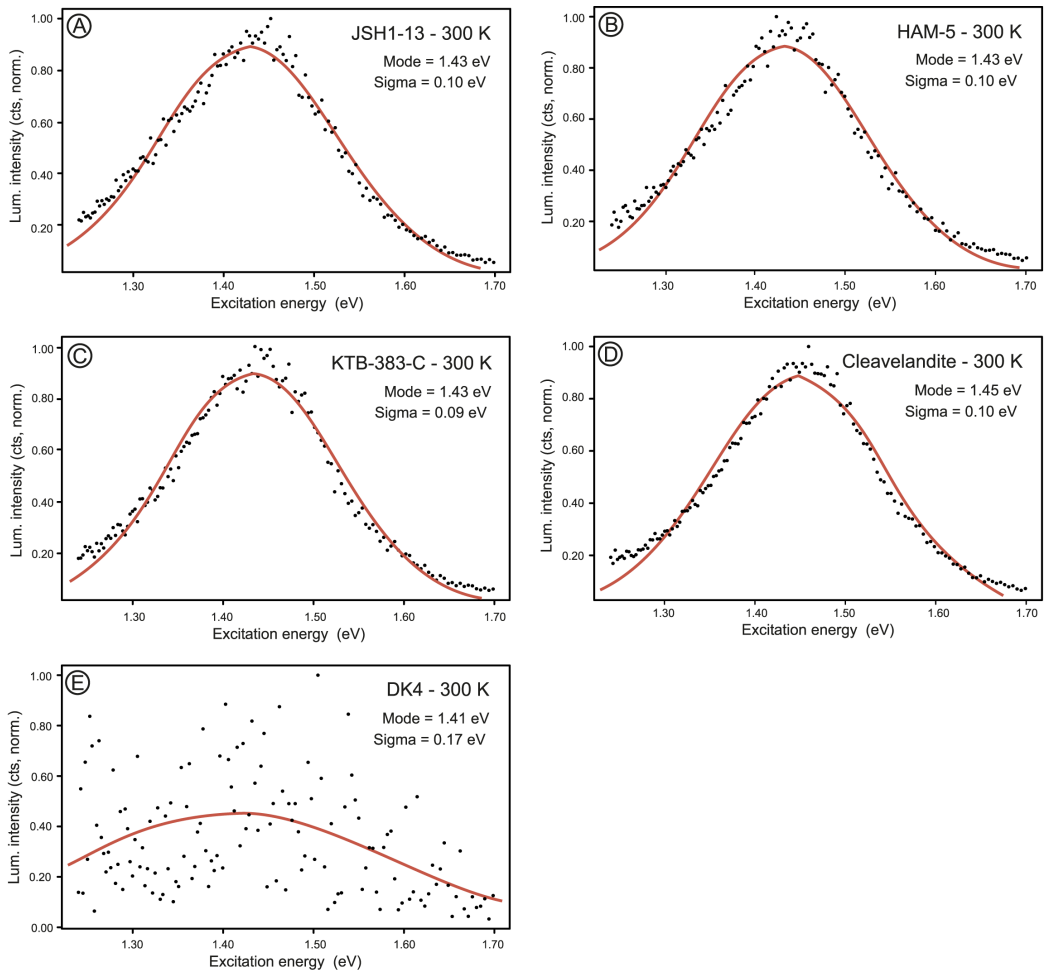

Figure S4.5: *Excitation spectra showing the fit of the IR resonance peak of samples JSH1-13, HAM-5, KTB-383-C, Cleavelandite and DK4 with a single Gaussian distribution (eq. 4.2).*

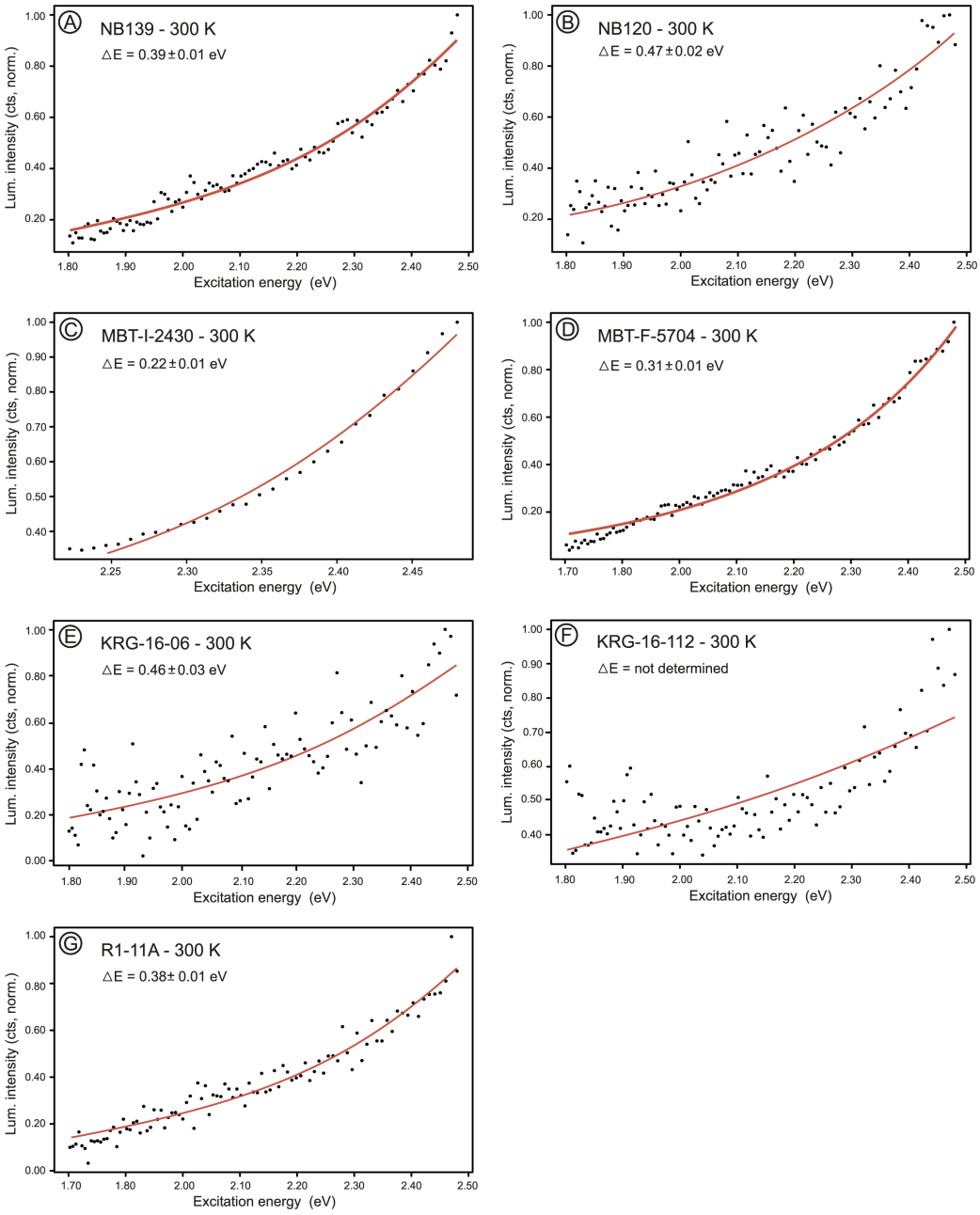

Figure S4.6: *Excitation spectra of samples NB139, NB120, MBT-I-2430, MBT-F-5704, KRG-16-06, KRG-16-112 and R1-11A fitted with equation 4.3 (Poolton et al., 2009) to obtain the width of the band-tail accessible from the ground state of the trap (ΔE).*

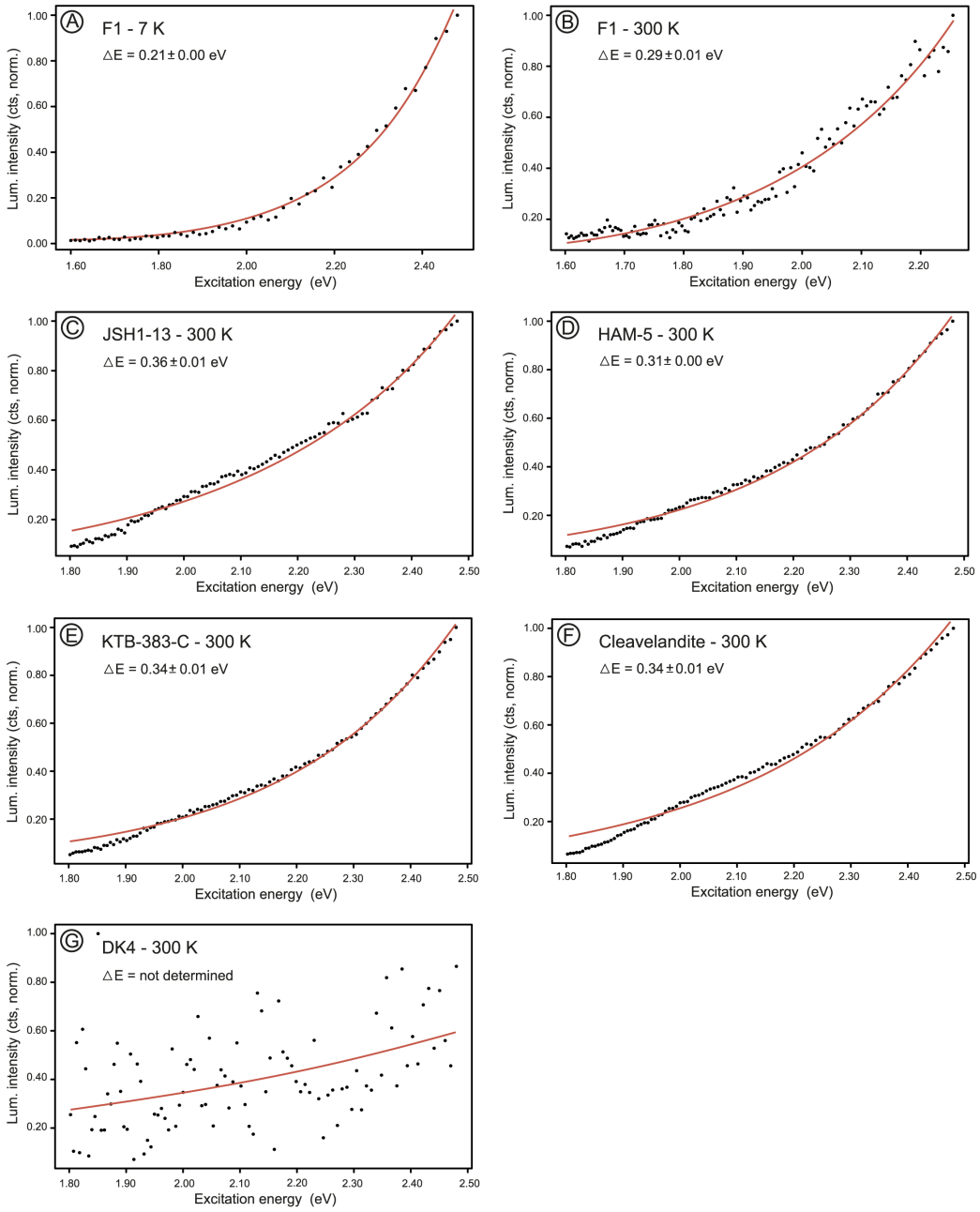

Figure S4.7: *Excitation spectra of samples F1 (300 K and 7 K), JHS1-13, HAM-5, KTB-383-C, Cleavelandite and DK4 fitted with equation 4.3 (Poolton et al., 2009) to obtain the width of the band-tail accessible from the ground state of the trap (ΔE).*

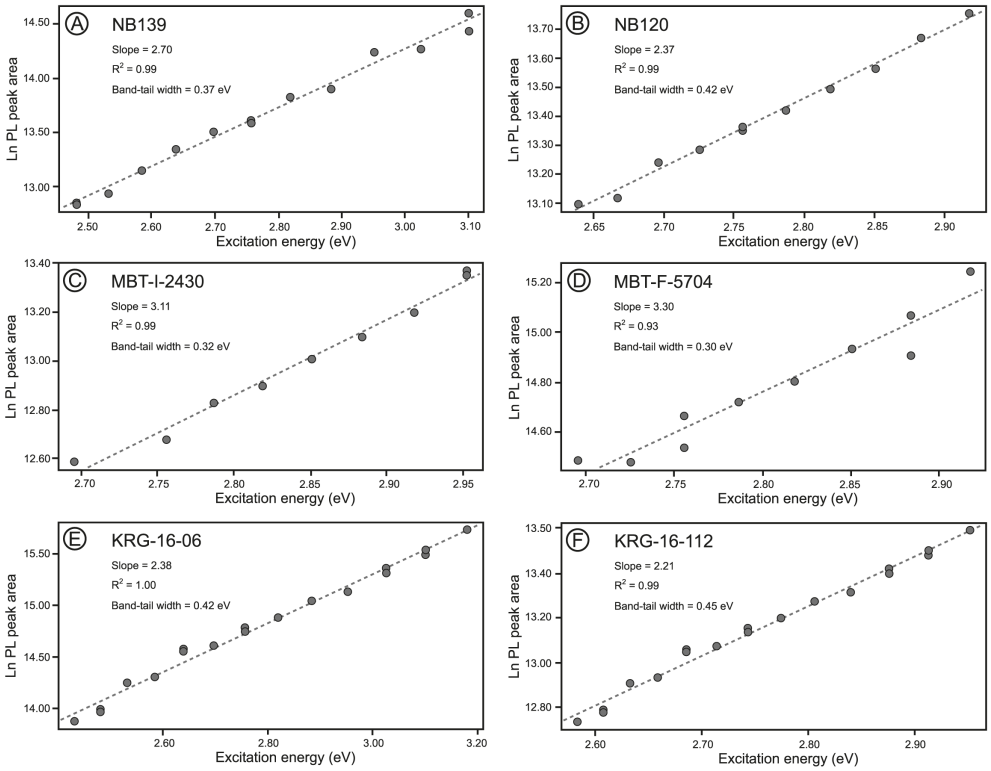

Figure S4.8: *Exponential relationship of the integrated area under the PL peak and the corresponding excitation energy of samples NB139, NB120, MBT-I-2430, MBT-F-5704, KRG-16-06 and KRG-16-112. The inverse of the slope gives the band-tail width (E_u).*

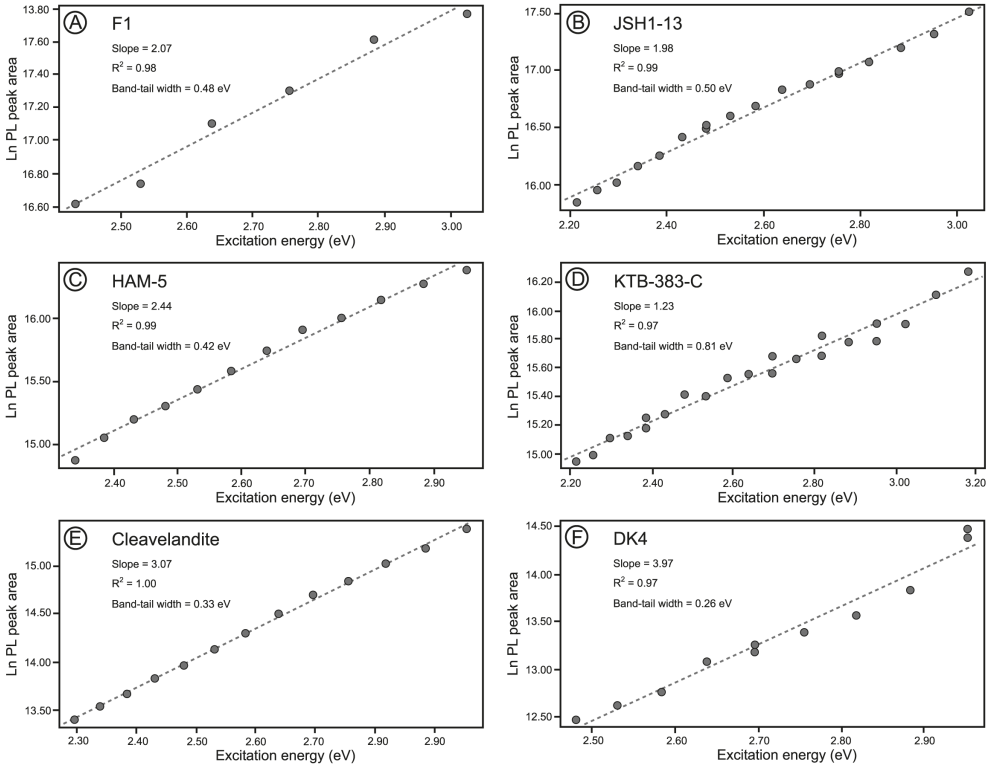

Figure S4.9: *Exponential relationship of the integrated area under the PL peak and the corresponding excitation energy of samples F1, JHS1-13, HAM-5, KTB-383-C, Cleavelandite and DK4. The inverse of the slope gives the band-tail width (E_u).*

Preface to Chapter 5

Chapter 4 *Optical determination of the width of the band-tail states, and the excited and ground state energies of the principal dosimetric trap in feldspar* presented new results regarding physical properties of one type of electron trap in feldspars and regarding the sub-conduction band-tail states. A comparison of obtained trap parameters with the chemical composition of the samples, particularly the K-content, revealed only little variations between samples. However, the samples used in this chapter were mainly bulk feldspar material extracted from either sediment or bedrock. Thus it is likely that the results represent an average of a variety of chemically and structurally different grains present within one sample.

To allow more in-depth analyses of physical properties governing electron trapping, de-trapping and re-trapping in feldspar, the following Chapter 5 (*Site-selective characterisation of electron trapping centres in relation to chemistry, structural state and mineral phases present in single crystal alkali feldspars*) focusses on single crystal specimens. In addition to the chemistry of the samples, potential influence of the sample′s structural state and the number of phases present within a single crystal (whether the sample is single-phase or perthitic) on the luminescence properties, particularly the electron trap, is investigated.

The results in Chapter 4 were obtained by fitting the excitation spectra of the different feldspar samples. This was done to obtain numerical values for trapping site parameters and band-tail states width. However, particularly the fits for the IR resonance peak are of poor quality. Previous work by others (e.g. Baril and Huntley, 2003; Andersen et al., 2012) has shown the complexity of fitting the IR resonance peak. Following the own experience from Chapter 4 and previous investigations by e.g. Baril and Huntley (2003) and Andersen et al. (2012) the IR resonance peaks will not be fitted in the following chapter. Additionally, Chapter 5 will further explore why the IR resonance peak position is mostly invariant between samples.

In Chapter 4 fitting was also used to constrain the width of the band-tail states accessible from the ground state of the electron traps in feldspars. However, in some samples (see Figure S4.7) the data does not follow the described single exponential function. In contrast, small bumps are visible from the figures, particularly in the range from 2.0 eV to 2.2 eV. Similar features have been described previously in theoretical considerations by Poolton et al. (1994). These authors suggested that features superimposed on the exponentially rising luminescence curves obtained from excitation spectra could be associated with defects located either on Si or O substitutional sites. To further explore variations of these superimposed features excitation spectra of multiple sub-samples of well-characterised samples should be made in this excitation energy region. Whilst this is not further considered in this thesis, the next chapter will explore potential effects of framework disorder on an excitation peak, which lies within this energy range.

References

Andersen, M.T., Jain, M., Tidemann-Lichtenberg, P., 2012. Red-IR stimulated luminescence in K-feldspar: Single or multiple trap origin? Journal of Applied Physics 112, 043507.

Baril, M.R., Huntley, D.J., 2003. Optical excitation spectra of trapped electrons in irradiated feldspars. Journal of Physics: Condensed Matter 15, 8011-8027.

Poolton, N.R.J., Bøtter-Jensen, L., Ypma, P.J.M., Johnsen, O., 1994. Influence of crystal structure on the optically stimulated luminescence of feldspars. Radiation Measurements 23, 551-554.

Five

Site-selective characterisation of electron trapping centres in relation to chemistry, structural state and mineral phases present in single crystal alkali feldspars

This chapter is in preparation for submission to the *Journal of Luminescence* as

Riedesel, S., Kumar, R., Duller, G.A.T., Roberts, H.M., Bell, A.M.T., Jain, M. *Site-selective characterisation of electron trapping centres in relation to chemistry, structural state and mineral phases present in single crystal alkali feldspars.*

Abstract

Feldspars are ubiquitous natural dosimeters widely used in luminescence dating. Despite decades of research, the lattice defects as well as the mechanisms involved in luminescence production in feldspars remain poorly understood. The recently developed method of infrared-photoluminescence (IRPL) excitation-emission spectroscopy has revealed the presence of two electron trapping centres emitting IRPL at 1.3 eV and 1.41 eV ($IRPL_{1.3}$ and $IRPL_{1.41}$ centres), and it enables detailed investigations into the ground and excited state energies of these centres.

Here we make measurements of a range of single crystal alkali feldspars to understand the effects of feldspar chemical composition, crystal structure and framework disorder on the physical characteristics of $IRPL_{1.3}$ and $IRPL_{1.41}$ electron trapping centres. Measurements of our sample suite reveals IRPL and IR-RL emissions at 1.41 eV, 1.3 eV and, for the first time, at 1.2 eV. Our results show that whilst the $IRPL_{1.3}$ trapping centre is unaffected by the M site cation occupancy, the presence of $IRPL_{1.41}$ trapping centres seems to be linked to the presence of K^+ ions on M sites. However, no clear trends in IRPL and IR-RL emission energies and signal intensities with chemical composition of the samples were found. Exploring the effect of framework disorder on $IRPL_{1.3}$ and $IRPL_{1.41}$ emissions revealed no significant changes to IRPL and IR-RL emission energies or ground state energies of the trapping centres, suggesting that the corresponding defects are not located on bridging O ions. Variations in ground state energies across the whole sample suite range from 2.04 eV to 2.20 eV for the $IRPL_{1.3}$ centre and from 2.16 eV to 2.46 eV for the $IRPL_{1.41}$ centre. Variations in trap depth seem to be driven by other factors than sample chemistry, degree of Al^{3+} disorder and number of phases present in a single crystal feldspar. Interestingly, the IR resonance peak is invariant between samples.

Regarding the use of IRPL in luminescence dating, we show that optical resetting differs for the three different emissions, with the emission at ∼1.41 eV not being reset in some samples even after 18 hours of solar bleaching.

5.1 Introduction

Due to their ability to store charge within defects in the crystal lattice, feldspar minerals are widely used as natural luminescence dosimeters (e.g. Huntley et al., 1985; Hütt et al., 1988). Despite their routine and widespread use, the crystal defects and the physical processes involved in luminescence production in feldspars are not yet fully understood. In particular the crystal defects responsible for the electron trapping centres in feldspars remain unknown, and the observed variations in luminescence across samples, or across grains within the same samples remain poorly understood.

By comparing photoluminescence (PL) and radioluminescence (RL) emissions of a lead-rich K-feldspar (amazonite) with lead-doped potassium chloride, Erfurt (2003) suggested that the electron trap in feldspars is associated with Pb^{2+} ions substituting for K^{+} ions in the lattice of K-feldspars. Based on observing polarization effects during optical transitions in a sample of orthoclase, Short (2004) inferred a type of electron trap in that sample to be located at a tetrahedral site on the framework. More recently, based on infrared photoluminescence (IRPL), Kumar et al. (2018, 2020a) proposed that the defect acting as electron trapping centre is located in two different lattice environments within the feldspar lattice resulting in two different types of trapping centres (referred to as the $IRPL_{1.41}$ and $IRPL_{1.3}$ centre, where the subscript denotes the emission energy in eV). The observations by Erfurt (2003) and Short (2004) are only based on single alkali feldspar samples and the samples used by Kumar et al. (2018, 2020a) were primarily feldspars separated from sediments which therefore inevitably consisted of grains with a range of chemical compositions. Kumar et al. (2020a) also presented results for two single crystal specimens; one of these samples is a microcline perthite (K8, Baril, 2004) and for the other sample (R28) only the chemical composition is available. Kumar et al. (2020a) found that the electron trap depth varied from sample to sample and between the two measured IRPL emissions, with a minimum trap depth of 1.90 eV ($IRPL_{1.3}$ centre) and a maximum trap depth of 2.38 eV ($IRPL_{1.41}$ centre).

Since feldspars are complex framework silicates, properties inherent to the sample′s crystal structure, in addition to the chemistry, could influence electron trapping centres in feldspars. Despite previous efforts, it remains to be confirmed whether (i) electron traps in in feldspars are associated with K^{+} ions (Erfurt, 2003), (ii) if they occupy tetrahedral sites (Short, 2004), (iii) whether the same

crystal defect which captures electrons in the feldspar crystal lattice is indeed located in two different crystallographic environments resulting in two different trapping centres (Kumar et al., 2018, 2020a) or (iv) if neither of these suggestions holds true and further possibilities need to be considered.

Recently, Kumar et al. (2020a) described an approach for constraining electron trap ground and excited state energies using low temperature infrared-photoluminescence (IRPL) excitation-emission spectroscopy. In this paper we apply this technique to a range of chemically and structurally different single crystal feldspars. We have purposefully chosen single crystal feldspars to avoid any averaging of the measured luminescence arising due to a variety of grains present within a sediment sample. The samples used in the present study have previously been explored by Riedesel et al. (2021), who investigated changes in the recombination centres due to variations in samples chemistry, structural state (distribution of Al^{3+} ions on T sites) and number of phases present within a single crystal (i.e. single phase feldspars and perthites). By measuring thermoluminescence (TL) emission spectra and infrared stimulated luminescence (IRSL) fading rates, Riedesel et al. (2021) found that the structural state and the presence of perthite interfaces influence the blue luminescence emission and its fading rate. Here we aim to see whether these chemical and mineralogical properties inherent to the samples investigated also influence electron trapping centres in feldspar and we explore the following questions: (1) Are the electron trapping centres in feldspars related to the K- or Na- content of the samples? (2) Does the number of phases present within a single crystal (i.e. whether it is perthitic or single phase) influence the electron trapping centres? (3) Does the relative degree of disorder of Al^{3+} on the framework influence the electron trapping centres? We hope that answers to these questions will help to improve our understanding of luminescence production in feldspars.

5.2 Brief overview of the structure and chemistry of feldspar

Feldspars are complex framework silicates, consisting of $(Si,Al)O_4$ tetrahedra, which build the framework of the feldspar crystal lattice. Within the framework are four tetrahedral positions occupied by Si^{4+} or Al^{3+} ions. The framework has a net negative charge, which is offset by large cations, predominantly Na^+, K^+

and Ca^{2+}. These cations occupy cavities in the framework termed M sites (Deer et al., 2013, p. 248). The compositional variability of most feldspars is accommodated by three end members, each with a different M site cation: $KAlSi_3O_8$ (K-feldspar), $NaAlSi_3O_8$ (Na-feldspar) and $CaAl_2Si_2O_8$ (Ca-feldspar). The solid solution between K- and Na-feldspars is termed the alkali feldspar series and the solid solution between Na- and Ca-feldspars is referred to as plagioclases. In this paper we focus on the alkali feldspar solid solution series and its end members. In alkali feldspars the ratio of Si^{4+} and Al^{3+} on the framework is 3:1, and the degree of disorder of the tetrahedral site occupancy by these ions dictates the structural state of alkali feldspars. In the high-temperature K-feldspar (monoclinic high sanidine), Al^{3+} has an equal (25 %) chance of occupying any of the four tetrahedral sites ($T_1(0)$, $T_1(m)$, $T_2(0)$ and $T_2(m)$) within the more open alkali feldspar framework. During slow cooling, as the framework contracts, Al^{3+} diffuses into either of the two T_1 sites (giving the monoclinic low sanidine, also referred to as orthoclase). With continued slow-cooling, Al^{3+} preferentially diffuses into one of the two T_1 sites ($T_1(0)$), causing a change in symmetry from monoclinic (sanidine, with the greatest disorder) to triclinic (ordered K-feldspar maximum microcline, e.g. Stewart and Ribbe, 1969; Deer et al., 2013, p. 256-257). Another impact of cooling of feldspar is exsolution. Whilst at high temperature (> 1000 ∘C) a solid solution between the alkali feldspar end members exists, cooling of magma and of metamorphic rocks results in unmixing of K- and Na-rich phases in the alkali feldspar. Alkali feldspars with exsolution features, where K- and Na-rich phases form intergrowths, are termed perthites.

Variations in sample chemistry, exsolution and the degree and range of disorder of Al^{3+} on the framework might influence the luminescence of feldspars. It has been shown that impurity ions (e.g. Fe^{3+} or Mn^{2+}) can function as luminescence centres in feldspars (e.g. Telfer and Walker, 1978) and that the degree of disorder influences the blue luminescence emission intensity and its stability (Finch and Klein, 1999; Riedesel et al., 2021). Suggestions have been made regarding potential electron traps in feldspar (Speit and Lehmann, 1982a) and their locations (Erfurt, 2003; Short, 2004), however more work is needed to successfully link electron trapping centres to physical defects or structural variations in the feldspar crystal lattice.

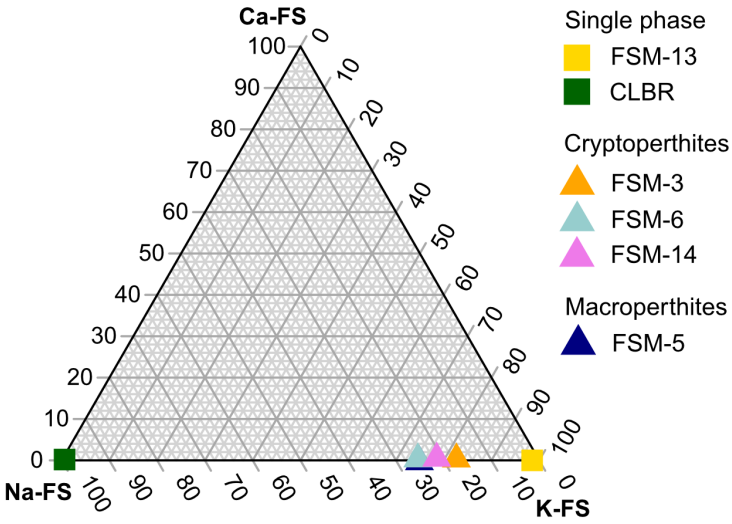

Figure 5.1: *Feldspar composition of the samples. The relative compositions of K-, Na- and Ca-feldspar were calculated using stoichiometric conversion of XRF results.*

5.3 Material and methods

5.3.1 Samples

The suite of eight feldspar samples used in this study consists of single crystal feldspar specimens of the alkali feldspar solid solution series and their end members, microcline and albite. The samples were previously investigated by Riedesel et al. (2021) who explored potential variability in TL emission spectra and IRSL fading rates with mineralogical properties of the samples. The chemistry of the samples was constrained using X-ray fluorescence (XRF), and semi-quantitative phase analyses were achieved using X-ray diffraction (XRD). Details regarding XRD and XRF measurement conditions and results can be found in Riedesel et al. (2021).

The samples include a range of alkali feldspar varieties including end members (Fig. 5.1). Sample FSM-13 is a single-phase microcline (98.5 % K-feldspar) and CLBR a single-phase albite specimen (99.3 % Na-feldspar). FSM-3 (82.5 % K-feldspar), FSM-14 (78.3 % K-feldspar) and FSM-5 (74.8 % K-feldspar) are perthites, as identified by XRD and optical examination using an optical microscope. These perthites are comprised of microcline and albite. FSM-6 (74.4 % K-feldspar) is a perthite, which consists of orthoclase and albite. FSM-3, FSM-6 and FSM-14 are cryptoperthites. FSM-5 is a macroperthite.

Whilst these samples allow a comparison of excitation and emission spectra

in regard to sample chemistry and the number of phases present (i.e. single phase or perthitic), two samples (FSM-6 and FSM-13) were selected for a heating experiment with the aim to artificially disorder the tetrahedral site occupancy by Al^{3+} ions. Details regarding this experiment are given in Riedesel et al. (2021). The success of the heating experiment was checked by analysing X-ray diffraction peak shape and position and this revealed that samples FSM-6 and FSM-13 were successfully disordered during the experiment (Riedesel et al., 2021). The samples are designated FSM-6LH and FSM-13LH after the heating experiment.

5.3.2 Radioluminescence and photoluminescence emission spectra

Radioluminescence (RL) and photoluminescence (PL) emission spectra were measured using the Risø station for CryOgenic Luminescence Research (COLUR) at DTU Physics, Technical University of Denmark. Prior to any luminescence measurements, the samples were bleached for 18 hours in a Hönle SOL2 solar simulator. Afterwards the sample material was mounted as grains or shards (max. 1 mm diameter) on a Cu sample holder using carbon tape. The sample holder of COLUR is attached to a closed-loop He-cryostat, allowing measurements to be performed between 7 and 300 K. All RL and PL emission spectra presented in this paper were measured at 7 K. One sub-sample was measured per sample.

RL emission spectra were measured during irradiation using a filament-based X-ray tube with a Cu anode, operated at 40 kV anode voltage and 100 μA anode current, delivering $\sim$0.06 Gy/s at the sample position. PL emission spectra were measured before and between irradiation steps. RL and PL emission spectra were recorded in the wavelength range from 850 nm to 1000 nm using a liquid nitrogen cooled CCD coupled to a Horiba iHR320 imaging spectrometer. The CCD (Horiba Symphony II) attached to the spectrometer has a resolution of 26 μm pixels and results in a typical spectral resolution of 0.79 nm with the chosen grating of 300 lines/mm and a 500 nm blaze. The monochromator exit slit width was 2 nm for collecting PL and 14 nm for RL emissions. For PL, the signal was integrated over a time period of 0.5 s and for RL over 30 s. The PL response was measured using 830 nm continuous-wave laser excitation. Two LP850 interference filters were placed in front of the spectrometer to reject emissions <850 nm. All obtained signals were corrected for the instrument response prior to further processing. Prior to fitting using up to three Gaussian functions, emission spectra

were converted from wavelength to energy space by multiplying the emission intensity with hc/E^2, where h is Planck′s constant, c the speed of light and E the emission energy, following Hamilton et al. (1978) and Mooney and Kambhampati (2013). All recorded spectra were corrected for the instrumental background by subtracting an empty sample holder measurement from the PL spectrum of each sample. For each sample, a PL measurement was performed on the bleached sample material prior to administering an X-ray dose. The first RL measurement was made immediately after turning on the X-ray source (which results in a maximum irradiation time of ∼1 min of X-ray irradiation and thus the irradiation dose is estimated at ∼3 Gy). Subsequent RL and PL emission spectra were measured once per hour, with irradiations up to 4 hours (∼800 Gy), depending on the brightness of the sample. Measurements after different doses were performed to check for PL signal growth with dose, and RL signal decrease with increasing dose.

5.3.3 Excitation spectra

Excitation spectra were recorded on the same subsamples as the emission spectra after the samples were irradiated to doses ranging from 400 to 800 Gy, using the same X-ray source as described in section 3.2. Excitation spectra were measured at 7 K using COLUR. A Xe-lamp was used as an excitation source. Excitation wavelengths ranged from 460 nm to 820 nm for the 880 nm emission detection and from 495 nm to 912 nm for the 955 nm emission detection. A slit width of 3 nm was used for both excitation and emission monochromators and an integration time of 3 s was used for data collection. Excitation spectra were measured for emissions around ∼880 nm (∼1.41 eV, termed $IRPL_{1.41}$) and ∼955 nm (∼1.30 eV, termed $IRPL_{1.3}$) using the same liquid nitrogen cooled CCD coupled to a Horiba iHR320 imaging spectrometer as described in section 3.2. For recording $IRPL_{1.41}$ excitation spectra two LP850 nm interference filters were placed in front of the spectrometer, and for $IRPL_{1.3}$ excitation spectra two LP925 interference filters were used. The emission was then recorded from 850 nm to 1000 nm for $IRPL_{1.41}$, and from 925 nm to 1000 nm for $IRPL_{1.3}$. From these three-dimensional excitation-emission spectra the emission bands at 880 ± 5 nm ($IRPL_{1.41}$) and 955 ± 5 nm ($IRPL_{1.3}$) were isolated and plotted as a function of excitation wavelength. The obtained spectra were corrected for the excitation light flux of the Xe-lamp and the instrument response of the detection unit. The data were converted from

wavelength to energy space prior to fitting analysis following the same approach as outlined for the RL and PL emission spectra in section 3.2.

5.4 Results

Here we describe the results obtained from IRPL and IR-RL emission spectroscopy and IRPL excitation spectroscopy, by first comparing the optical resetting behaviour of the PL emissions and then examining the potential influence of sample chemistry and structural state on IRPL and IR-RL emissions and the electron trap emitting IRPL/IR-RL at 1.3 eV and 1.41 eV.

5.4.1 IR-RL and IRPL emission spectra

General shape and optical resetting behaviour of the $IRPL_{1.3}$ and $IRPL_{1.41}$ emissions

Emission spectra were recorded after different durations of X-ray irradiation. Representative examples of the recorded IRPL emission spectra are shown in Figure 5.2, and all IRPL and IR-RL spectra are displayed in Figure S5.1 in the supplementary material.

PL and RL emission spectra recorded for various samples show variations in signal intensities with emission wavelength/energy. Generally, the spectra show their highest intensities either around ∼1.41 eV (∼880 nm) or around ∼1.3 eV (∼955 nm) (see examples in Fig. 5.2). PL emission intensities increase with increasing irradiation dose, whilst RL emission intensities decrease with increasing irradiation dose. The rate of PL increase and RL decrease with increasing dose administered to the sample varies between samples and between emissions within a sample (cf. Fig. 5.2).

PL emission spectra recorded prior to switching on X-rays give information on the PL residual signal remaining after 18 hours of solar bleaching (see orange line in Fig. 5.2). The size of these residuals differs between samples; in some samples the PL signal is fully reset after 18 hours of solar bleaching (Fig. 5.2A for FSM-13LH), in others it is only partially reset (Fig. 5.2B for FSM-3) or even untouched (Fig. 5.2C for FSM-5). For samples FSM-13 (single phase microcline, 98.5 % K-feldspar), FSM-13LH (artificially disordered counterpart, Fig. 5.2A), FSM-6 (cryptoperthite, 74.4 % K-feldspar), FSM-6LH (disordered counterpart) and CLBR (single phase albite, 0.5 % K-feldspar) the PL signal was reset to a

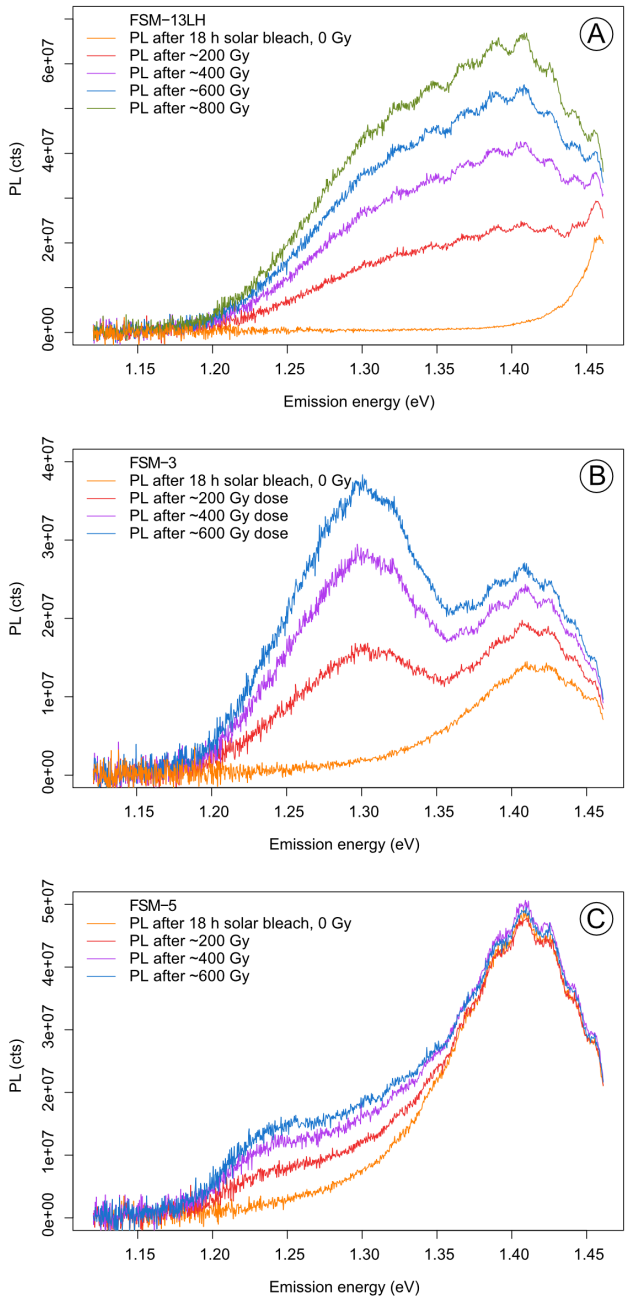

Figure 5.2: *Examples of IRPL emission spectra, which represent the range of spectra observed from our samples. Whilst the PL signal is reset to a background level (see orange curve recorded after 18 hours of solar simulator bleaching and before administering an X-ray dose) for FSM-13LH (A), the $IRPL_{1.3}$ (∼955 nm) and $IRPL_{1.41}$ (∼880 nm) signals reset to varying extend in the case of FSM-3 (B) and FSM-5 (C). The figures also show the different response of the three exemplary samples to X-ray doses of up to ∼800 Gy, and how the two IRPL emissions react differently to dosing. It is particularly interesting that the $IRPL_{1.41}$ emission in FSM-5 does not bleach during 18 hours of solar simulator bleaching and that this emission does not grow with increasing X-ray dose.*

Table 5.1: *Results of Gaussian fit of RL and PL emission spectra. K-FS (%) refers to the K-feldspar content calculated from oxide concentration obtained using XRF.*

Sample ID	K-FS (%)	Phases	RL				PL			
			μ (eV)	σ (eV)	μ (nm)	Dose (Gy)	μ (eV)	σ (eV)	μ (nm)	Dose (Gy)
FSM-13	98.5	single-phase microcline	1.33 1.42	0.06 0.04	935 871	∼3 Gy	1.31 1.43	0.05 0.04	948 870	∼800 Gy
FSM-13LH	98.5	slightly disordered single-phase microcline	1.32 1.41	0.06 0.04	937 879	∼3 Gy	1.32 1.42	0.06 0.04	936 875	∼800 Gy
FSM-3	82.5	perthite (microcline and albite)	1.30 1.41	0.05 0.03	956 878	∼3 Gy	1.30 1.42	0.05 0.03	954 876	∼800 Gy
FSM-14	78.3	perthite (microcline and albite)	1.30 1.42	0.05 0.03	953 874	∼3 Gy	1.32 1.41	0.06 0.03	941 877	∼400 Gy
FSM-5	74.8	perthite (microcline and albite)	1.22 1.35 1.42	0.02 0.08 0.03	1016 917 873	∼3 Gy	1.32 1.30 1.39	0.03 0.03 0.04	1010 951 890	∼600 Gy
FSM-6	74.4	perthite (orthoclase and albite)	1.32 1.40	0.06 0.05	938 885	∼3 Gy	1.31 1.40	0.05 0.05	945 877	∼400 Gy
FSM-6LH	74.4	sanidine	1.26 1.38	0.04 0.06	982 899	∼3 Gy	1.26 1.36	0.03 0.07	985 910	∼400 Gy
CLBR	0.5	single-phase albite	1.30	0.05	953	∼3 Gy	1.28	0.05	971	

Table 5.2: *Results of excitation spectra with emissions recorded at ~880 nm ($IRPL_{1.41}$) and ~955 nm ($IRPL_{1.3}$). K-FS (%) refers to the K-feldspar content calculated from oxide concentration obtained using XRF. The relative feldspar compositions were obtained using stoichiometry. Et refers to the transition from the ground state of the electron trap to the edge of the conduction band. Data for R28 and K8 are from Kumar et al (2020a).* [1] *The association of R28 as orthoclase is solely based on information given in Poolton et al. (2009), however, these authors do not present any analytical data (i.e. XRD or related).*

Sample ID	K-FS (%)	Phases	$IRPL_{1.41}$			$IRPL_{1.3}$		$IRPL_{1.2}$	
			E_t (eV)	FWHM (eV)	IR res. (eV)	FWHM (eV)	E_t (eV)	FWHM (eV)	E_t (eV)	FWHM (eV)
FSM-13	98.5	single-phase microcline	2.21	0.47	1.45	0.09	2.04	0.24	NA	NA
FSM-13LH	98.5	slightly disordered single-phase microcline	2.16	0.47	1.47	0.11	2.11	0.50	NA	NA
FSM-3	82.5	perthite (microcline and albite)	2.29	0.62	1.44	0.11	2.05	0.22	NA	NA
FSM-14	78.3	perthite (microcline and albite)	2.27	0.44	1.46	0.11	2.04	0.25	NA	NA
FSM-5	74.8	perthite (microcline and albite)	2.46	0.63	1.46	0.14	NA	NA	2.25	0.36
FSM-6	74.4	perthite (orthoclase and albite)	2.20	0.47	1.46	0.12	2.13	0.42	NA	NA
FSM-6LH	74.4	sanidine	2.18	0.51	1.46	0.15	2.20	0.53	NA	NA
CLBR	0.5	single-phase albite	NA	NA	1.47	0.14	2.09	0.35	NA	NA
R28	95	orthoclase[1]	2.31	NA	1.46	NA	2.15	NA	NA	NA
K8	84	microcline perthite (Baril, 2004)	2.18	NA	1.46	NA	2.09	NA	NA	NA

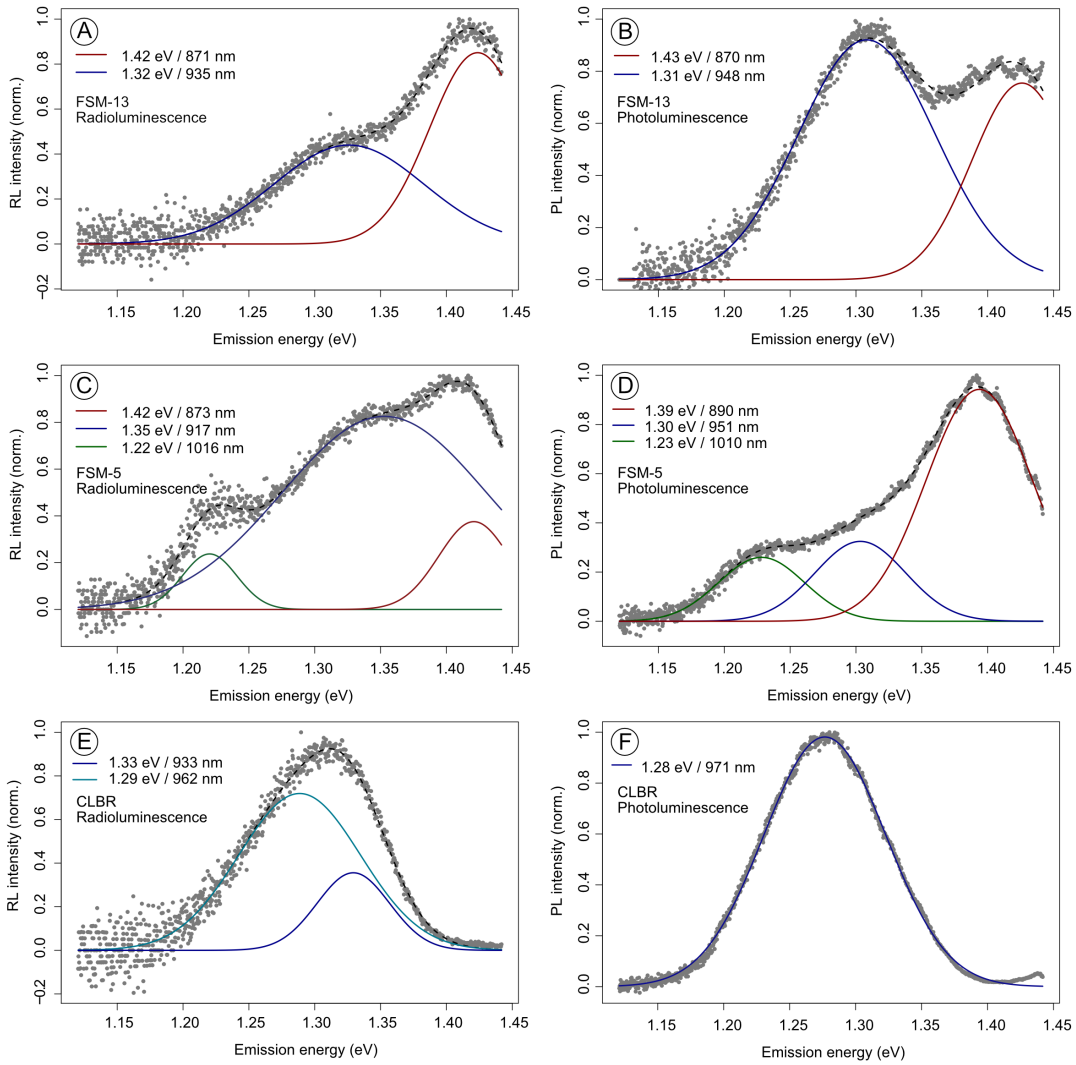

Figure 5.3: *Examples of radioluminescence (A, C, E) and photoluminescence (B, D, F) emission spectra of samples FSM-13 (A, B), FSM-5 (C, D) and CLBR (E, F). The recorded spectra were fitted using up to three Gaussian functions. The mean of the distribution is given in the individual figures for both distributions. Further details of the fit are also presented in Table 5.1. RL and PL emission spectra of the other samples are shown in Figure S5.2 and results of the fitting of those spectra are also given in Table 5.1.*

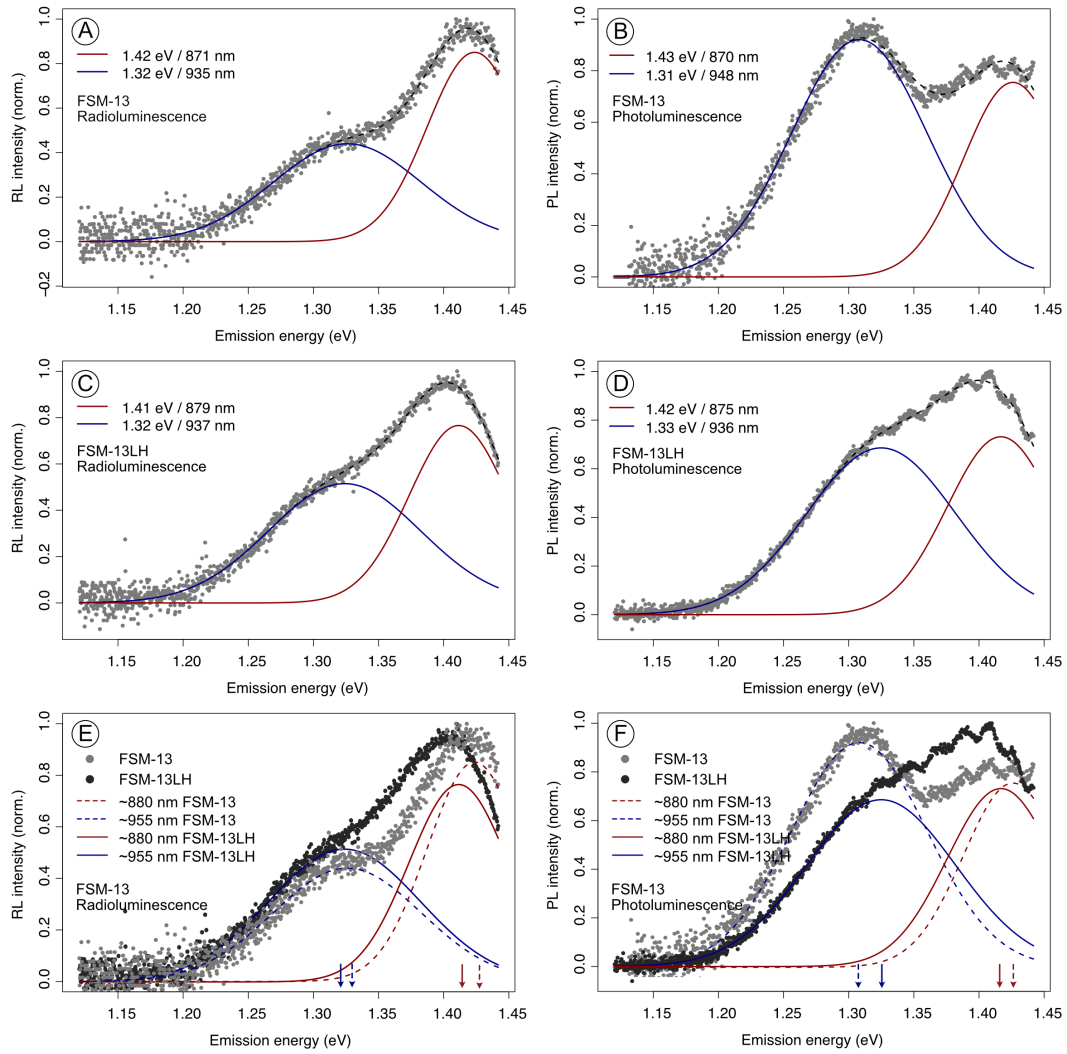

Figure 5.4: *Comparison of RL (A, C, E) and PL (B, D, F) emission spectra of FSM-13 (unheated material) and FSM-13LH (heated material). The emission spectra were fitted using two Gaussian functions and the mean of the obtained distributions is given in the figures. Details of the fit are given in Table 5.1. Figures E and F show a comparison of the RL (E) and PL (F) emission spectra of the heated and unheated material. The dashed lines and light grey points correspond to the unheated material (FSM-13) and the solid lines and dark grey points to the heated material (FSM-13LH). The arrows pointing towards the x-axis show the change in emission peak position for the unheated (dashed line) and heated (solid line) material.*

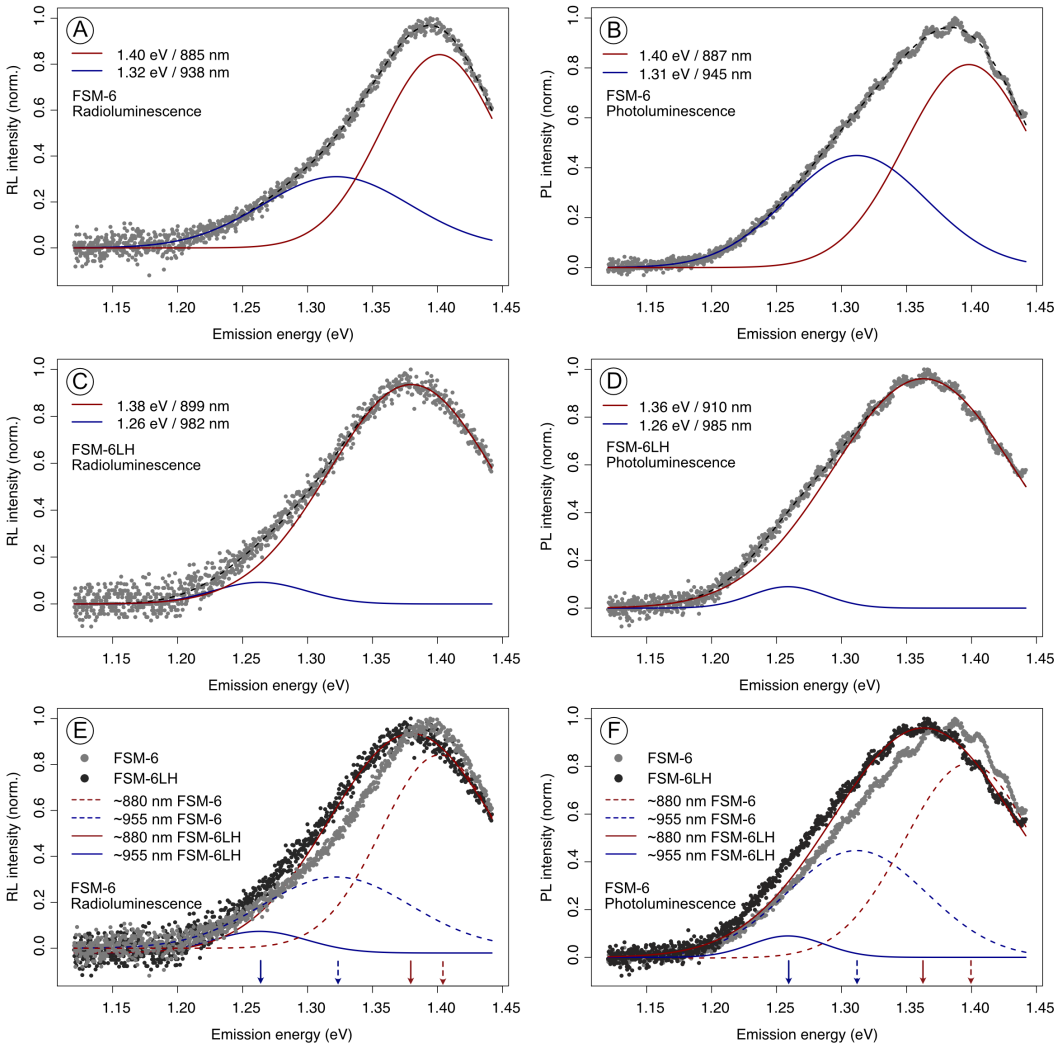

Figure 5.5: *Comparison of RL (A, C, E) and PL (B, D, F) emission spectra of FSM-6 (unheated material) and FSM-6LH (heated material). The emission spectra were fitted using two Gaussian functions and the mean of the obtained distributions is given in the figures. Details of the fit are given in Table 5.1. Figures E and F show a comparison of the RL (E) and PL (F) emission spectra of the heated and unheated material. The dashed lines and light grey points correspond to the unheated material (FSM-6) and the solid lines and dark grey points to the heated material (FSM-6LH). The arrows pointing towards the x-axis show the change in emission peak position for the unheated (dashed line) and heated (solid line) material.*

lower level during bleaching (Fig. S5.1B, D, L, N and P). Interestingly, samples FSM-3 (cryptoperthite, 82.5 % K-feldspar, Fig. 5.2B) FSM-14 (cryptoperthite, 78.3 % K-feldspar) and FSM-5 (macroperthite, 74.8 % K-feldspar, Fig. 5.2C) showed a residual PL signal. For samples FSM-14 and FSM-5, the PL signal with an emission centred around 880 nm ($IRPL_{1.41}$) did not grow further with dose (Figs. 2C, S1H, J). The partially reset $IRPL_{1.41}$ emission in sample FSM-3 grows with dose, but not to the same extent as the $IRPL_{1.3}$ emission (Fig. 5.2B). The 18 hour solar simulator bleach reset the $IRPL_{1.3}$ in most samples, except for FSM-14 (Fig. S5.1H) and FSM-5 (Fig. 5.2C), where a residual remains.

Intensities and energies of IRPL and IR-RL emissions

Kumar et al. (2018, 2020a) showed the presence of two IRPL and IR-RL emissions with peak maxima around 1.3 eV and 1.41 eV in their emission spectra. To investigate the number of emission peaks in the infrared in the present study and whether the emission peaks occur at the same wavelength for all samples, the spectra were fitted in R using the nls function (Bates and DebRoy, 2018), which uses a non-linear least squares approach to iteratively find the most suitable fitting parameters for the given equation. Different numbers of Gaussian functions were fitted to the measured spectra, and the most suitable solution was determined by comparing the residuals between the measured spectra and the obtained fit. It was aimed at describing the spectra with as few Gaussian functions as possible, while keeping the residuals at a minimum. Equation 5.1 represents one Gaussian function, where k is a constant, E the emission energy (in eV), μ the mean energy of the Gaussian distribution (in eV) and σ the standard deviation (in eV). For each sample, the RL spectrum after a dose of ~3 Gy and the PL spectrum after the longest irradiation was chosen for fitting (Table 5.1). The measured emission spectra and corresponding fits are shown in Figure 5.3 for samples FSM-13, FSM-5 and CLBR. Emission spectra for all samples are shown in Figure S5.3.

$$f(E) = k * exp(-\frac{1}{2} * \frac{(E-\mu)^2}{\sigma^2}) \tag{5.1}$$

The number of Gaussian functions used to describe the measured spectra varies between samples, but stays the same within one sample for RL and PL, respectively, with the exception of CLBR. The RL spectrum of CLBR (single phase albite, 0.5 % K-feldspar) can be fitted using two Gaussian functions with

mean energies at 1.29 ± 0.05 eV and at 1.33 ± 0.03 eV (Fig. 5.3E). In contrast the PL spectrum of this sample can only be described by one Gaussian function with a mean energy of 1.28 ± 0.05 eV (Fig. 5.3F). Single phase microcline sample FSM-13 shows RL and PL emission spectra that are described by a sum of two Gaussian functions. In the RL spectrum of FSM-13, the emissions are centred around 1.33 ± 0.06 eV and around 1.42 ± 0.04 eV (Fig. 5.3A), whereas in the PL spectra the emissions are centred at 1.31 ± 0.05 eV and 1.43 ± 0.04 eV (Fig. 5.3B).

Perthitic samples FSM-3, FSM-14 and FSM-6 also show RL and PL spectra that can be described by two Gaussian functions (Fig. S5.2). The peak positions of the emissions are similar to those recorded for FSM-13, with one emission being centred around 1.3 eV and the other around 1.41 eV (Table 5.1). The RL (Fig. 5.3C) and PL (Fig. 5.3D) emission spectra for FSM-5 are different to the other perthites, because they require three Gaussian functions for fitting as opposed to two. In addition to RL and PL emissions around ∼1.4 eV and ∼1.3 eV, a third additional emission is recorded at 1.22 ± 0.02 and at 1.23 ± 0.03 eV for RL and PL, respectively (Fig. 5.3C, D).

The effect of framework disorder on RL and PL emission spectra recorded in the infrared was tested for two samples: one single phase microcline (FSM-13, referred to as FSM-13LH after heating) and one perthite (FSM-6, referred to as FSM-6LH after heating, Figs. 5.4 and 5.5, respectively). Figure 5.4 shows the RL emission spectra for samples FSM-13 (Fig. 5.4A) and FSM-13LH (Fig. 5.4C) and both in direct comparison (Fig. 5.4E). The same is shown for PL emission spectra in Figures 5.4B, D and F, respectively. The RL emission spectrum of the heated sample FSM-13LH, compared to the unheated material (FSM-13) shows only very subtle changes in shape. Both emission peaks are present with similar relative intensities within the RL spectra of FSM-13 and FSM-13 LH (Fig. 5.4E). Fitting of the RL emission peaks results in mean emission energies of 1.33 ± 0.06 eV (FSM-13) and 1.32 ± 0.06 eV (FSM-13LH) and of 1.42 ± 0.04 eV (FSM-13) and 1.43 ± 0.04 eV (FSM-13LH). In contrast, the PL emission spectrum of heated sample FSM-13LH, compared to FSM-13, shows changes in shape and in the relative intensities of the two identified emission maxima. Whilst in the PL spectrum of FSM-13 the $IRPL_{1.3}$ emission is more prominent, the $IRPL_{1.41}$ emission is the dominant emission in the spectrum of the heated sample FSM-13 (Fig. 5.4F). The peak maxima are found at 1.31 ± 0.05 eV and 1.43 ± 0.04 eV for FSM-13 and at 1.32 ± 0.06 eV and 1.42 ± 0.04 eV for the heated sample

FSM-13LH (Fig. 5.4F).

For FSM-6 and the heated material of FSM-6LH, a first visual examination of the shapes of the RL and PL emission spectra (Figs. 5E, F) does not indicate any significant changes, however, fitting of the RL and PL emission spectra reveals differences in relative intensities and the mean energy of the fitted Gaussian distributions: In the case of RL (Fig. 5.5E) and PL (Fig. 5.5F), the relative intensity of the fitted 1.3 eV emission decreases when comparing the unheated material (FSM-6) to the heated material (FSM-6LH). Whilst the mean energy of this emission is found at 1.32 ± 0.06 eV in the RL emission spectrum of FSM-6, it apparently shifts to 1.26 ± 0.04 eV in the spectrum of heated sample FSM-6LH (Fig. 5.5E). Similarly, in PL emission spectra of FSM-6 and FSM-6LH (Fig. 5.5F) the $IRPL_{1.3}$ emission occurs at 1.31 ± 0.05 eV and at 1.26 ± 0.03 eV, respectively. The higher energy ∼1.41 eV RL emission occurs at 1.40 ± 0.05 eV in FSM-6 consistent with 1.38 ± 0.06 eV in FSM-6LH. Similarly, in PL this emission ($IRPL_{1.41}$) peaks at 1.40 ± 0.05 eV in FSM-6 (unheated) and at 1.36 ± 0.07 eV FSM-6LH (heated) (Fig. 5.5F).

5.4.2 Excitation spectra

IRPL excitation spectra recorded from ∼1.4 eV to ∼2.6 eV for all samples reveal excitation peaks in the infrared (∼1.45 eV, peak 1 in Fig. 5.6A) and in the yellow to blue region (1.9 to 2.5 eV, peak 2 in Fig. 5.6) for $IRPL_{1.3}$ and $IRPL_{1.41}$ emissions, and additionally for the $IRPL_{1.2}$ emission in FSM-5 only. The excitation peak in the infrared was fully characterised for the $IRPL_{1.3}$ emission, but not to its full extent for the $IRPL_{1.41}$ emission, due to instrumental limitations.

The excitation peak in the IR has first been observed in alkali feldspar excitation spectra recorded with the emission in the UV by Hütt et al. (1988) and has been described as the IR resonance peak. This peak is marked as peak 1 and IR resonance peak in Figure 5.6A. Kumar et al. (2020a) described a second excitation peak, denoted as peak 2, in IRPL excitation spectra of chemically different feldspars. The range of excitation energy at which peak 2 was observed by Kumar et al. (2020a) overlaps with the values of trap depth obtained using UV signals by Kars et al. (2013) and Riedesel et al. (2019) for a range of chemically different feldspars. Based on the comparison with these earlier studies, and measurements and analyses of an UV excitation spectrum of their samples, Kumar et al (2020a) concluded that peak 2 in their IRPL excitation spectra reflects the

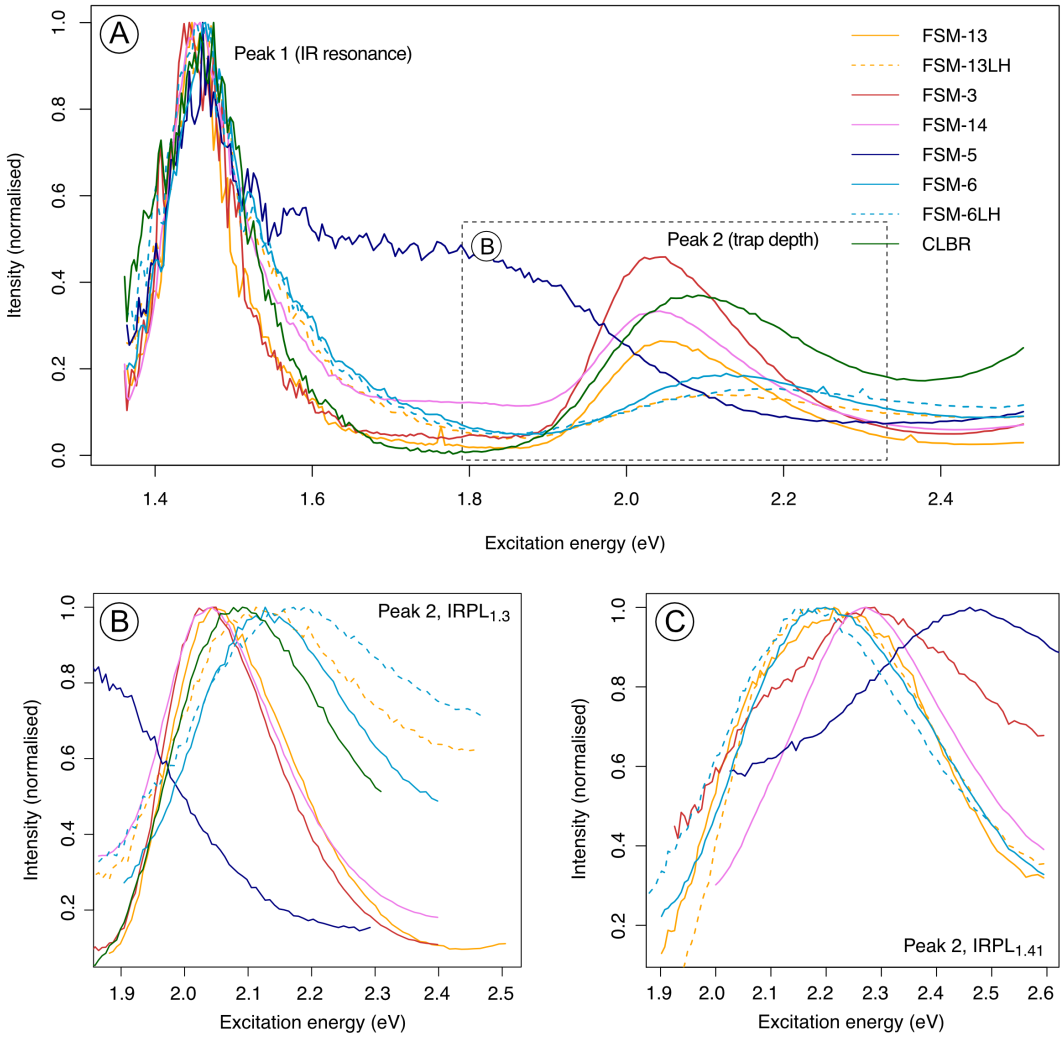

Figure 5.6: *A) Excitation spectra of all samples investigated recorded with excitation energies ranging from ∼1.36 to ∼2.51 eV. The emission was recorded at 1.3 eV ($IRPL_{1.3}$). Data have been normalised to the intensity of the IR resonance peak at ∼1.45 eV. The dashed box indicates the excitation energy range isolated for B. B) Close-up of excitation peak 2 from $IRPL_{1.3}$ excitation spectra. C) Close-up of excitation peak 2 from $IRPL_{1.41}$ excitation spectra. The full $IRPL_{1.41}$ excitation spectra for all samples are shown in Fig. S5.3. Since single phase albite CLBR does not show an $IRPL_{1.41}$ emission, no excitation spectrum of this sample is displayed in C. Macroperthite FSM-5 also shows an emission at 1.2 eV, but for simplification excitation spectra recorded for this emission are not displayed in this figure, but can be found in Figure 5.7C and D.*

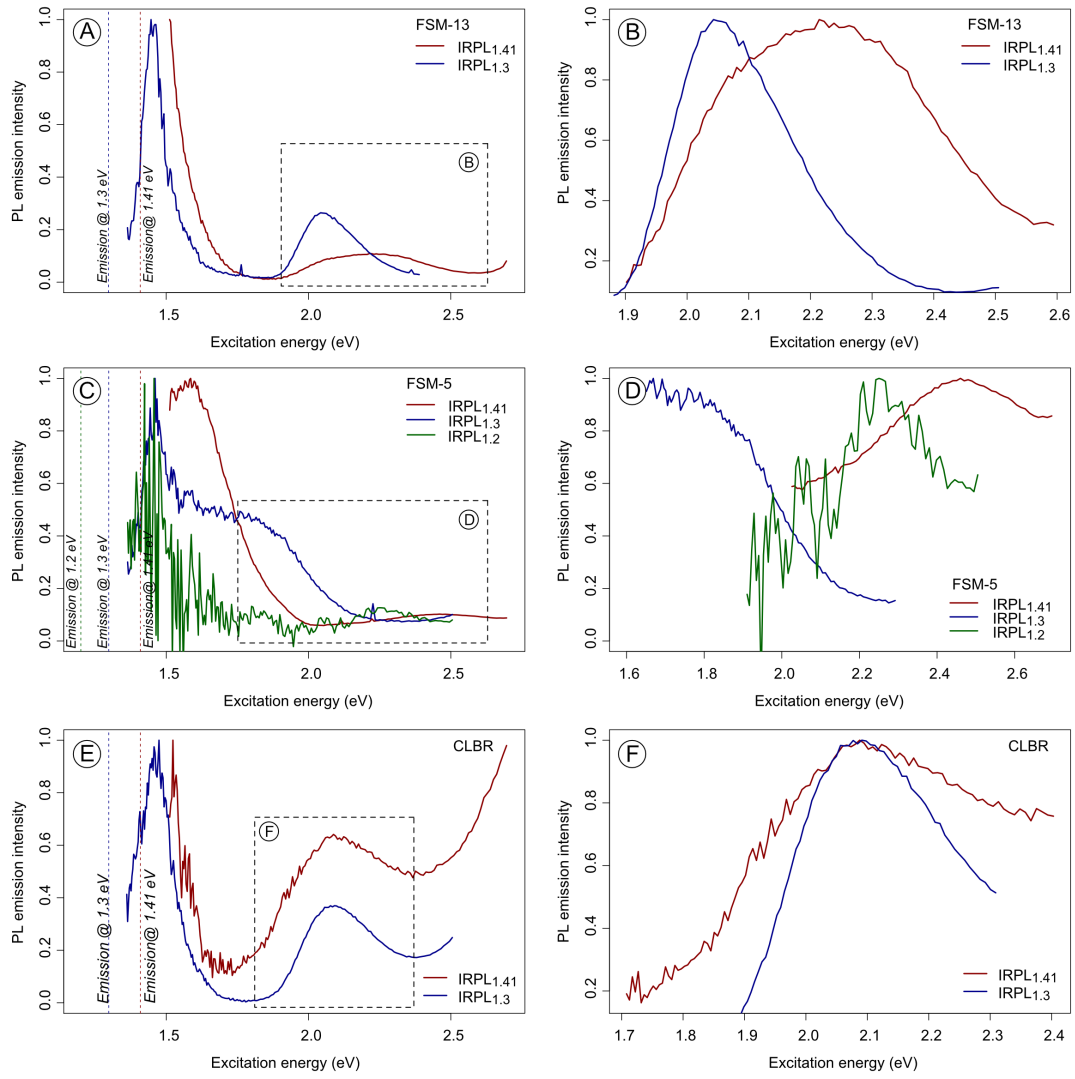

Figure 5.7: *Selected examples of excitation spectra for the $IRPL_{1.41}$ and $IRPL_{1.3}$ nm emissions of samples FSM-13 (A, B), FSM-5 (C, D) and CLBR (E, F). The graphs were normalised to the point of highest signal intensity. For figures B, D and F, excitation peak 2 was isolated and normalised separately. These graphs were used to obtain the trap depth, by picking the point of highest intensity for the individual curves. The thus obtained mode (in eV and µm) are given in Table 5.2 for all samples and excitation spectra measured for all samples can be found in Figure S5.3. The emission window is indicated in A, C and E with dashed vertical lines.*

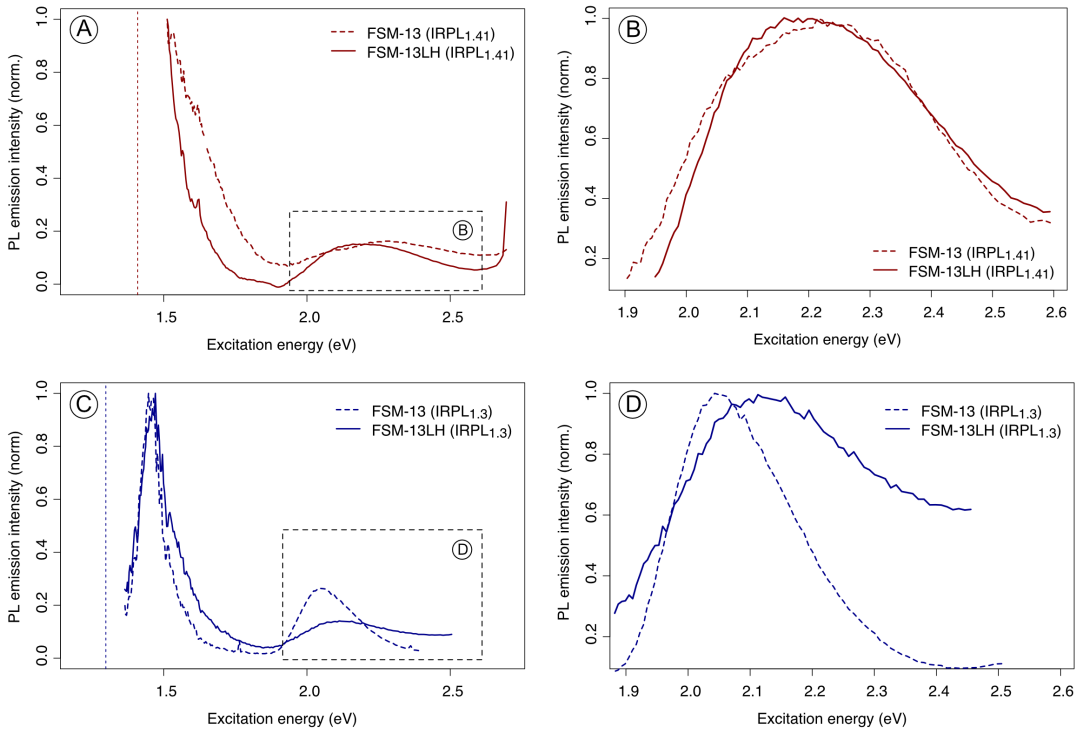

Figure 5.8: *Excitation spectra of samples FSM-13 (unheated material, dashed line) and FSM-13LH (heated material, solid line) in comparison for the $IRPL_{1.41}$ emission A and B) and the $IRPL_{1.3}$ emission (C and D). A and C show the complete excitation spectra measured for both samples and both emissions. The graphs were normalised to the highest intensity. B and D focus on a comparison of excitation peak 2. For these two graphs this excitation peak was isolated and then the spectra were normalised to the highest intensity.*

electron transition from the ground state of the electron trap to the conduction band and thus describes the trap depth of the electron trap (Kumar et al., 2020a).

Trap depth

Following the approach by Kumar et al. (2020a) we investigate sample-to-sample variations in shape and position of excitation peak 2 in order to obtain information on the electron trap depths in the samples investigated. Figure 5.6 enables a comparison between the position and shape of peak 2 of all samples investigated, and Figure 5.7 allows a comparison of peak 2 recorded in $IRPL_{1.3}$ and $IRPL_{1.41}$ excitation spectra for selected samples FSM-13, FSM-5 and CLBR. Excitation spectra for both emissions and all samples are shown in Figure S5.3. Besides qualitative descriptions, we quantify potential variations in peak 2, and thus the trap depth, by selecting the excitation energy at which peak 2 has its highest IRPL emission intensity. Since the spectra were recorded with a measurement resolution of 2 nm, we are able to determine the peak position with a precision

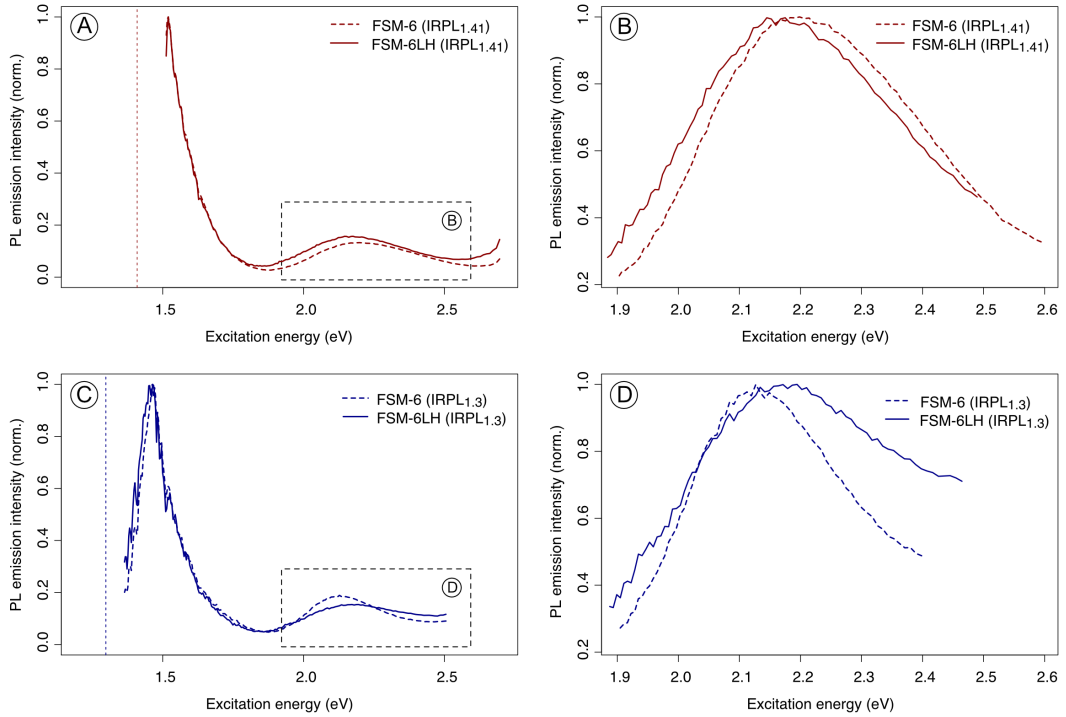

Figure 5.9: *Excitation spectra of samples FSM-6 (unheated material, dashed line) and FSM-6LH (heated material, solid line) in comparison for the $IRPL_{1.41}$ emission (A and B) and the $IRPL_{1.3}$ emission (C and D). A and C show the complete excitation spectra measured for both samples and both emissions. The graphs were normalised to the highest intensity. B and D focus on a comparison of excitation peak 2. For these two graphs this excitation peak was isolated and then the spectra were normalised to the highest intensity.*

of at least ± 0.02 eV, since this is the largest step in energy space observed from the excitation energy range measured. However, this estimate is only based on the measurement resolution. To enable a comparison of the width of the peaks, the full width half maximum (FWHM) of peak 2 was calculated and results are given in Table 5.2 and Figure 5.10B.

Figures 5.6B and 5.6C show variations in the shape of peak 2 and in the position of the maximum intensity. Peak 2 and thus the trap depth for $IRPL_{1.3}$ varies between 2.04 eV (FSM-13 and FSM-14) and 2.20 eV (FSM-6LH), and from 2.16 eV (FSM-13LH) to 2.46 eV (FSM-5) for $IRPL_{1.41}$ (Table 5.2, Fig. 5.6B, C). The width (FWHM) of peak 2 varies from 0.22 eV (FSM-3) to 0.53 eV (FSM-6LH) for $IRPL_{1.3}$ and from 0.44 eV (FSM-14) to 0.63 eV (FSM-5) for $IRPL_{1.41}$ (Table 5.2, Fig. 5.6B, C.)

The $IRPL_{1.3}$ excitation spectra of single phase albite CLBR shows a trap depth of 2.09 eV (FWHM: 0.35 eV; Fig. 5.7F). No trap depth was calculated for the $IRPL_{1.41}$ emission, since the luminescence recorded is identified as the tail of

the $IRPL_{1.3}$ emission, thus a calculated trap depth would only reflect the depth of the trap responsible for the $IRPL_{1.3}$ emission. Single phase microcline FSM-13 (Fig. 5.7A) has an optical trap depth of 2.21 eV (FWHM of 0.47 eV) for $IRPL_{1.41}$ and a shallower trap depth of 2.04 eV (FWHM of 0.24 eV) for $IRPL_{1.3}$.

All perthitic samples show a similar pattern as FSM-13, where the trap depth is shallower for $IRPL_{1.3}$, compared to $IRPL_{1.41}$ (Table 5.2, Figure 5.10B). In the perthitic samples the trap depth for $IRPL_{1.41}$ ranges from 2.20 eV in FSM-6 (FWHM of 0.47 eV, Figs. 9B, D) to 2.46 eV in FSM-5 (FWHM of 0.63 eV, Figs. 7C, D) and for $IRPL_{1.3}$ from 2.05 eV (FSM-3, FWHM of 0.22 eV) to 2.13 eV (FSM-6, FWHM of 0.42 eV). Macroperthite FSM-5 does not show a peak between 2 eV and 2.5 eV in $IRPL_{1.3}$ excitation spectra, but rather a shoulder on the IR resonance peak is seen which stretches up to ∼2.1 eV (Fig. 5.7C). Thus, a trap depth cannot be defined for the $IRPL_{1.3}$ centre of FSM-5. FSM-5 is also different to other samples because a third emission ($IRPL_{1.2}$) was found in the excitation spectra of FSM-5 (Fig. 5.7C and D). Although the spectrum is less intense for an emission at 1.2 eV, both excitation peaks are recognisable and fully characterised. Excitation peak 2 occurs at lower excitation energy (2.25 eV) in case of IRPL1.2, compared to $IRPL_{1.41}$, where a trap depth of 2.46 eV is measured.

The $IRPL_{1.3}$ and $IRPL_{1.41}$ excitation spectra of the two samples used in the heating experiment (FSM-13LH and FSM-6LH; see section 3.1 for details) show subtle changes compared to the excitation spectra of the unheated counterparts (single phase microcline FSM-13 and perthite FSM-6, cf. Figs. 8 and 9). Figure 5.8 shows the excitation spectra of heated sample FSM-13LH, in comparison to the unheated sample material (single phase microcline FSM-13). The $IRPL_{1.41}$ excitation spectra of FSM-13 and FSM-13LH are relatively similar, with a slight shift of the entire excitation spectra towards lower energy from the ordered specimen FSM-13 to the disordered sample FSM-13LH (Fig. 5.8A). Trap depths associated with the $IRPL_{1.41}$ emission are 2.21 eV for FSM-13 compared to 2.16 eV for FSM-13LH (Fig. 5.8B). In case of the $IRPL_{1.3}$ excitation spectra of FSM-13 and FSM-13LH the obtained trap depths are 2.04 eV (FSM-13) and 2.11 eV (FSM-13LH, Fig. 5.8D), respectively, and the FWHM change from 0.24 eV in the unheated sample FSM-13 to 0.50 eV in the heated sample FSM-13LH. Additionally, a change in relative intensity between the IR resonance peak and excitation peak 2 is observed for $IRPL_{1.3}$: peak 2 has an intensity of ∼30 % and ∼10 % of the corresponding IR resonance peaks in the unheated and heated materials,

respectively.

The comparison of $IRPL_{1.3}$ and $IRPL_{1.41}$ excitation spectra measured for perthitic sample FSM-6 and the heated material of FSM-6LH are shown in Figure 5.9. Whilst the IR resonance peak for $IRPL_{1.3}$ and $IRPL_{1.41}$ remains largely identical between the heated and unheated sample material, excitation peak 2 changes slightly for both emissions recorded. The maximum of peak 2 in the $IRPL_{1.41}$ excitation spectra is recorded at 2.20 eV for FSM-6 and at 2.18 eV for FSM-6LH (Fig. 5.9B). For the $IRPL_{1.3}$ emission the position of the highest intensity of peak 2 is recorded at 2.13 eV for FSM-6 and at 2.20 eV for FSM-6LH. Additionally, peak 2 is 0.11 eV wider in case of $IRPL_{1.3}$ excitation spectra of FSM-6LH compared to FSM-6 (Fig. 5.9D).

IR resonance peak

The IR resonance peak is thought to reflect an excited state of an electron trapping centre in feldspar (Hütt et al., 1988; Bailiff and Poolton, 1991; Poolton et al., 1995). The IR resonance peak is fully characterised in $IRPL_{1.3}$ excitation spectra of all samples, which allows for a quantification of the resonance energy, by selecting the IR resonance peak maximum and by calculating the FWHM of this peak (Table 5.2). For this purpose, the data was smoothed by calculating a running average of three data points. From the smoothed data the maximum peak intensity was selected as peak position and the FWHM of the smoothed peak was calculated. A direct sample-to-sample comparison of the IR resonance peak (unsmoothed data) shows only little variation in the shape and peak position (Fig. 5.6A), compared to the variation observed for excitation peak 2 for $IRPL_{1.3}$ excitation spectra (Fig. 5.6B) and $IRPL_{1.41}$ excitation spectra (Fig. 5.6C). Also, the from the smoothed data identified IR resonance peak position vary from 1.45 eV (FSM-3, FSM-14) to 1.47 eV (FSM-6LH) and the FWHM varies from 0.08 eV (FSM-13) to 0.15 eV (CLBR).

5.5 Discussion

Previous studies have suggested different locations for electron trapping centres in feldspars: substitution of Pb^{2+} for K^{+} on M sites (Erfurt, 2003), occupancy of tetrahedral sites of the Si,Al-framework (Short, 2004), or occupancy of an unknown lattice site, but located in two different crystallographic environments (Kumar et al., 2018, 2020a). However, these studies were conducted on a lim-

ited number of feldspar samples, covering a narrow chemical range, or on grain mixtures extracted from sediment, which likely contain grains of different geological origin and different chemical composition. With this paper and the samples

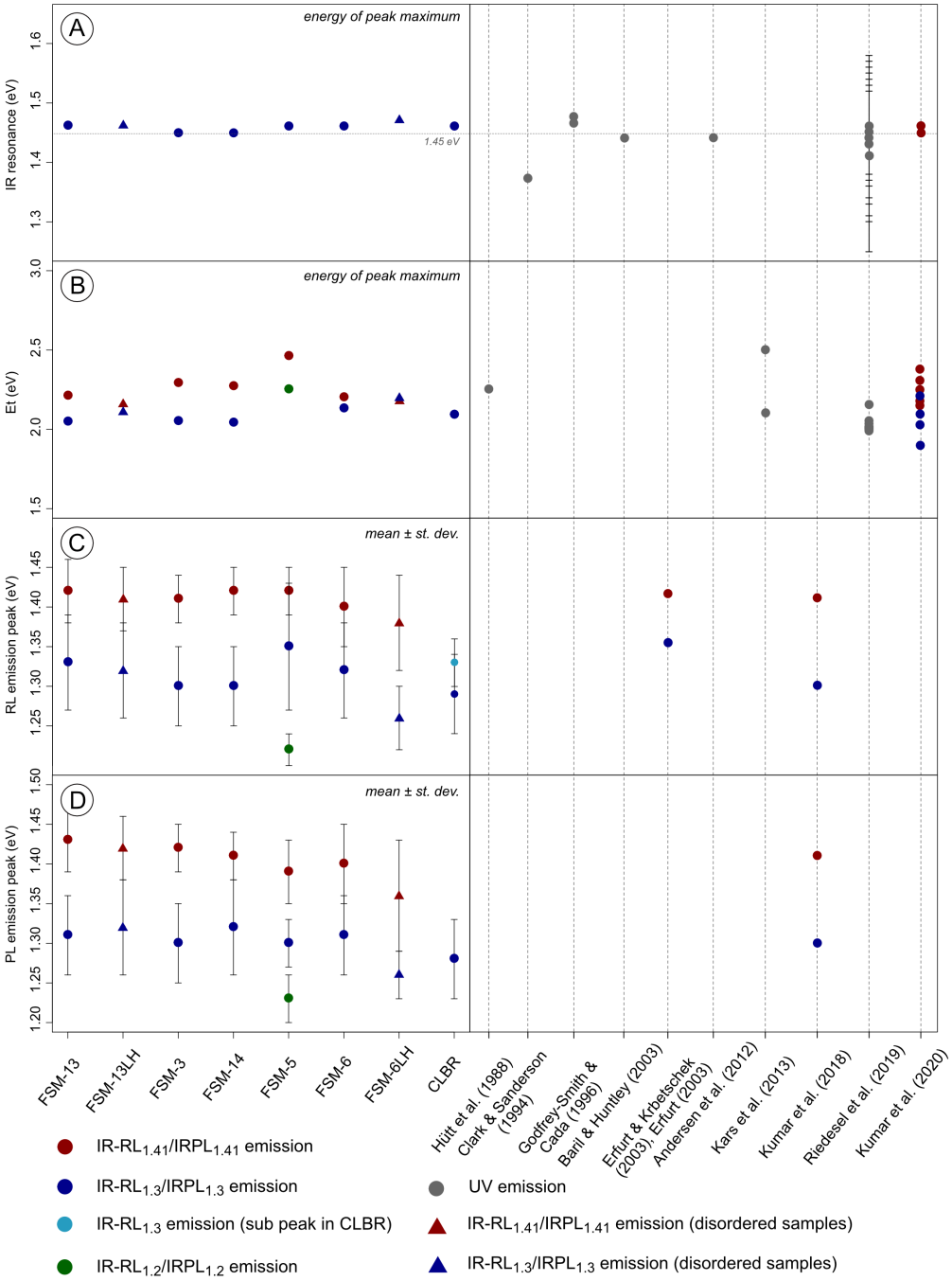

Figure 5.10: *(see next page)*

Figure 5.10* (previous page)*: *Summary figure of results presented in this paper in comparison with selected published results. For Hütt et al. (1988), Baril and Huntley (2003) and Andersen et al. (2012) examples of their experimental results were picked (n = 1). Baril and Huntley (2003) and Andersen et al. (2012) fitted the IR resonance peak in their excitation spectra with various equations or multiple Gaussian distributions. Thus a comparison of the numerical values obtained by these authors and the data measured in the present paper is difficult. For this reason only examples of one sample each were picked and uncertainties are not displayed in the case of Baril and Huntley (2003) and Andersen et al. (2012). For Clark and Sanderson (1994) only their measurement of F1 reference feldspar using a halogen lamp is displayed. Godfrey-Smith and Cada (1996) identify the IR resonance peak centred around 840 nm (∼1.48 eV) in nearly pure Na-feldspar end members and around 845 nm (∼1.47 eV) in microcline, plagioclase and in feldspars extracted from sediments. The data points related to Kars et al. (2013, n = 2) and Riedesel et al. (2019, n = 17) are based on fitting a rising continuum in excitation spectra using the equation for the photo-ionisation cross-section (Bøtter-Jensen et al., 2003). Kars et al. (2013) did not provide uncertainties for their trap depth values. The uncertainties provided on the trap depth by Riedesel et al. (2019) represent only uncertainties on the fit, not on the trap depth. Riedesel et al. (2019) fitted the IR resonance peak with a single Gaussian distribution, subsequently the values presented in this figure represent the mean and standard deviation of this fit. Kumar et al. (2020a) obtained the trap depth for the excitation spectra recorded in the infrared by picking the highest point of a specific excitation peak (n = 6). These authors provide an uncertainty of 0.02 eV on all trap depth values. For the IR resonance peak position Kumar et al. (2020a) give results for the emission recorded at 1.3 eV. No uncertainties on the peak position of the six samples investigated are given.*

investigated we contribute to the growing body of knowledge on electron trapping centres in feldspars by investigating a suite of single crystal feldspars that span the entire alkali feldspar solid solution, including K- and Na-feldspar end members, and the results are discussed below.

5.5.1 Sample-dependent variations in IRPL and IR-RL emission spectra

Erfurt (2003) and Erfurt and Krbetschek (2003) observed IR-RL emissions at 1.36 eV (910 nm) and at 1.43 eV (865 nm) in a single crystal feldspar and in feldspars extracted from sediment. Kumar et al. (2018) measured emission energies of 1.3 eV (955 nm) and 1.41 eV (880 nm) in the IR-RL and IRPL emission spectra of their alkali feldspars in single crystal feldspars and sediment extracts. IR-RL and IRPL emission energies measured in this paper are within the range of emission energies observed by Erfurt (2003), Erfurt and Krbetschek (2003) and Kumar et al. (2018, 2020a), but slightly more consistent with the results of Kumar et al. (2018, 2020a). This closer agreement with the results in the present study and those by Kumar et al. (2018, 2020a) might indicate a slight dependency of the measurement results on the measurement conditions; the instrument used here is the same as used by Kumar et al. (2018, 2020a).

Our IRPL and IR-RL emission spectra show that emissions centred around 1.3 eV are present in all samples investigated. Similar observations were made for the IRPL and IR-RL emissions centred around 1.41 eV, except the emission is absent in our only single phase albite CLBR (which only contains 0.5 % K-feldspar). The IR-RL emission spectrum of CLBR can be fitted using the sum of two Gaussian functions, however both fitted Gaussian distributions are centred around 1.3 eV (Table 5.1, Fig. 5.3E). The IRPL emission spectrum of CLBR can only be described with a single Gaussian function centred at ∼1.3 eV (Table 5.1, Fig. 5.3F). It is interesting to note that both of the ordered single phase samples (FSM-13 and CLBR) show an IRPL and IR-RL emission centred around 1.3 eV, but only the ordered single phase microcline (FSM-13) shows an emission at ∼1.41 eV (cf. Fig. 5.3A, B and Fig. 5.3E, F). The difference between these two ordered single phase single crystal feldspars is their chemical composition: Whilst single phase microcline sample FSM-13 contains 98.5 % K-feldspar, single phase albite (CLBR) contains only 0.5 % K-feldspar; this potentially suggests that the 1.3 eV emission is independent of the cation on M sites in the crystal, whereas the 1.41 eV emission might be linked to the presence of K^+ ions on M sites. However, we can only base this on the measurement of these two alkali feldspar end member samples and further research is necessary to validate our results. Additionally, it should be noted here that, in contrast to our results, Kumar et al. (2020b), who used a cathodoluminescence attachment to a scanning electron microscope, found that cathodoluminescence emissions in the IR at ∼1.3 eV are more prominent in K-rich feldspar grains, compared to K-poorer grains. Despite opposite trends, results by Kumar et al. (2020b) and presented here indicate that the suggestion by Erfurt (2003) of electron trapping centres being created on M sites due to the substitution of K^+ ions by Pb^{2+} ions might not hold true. Both, Kumar et al. (2020b) and we in this present study, show that at least one IRPL emission is independent of the M site cation occupancy, whilst Erfurt (2003) linked both emissions to the same defect type on M sites. It is also interesting to note that macroperthite FSM-5 (74.8 % K-feldspar) is the only sample which shows an additional PL and RL emission at ∼1.2 eV, which also indicates that additional factors, other than the M site cation occupancy, influence electron trapping centres in feldspars.

When comparing sample-to-sample variations in 1.3 eV and 1.41 eV IRPL and IR-RL emissions, we do not observe significant differences between the IR-RL and IRPL emission energies for a sample, or when comparing all the samples

investigated here (Table 3, Fig. 5.10C, D). Furthermore, even in the case of the unheated and heated sample pairs, only small changes in emission peak energy were observed (Fig. 5.4 for FSM-13/FSM-13LH, Fig. 5.5 for FSM-6/FSM-6LH). An absolute comparison of IRPL signal intensities of the unheated and heated sample pairs cannot be conducted, because it was not possible to fix an exact sample mass on the cold finger. However, even when comparing the recorded IRPL intensities of FSM13/FSM-13LH and FSM-6/FSM-6LH (data not shown) no obvious trends could be observed. This suggests that the IRPL and IR-RL emissions centred at 1.3 eV and 1.41 eV are largely unaffected by changes to the tetrahedral site occupancy of Al^{3+} ions. This is interesting, as disordering Al^{3+} ions on the framework of samples FSM-13LH and FSM-6LH resulted in a significant increase of the blue luminescence emission (∼410 nm), a change in the TL curve shape, particularly of the blue emission, and increased the fading rate of the blue IRSL signal (Riedesel et al., 2021). Thus, whilst the recombination centres related to the blue emission are highly affected by framework disorder, most likely due to their location on Al-O-Al bridges (Finch and Klein, 1999; Riedesel et al., 2021), the electron trapping centres seem to be relatively independent from the degree of framework disorder in feldspars.

Since the IRPL signal is intended for use in luminescence dating, the optical resetting of the $IRPL_{1.3}$ and $IRPL_{1.41}$ emissions is of importance for studies constraining the feldspar sample's last exposure to light. Kumar et al. (2020a) analysed a single feldspar sample separated from sediment (R47) and found that irrespective of the light source used for bleaching (405 nm, 470 nm or 880 nm LEDs, or a SOL2 solar simulator), the IRPL emission centred around ∼1.41 eV depletes more slowly than the emission around 1.3 eV. After 24 hours exposure to the SOL2, their signals had fallen to ∼5 % for the 1.3 eV emission and between 5 % and 10 % for the 1.41 eV emission. Duller et al (2020) studied bleaching of the $IRPL_{1.3}$ signal. They used feldspars separated from a dune sand and found that the $IRPL_{1.3}$ signal fell to ∼3 % after bleaching using a 1 W 365 nm LED for 5.5 hours. From our experiments it is evident that the two IRPL emission peaks respond differently to solar simulator bleaching. Whilst the $IRPL_{1.3}$ emission (and the $IRPL_{1.2}$ emission for sample FSM-5) is completely reset by an 18 hour solar simulator bleach for most samples (Figs. 5.2A, S5.1), the extent to which the $IRPL_{1.41}$ emission bleaches varies significantly between samples (Fig. 5.2B, C). These results suggest that the extent of IRPL signal depletion is sample dependent, and this may have significant implications for the application of

IRPL for dating and strengthen the need for single grain IRPL analyses (Duller et al. 2020). However, further and more detailed bleaching experiments of chemically and structurally well-constrained samples are necessary to be able to link variations in signal depletion with physical properties of the samples.

5.5.2 Variations in excitation spectra of alkali feldspars

Our $IRPL_{1.3}$ and $IRPL_{1.41}$ excitation spectra revealed differences in the position of excitation peak 2, which was interpreted as reflecting the trap depth following Kumar et al. (2020a). For all our samples we observed a larger trap depth related to the $IRPL_{1.41}$ emission, compared to the $IRPL_{1.3}$ emission. The trap depth of the $IRPL_{1.3}$ trapping centre varies from 2.04 eV (FSM-13 and FSM-14) to 2.20 eV (FSM-6LH) and for the $IRPL_{1.41}$ trapping centre from 2.16 eV (FSM-13LH) to 2.46 eV (FSM-5). The trap depths obtained here are similar to those measured by Kumar et al. (2020a). These authors also observed smaller trap depths for the $IRPL_{1.3}$ centre compared to the $IRPL_{1.41}$ centre and respective trap depths varied from 1.90 eV to 2.21 eV and from 2.18 eV to 2.38 eV, for $IRPL_{1.3}$ and $IRPL_{1.41}$, respectively. When comparing our $IRPL_{1.3}$ and $IRPL_{1.41}$ trap depth values and those presented by Kumar et al. (2020a), we do not observe any trends in trap depth with chemistry of the samples, e.g. K-feldspar content (Fig. 5.10B, Table 5.2). However, the absence of the $IRPL_{1.41}$ emission in our single phase albite CLBR (0.5 % K-feldspar) potentially suggests that the $IRPL_{1.41}$ trapping centre is related to the presence of K^+ ions on M sites and that a certain number of K^+ ions have to occupy M sites to enable the presence of the $IRPL_{1.41}$ trapping centre in feldspars.

Artificial framework disorder (produced by laboratory heating of a sub-sample of samples FSM-13LH and FSM-6LH) influences the trap depth of both centres slightly, and in both samples the $IRPL_{1.3}$ trapping centres seems to be affected more, compared to the $IRPL_{1.41}$ trapping centre (Fig. 5.8B, C and Fig. 5.9B, C). Additionally, the FWHM of excitation peak 2 increases in the heated samples (FSM-13LH and FSM-6LH) compared to the unheated material (FSM-13 and FSM-6, Fig. 5.8 and 9), especially in the case of $IRPL_{1.3}$ excitation spectra. Since the rising limb of the peak was suggested to be related to the optical transitions in the band tail states (Prasad et al., 2017; Kumar et al., 2020a), the increase in the peak width for the heated samples may suggests that disordering the Al,Si-framework changes the band-tail width. This interpretation is consistent with the

suggestion of band tail states being associated with variations in bonding angles in the lattice (Poolton et al., 2002a). Artificial disordering of the framework in our samples potentially influences the bonding angles within the crystal and results in a change in symmetry as a consequence of the re-distribution of Al^{3+} ions within the crystal (e.g. Goldsmith and Laves, 1954; Stewart and Ribbe, 1969; Deer et al., 2013, p. 256-257). The presence of sub-conduction band-tail states could also explain why excitation peak 2 is much wider, compared to the width of the IR resonance peak (cf. Table 5.2). Alternatively, it could be considered that the large width of peak 2 could potentially reflect a distribution of ground state energies for this type of electron trapping centre. It has been argued previously that luminescence from feldspars arises due to a distribution of ground state energies of electron trap(s) (e.g. Strickertsson, 1985; Garcia-Guinea et al., 2003), however, these suggestions are mainly based on analyses of thermoluminescence curve shapes.

Beside the trap depth, $IRPL_{1.3}$ excitation spectra also reveal information on the IR resonance peak. From $IRPL_{1.3}$ excitation spectra we obtained the IR resonance peak position with a mean energy of 1.46 ± 0.01 eV. These results are in good agreement with previous work (e.g. Fig. 5.10A; Hütt et al., 1988; Clark and Sanderson, 1994; Godfrey-Smith and Cada, 1996; Baril and Huntley, 2003; Andersen et al., 2012; Riedesel et al., 2019). In accordance with Bøtter-Jensen et al. (1994) we observed similar IR resonance peak positions and shapes for the K- and Na-feldspar end members.

Interestingly, whilst we observed changes in trap depth between samples, the IR resonance peak is invariant between samples (Figs. 5.6A and 5.10A, Table 5.2). Assuming a simple hydrogen model (eq. 5.2) to be applicable for feldspars, Poolton et al. (2002b) predicted a ground state energy (n = 1) of 1.97 eV from the conduction band edge and a transition from the ground state to the excited state (1s → 2p optical transition) of 1.48 ± 0.04 eV, both of which are based on the same variables for the effective electron mass ($m_e^* = (0.79 \pm 0.02)m_e$, Poolton et al., 2001) and the relative permittivity of the material of $\epsilon r = 2.33$ (for Na-feldspar end member, Keller, 1966).

$$E_n = -\frac{2\pi^2 m_e^*}{h^2}[\frac{e^2}{4\pi\epsilon_0\epsilon_r}]^2(\frac{1}{n^2}) \tag{5.2}$$

For a given trap depth, we can predict the excited state (n = 2) in our samples using equation 5.2. The first part of equation 5.2 represents the trap depth (Et). Thus, equation 5.2 can be rewritten as:

$$E_n = -E_t(\frac{1}{n^2}) \tag{5.3}$$

As an example: FSM-6 ($IRPL_{1.3}$ centre) has a trap depth of $E_t = 2.13$ eV and an IR resonance peak at 1.46 eV. Using equation 5.3 and $E_t = 2.13$ eV (n = 1), the excited state (n = 2) is calculated to be located at 1.60 eV above the ground state. The discrepancy of 0.14 eV between model predictions and experimental observation could either indicate the limitation of this simple model to extract precise energies, and/or the limitation of our interpretation of peak 1 and peak 2 in terms of the excited and ground state of the trap. In addition to developing a refined model, resolving this discrepancy requires a better understanding of whether peak 2 represents a single trap depth or a distribution of trap depths where each defect is influenced by its local crystal field. Further investigations of this aspect necessitate spatially resolved excitation spectra measurements, ultimately at the scale of a single defect. IRPL because of its non-destructive nature potentially makes such measurements possible for the first time.

5.6 Conclusion

In this paper we investigated potential causes of variations seen in IRPL and IR-RL emission spectra and in IRPL excitation spectra of chemically and structurally different single crystal alkali feldspars. We applied the novel site-selective method of IRPL excitation-emission spectroscopy (Kumar et al., 2020a) to link occurrences and characteristics of the two IRPL trapping centres ($IRPL_{1.3}$ and $IRPL_{1.41}$ trapping centre) with mineralogical properties of the samples.

For our chemically and structurally different samples we observed IRPL and IR-RL emissions at 1.2 eV, 1.3 eV and at 1.41 eV, and the mean emission energies are similar in IR-RL and IRPL within a sample. We observed sample-dependent variations in emission peak occurrences, emission peak energies, as well as in the trap depth of the $IRPL_{1.3}$ and $IRPL_{1.41}$ centres. Our results suggest that the $IRPL_{1.41}$ trapping centre and related $IRPL_{1.41}$ and $IR\text{-}RL_{1.41}$ emissions may be linked to the presence of K^+ ions on M sites in the crystal. In contrast, the $IRPL_{1.3}$ trapping centre and related emissions are independent of the chemical composition of the crystal, likely excluding M sites as potential host lattice sites for electron trapping centres in feldspars. Whilst previous research on the same samples revealed significant changes to the blue luminescence emission and its fading rate due to artificial disordering of the framework (Riedesel et al., 2021),

IRPL and IR-RL emissions explored in the present study seem to be largely independent of changes to the distribution of Al^{3+} ions on the Al,Si-framework. This suggests that crystal defects acting as electron trapping centres are not located on Al-bridging O ions. This contrasts with observations on blue luminescence centres, which are suggested to be related to Al-bridging O ions (Speit and Lehmann, 1982b; Finch and Klein, 1999; Riedesel et al., 2021). A comparison of IRPL and IR-RL emissions of single phase feldspars and perthites do not reveal any relationships between phases present in a single crystal and number of IRPL or IR-RL emission peaks or their positions.

We observed sample-to-sample variations in the extent to which the $IRPL_{1.3}$ and $IRPL_{1.41}$ emissions reset optically. Residual $IRPL_{1.41}$ emissions after 18 hours of solar simulator bleaching indicate that the degree of IRPL signal depletion is sample dependent, and this may have significant implications for the use of IRPL in luminescence dating.

Acknowledgements

SR would like to thank Aberystwyth University for funding her PhD research through an AberDoc PhD scholarship (Aberystwyth University). SR would like to thank Andrew Brown (Aberystwyth University) for laboratory assistance during the heating experiments. We thank Prof Javier Garcia-Guinea (Museo Nacional de Ciencias Naturales, Madrid) and Prof Adrian A. Finch (University of St. Andrews) for sample CLBR and Prof Nick J. Pearce (Aberystwyth University) for samples FSM-3, FSM-5 and FSM-14.

References

Andersen, M. T., Jain, M., Tidemann-Lichtenber, P., 2012. Red-IR stimulated luminescence in K-feldspar: Single or multiple trap origin? Journal of Applied Physics 112, 043507.

Bailiff, I.K., Poolton, N.R.J., 1991. Studies of charge transfer mechanisms in feldspars. Nuclear Tracks and Radiation Measurements 18, 111-118.

Bates, D.M., DebRoy, S., 2018. nls function – Nonlinear least squares. In: R Core Team and contributors worldwide, 2018. The R stats package version 3.5.0 (2018).

Baril, M.R., Huntley, D.J., 2003. Optical excitation spectra of trapped electrons in irradiated feldspars. Journal of Physics: Condensed Matter 15, 8011-8027.

Baril, M.R., 2004. CCD imaging of the infra-red stimulated luminescence of feldspar. Radiation Measurements 38, 81-86.

Clark, R.J., Sanderson, D.C.W., 1994. Photostimulated luminescence excitation spectroscopy of feldspars and micas. Radiation Measurements 23, 641-646.

Deer, W.A., Howie, R.A., Zussman, J., 2013. An introduction to the rock-forming minerals. Third Edition. Mineralogical Society of Great Britain and Ireland.

Duller, G.A.T., Gunn, M., Roberts, H.M., 2020. Single grain infrared photoluminescence (IRPL) measurements of feldspars for dating. Radiation Measurements 133, 106313.

Erfurt, G., 2003. Infrared luminescence of Pb^{+} centres in potassium-rich feldspars. Physica Status Solidi 200, 429-438.

Erfurt, G., Krbetschek, M.R., 2003. Studies on the physics of the infrared radioluminescence of potassium feldspar and on the methodology of its application to sediment dating. Radiation measurements 37, 505-510.

Finch, A.A., Klein, J., 1999. The causes and petrological significance of cathodoluminescence emissions from alkali feldspars. Contributions to Mineralogy and Petrology 135, 234-243.

Garcia-Guinea, J., Townsend, P.D., Sanchez-Muños, Rojo, J.M., 1999. Ultraviolet-blue ionic luminescence of alkali feldspars from bulk and interfaces. Physics and Chemistry of Minerals 26, 658-667.

Godfrey-Smith, D.I., Cada, M., 1996. IR stimulation spectroscopy of plagioclase and potassium feldspars, and quartz. Radiation Protection Dosimetry 66, 379-385.

Goldsmith, J.R., Laves, F., 1954. The microcline-sanidine stability relations. Geochimica et Cosmochimica Acta 5, p. 1-19.

Hamilton, T.D.S., Munro, I.H., Walker, G., 1978. Luminescence instrumentation. In Lumb, M.D. (Ed.). Luminescence spectroscopy. Academic Press, London.

Harrison, T. N., Parsons, I., Brown, P. E., 1990. Mineralogical evolution of fayalite-bearing rapakivi granites from the Prins Christians Sund pluton, South Greenland. Mineralogical Magazine 54, 57–66.

Hütt, G., Jaek, I., Tchonka, J., 1988. Optical dating: K-feldspars optical response stimulation spectra. Quaternary Science Reviews 7, 381-385.

Kars, R.H., Poolton, N.R.J., Jain, M., Ankjærgaard, C., Dorenbos, P., Wallinga, J., 2013. On the trap depth of the IR-sensitive trap in Na- and K-feldspar. Radiation Measurements 59, 103-113.

Keller, G.V., 1966. Electrical properties of rocks and minerals. Geological Society of America Memoir 97, 552-577.

Kumar, R., Kook, M., Murray, A.S., Jain, M., 2018. Towards direct measurement of electrons in metastable states in K-feldspar: Do infrared-photoluminescence and radioluminescence probe the same trap? Radiation Measurements 120, 7-13.

Kumar, R., Kook, M., Jain, M., 2020. Understanding the metastable states in K-Na aluminosilicates using novel site-selective excitation-emission spectroscopy. Journal of Physics D: Applied Physics 53, 465301.

Kumar, R., Kook, M., Jain, M., 2020a. Understanding the metastable states in K-Na aluminosilicates using novel site-selective excitation-emission spectroscopy. Journal of Physics D: Applied Physics 53, 465301.

Kumar, R., Martin, L.I.D.J., Poelman, D., Vandenberghe, D., De Grave, J., Kook, M., Jain, M., 2020b. Sie-selective mapping of metastable states using electron-beam induced luminescence microscopy. Scientific Reports 10: 15650.

Mooney, J., Kambhampati, P., 2013. Get the basics right: Jacobian conversion of wavelength and energy scales for quantitative analysis of emission spectra. Journal of Physical Chemistry Letters 4, 3316-3318.

Poolton, N.R.J., Bøtter-Jensen, L., Johnsen, O., 1995. Influence on donor electron energies of the chemical composition of K, Na and Ca aluminosilicates. Journal of Physics: Condensed Matter 7, 4751-4762.

Poolton, N.R.J., Nicholls, J.E., Bøtter-Jensen, L., Smith, G.M., Riedi, P.C., 2001. Observation of free electron cyclotron resonance in $NaAlSi_3O_8$ feldspar: Direct determination of the effective electron mass. Physica Status Solidi 225, 467-475.

Poolton, N.R.J., Ozanyan, K.B., Wallinga, J., Murray, A.S., Bøtter-Jensen, L., 2002a. Electrons in feldspar II: a consideration of the influence of conduction band-tail states on luminescence processes. Physics and Chemistry of Minerals 29, 217-225.

Poolton, N.R.J., Wallinga, J., Murray, A.S., Bulur, E., Bøtter-Jensen, L., 2002b. Electrons in feldspar I: on the wavefunction of electrons trapped at simple lattice defects. Physics and Chemistry of Minerals 29, 210-216.

Poolton, N.R.J., Kars, R.H., Wallinga, J., Bos, A.J.J., 2009. Direct evidence for the participation of band-tail states and excited state tunnelling in the lu-

minescence of irradiated feldspars. Journal of Physics: Condensed Matter 21, 485505.

Prasad, A.K., Poolton, N.R.J., Kook, M., Jain, M., 2017. Optical dating in a new light: A direct, non-destructive probe of trapped electrons. Scientific Reports 7: 12097.

Riedesel, S., King, G.E., Prasad, A.K., Kumar, R., Finch, A.A., Jain, M., 2019. Optical determination of the width of the band-tail states, and the excited and ground state energies of the principal dosimetric trap in feldspar. Radiation Measurements 125, 40-51.

Riedesel, S., Bell, A.M.T., Duller, G.A.T., Finch, A.A., Jain, M., King, G.E., Pearce, N.J., Roberts, H.M., 2021. Exploring sources of variation in thermoluminescence emissions and anomalous fading in alkali feldspars. Radiation Measurements 141, 106541.

Short, M.A., 2004. Determining the possible lattice sites of two unknown defects in orthoclase from the polarization effects in their optical transitions. Journal of Physics: Condensed Matter 16, 7405-7417.

Speit, B., Lehmann, G., 1982a. Radiation Defects in Feldspars. Physics and Chemistry of Minerals 8, 77-82.

Speit, B., Lehmann, G., 1982b. A comparative study of thermoluminescence and isothermal destruction of radiation defects in feldspars. Journal of Luminescence 27, 127-136.

Stewart, D.B., Ribbe, P.H., 1969. Structural explanation for variations in cell parameters of alkali feldspar with Al/Si ordering. American Journal of Science 267-A, 444-462.

Strickertsson, K., 1985. The thermoluminescence of potassium feldspars – glow curve characteristics and initial rise measurements. Nuclear Tracks 10, 613-617.

Telfer, D.J., Walker, G., 1978. Ligand field bands of Mn^{2+} and Fe^{3+} lumines-

cence centres and their site occupancy in plagioclase feldspars. Modern Geology 6, 199-210.

Supplementary Material - Site-selective characterisation of electron trapping centres in relation to chemistry, structural state and mineral phases present in single-crystal alkali feldspars

This chapter contains supplementary material to the article in preparation for submission to the *Journal of Luminescence* as

Riedesel, S., Kumar, R., Duller, G.A.T., Roberts, H.M., Bell, A.M.T., Jain, M., in preparation. *Site-selective characterisation of electron trapping centres in relation to chemistry, structural state and mineral phases present in single-crystal alkali feldspars.*

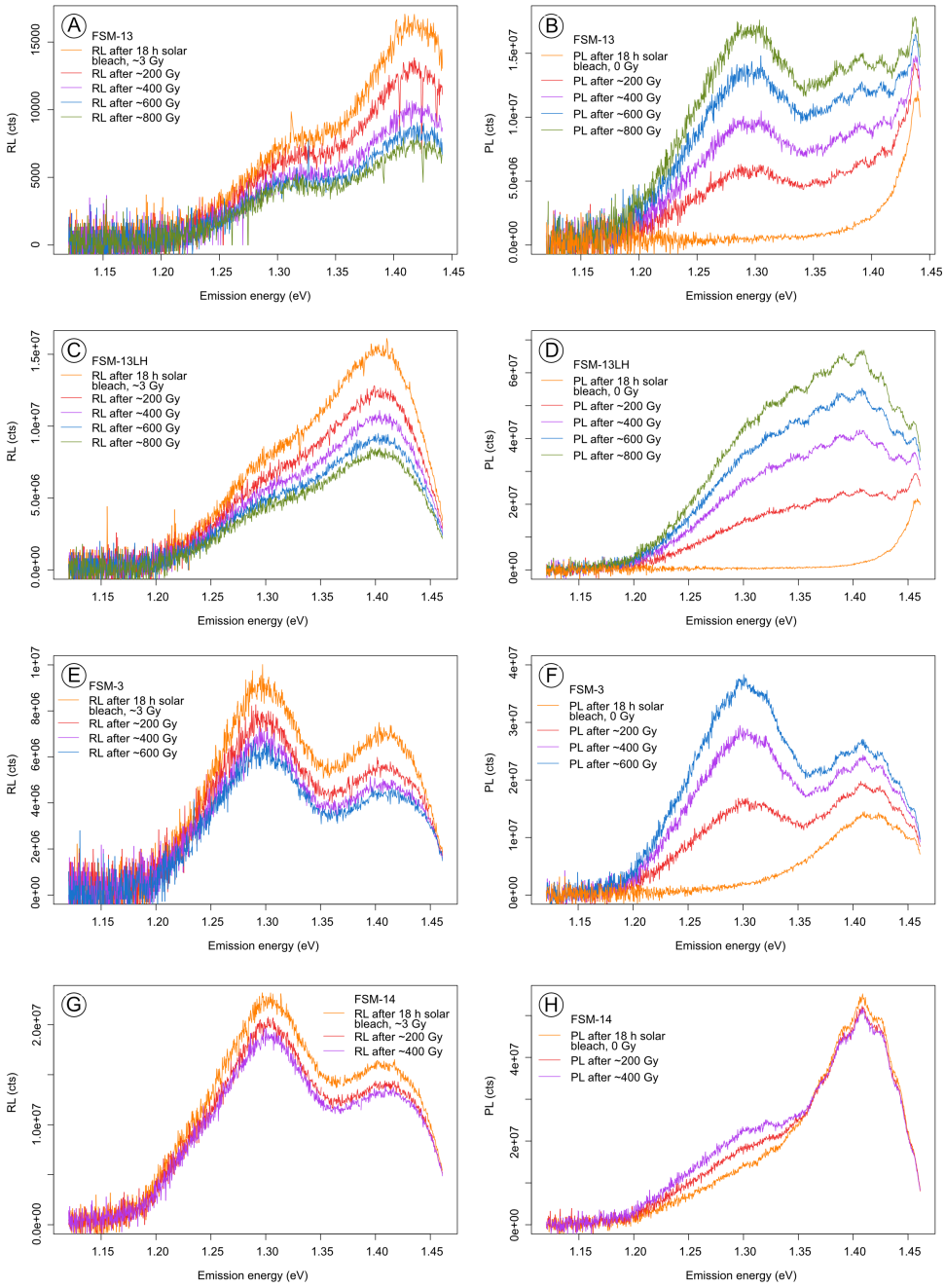

Figure S5.1: *RL (A, C, E, G) and PL (B, D, F, H) emission spectra, measured after different duration of X-ray irradiation for samples FSM-13, FSM-13LH, FSM-3 and FSM-14. The orange curve in the PL spectra is the residual signal measurement after 18 hours of solar simulator bleaching and prior to any dose administered.*

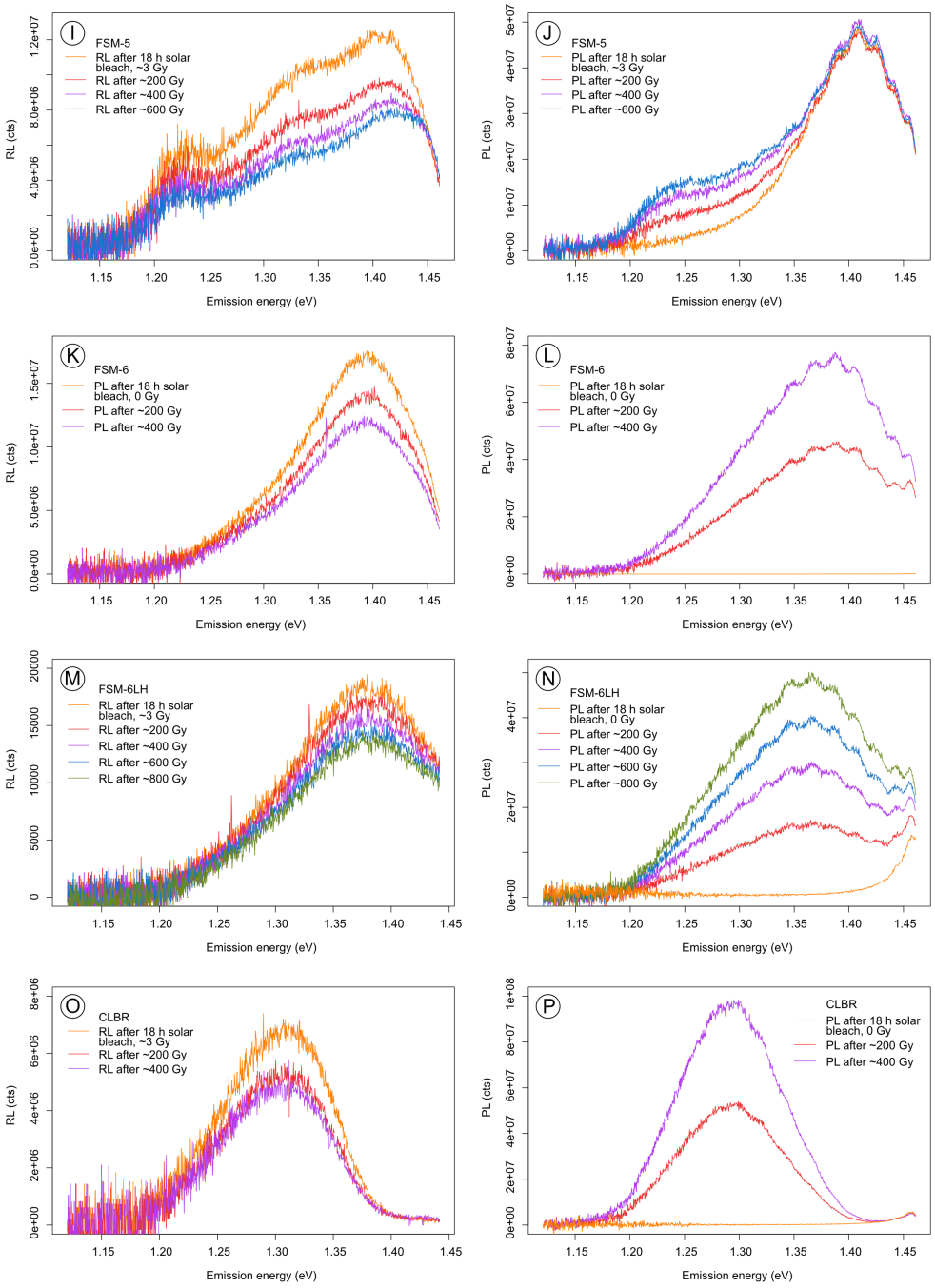

Figure S5.1 (continued): *RL (I, K, M, O) and PL (J, L, N, P emission spectra, measured after different duration of X-ray irradiation for samples FSM-5, FSM-6, FSM-6LH and CLBR. The orange curve in the PL spectra is the residuals signal measurement after 18 hours of solar simulator bleaching and prior to any dose administered.*

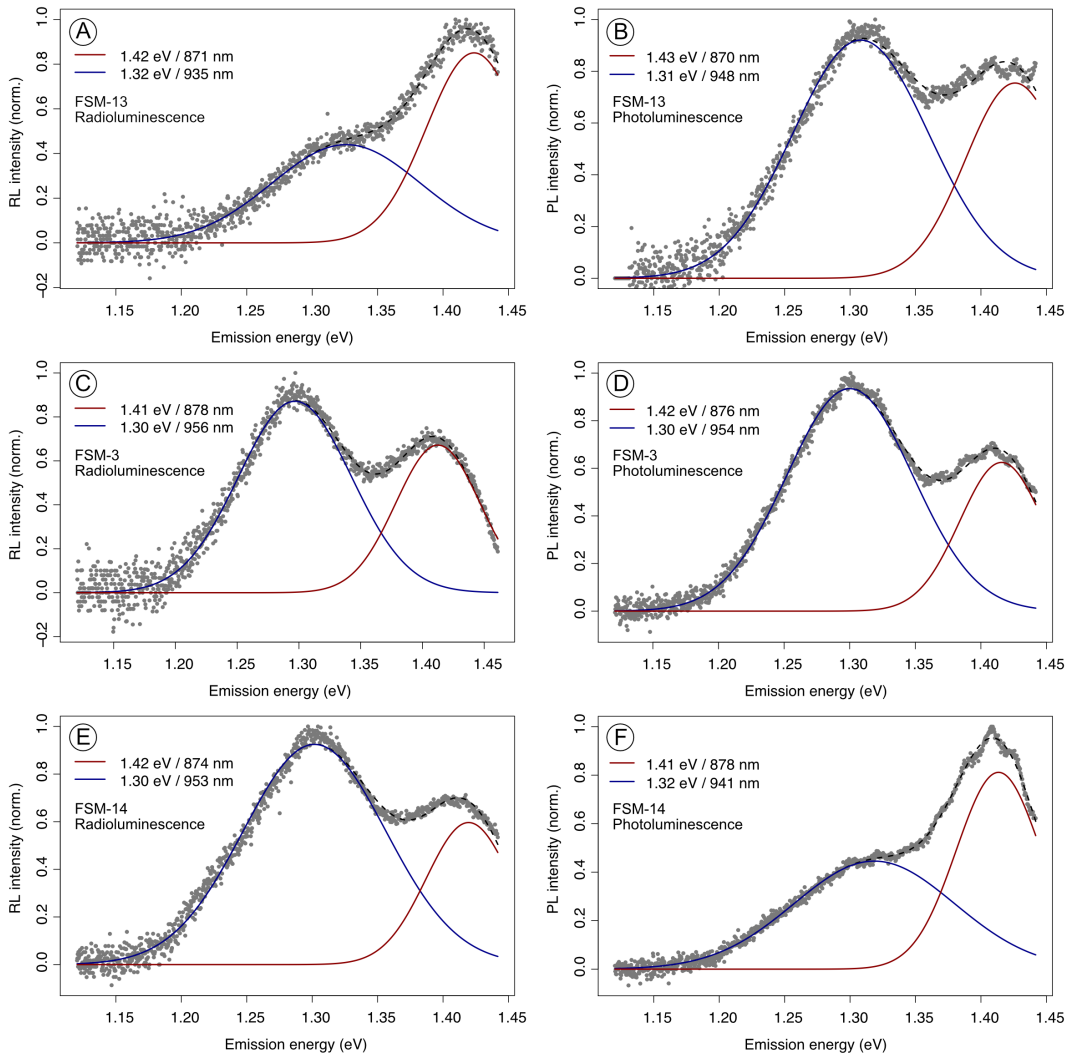

Figure S5.2: *Radioluminescence (A, C, E) and photoluminescence (B, D, F) emission spectra of samples FSM-13 (A, B), FSM-3 (C, D) and FSM-14 (E, F). The recorded spectra were fitted using two Gaussian functions. The mean of the distribution is given in the individual figures for both distributions. Further details of the fit are also presented in Table 5.2.*

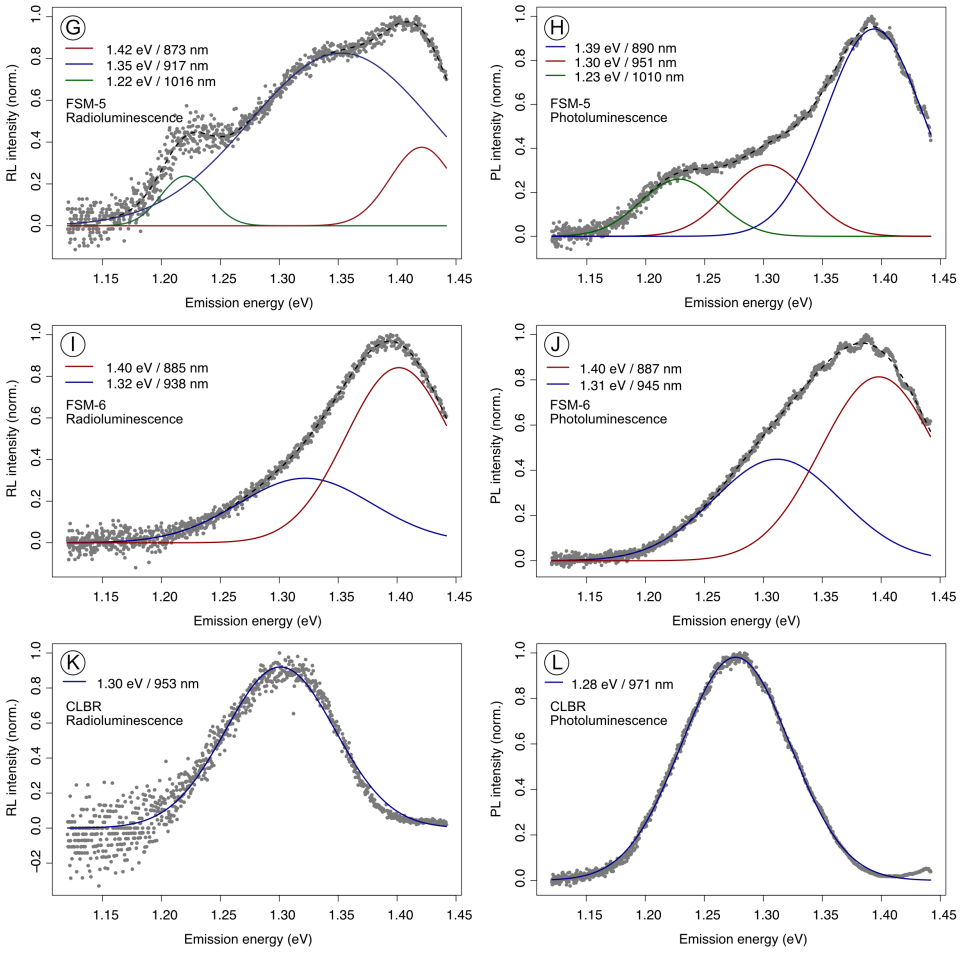

Figure S5.2 (continued): *Radioluminescence (G, I, K) and photoluminescence (H, J, L) emission spectra (continued) of samples FSM-5 (G, H), FSM-6 (I, J) and CLBR (K, L). The recorded spectra were fitted using up to three Gaussian functions. The RL and PL emission spectra of the albite sample CLBR were only fitted using a single Gaussian distribution. The mean of the distribution is given in the individual figures. Further details of the fit are also presented in Table 5.2.*

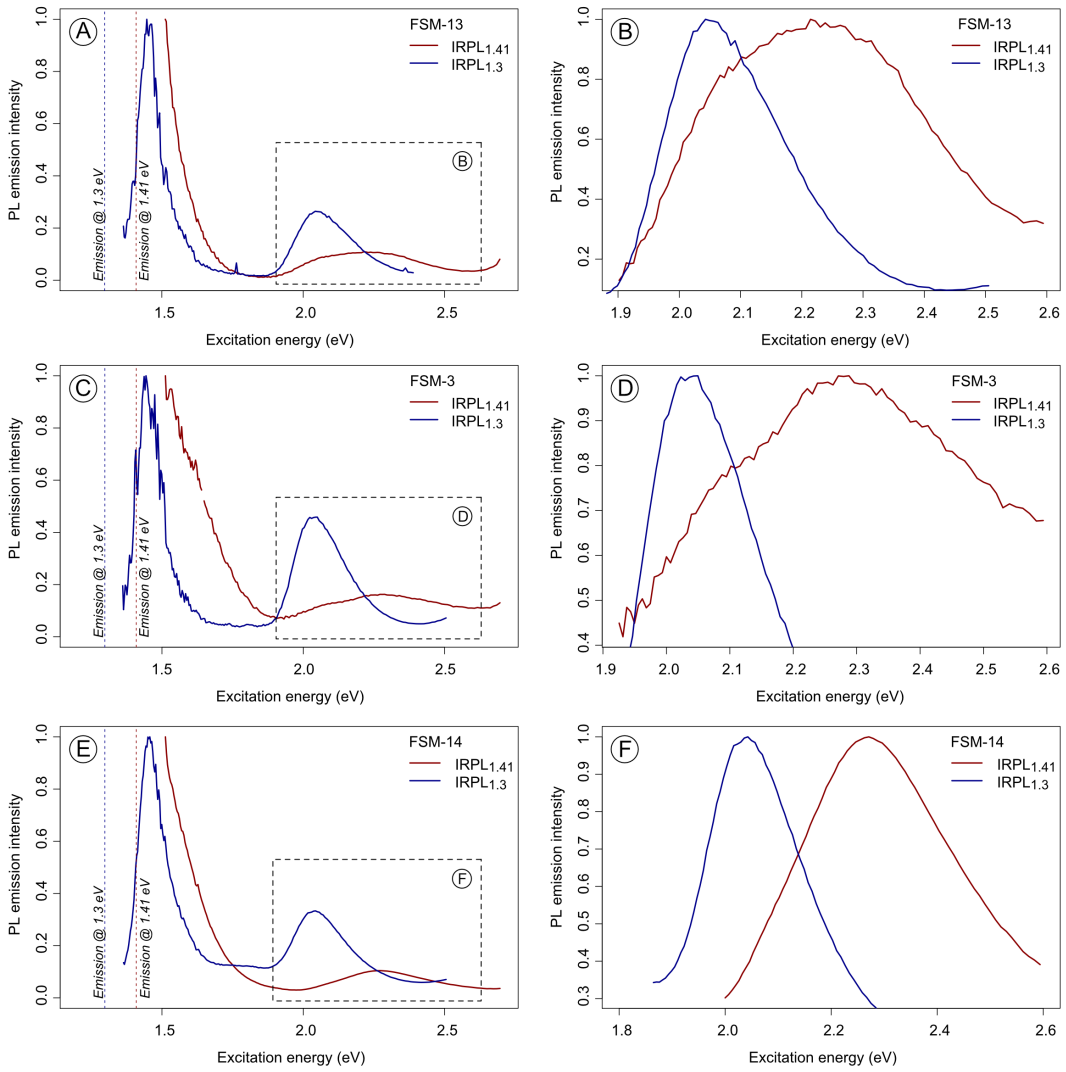

Figure S5.3: *Excitation spectra for the $IRPL_{1.41}$ and $IRPL_{1.3}$ emissions of samples FSM-13 (A, B), FSM-3 (C, D) and FSM-14 (E, F). The graphs were normalised to the point of highest signal intensity. For figures B, D and F, excitation peak 2 was isolated and normalised separately. These graphs were used to obtain the trap depth of the principal dosimetric trap in feldspars, by picking the point of highest intensity for the individual curves. The thus obtained mode (in eV and µm) are given in Table 5.3. The emission window is indicated in A, C and E with dashed vertical lines.*

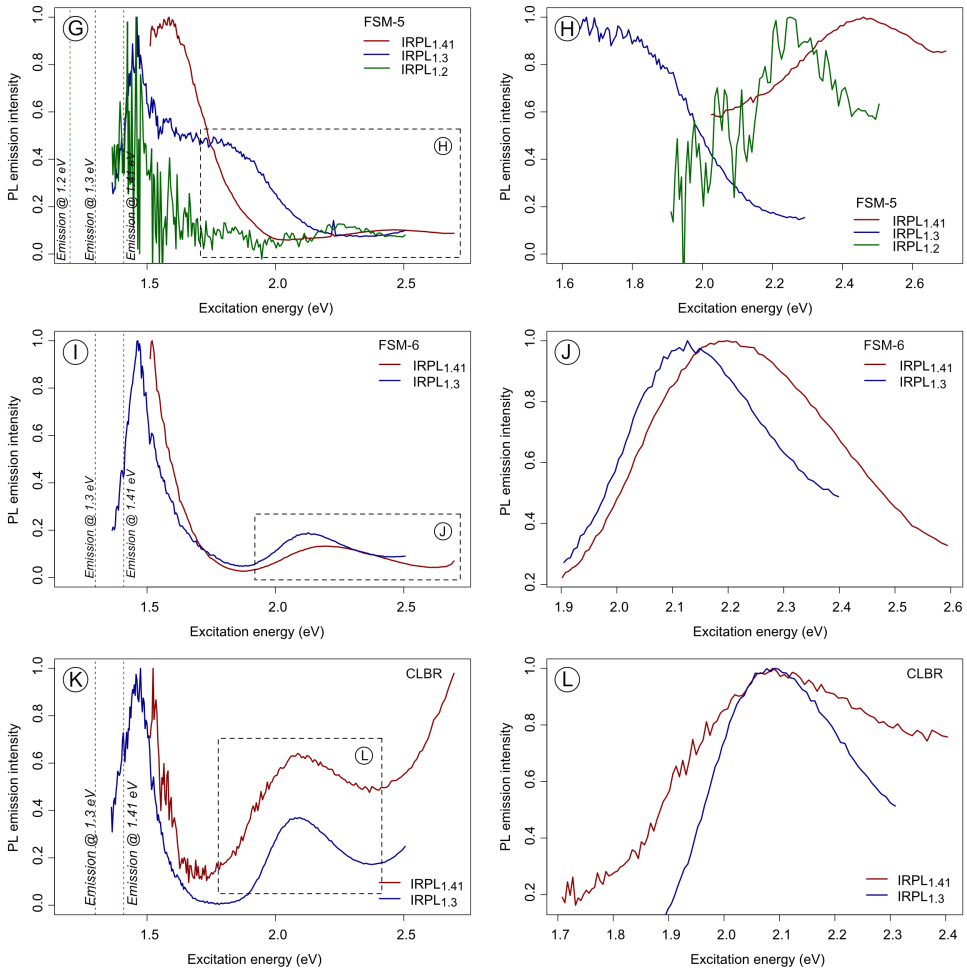

Figure S5.3 (continued): *Excitation spectra with $IRPL_{1.3}$ and $IRPL_{1.41}$ emission recorded for samples FSM-6 (I, J) and CLBR (K, L), and with $IRPL_{1.2}$, $IRPL_{1.3}$ and $IRPL_{1.41}$ emissions recorded for sample FSM-5 (G, H). The emission windows are indicated in G, I and K with vertical dashed lines. The graphs were normalised to the point of highest signal intensity. For figures H, J and L, excitation peak 2 was isolated and normalised separately. These graphs were used to obtain the trap depth of the principal dosimetric trap in feldspars, by picking the point of highest intensity for the individual curves. The thus obtained mode (in eV and μm) of the peaks are given in Table 3. For FSM-5 (G and H) excitation peak 2 overlaps with the IR resonance peak, which complicates the estimation of the trap depth in the case of the $IRPL_{1.3}$ emission of this sample. For CLBR the $IRPL_{1.41}$ emission is much dimmer than the $IRPL_{1.3}$ emission, which is due to the $IRPL_{1.41}$ emission being only the tail of the $IRPL_{1.3}$ emission. This also explains, why excitation peak 2 overlaps for both emissions. We therefore do not attempt to calculate a trap depth for the $IRPL_{1.41}$ emission of CLBR.*

Preface to Chapter 6

The data presented in Chapter 5 (*Site-selective characterisation of electron trapping centres in relation to chemistry, structural state and phases present in single-crystal alkali feldspars*) revealed, in agreement with Chapter 4, that the IR resonance peak, which likely reflects the first excited state of the electron trap in feldspar, remains unchanged, regardless of the sample chemistry or the structural state. However, the trap depth varies between samples and is likely to be affected by changes in its local crystallographic environment. Experiments in Chapter 5 revealed IRPL and IR-RL emissions at 1.41 eV, 1.3 eV and, for the first time, at 1.2 eV. Chapter 5 showed that whilst the $IRPL_{1.3}$ centre seems to be independent of the cation on M sites, the $IRPL_{1.41}$ trapping centres is proposed to be linked to the presence of K^+ ions on M sites. Exploring the effect of framework disorder on $IRPL_{1.3}$ and $IRPL_{1.41}$ emissions revealed no significant changes to IRPL and IR-RL emission energies or ground state energies of the trapping centres. Whether changes to the Al^{3+} distribution on T sites will affect the blue luminescence intensity and its fading rate will be explored in the following Chapter 6 (*Exploring sources of variation in thermoluminescence emissions and anomalous fading in alkali feldspars*).

Whilst Chapters 4 and 5 focussed on the electron trapping site in feldspars, Chapter 6 aims at developing a better understanding of the recombination site in feldspars, particularly the blue luminescence emission. To enable an overview of emissions present in a variety of alkali feldspars and their end members, TL emission spectra of selected single crystal feldspar specimens and samples used in luminescence dating studies are recorded. Since fading is the major limitation of the blue luminescence emission in feldspar, potential relationships between the fading rate and crystallographic properties of the samples are explored.

Six

Exploring sources of variation in thermoluminescence emissions and anomalous fading in alkali feldspars

This chapter is published in *Radiation Measurements* as

Riedesel, S., Bell, A.M.T., Duller, G.A.T., Finch, A.A., Jain, M., King, G.E., Pearce, N.J., Roberts, H.M., 2021. *Exploring sources of variation in thermoluminescence emissions and anomalous fading in alkali feldspars.* Radiation Measurements 141, 106541.

Abstract

Alkali feldspars are routinely used in retrospective dosimetry using luminescence methods. However there is a signal loss over time, termed 'anomalous fading', which results in age underestimation if uncorrected. Although significant improvements have been made in recent years, luminescence dating of feldspars remains challenging. This paper investigates the relationships between chemistry, structural state and the scale of exsolution with thermoluminescence (TL) emission spectra and infrared stimulated luminescence (IRSL) fading rates. We measure TL emission spectra, where possible linking the recombination site to physical features of the feldspar crystals. We show that fading rates are lowest in ordered end-member Na- and K-feldspars but significantly greater in disordered end-members, showing that Al-Si order influences fading. As well as having very low fading rates, ordered end-member samples have distinctive TL emission spectra, with the yellow-green emission dominant, while all other samples have a dominant blue emission. Perthite, i.e. exsolved members of the (Na,K)-feldspar solid solution, show greater fading than disordered end-members and fading is greatest in semi-coherent macroperthite. We propose that the state of Al-Si-order, and the occurrence of defects and dislocations at the perthite lamellar interfaces influence anomalous fading rates in feldspar.

6.1 Introduction

Luminescence dating of feldspars is routinely conducted using the infrared stimulated luminescence (IRSL) signal and by measuring the emission in the blue (∼410 nm) (e.g. Buylaert et al., 2012; Reimann et al., 2012; Smedley et al., 2016; Riedesel et al., 2018). However, feldspar IRSL dating has a major limitation, because it suffers from a signal loss at ambient temperatures, termed anomalous fading (Wintle, 1973; Visocekas, 1985), which results in age underestimation if uncorrected. A range of correction methods has been developed (e.g. Huntley and Lamothe, 2001; Kars et al., 2008), but these often result in large uncertainties on the final age. To circumvent the issues associated with having to quantify and try to correct for fading, research over the past decade has focussed on the isolation of an IRSL signal from feldspar that minimises anomalous fading. Lower fading rates have been obtained by increasing the stimulation temperature (Thomsen et al., 2008) and reduced further by using the signal arising from a second IR stimulation at elevated temperature (termed post-infrared infrared stimulated luminescence signal, post-IR IRSL, e.g. Thomsen et al., 2008; Thiel et al., 2011; Buylaert et al., 2012), or by using a series of IR stimulations at increasing temperatures (termed multiple-elevated-temperature protocols, MET, e.g. Li and Li, 2011).

The cause of anomalous fading has been debated for more than 40 years (e.g. Wintle, 1977; Templer, 1986; Sanderson, 1988; Visocekas et al., 2014) and a loss of charge from electron traps over time, due to quantum mechanical tunnelling, is the most widely accepted explanation (e.g. Visocekas, 1985). The rate of anomalous fading has been linked to the density of available recombination centres (Huntley, 2006) and significant variations in the rate of fading have been observed in single-crystal feldspars (e.g. Spooner, 1992, 1994; Huntley and Lian, 2006) and in feldspar (single) grains extracted from sediments and bedrock (e.g. Neudorf et al., 2012; Trauerstein et al., 2012; Valla et al., 2016). Visocekas and Zink (1995) measured tunnelling afterglow in microcline and sanidine feldspars and inferred that increased anomalous fading of volcanic feldspars arises due to large concentrations of defects in the crystal caused by Al^{3+} and Si^{4+} disorder on the framework, and additionally due to the inclusion of Fe^{3+} on tetrahedral sites. Based on this observation, Visocekas and Zink (1995) suggested that ordered feldspars, such as microcline, could be dated, because their ordered structure would prevent fading. Indeed, Spooner (1994) observed a stable IRSL signal

with the emission recorded between ∼330 nm and ∼630 nm (using 2 mm Schott BG39 filter) for one of his microcline feldspars and also for an Amelia albite specimen. In contrast, Huntley and Lian (2006) measured IRSL fading rates of the ∼360 to ∼620 nm emission (using BG39 and Kopp 4-97 filters) of up to 12 % in feldspars that they describe as microclines.

However, in most studies the samples are only characterised by their chemical composition, and although a description, which includes the structural state of the feldspar is often included (terminologies such as microcline or sanidine), no data are shown that proves this association. Thus it is difficult to compare fading rates measured with any other mineralogical property of the samples other than the chemical composition. Anomalous fading has often been observed and associated with the volcanic origin of the samples (e.g. Wintle, 1973; Visocekas and Zink, 1995, 1999; Guérin and Visocekas, 2015). However, few fading feldspars used in luminescence dating are of volcanic origin (e.g. Valla et al., 2016; King et al., 2016; Jenkins et al., 2018).

Due to exsolution in alkali feldspars during slow cooling in plutonic rocks, such as granite, feldspars are often perthitic (e.g. Parsons et al., 2015). A relationship between interfaces in perthites and the intensity of the UV emission (∼290 nm) has been found (Garcia-Guinea et al., 1996). Baril (2004) observed phase-dependent variations of violet and yellow luminescence emissions in perthites, and Correcher et al. (2000) linked the blue luminescence in feldspars with alkali self-diffusion along interfaces offset by hole centres. Spooner (1992) observed variable fading in his feldspars, which contain Na and K. However, no clear relationship between exsolution features and anomalous fading rates has yet been established. Additionally, earlier studies often analysed the IRSL signal of feldspars with a wide emission range (e.g. Spooner, 1992, 1994; Visocekas and Zink, 1999; Huntley and Lian, 2006), likely including emissions arising from different defect types (cf. Krbetschek et al. (1997) for a review on emission centres and associated crystal defects in feldspars). Developments within the last decade have changed measurement protocols (e.g. Thomsen et al., 2008; Li and Li, 2011) and a wide range of available optical filters enables the isolation of a narrow emission window, which allows a specific emission to be selected. Thus, there is the need for a re-investigation of potential causes of anomalous fading of the blue IRSL signal in chemically and structurally different feldspars.

This paper investigates the links between the blue luminescence emission, the anomalous fading rate of the blue IRSL signal and multiple mineralogical char-

acteristics in alkali feldspars. It explores temperature- and wavelength-resolved variations in the blue luminescence intensity and variations in anomalous fading rates of 12 single-crystal alkali feldspars, and three feldspar grain mixtures extracted from bedrock and sediment. This suite of samples enables the investigation of potential relationships between variations seen in the intensity and anomalous fading rate of the blue luminescence emission and (i) the chemistry of the samples, (ii) the number of phases present in a single crystal specimen (i.e. whether they are single phase or perthitic) and (iii) the degree of framework disorder of the samples.

6.2 Overview of the chemistry and structure of feldspars

The crystal lattice of feldspar is made up of $(Al,Si)O_4$ tetrahedra, each connected to four others by shared or "bridging" oxygen ions at their vertices, forming a continuous, interconnected framework. There are four tetrahedral positions within the framework (two of each of the so-called T_1 and T_2-sites), which are occupied by Si^{4+} or Al^{3+}. The framework has a net negative charge, which is offset by large cations (predominantly Na^+, K^+, Ca^{2+}) occupying cavities in the framework termed M-sites (Deer et al., 2013). The compositional variability of most feldspars is accommodated by three end members, each with a different M-site cation: $KAlSi_3O_8$ (K-feldspar), $NaAlSi_3O_8$ (Na-feldspar) and $CaAl_2Si_2O_8$ (Ca-feldspar). The solid solution between K- and Na-feldspars produces the alkali feldspar series; the solid solution between Na- and Ca-feldspar is termed plagioclase. There is very limited solid solution between K- and Ca-feldspar (<10 %). At high temperature (> 1000 °C), complete solid solution across the plagioclase and alkali feldspar series occurs (see Parsons 2010).

Here we consider the alkali feldspar solid solution series between K- and Na-feldspar. The structural state of alkali feldspar is an important indicator of the temperature of crystallisation and subsequent thermal history (Deer et al., 2013) and hence alkali feldspar is divided broadly into low- and high-temperature members. The structural state of low- and high-temperature alkali feldspars is dictated by the degree of ordering of Al and Si within the framework and, in the case of albite (Na-feldspar), coupled with displacive distortions to the framework. Ordered feldspar is equilibrated at low (e.g. <300°C) temperatures. Generally,

increased ordering of Al and Si within the framework takes place during slow cooling, e.g. in plutonic rocks. During rapid cooling a disordered distribution of Al and Si at high temperatures is quenched (e.g. sanidine, the monoclinic K-feldspar in volcanic rocks) (Deer et al., 2013).

The progressive ordering in alkali feldspars can be understood in terms of the distribution of Al^{3+} on the framework. In the high-temperature K-feldspar (monoclinic high sanidine), Al^{3+} has an equal (25 %) chance of occupying any of the four tetrahedral sites ($T_1(0)$, $T_1(m)$, $T_2(0)$ and $T_2(m)$) within the more open alkali feldspar framework. During slow cooling, as the framework contracts, Al^{3+} diffuses to occupy preferentially one of the two T_1-sites (giving the monoclinic low sanidine). With continued slow-cooling, Al^{3+} preferentially diffuses into one of the T_1-sites ($T_1(0)$, see Parsons 2010), causing a change in symmetry from monoclinic (sanidine, with the greatest disorder) to triclinic, the ordered K-feldspar maximum microcline (Deer et al., 2013). Associated with this drop in symmetry, microcline adopts repeated twinning in two different orientations visible in a polarising microscope, termed tartan or tweed twinning (Deer et al., 2013). Although alkali feldspar is a continuous solid solution at high temperature, the small ionic radius of Na^+ (0.118 nm) triggers a displacive collapse of the framework around Na^+ as the structure attempts to maintain bonding to the smaller Na^+ ion. The feldspar framework cannot collapse around the larger K^+ ion (0.151 nm), hence the alkali feldspar solid solution becomes unstable on cooling and unmixing (exsolution) of the K- and Na-rich phases in alkali feldspar occurs. Such alkali feldspars are single crystals comprising intergrowths of separate K- and Na-rich feldspars, termed perthite; perthites are further divided into crypto-, micro- and macroperthite, dependent on the scale of the intergrowths (from sub-optical, nanometre scale cryptoperthite, microperthite with lamellae visible under a petrographic microscope, and macroperthite whose lamellae are visible to the naked eye). The cooling rate and fluid interaction after crystallisation of the magma influence the size of the perthite lamellae, with cryptoperthite forming earlier in cooling (Brown and Parsons, 1984a) and coarsening over time. Fluid interaction is involved in the coarsening process of micro- and macro-perthite (e.g. Parsons, 1978). Near-pure Na and K feldspars may occur in a variety of environments including deep, high pressure (>0.5 GPa) or high-water content crystallisation of granites/pegmatites (including samples used here e.g. from Minas Gerais, Brazil, CLBR, Table 6.1, Cassedanne and Roditi, 1996) or wet (low-intermediate grade) metamorphic settings (e.g. albite Al-I, Table 6.1, Govindaraju, 1995). In these

cases, the alkali-feldspar phase relationships during various combinations of slow-cooling, water content and magma or protolith composition can produce almost pure end-member ordered alkali feldspars (see Deer et al., 2013, Parsons, 1978; Parsons et al., 2005). The homogeneity of samples from some of these exotic environments (e.g. pegmatites) mean that such pure end-member samples are often used as reference materials or samples for experimentation.

6.3 Materials and methods

6.3.1 Samples

The samples used in this study can be split into two groups, single crystal feldspar specimens and examples of feldspars routinely used for sediment dating and luminescence thermochronometry. The chemical composition of the samples and the mineral phases present were determined by X-ray fluorescence (XRF) and X-ray diffraction (XRD), respectively. Additionally, the samples were examined optically for their colour and the coarseness of any perthite lamella that may be present. We combined our visual inspection, following the definition of perthite microstructures by Deer et al. (2013, p. 253), and the results of the semi-quantitative phase analyses using XRD to separate the perthitic samples into two groups: Both groups have in common that they were determined to be two-phase using XRD. One group of perthites has K- and Na-feldspar lamellae on the optical scale, so that we were able to identify them by eye or using a hand lens. We refer to these feldspar samples as macroperthite. The second group consists of perthite where XRD results defined them as two-phase, but where we were unable to see the lamellae with the naked eye or even through an optical microscope. We refer to these feldspars as cryptoperthite.

The chemical composition of the samples was determined by XRF. For XRF measurements 2 g of cellulose binder was placed into an Al sample boat. Powdered sample (0.1 g) was then mixed with cellulose binder (0.1 g) and this mixture was spread on top of the cellulose binder in the Al sample boat. Each boat was then pressed at 20 t to pellets for XRF measurements using a PANalytical MagiX PRO XRF spectrometer equipped with a Rh anode X-ray source. The spectra were collected over ten different energy ranges and then analysed to obtain semi-quantitative results. For the analyses, it was assumed that all elements, except for Cl, were present as oxides. The chemical composition of all samples

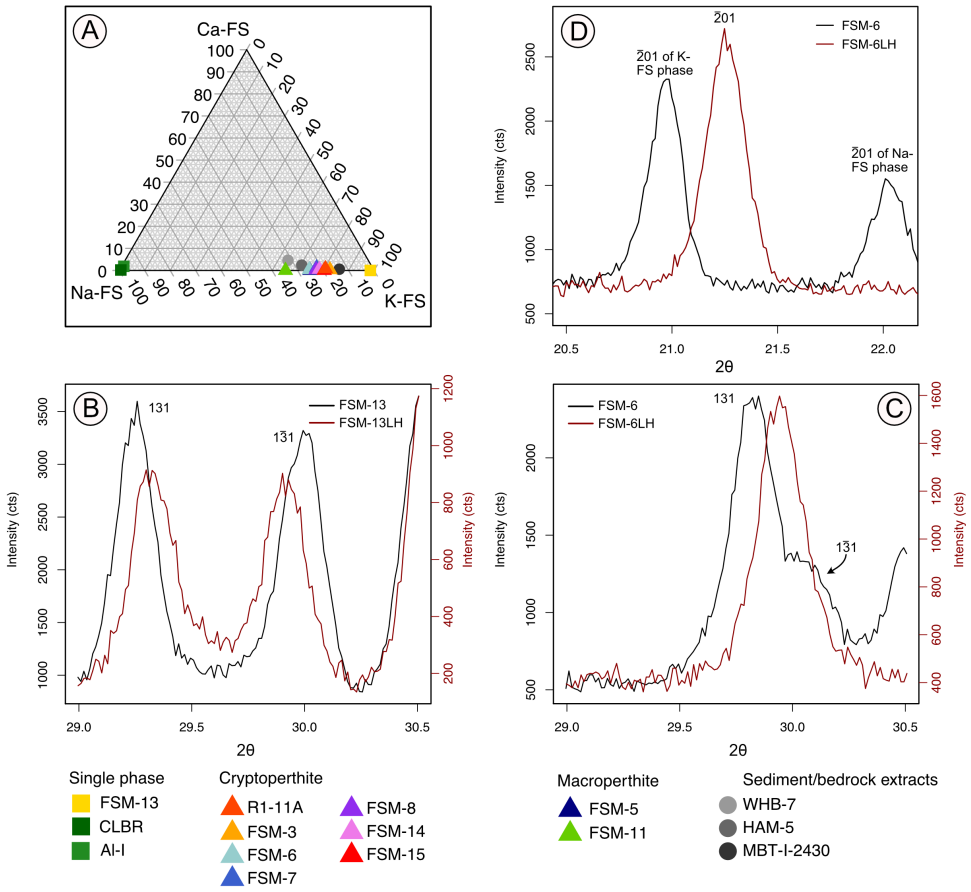

Figure 6.1: *A) Relative feldspar composition (%) of the samples. The relative compositions of K-, Na- and Ca-feldspar were calculated using stoichiometric conversion of XRF results. B) X-ray diffraction pattern of FSM-13 (black line) and FSM-13LH (red line) in the range of 29.0° 2θ to 30.5° 2θ. Visible are the (131) and ($1\bar{3}1$) diffraction maxima. These two diffraction maxima move closer together due to the heating of the sample material. C) X-ray diffraction pattern of FSM-6 (black line) and FSM-6LH (red line) in the range of 29.0° 2θ to 30.5° 2θ. For FSM-6 (black line) a prominent (131) diffraction maxima is visible in the figure, and in addition a minor peak, which is the remainder of the ($1\bar{3}1$) diffraction peak. After heating and rapidly cooling, only a single (131) diffraction peak remains in FSM-6LH (red line). This indicates that the original material of FSM-13 (black line in B) is more ordered than the starting material of FSM-6 (black line in C). For both samples, the X-ray diffraction pattern indicate the success of the heating experiment, as both samples are slightly more disordered than their starting material. However, it is expected that FSM-6LH is relatively more disordered than FSM-13LH. D) Comparison of the $\bar{2}01$ diffraction peak in perthite FSM-6 and in sanidine FSM-6LH. The heating experiment caused a homogenisation of the distribution of K^+ and Na^+ ions within the crystal. Whilst FSM-6 shows two $\bar{2}01$ diffraction peaks (on for each phase), FSM-6LH only shows a single diffraction peak, reflecting the homogeneous distribution of the cations. Radiation used in XRD analysis was Cu Kα.*

Table 6.1: *Details regarding the origin, chemical composition, phases and size of perthite lamella for samples investigated. The chemical composition in % feldspars, was done using stoichiometric conversion of the semi-quantitative XRF data. Chemical composition and present phases of R1-11A was taken from Harrison et al. (1990). Present phases are based on semi-quantitative XRD analyses.*

Sample ID	Origin	Chemical composition (FS %)			Phases						Perthite development	Reference
		K-FS	Na-FS	Ca-FS	Microcline	Orthoclase	Sanidine	Albite	Anorthite	Other		
FSM-13	Brazil	98.5	1.5	0.0	100	-	-	-	-	-	None	-
FSM-13LH	Brazil	98.5	1.5	0.0	100	-	-	-	-	-	None	-
FSM-3	Granite pegmatite, Toe Head, South Harris, Scotland, UK (Cunningham, 1981)	82.5	17.2	0.3	78.0	-	-	22.0	-	-	microperthite	-
R1-11A	Rapakivi Granite, South Greenland	81.0	19.0	1.0	Microcline and albite (Harrison et al., 1990)						Cryptoperthite	Harrison et al., 1990; Finch and Klein, 1999; Riedesel et al., 2019
FSM-15	Quebec, Canada	80.4	19.6	0.0	82.0	-	-	18.0	-	-	microperthite	-
FSM-14	Iveland, Southern Norway	78.3	21.2	0.5	54.0	-	-	46.0	-	-	microperthite	-
FSM-8	Norway	77.1	22.6	0.3	68.0	-	-	32.0	-	-	microperthite	-
FSM-7	Unknown	76.8	22.0	1.2	48.0	-	-	51.0	-	1.0	microperthite	-
FSM-5	Unknown	74.8	25.2	0.0	57.0	-	-	43.0	-	1.0	macroperthite	-
FSM-6	Granite pegamite, Trezaise Quarry, Cornwall, UK (see Ussher et al., 1909)	74.4	25.3	0.3	-	38.0	-	62.0	-	1.0	microperthite	-
FSM-6LH	Trezaise Quarry, Cornwall, UK	74.4	25.3	0.3	-	-	100.0	-	-	-	None	-
FSM-11	Perth, Canada	65.2	34.8	0.0	62.0	-	-	38.0	-	1.0	macroperthite	-
Al-I	Pinzele, Trente, Italy	1.0	97.0	2.0	-	-	-	95.0	-	5.0	None	-
CLBR	Pegmatite, Golonca District, Minas Gerais, Brazil	0.5	99.3	0.2	-	-	-	100.0	-	-	None	Rendell and Clarke (1997); Garcia-Guinea et al., 1999; Riedesel et al., 2019

Table 6.2: *Details on feldspar extracted from sediment and bedrock samples. The chemical composition in % feldspars, was done using stoichiometric conversion of the semi-quantitative XRF data. Present phases are based on semi-quantitative XRD analyses.*

Sample ID	Origin	Chemical composition (FS %)			Phases					Perthite development	Reference
		K-FS	Na-FS	Ca-FS	Microcline	Orthoclase	Sanidine	Albite	Anorthite	Other	
MBT-I-2430	Mont Blanc, Italy	86.1	13.4	0.6	85.0	-	-	15.0	-	-	-	Lambert,2018; Riedesel et al., 2019
HAM-5	Lake Hamana, Japan	70.4	27.2	2.4	-	30.0	-	27.0	-	43.0	-	Riedesel et al., 2019
WHB-7	Channelled Scablands, Washington State, USA	63.9	31.5	4.6	37.0	-	-	30.0	-	33.0	-	-

is summarised in Table S6.1. Individual sample compositions were calculated to give the molecular formula of the feldspar based on eight oxygen, following stoichiometry. The results are shown in Figure 6.1A and given in Table 6.1.

Semi-quantitative phase analysis results of the samples were obtained using XRD. The measurements were carried out using a PANalytical X'Pert MPD powder diffractometer operating with Cu Kα X-rays and a PIXCEL-1D area detector. For these measurements 0.1 g of powdered sample was mounted on a low-background silicon XRD sample holder using acetone. Data were collected over the range of 5-100 degrees 2θ , each scan took just over 1 hour.

Because of the limited availability of sample material for samples R1-11A and CLBR, and since very detailed characterisation is already published, detailed XRF and XRD measurements were not performed. The chemistry and mineralogy of R1-11A was investigated in detail by Harrison et al. (1990) and the results from their study are used here and are presented in Table 6.1. The chemical composition determined by Harrison et al. (1990) is based on electron probe microanalyses. Rendell and Clarke (1997) and Garcia-Guinea et al. (1999) performed luminescence experiments and mineralogical investigations of CLBR and determined its structural state as low albite. Additionally, Riedesel et al. (2019) assessed its chemical composition using an XRF detection head attached to a Risø TL/OSL reader (Kook et al., 2012; and see the supplementary material of Stevens et al., 2018). For this measurement a shard of the sample ($\sim$1 mm diameter) was placed on a Mo cup (without silicone spray) and the chemical composition was measured three times. The result of this measurement procedure is given, alongside the chemistry of the other samples, in Table 6.1.

Details regarding the origin of the samples, their chemical composition and mineralogical properties as determined using the analyses described above are given in Table 6.1 for the single crystal specimens, and in Table 6.2 for bedrock and sediment extracts. Single-phase feldspars included in the sample suite are single-phase microcline (FSM-13), and single-phase albite (CLBR and Al-I). Note that Al-I includes 5 % quartz, based on semi-quantitative XRD measurements. Photoluminescence and excitation spectra of CLBR were presented by Riedesel et al. (2019, referred to as Cleavelandite).

FSM-5 and FSM-11 are macroperthite, with the perthite lamellae visible with the naked eye. Based on semi-quantitative phase analyses using XRD the phases present in these two samples are albite and microcline. Cryptoperthite are R1-11A, FSM-3, FSM-7, FSM-8 FSM-14 and FSM-15. The perthite phases are

microcline and albite in the case of R1-11A, FSM-3, FSM-7, FSM-8, FSM-14 and FSM-15, and orthoclase and albite for FSM-6, as determined using XRD. Photoluminescence, excitation spectra and cathodoluminescence of R1-11A were presented by Riedesel et al. (2019) and Finch and Klein (1999).

WHB-7, the density separated feldspar extract from unconsolidated sediment, consists of microcline and albite, but XRD also showed the presence of muscovite and quartz. HAM-5, another feldspar extract from sediment, consists of orthoclase, albite, quartz and illite, based on semi-quantitative XRD results. The thermochronometry sample MBT-I-2430 consists of feldspar only, in this case microcline and albite. Excitation spectra of HAM-5 and MBT-I-2430 were presented by Riedesel et al. (2019).

Whilst all these samples allow us to investigate the influence of differences in the chemical composition and the mineral phases, laboratory heating experiments on FSM-6 and FSM-13 were conducted to enable the investigation of potential effects of framework disorder on the luminescence emissions and fading rates.

To explore the effect of Si and Al disorder on luminescence properties, 0.5 g of powdered sample material of samples FSM-6 and FSM-13 (referred to as FSM-6LH and FSM-13LH after heating) were placed in acid cleaned Pt crucibles and heated to 105 °C overnight to remove any potential liquid present in the sample material. The Pt crucibles with the sample material were then placed in a preheated furnace at 1050 °C and covered with fitted Pt lids. The samples remained in the furnace at 1050 °C for 5 days (FSM-6LH) and 10 days (FSM-13LH) to allow disordering of Si and Al on the framework. To keep the disordered structure, the samples were rapidly cooled by placing the Pt crucibles in cooled sample holders. Comparison of X-ray diffraction patterns of the unheated and heated material of samples FSM-13/FSM-13LH and FSM-6/FSM-6LH reveals differences linked to states of Al-Si order (Fig. 6.1B, C). The (131) diffraction peak indicates the triclinicity of the material (a narrow single peak if the sample is triclinic, two peaks if the sample is monoclinic, e.g. Garcia-Guinea et al., 1999). Firstly, Figure 6.1B and C indicate different degrees of disorder of the two starting materials of FSM-13 and FSM-6 in their X-ray diffraction pattern. Whilst the XRD pattern of FSM-13 shows two fully defined diffraction peaks (131 and $1\bar{3}1$) between 29° and 32° 2θ, FSM-6 shows only a single peak (131) at 29.8° 2θ with a minor peak ($1\bar{3}1$) around 30° 2θ. This supports results from semi-quantitative phase analyses, based on which FSM-13 was defined as microcline and FSM-6 as two-phase consisting of albite and orthoclase (Table 6.1). Samples

described as orthoclase are microcline with incomplete order of Al^{3+} on T_1-sites (Deer et al., 2013, p. 256-257) Secondly, as a result of the heating experiment, the two individual peaks in the diffractogram of FSM-13 (Fig. 6.1B) move closer together (see red line) and the minor diffraction peak in the diffraction pattern of FSM-6 (Fig. 6.1C) disappears and only a single diffraction peak around 30° 2θ is visible after heating (FSM-6LH, Fig. 6.1C, red line). This shows that the heating experiment is successful in disordering both samples, but that the heated material of FSM-6LH is relatively more disordered compared to FSM-13LH.

In addition to changes of tetrahedral site occupancy by Al^{3+}, prolonged heating is expected to influence the distribution of K^+ and Na^+ ions within the perthitic sample FSM-6. Whilst semi-quantitative phase analyses of the unheated sample FSM-6 characterised it as two-phase, with albite and orthoclase as the phases present, the heated sample FSM-6LH is defined as sanidine by XRD, where Na^+ and K^+ ions are distributed randomly throughout the crystal and not separated in perthite lamellae of K- and Na-feldspar. This becomes apparent when comparing the position of the $(\bar{2}01)$ diffraction peak (Deer et al., 2013, p. 260). In the X-ray diffraction pattern of perthitic sample FSM-6 are two $(\bar{2}01)$ peaks, one for each phase (at 20.98° 2θ for the microcline phase, at 22.01° 2θ for the albite phase). In contrast, there is only a single $(\bar{2}01)$ diffraction peak in FSM-6LH at 21.25° 2θ (Fig. 6.1D).

We also attempted Rietveld refinement, to refine the crystal structure and to quantify the tetrahedral site occupancy by Al^{3+} and Si^{4+} ions. However, due to a strong preferred orientation of the sample material a quantification of the tetrahedral site occupancy was not possible. When using XRD in this manner, we recognise that XRD is a measure of long-range tetrahedral site order (i.e. the development of large, e.g. 100s nm, ordered domains) and relatively insensitive to local short-range order which is better explored by local probes such as Nuclear Magnetic Resonance (NMR, Xiao et al. 1995).

6.3.2 TL emission spectra

Thermoluminescence (TL) emission spectra were measured using an Andor spectrometer (Prasad, 2017) attached to a Risø DA20 TL/OSL reader equipped with a $^{90}Sr/^{90}Y$ beta source delivering ~0.1 Gy/s at the sample position and a DASH (Lapp et al., 2015). The single-photon EMCCD-based spectrograph, used to record the spectra, is attached to the Risø reader via a fibre optic bundle cable.

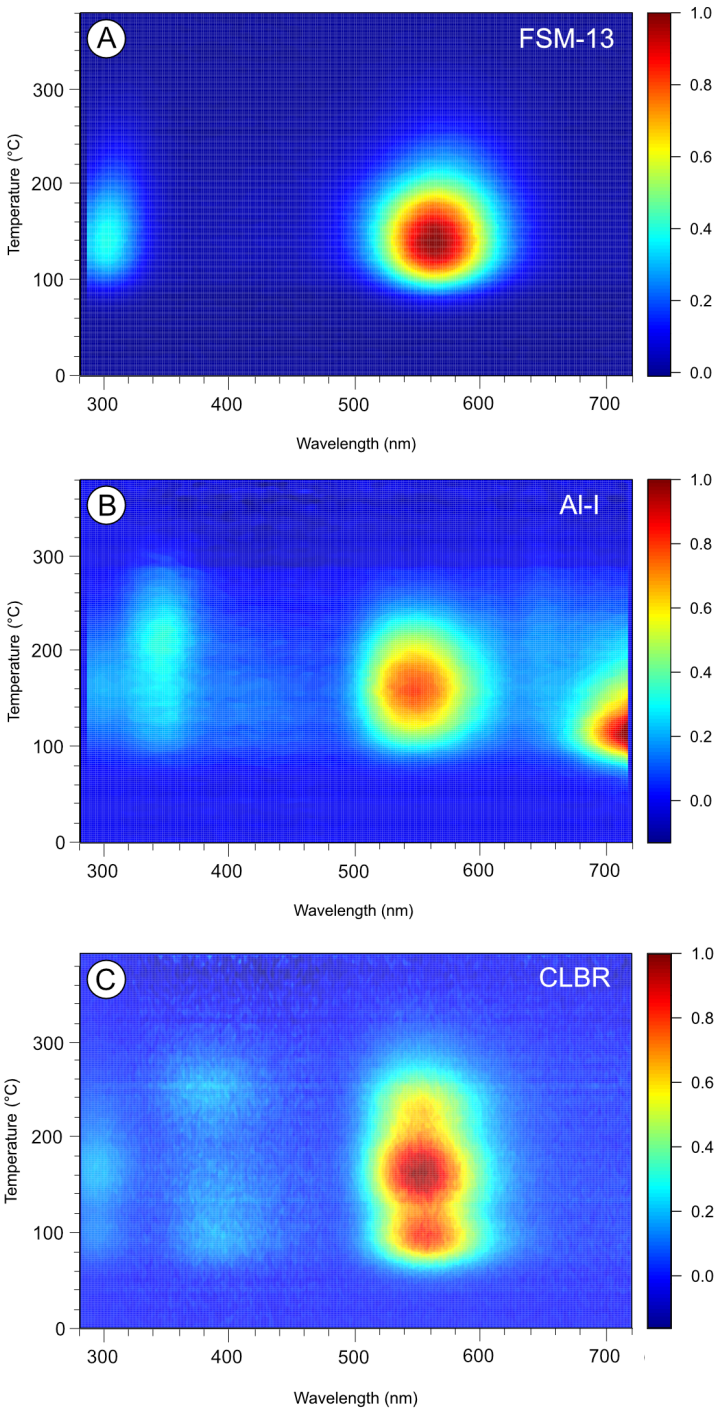

Figure 6.2: *TL emission spectra recorded up to 380 °C, from 280 to 720 nm. The samples shown in this figure are single-phase feldspar. FSM-13 is a microcline (A) and Al-I (B) and CLBR (C) are albite, with Al-I containing 5 % quartz. The TL intensities are normalised to the data point with the highest intensity.*

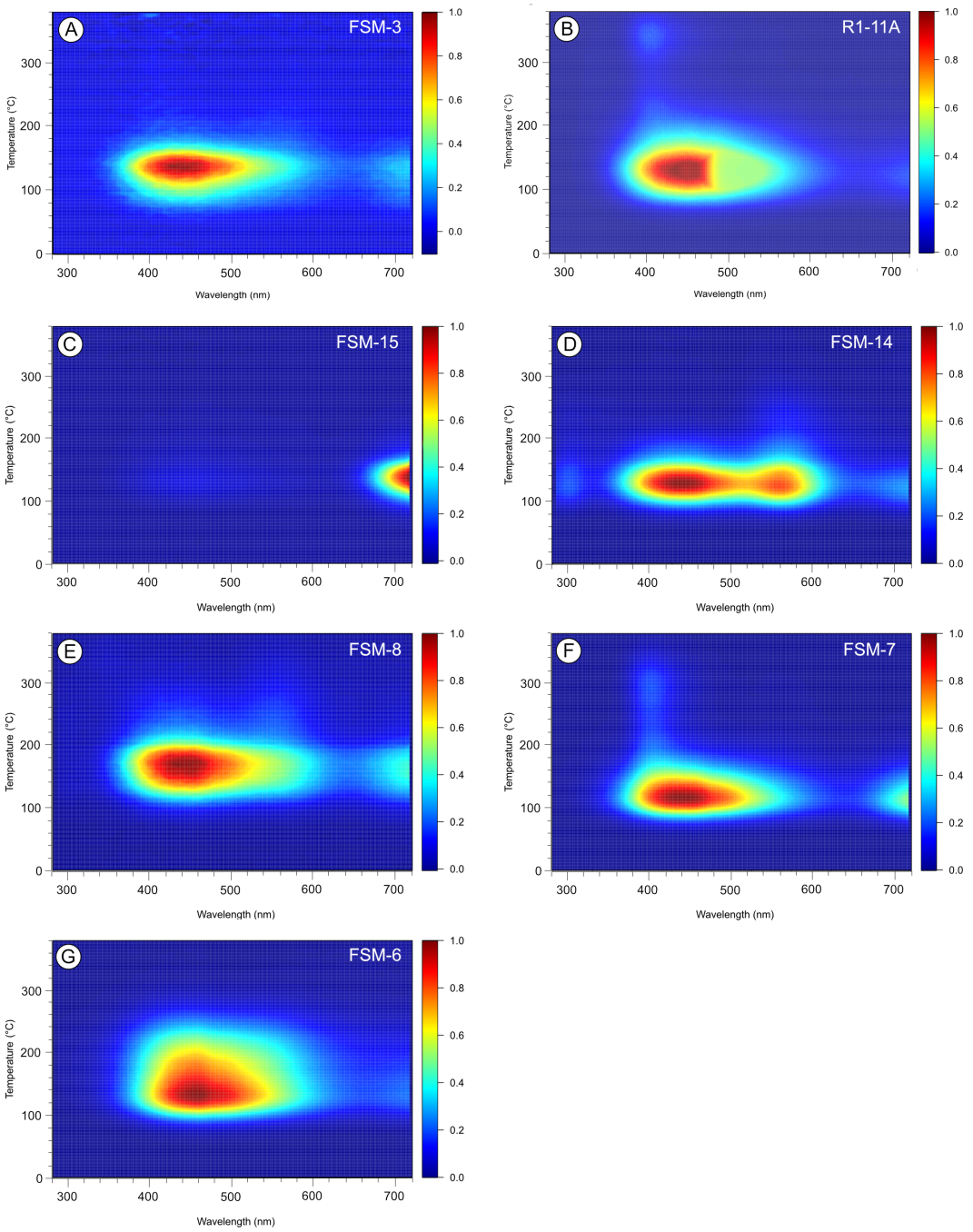

Figure 6.3: *TL emission spectra recorded up to 380 °C, from 280 to 720 nm. The samples shown in this figure are cryptoperthite: FSM-15 (C) is the only sample of the displayed samples, where Fe was detected during the XRF measurements. All samples consist of microcline and albite (A-F), except for FSM-6 (G), which consists of orthoclase and albite. The TL intensities are normalised to the data point with the highest intensity.*

The thermoelectrically cooled EMCCD camera (Andor iXon Ultra 888) has a 1024 x 1024 sensor format and a pixel size of 13 μm. The spectral resolution of the system is 13 nm for all spectra recorded. The TL signal was recorded without any optical filters, to allow the emission spectrum to be recorded in a wide range of wavelengths ($\sim$280 to $\sim$720 nm). The grating of the spectrograph was set to 150 lines/mm and 500 nm blaze. The resulting spectra consist of 1024 bins, ranging from 280.68 nm to 718.94 nm, with a bin width of 0.43 nm. The electron-multiplying gain (EM) varied for individual measurements, dependent on the sample brightness, except for the unheated and heated material of FSM-13/FSM-13LH and FSM-6/FSM-6LH, where the EM gain was kept the same, to allow absolute signal intensity comparisons.

For TL spectra measurements, samples were placed on stainless steel cups and were beta irradiated using different doses (ranging from 60 to 1,000 Gy), to yield optimal signal output for the samples analysed. To be able to compare absolute intensities for the unheated and heated material of FSM-13 and FSM-13LH as well as FSM-6 and FSM-6LH the same sample mass (10 mg) and irradiation dose were used (400 Gy for FSM-13 and FSM-13LH; 200 Gy for FSM-6 and FSM-6LH). A 1000 s pause was inserted after irradiation to allow potential phosphorescence to decay prior to the TL measurement up to 380 °C (heating rate 1 °C/s). A second TL measurement was performed, immediately after the first and used for background subtraction. Repeat measurements were performed and the impact of changing the size of the given dose was tested, to check for reproducibility. All spectra were corrected for the response of the instrument.

6.3.3 IRSL fading measurements

Infrared stimulated luminescence (IRSL) fading measurements were performed using Risø DA20 TL/OSL readers equipped with ^{90}Sr/^{90}Y beta sources delivering $\sim$0.03 Gy/s and $\sim$0.1 Gy/s at the sample position. Sample material was placed on stainless steel cups. Typically, three aliquots per sample were measured.

Fading was measured for a signal in response to $\sim$90 Gy using a post-IR$_{50}$IRSL$_{225}$ protocol (Table 6.3) with a preheat at 250 °C for 60 s. The test dose signal was measured after a beta dose of $\sim$30 Gy. The IRSL$_{50}$ and post-IR IRSL$_{225}$ signals were recorded through a combination of a Schott BG39 and a Corning 7-59 filter (transmission greater than 10 % from 340 nm to 470 nm) using a UV-sensitive photo-multiplier tube (PMT). To ensure stable heating for the IRSL signal mea-

Table 6.3: *$PostIR_{50}IRSL_{225}$ protocol used for the determination of fading rates.*

Step	Details	Obtained
1	Beta dose ∼90 Gy	
2	Preheat for 60 s at 250 °C	
3	IR stimulation at 50 °C for 200 s ($IRSL_{50}$)	Lx_1 ($IRSL_{50}$)
4	IR stimulation at 225 °C for 300 s (post-IR $IRSL_{225}$)	Lx_2 ($postIR_{50}IRSL_{225}$)
5	Beta dose ∼30 Gy	
6	Preheat for 60 s at 250 °C	
3	IR stimulation at 50 °C for 200 s ($IRSL_{50}$)	Tx_1 ($IRSL_{50}$)
4	IR stimulation at 225 °C for 300 s (post-IR $IRSL_{225}$)	Tx_2 ($postIR_{50}IRSL_{225}$)

surements, the sample was held at the measurement temperature for 30 s, prior to switching on the IR LEDs. Due to the high signal intensities of FSM-13LH, a ND 1.0 filter was added to the blue filter combination. Delays between different fading measurements ranged from prompt measurements with delays of ∼500 to ∼800 s between the end of irradiation and luminescence measurement, depending on the instrument, to at least 1,000,000 s. For both signals investigated, the first 10 s were integrated as a signal, and background corrected by subtracting the signal integrated over the last 20 s of each decay curve. Fading rates, expressed as g-values, were calculated using the Analyst software (Duller, 2015) and all g-values presented are normalised to two days (Huntley and Lamothe, 2001).

6.4 Results

6.4.1 TL emission spectra

TL emission spectra of all samples investigated are recorded in the wavelength range from 280 to 720 nm and will thus give insights into recombination centres which emit in this part of the electromagnetic spectrum. The main emissions observed are centred at ∼300 nm, ∼400 nm, ∼550 nm and >700 nm (e.g. Krbetschek 1997). However, the intensity of these emissions and the temperature at which the emissions occur varies between samples. The emission spectra from the samples can be divided into four groups: those from single-phase feldspars,

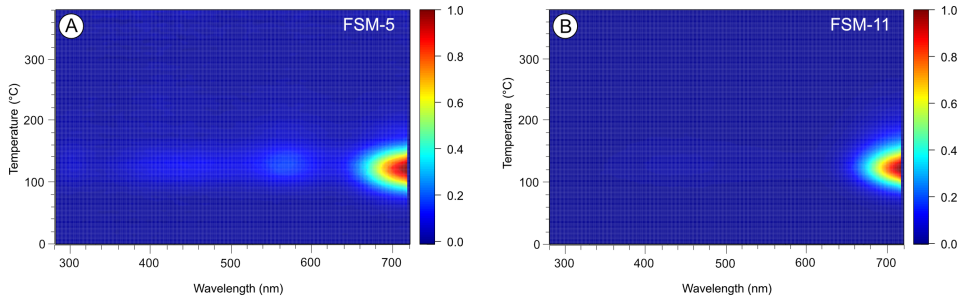

Figure 6.4: *TL emission spectra of perthites with coarse perthite lamella, visible with the naked eye: macroperthite. FSM-5 (A) is an amazonite sample, which shows twinning in the albite phase. XRF- measurements showed the presence of Fe in FSM-11 (B), which also is of orange colour in the microcline phase. The TL intensities are normalised to the data point with the highest intensity.*

perthite with lamellae visible with the naked eye (macroperthite), perthite with lamellae on the sub-optical scale (cryptoperthite) and feldspar extracted from sediments and bedrock, which may contain grains of numerous, (possibly different) feldspar group minerals.

The emission spectra recorded for the single-phase feldspars (FSM-13, Al-I and CLBR, Fig. 6.2), show their brightest emission around 550 nm. Additionally, all three samples show an emission around ∼300 nm. The two albite specimens (CLBR and Al-I) also show an emission in the blue (∼400 nm) and sample Al-I a tail of a red emission around ∼720 nm. The emissions at ∼300 and ∼550 nm of FSM-13 are most intense at ∼100 °C (Fig. 6.2). The temperatures at which the emissions of Al-I and CLBR show their maximum intensity differ slightly for each emission (Fig. 6.2). For Al-I, the peak of the red emission occurs at the lowest temperature (∼100 °C). This is followed by the relatively weak blue emission around ∼150 °C and the UV (∼300 nm) and yellow-green emission (∼550 nm) peak around ∼170 °C (Fig. 6.2). Whilst FSM-13 and Al-I show one TL peak at any given emitting wavelength, CLBR displays a number of TL peaks. The strongest emission for CLBR, the yellow-green, shows a low temperature peak around ∼95 °C, a second peak at ∼170 °C and a shoulder around ∼250 °C. Similar behaviour is also visible for the weaker blue emission around ∼400 nm. The UV emission (∼300 nm) also emits around ∼95 °C and around ∼170 °C (Fig. 6.2).

Perthite in this study are divided into macroperthite and cryptoperthite. Figure 6.3 shows the emission spectra for all cryptoperthite used in this study. The emission spectra of these samples commonly share a broad emission ranging from ∼350 to ∼600 nm. Mostly this emission occurs around ∼100 °C (Fig. 6.3), but

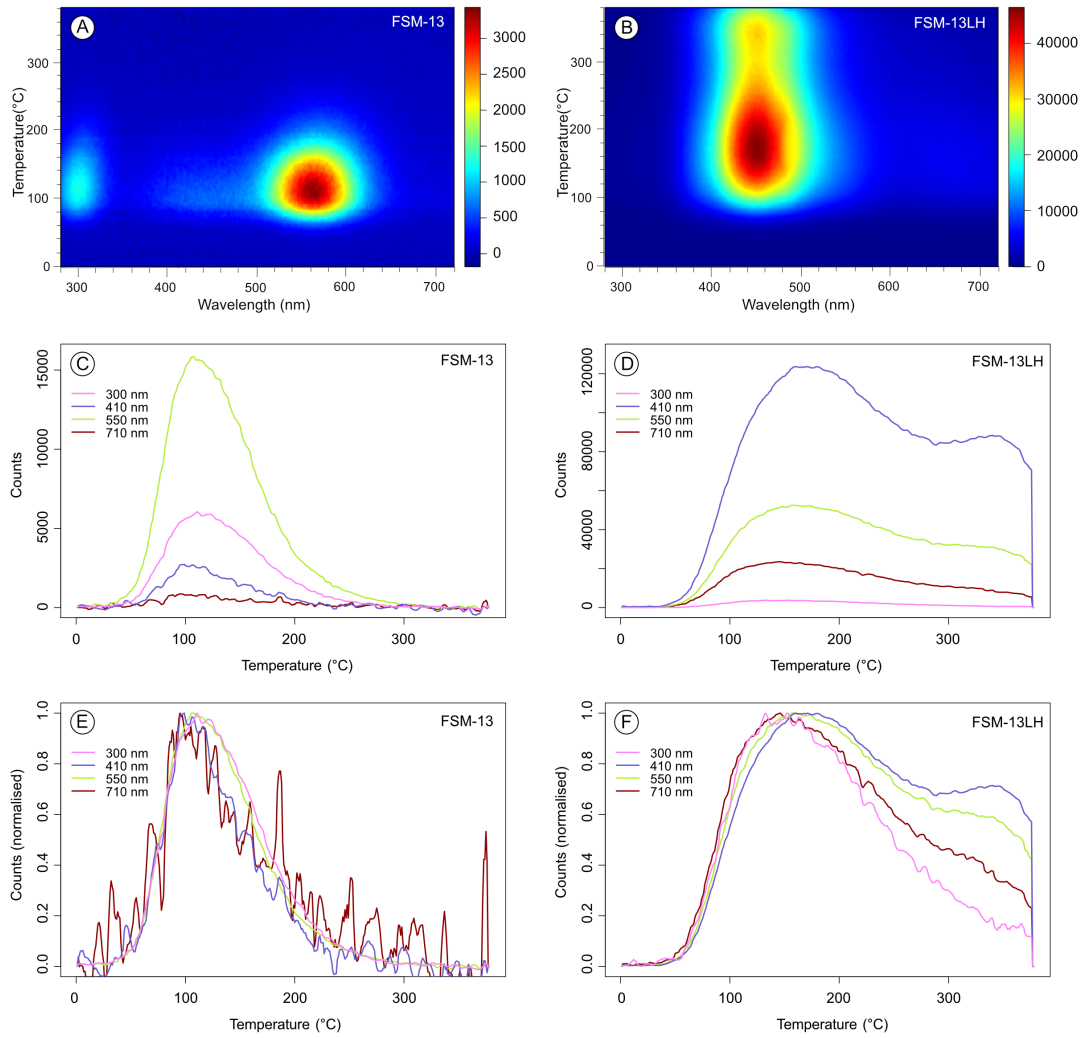

Figure 6.5: *Effect of heating sample FSM-13 (single phase microcline) at 1050 °C for 10 days. (A) TL spectra of the unheated material of FSM-13, (B) TL spectra of the heated fraction. (C) and (D) show the TL curve extracted from the TL spectra for different wavelengths for FSM-13 and FSM-13LH, respectively. (E) and (F) show the same data as (C) and (D), but normalised to the highest intensity for each TL curve. The measured intensities are absolute intensities in counts/0.4 nm/°C. For these measurements the same mass of sample material was used and the samples were measured during the same measurement sequence.*

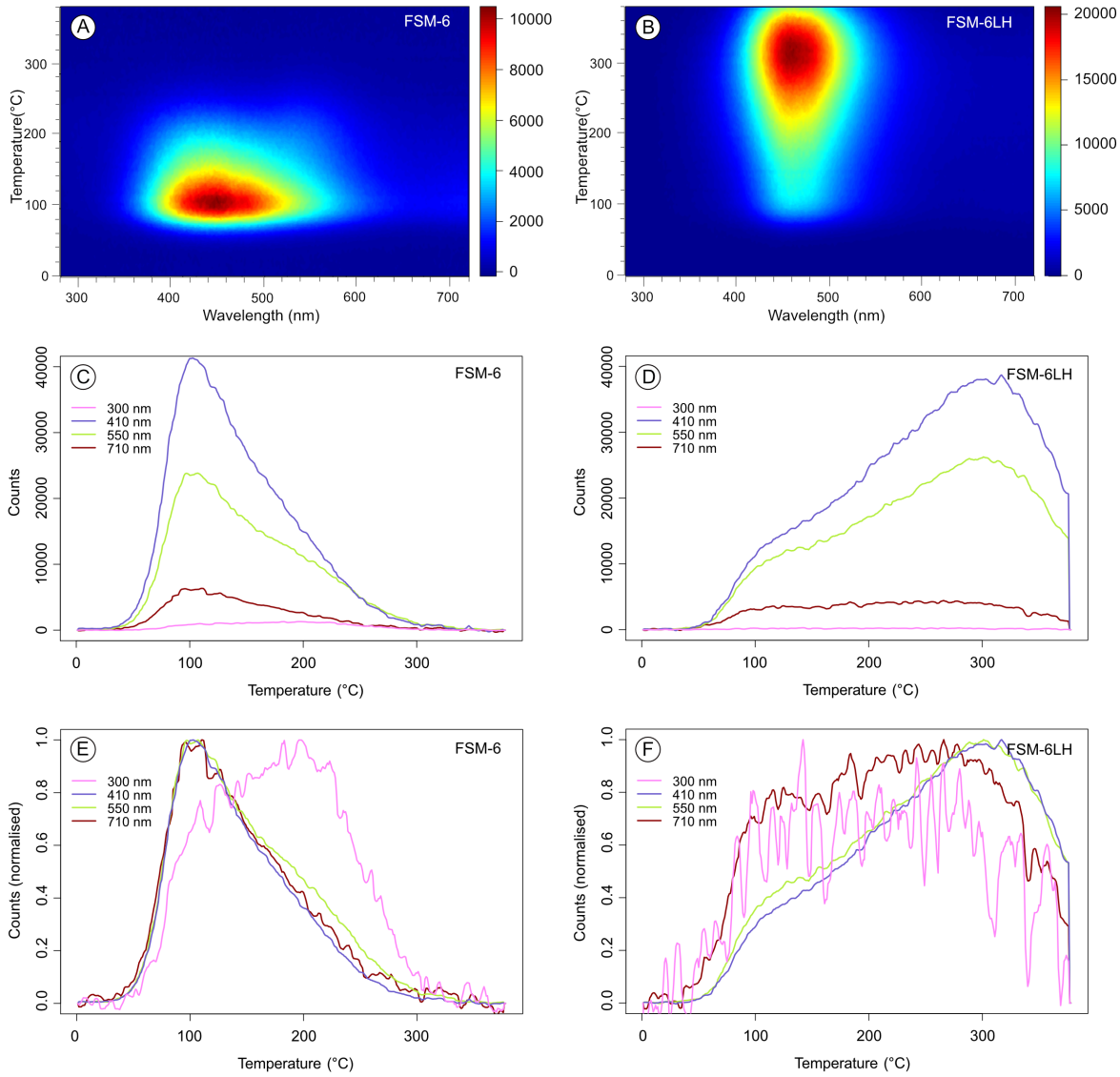

Figure 6.6: *Effect of heating sample FSM-6 (orthoclase and albite) at 1050 °C for 10 days. (A) TL spectra of the unheated material of FSM-6, (B) TL spectra of the heated fraction. (C) and (D) show the TL curve extracted from the TL spectra for different wavelengths for FSM-6 and FSM-6LH, respectively. (E) and (F) show the same data as (C) and (D), but normalised to the highest intensity for each TL curve. The measured intensities are absolute intensities (in cts/0.4 nm/°C). For these measurements the same mass of sample material was used and the samples were measured during the same measurement sequence.*

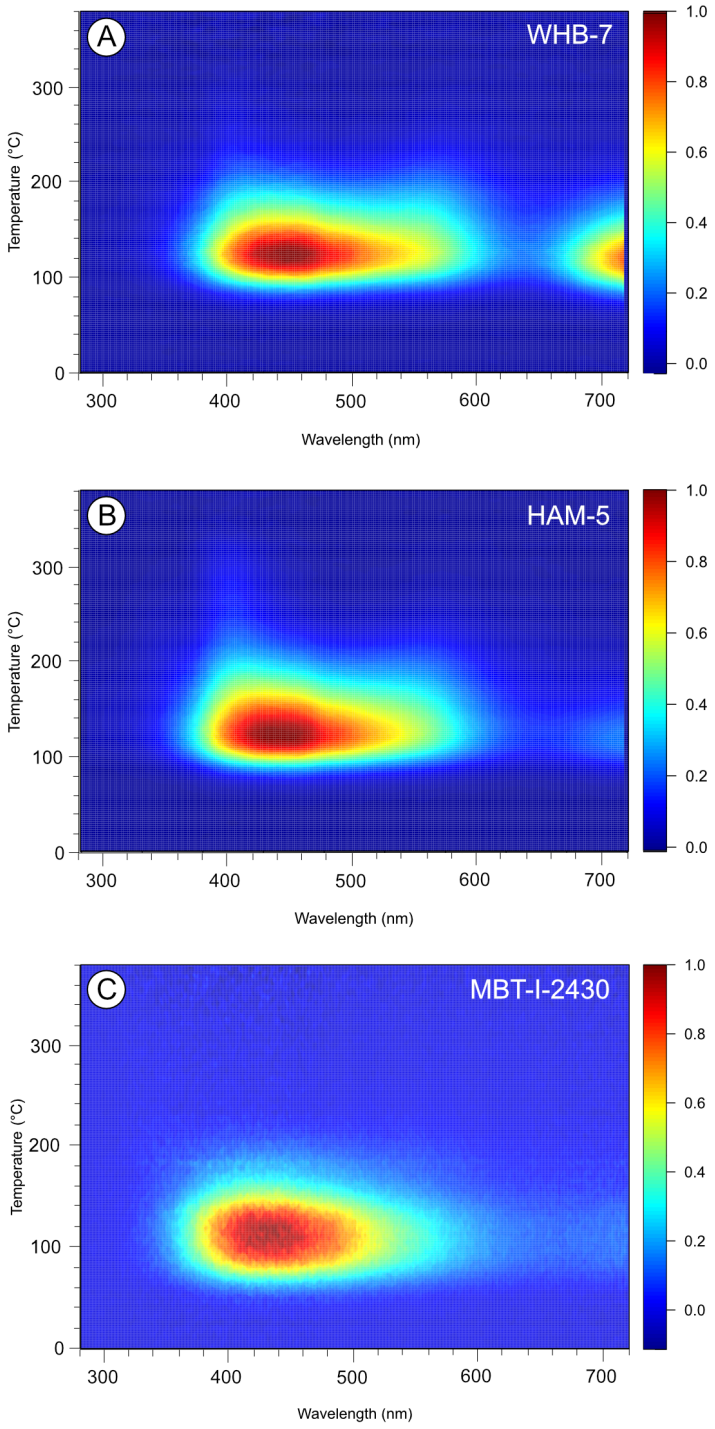

Figure 6.7: *TL emission spectra of alkali feldspars extracted from sediments (WHB-7, HAM-5) and bedrock (MBT-I-2430). The TL intensities are normalised to the data point with the highest intensity.*

R1-11A (Fig. 6.3B) and FSM-7 (Fig. 6.3F) also show an emission tail towards higher temperatures, resulting in a minor peak around ∼350 °C for the emission centred around ∼400 nm (Fig. 6.3). Additionally, all cryptoperthite show the short wavelength tail of a red emission (∼700 nm). This emission is strongest for sample FSM-15 (Fig. 6.3C), a pinkish cryptoperthite, which contains 0.2 wt% FeO.

The emission spectra of the macroperthite samples FSM-5 and FSM-11 (Fig. 6.4A and B) are similar to those of the cryptoperthite (Fig. 6.3), as the emissions of these two samples also occur at low temperature (∼100 °C). However, the macroperthite show a stronger red emission, compared to the broad blue to yellow emission, which was observed as being dominant in the majority of the cryptoperthite with the exception of FSM-15 (compare Fig. 6.3 and 4). All emissions for these two samples exhibit a peak at the same temperature (Fig. 6.4). Sample FSM-11 contains 0.5 wt% FeO, which is consistent with this dominant red emission, though the XRF data for FSM-5 registers no Fe above the detection limit.

Further investigation focuses on the effect of prolonged heating to 1050 °C in a furnace and subsequent rapid cooling on TL emission spectra of single-phase feldspars using samples FSM-6LH and FSM-13LH. Figure 6.6 shows the TL emission spectra for FSM-13 and FSM-13LH, the latter was artificially disordered through heating and rapid cooling as described in section 2.1. The TL spectrum of FSM-13 shows a dominant emission around ∼550 nm and a dimmer one around ∼300 nm (Fig. 6.5). A weak blue emission (∼400 nm) is also present. The maximum intensity of the TL spectrum of FSM-13 of just over 3000 cts/°C/0.4 nm is recorded around ∼560 nm and at ∼100 °C (Figs. 5A and C). The emission spectrum of FSM-13LH differs from the spectrum of FSM-13. FSM-13LH shows its main emission in the blue region of the spectrum, with a peak emission of over 40,000 cts/°C/0.4 nm around ∼150 °C (Fig 5B). Additionally, the signal now spreads towards higher temperatures, with the blue emission showing a secondary peak around 350 °C (Fig. 6.5D). A similar shift towards an emission at higher temperature is observed when comparing the TL emission spectra of FSM-6 and FSM-6LH (Fig. 6.6). Whilst FSM-6 already emitted in the blue region prior to disordering, the spectrum of disordered FSM-6LH shows intensities in the blue emission twice as large as recorded for its unheated counterpart and a narrowing of the emission peak is also observed (Fig. 6.6A and B). On the basis of the findings for samples FSM-13LH and FSM-6LH, we observe that disordering results in i)

an increase in the intensity of the blue luminescence and ii) a shift of the TL emission peak temperature towards higher temperatures.

To relate features observed from TL emission spectroscopy of single crystals to material generally used in luminescence dating or thermochronometry, TL spectra were recorded from feldspar extracts from sediments (WHB-7, Fig. 6.7A and HAM-5, Fig. 6.7B) and bedrock (MBT-I-2430, Fig. 6.7C). The emission spectra of these sand-sized feldspar grain mixtures show similar characteristics to the perthitic samples: TL maxima mainly around ∼100 °C, a broad emission ranging from ∼350 to ∼600 nm, and the tail of the red emission (Fig. 6.7).

6.4.2 Fading rates

Fading measurements were performed on all samples using a post-$IR_{50}IRSL_{225}$ protocol (Table 6.3). This protocol is chosen as it enables the measurement of two IRSL signals, one at low temperature (50 °C), and a second IRSL signal measured at elevated temperature (225 °C). The data from all $IRSL_{50}$ fading measurements, shown as Lx/Tx ratios after different delays, are presented in Figures S6.1 to S6.4 in the supplementary material. In agreement with results shown by Thomsen et al. (2008), we observe consistently lower fading rates for the post-IR $IRSL_{225}$ signal compared to the fading rates of the $IRSL_{50}$ signal of our samples (Table 6.4). We also observe a proportional relationship between the fading rates obtained for the two IRSL signals (Fig. 6.8A). Şahiner et al. (2017) have shown that the first IRSL measurement step in a post-IR IRSL or post-IR-MET procedure results in the recombination of electrons with the most proximal recombination centres, implying that fading of this first IRSL measurement can give information on the proximal recombination centres. All g-values (%/decade) presented in the following discussion are those obtained for the $IRSL_{50}$ signal. The average g-value (± 1 standard deviation) for each sample is shown as a function of their K-feldspar content in Figure 6.8B.

Single-phase albite (CLBR and Al-I) show the lowest fading amongst this suite of samples for the $IRSL_{50}$ signal, resulting in g-values of 0.36 ± 0.60 and 0.58 ± 0.30 %/decade respectively. The other single-phase sample (microcline FSM-13) was unique in giving very variable g-values, and hence nine sub-samples were measured. Five aliquots yielded g-values of less than 1%/decade (n = 5, average value is -0.23 ± 0.76 %/decade), one aliquot gave 1.14 ± 0.72 %/decade, and the three others showed fading rates between 2.00 and 3.12 %/decade. Considering

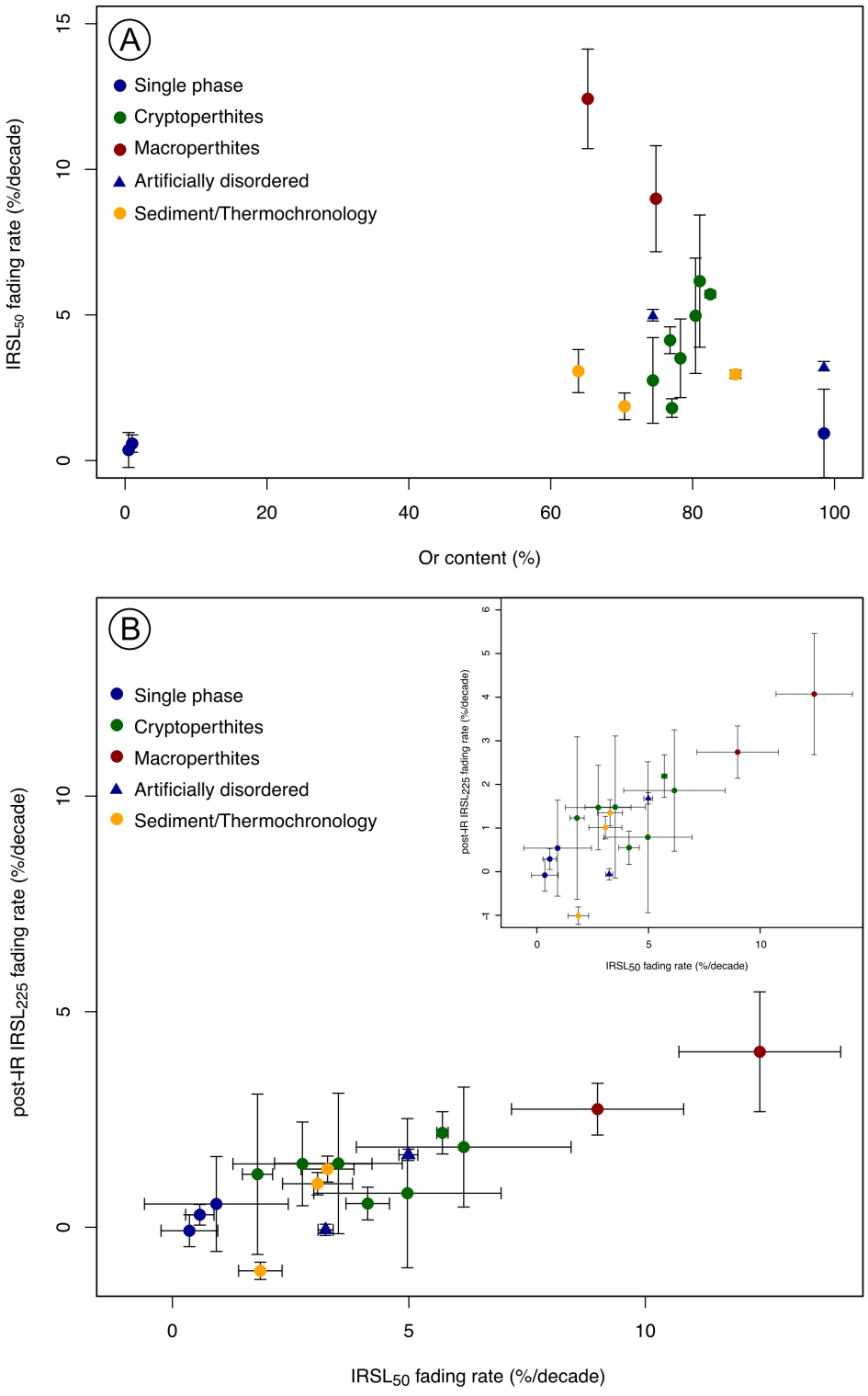

Figure 6.8: *A) Comparison of fading rates of the post-IR $IRSL_{225}$ signal and the $IRSL_{50}$ signal, obtained using the post-IRIRSL protocol. The inset is a close-up version of B. The data points in A and B are the average fading rate of the measured aliquots for each sample and the standard deviation of these measurements. B) Fading rates for the $IRSL_{50}$ signal measured using a post-$IR_{50}IRSL_{225}$ protocol, with a 250 °C preheat for 60 s.*

Table 6.4: *Fading rates for the two luminescence signals recorded using a post-IR_{50} $IRSL_{225}$ protocol. The samples were preheated to 250 °C for 60 s, prior to IRSL measurements.*

Group	Sample ID	Fading rate ($g_2$days, %/decade)	
		$IRSL_{50}$	Post-IR $IRSL_{225}$
Single phase			
	Al-I	0.58 ± 0.30	0.29 ± 0.24
	CLBR	0.36 ± 0.60	-0.08 ± 0.37
	FSM-13	0.93 ± 1.52	0.54 ± 1.10
Macroperthite			
	FSM-5	8.99 ± 1.82	2.74 ± 0.60
	FSM-11	12.42 ± 1.71	4.07 ± 1.39
Cryptoperthite			
	FSM-3	5.71 ± 0.12	2.19 ± 0.49
	R1-11A	6.72 ± 2.51	1.86 ± 1.39
	FSM-15	4.97 ± 1.98	0.79 ± 1.73
	FSM-14	3.51 ± 1.35	1.48 ± 1.63
	FSM-8	1.80 ± 0.32	1.23 ± 1.86
	FSM-7	4.13 ± 0.46	0.55 ± 0.38
	FSM-6	2.75 ± 1.47	1.47 ± 0.97
Artificially disordered			
	FSM-13LH	3.24 ± 0.16	-0.06 ± 0.13
	FSM-6LH	4.99 ± 0.20	1.68 ± 0.13
Sediments/rocks			
	HAM-5	1.86 ± 0.46	-1.01 ± 0.20
	WHB-7	3.07 ± 0.74	1.01 ± 0.26
	MBT-I-2430	3.28 ± 0.14	1.35 ± 0.30

the data together by calculating the average and standard deviation results in a very low g-value but with a high uncertainty (0.93 ± 1.52 %/decade, n = 9). The reason for the variability is not known, but we hypothesise that it is due to small-scale variations of structural state within the sample. Solid solutions of microcline are rarely found in nature and, although this sample was determined as single phase microcline, we cannot exclude perthitic patches or local Al disorder within the sample, which cannot be detected by XRD, but which may influence the fading rates.

The second group of samples are perthites. The macroperthites (FSM-5 and FSM-11) exhibit the highest fading rates (8.99 ± 1.82 %/decade, FSM-5, n = 3; and 12.42 ± 1.71 %/decade, FSM-11, n = 3). Cryptoperthite show fading rates

ranging from 1.80 ± 0.32 %/decade (FSM-8, n = 3) to 6.72 ± 2.51 %/decade (R1-11A, n = 3), but all the values are below those recorded for macroperthite.

The effect of framework Al disorder on the fading rate was explored using the artificially disordered samples FSM-6LH and FSM-13LH. Heated sample FSM-6LH showed an increase in fading (4.99 ± 0.20 %/decade, n = 3), compared to the unheated material (FSM-6, 2.75 ± 1.47 %/decade, n = 3); similarly, an increase in fading rate is observed for disordered FSM-13LH (3.24 ± 0.16 %/decade (n = 3), compared to 0.93 ± 1.52 %/decade (n = 9) for FSM-13).

Fading measurements were also performed on feldspars extracted from sediment and bedrock samples, to allow a comparison to material routinely used in luminescence dating studies. Here the fading rates measured are within the range of those determined for cryptoperthite. $IRSL_{50}$ fading rates for sediment samples WHB-7 and HAM-5 are 3.07 ± 0.74 and 1.86 ± 0.46 %/decade, respectively, while the fading rate for the bedrock sample MBT-I-2430 is 3.28 ± 0.14 %/decade.

6.5 Discussion

6.5.1 Thermoluminescence emissions in chemically and structurally different alkali feldspars

The TL emission spectra reveal significant differences in emission centres for single-phase feldspars in comparison to the perthites, particularly regarding the presence and intensity of the blue emission. Single-phase microcline (FSM-13) and albite (CLBR and Al-I) show little blue emission, compared to a relatively intense yellow-green emission, and additionally, an emission in the UV is present in the TL spectra of these samples (Fig. 6.2). In contrast, in perthitic feldspars (Fig. 6.3 and 4) the blue emission is dominant, only surpassed in intensity by the red emission in macroperthite (FSM-5 and FSM-11, Fig. 6.4) and cryptoperthite FSM-15 (0.2 wt% Fe, Fig. 6.3C). Disordering of samples FSM-13 (single-phase microcline) and FSM-6 (perthite: albite and orthoclase) results in an increase in the blue emission intensity recorded for FSM-13LH and FSM-6LH (Fig. 6.5 and 6.6). These results are consistent with the blue emission in alkali feldspars being associated with (dis)-ordering of the framework (Finch and Klein, 1999) and with the observed sensitisation of the blue emission due to alkali ion leakage caused by prolonged heating (Garcia-Guinea et al., 1999).

The defect giving rise to the blue emission in feldspars has been under investigation since the early 1980's and it has been suggested that it arises either due to a hole centre located on an Al-bridging oxygen ion (Al^{3+}-O^{1-}-Al^{3+}, e.g. Speit and Lehmann, 1982a; Finch and Klein, 1999) or (for plagioclase) due to Eu^{2+} substituting for Ca^{2+} on M-sites (Götze et al., 1999). A solution involving the silicate framework is the most likely and in alkali feldspar, where Ca^{2+} concentrations are minor (e.g. Table 6.1), a hole centre on an Al-bridging O is the most likely explanation and is consistent with the results of the present study. The Al-O-Al bridge will only occur where there is a degree of Al-Si framework disorder and it is hypothesised that it is stabilised at low temperatures by the addition of an electron hole (Speit and Lehmann, 1976; Speit and Lehmann, 1982b, Finch and Klein 1999). This is consistent with the spectra recorded for single-phase albite and microcline (CLBR, Al-I and FSM-13), which show very little blue TL emission (Fig. 6.2). Artificially induced disorder in the microcline sample FSM-13 enhances the blue emission in FSM-13LH, again supporting a model in which Al disorder is implicated in the blue emission intensity. However, the perthitic feldspars are two-phase mixtures of albite and microcline, both of which are partially ordered (Table 6.1). All perthitic feldspars investigated here emit in the blue (Fig. 6.3).

Garcia-Guinea et al. (1999) linked the UV emission to twin interfaces in the feldspar end-members. Albite and microcline both have multiple twinning, the result of the inversion from monoclinic to triclinic symmetry during cooling. Supporting this, Polymeris et al. (2013) observed more intense UV TL emission in ordered microcline, compared to disordered sanidine. Microcline shows repeated twinning, whilst sanidine does not (cf. Deer et al., 2013, p. 253). In perthite, the possible interfaces include not only the twins within each component phase, but also the interfaces between the K- and Na-feldspar end-members. According to heating experiments (Garcia-Guinea et al. 1999), luminescence attributed to twins contributes to the UV and part of the broad blue emission in perthite (cf. TL spectra in Fig. 6.3). This is supported by Correcher et al. (2000), who linked the blue luminescence in feldspars with alkali self-diffusion along interfaces offset by hole centres.

Perthitic feldspar FSM-6 shows an emission in the blue region. Prolonged heating of the sample material disordered both the Na- and K-feldspar end members, thereby reducing strain at the interfaces and (if accompanied by Na and K diffusion) creating single-phase alkali feldspar with a sanidine structure (FSM-

6LH, Table 6.1, Fig. 6.1D). Associated with this heating, we observe that the blue TL shifts towards higher temperatures, the emission band narrows and the signal intensity doubles from 10,000 to 20,000 cts/°C/0.4 nm (Fig. 6.6). This increase supports the suggestion that disorder of Si and Al is implicated in the intensity of the emission.

Whilst the blue emission is absent or weak in single-phase albite and microcline, the yellow-green emission (∼550 nm) is a key feature of their spectra (Fig. 6.2). Interestingly, this emission has been associated with Mn^{2+} substituting for Ca^{2+} on M-sites in plagioclase (e.g. Geake et al., 1971; Telfer and Walker, 1978), but it is also present in microcline sample FSM-13. This microcline sample has no detectable CaO content and hence it is unlikely that the emission around ∼550 nm of this sample is related to Mn^{2+}. Based on lifetime measurements of the green-yellow emission in a Na-feldspar sample, Prasad et al. (2016) argued that Mn^{2+} substituting for Ca^{2+} on M-sites cannot explain this emission; its recombination lifetime was too short for spin-forbidden Mn^{2+} transitions. Further work is needed to identify the physical nature of this recombination centre but we concur with the findings of Prasad et al. (2016) that it is inconsistent with Mn^{2+}.

6.5.2 Fading rates of chemically and structurally different alkali feldspars

Fading rates measured for the $IRSL_{50}$ signal (Table 6.4, Fig. 6.8B) of chemically and structurally different alkali feldspars range from 0.36 ± 0.6 %/decade (CLBR, n = 3) to 12.42 ± 1.71 %/decade (FSM-11, n = 3). Single-phase feldspars show the least fading, whilst macroperthites (FSM-5 and FSM-11) demonstrate the highest fading rates. Cryptoperthite show a similar fading behaviour to samples extracted from bedrock (MBT-I-2430) and sediment (WHB-7, HAM-5), and the fading rates observed for these, range in between those measured for macroperthite and single-phase feldspars (Table 6.4, Fig. 6.8B).

The low fading rates of the blue emission of the $IRSL_{50}$ signal for single-phase albite and microcline samples coincide with the relatively low blue luminescence signal intensities of these samples, in comparison to the green-yellow emission (compare Fig. 6.2, 3 and 4 for five samples as examples). Isolated centres are typically modelled in a manner whereby luminescence intensity and defect concentration are proportional (e.g. Speit and Lehmann, 1976, 1982a; Finch and

Klein, 1999). Fading, understood as tunnelling from an electron trap to a nearby recombination centre (e.g. Visocekas, 1985), is dependent on the density of recombination centres in the vicinity of the electron trap (Huntley, 2006). We infer that where the density of recombination centres increases, the distance between the electron trap as a donor and the recombination centre as the acceptor of the tunnelling electron will be smaller (Jain et al., 2012). In contrast, fewer blue recombination centres will result not only in lower signal intensities, but reduces the likelihood of a blue recombination centre being within tunnelling distance of an electron trap and lower fading rates will be observed.

Heating of samples FSM-13LH and FSM-6LH increases the blue luminescence emission intensity (Figs. 5 and 6), which we interpret as an increase in Al-Si disorder, populating Al-O-Al bridges and thus increasing the number of blue luminescence centres. Along with the increase in blue luminescence intensity, the fading rate increases (Table 6.4, Fig. 6.8B) from 0.93 ± 1.52 %/decade (FSM-13) to 3.24 ± 0.16 %/decade (FSM-13LH) and 2.75 ± 1.47 %/decade (FSM-6) to 4.99 ± 0.20 %/decade (FSM-6LH). Another interesting observation can be made when comparing Lx/Tx values of the unheated and heated samples FSM-13/FSM-13LH and FSM-6/FSM-6LH during the fading measurements (Figs. S1 A, B and S6.2 G, H). The unheated samples show very variable Lx/Tx values between the different aliquots (for instance ranging from ∼2.7 to 4.7 for FSM-13, Fig. S6.1 A) while the heated aliquots have very consistent values (∼2.7 for the prompt measurement of FSM-13LH, Fig. S6.1 B). It is also intriguing that the Lx/Tx values of the prompt measurement of the heated samples are similar to the long delay Lx/Tx values of the unheated counterparts. We cannot explain these two observations, but they may indicate that prolonged heating influences the luminescence sensitivity of the sample material, in a way which cannot be corrected by the test dose. A further observation based on the unheated and heated sample pairs is that while we observe an increase in fading of the $IRSL_{50}$ signal for the heated samples (FSM-13LH and FSM-6LH) compared with their unheated counterparts (FSM-13 and FSM-6), for the post-IR $IRSL_{225}$ signal there is no significant change in fading (Table 6.4). We conjecture that this could indicate that prolonged heating increases the density of recombination centres proximal to the electron trap (and this causes the increase in fading of the $IRSL_{50}$ signal and the increase in TL signal intensity), but that the heating does not change our ability to isolate distant recombination centres to select a signal with lower fading rate. The observations described above require further investigation

to be able to explain fully their implications.

Differences in fading rates are also observed for single-phase feldspars and perthites; the single-phase feldspars (CLBR, Al-I, FSM-13) show little signal loss, whereas perthites fade to varying, but significantly greater degrees. A first order model for the behaviour of a perthite is that its properties are a linear combination of the properties of the two end-members, since it is a physical intergrowth of the two end-member phases. However, this is clearly not the case. We can explain the anomalous behaviour of the intergrowths in two ways: a) the Na- and K-feldspar components of the perthites have greater disorder than the pure end-members or b) that the fading is related to the interfaces between the Na- and K-feldspar components. Hypothesis (a) is credible – we show above that increased disorder promotes fading. Furthermore, the lattice mismatch between Na- and K-feldspars increases as they become more ordered and lattice strain resists ordering (Deer et al., 2013, p. 263-264). Hence end member Na- and K-feldspar samples will have greater Al-Si order than a perthite grown under the same conditions. However, hypothesis (b) is also credible – interfaces are atypical regions which stabilise or destabilise defects and whose states of order may be locally different to the bulk feldspar. Garcia-Guinea et al. (1999) suggested that a component of the blue luminescence is related to twins. Interfaces may stabilise different defect types; two different defects that are unlikely to occur together in a random distribution in the bulk may occur in close proximity on an interface. This suggests that a single-phase solid solution may have different properties from a perthite of the same bulk composition.

To explore the two hypotheses a) and b) above, we contrast the behaviour of macroperthite and cryptoperthite. Cryptoperthites have nm-scale intergrowths and there is a greater volume of the feldspar bulk occupied by interface (Brown and Parsons, 1984b). Also, since the elastic interfacial strain in cryptoperthite is so high, one expects the Al-Si disorder to be greater in cryptoperthite compared to a macroperthite of the same composition. However, we observe that macroperthite show greater fading rates than cryptoperthite (Fig 6.8, Table 6.4). If the state of order (hypothesis a) were the sole driving factor, the opposite would have been observed. Our conclusion is therefore that the interfaces between the Na- and K-feldspar phases are implicated in the fading of perthite. In cryptoperthite, this may be elastic strain around the interfaces at which the two different feldspar lattices are forced to remain coherent (Brown et al. 1997). Since the fading rates of cryptoperthite and macroperthite are different, we explore the differences in

the morphologies of the interfaces. Boundaries between the K- and Na- feldspar phases in cryptoperthite are highly strained but fully coherent (i.e. the framework passes continuously from one phase to another, Brown et al., 1997). In macroperthite, interfaces are semi-coherent, i.e. the lattices are commonly joined across the boundary but not always, creating a region of dislocations and dangling bonds (e.g. Lee et al. 1995, Lee and Parsons, 1997; Parsons et al., 2015). Since fading is understood as the loss of charge from an electron trap to a nearby recombination centre, we hypothesise that a higher density of defects concentrated around semi-coherent interfaces in macroperthite are implicated in the higher fading rates. It may be that defect families such as regions of local disorder, dangling bonds, element substitutions etc. are all stabilised by their proximity to semi-coherent perthite interfaces, driving defects to cluster, which in turn allows direct defect-defect interactions. Interfaces are thus proposed as regions in which high defect densities result in shorter distances between donor and acceptor of a tunnelling electron (Jain et al., 2012).

Thus, we propose that fading in feldspars is not only a phenomenon of feldspars with a high-temperature (disordered) structural state, such as volcanic feldspars (e.g. Wintle, 1973; Visocekas and Zink, 1995; Visocekas et al., 2014; Guérin and Visocekas, 2015), but also related to perthite interfaces. Fading is controlled by the density of defects (Huntley, 2006) and defect clustering, which in turn is inferred to be influenced by (i) the degree of Si and Al ordering on the framework, (ii) the interfaces in perthites and (iii) elastic strain areas within the feldspar crystal. The only feldspars in this study, which show fading rates below 1 % are ordered single-phase albite and microcline. This observation of very low fading rates of ordered feldspars is in good agreement with suggestions by Visocekas and Zink (1995) and fading measurements on some microcline and albite specimen by Spooner (1994).

Our fading results show that for alkali feldspars, the structural state and the nature of interfaces within the crystal are more important than chemical composition when interpreting luminescence. The observation of increasing fading with increasing Al disorder on the framework is consistent with the properties of plagioclase in which fading rises almost linearly with increasing concentration of Ca^{2+} (Huntley and Lian 2006; Huntley et al. 2007) since Ca^{2+} substitution on the M-site is offset by increases in the Al content of the lattice and therefore Al-O-Al populations are dependent on Ca content.

Due to exsolution of feldspar during cooling in plutonic rocks (e.g. gran-

ite), most alkali feldspars in rocks and unconsolidated sediments are perthites (e.g. Deer et al., 2013). Unfortunately, perthites faded in our experiments. The feldspars extracted from unconsolidated sediments (WHB-7 and HAM-5) and from crushed bedrock material used in luminescence thermochronometry (MBT-I-2430) in this study exhibit fading rates of the $IRSL_{50}$ signal within the range seen for cryptoperthites in this study (Table 6.4, Fig. 6.8B). A similarity in fading rates and in TL emission spectra of sediment and thermochronometry samples and perthite is consistent with similar mechanisms playing a role in these sets of samples. The similarities hint that in feldspar grains extracted from sediment and rocks for optical dating and thermochronometry, Al-Si order, interface morphology and elastic strain are implicated both in the blue emission and in the fading rate.

6.6 Conclusion

The present study analysed the effects of chemistry, the number of phases present within a single crystal and the relative degree of framework disorder on TL emission spectra and fading rates of alkali feldspars. The investigated sample suite includes Na- and K-feldspar end members, perthites with K- and Na-feldspar lamellae on different scales, as well as material routinely used in luminescence dating studies and luminescence thermochronometry. We observed variations in the intensity of the blue luminescence emission and the rate of anomalous fading of the IRSL signal in our feldspars. We associate the blue luminescence with the blue recombination centre being located on an Al-O-Al bridge. The blue luminescence intensity increases as a function of the population of Al-O-Al bridges which increases with Al-Si disorder. Ordered, single-phase feldspars, such as albite and microcline, show very little fading, whereas the variations in fading rates in perthites are suggested to be linked to a) the degree of Si and Al order on the framework and b) defect clustering associated with semi-coherent perthite interfaces which modify the intensity of the blue emission and the extent to which this emission fades.

Our study highlights the importance of detailed mineralogical characterisation of feldspar samples in order to understand the complex drivers behind the variability seen in the blue luminescence intensity and anomalous fading rates of the IRSL signal. This paper combines information on sample chemistry, structural state, phases present, luminescence emissions and anomalous fading rate of

alkali feldspar. From these data we are able to differentiate between very low fading single-phase end members and perthitic feldspars which all fade. Interestingly, the same differentiation can be made from TL emission spectra, where single-phase feldspars show a more intense yellow-green emission, compared to the blue emission, while perthites show the opposite, with the blue emission being dominant. Perhaps it would be possible to identify those feldspar grains which are single phase (and hence likely to have a low fading rate) by looking for those with a high value for the ratio of the yellow-green to blue emission. Such measurements could be routinely feasible using automated filter changers in combination with an EMCCD camera, and may avoid the need for costly and time consuming chemical and structural analyses of individual grains.

Acknowledgements

SR would like to thank Aberystwyth University for funding her PhD research through an AberDoc PhD scholarship (Aberystwyth University). Sample WHB-7 was taken during a field campaign in May 2018, which was made possible by a RGS-IBG postgraduate research grant awarded to SR. Sample HAM-5 was taken in the framework of the QuakeRecNankai project, funded by the Belgian Science Policy Office (BELSPO BRAIN-be BR/121/A2). We thank Dr Javier Garcia-Guinea for CLBR and Dr Renske Lambert for MBT-I-2430. The authors would like to thank Prof Mike Henderson (Manchester University) for facilitating the introduction between some of the authors. SR would like to thank Karsten Bracht-Nielsen (Technical University of Denmark) for technical support with the Andor Spectrometer, and Andrew Brown (Aberystwyth University) for laboratory assistance during the heating experiments. We would like to thank three anonymous referees for their constructive comments, which improved the manuscript.

References

Baril, M.R., 2004. CCD imaging of the infra-red stimulated luminescence of feldspar. Radiation Measurements 38, 81-86.

Brown, W.L., Parsons, I., 1984a. The nature of potassium feldspar, exsolution microtextures and development of dislocations as a function of composition in perthitic alkali feldspars. Contributions to Mineralogy and Petrology 86, 335-341.

Brown, W.L., Parsons, I., 1984b. Exsolution and coarsening mechanisms and kinetics in an ordered cryptoperthites series. Contributions to Mineralogy and Petrology 86, 3-18.

Brown, W.L., Lee, M.R., Waldron, K.A., Parsons, I., 1997. Strain-driven disordering of low microcline to low sanidine during partial phase separation in microperthites. Contributions to Mineralogy and Petrology 127, 305-313.

Bussy, F., Von Raumer, J.F., 1993. U-Pb dating of Palaeozoic events in the Mont-Blanc crystalline massif, western Alps. Terra. Nova Abstracts 5, 382.

Bussy, F., Schaeltegger, U., Marro, C., 1989. The age of the Mont Blanc granite (western Alps): a heterogenous isotopic system dated by Rb-Sr whole rock determination on its microgranular enclaves. Schweizer Mineralogische und Petrologische Mitteilungen 69, 3–13.

Buyleart, J.-P., Jain, M., Murray, A.S., Thomsen, K.J., Thiel, C., Sohbati, R., 2012. A robust feldspar luminescence dating method for Middle and Late Pleistocene sediments. Boreas 41, 435-451.

Cassadanne, J.P., Roditi, M., 1996. The location, geology and mineralogy of gem tourmalines in Brazil. Journal of Gemmology 25 (4), 263–298.

Correcher, V., Garcia-Guinea, J., Delago, A., 2000. Influence of preheating treatment on the luminescence properties of adularia feldspar ($KAlSi_3O_8$). Radiation Measurements 32, 709-715.

Cunningham, G.J., 1981. Petrology and geochemistry of Lewisian pegmatites and granites, N.W., Scotland. PhD thesis, Imperial College London, United Kingdom.

Deer, W.A., Howie, R.A., Zussman, J., 2013. An introduction to the rock-forming minerals. Third Edition. Mineralogical Society of Great Britain and Ireland.

Duller, G.A.T., 2015. The Analyst software package for luminescence data: overview and recent improvements. Ancient TL 33, 35-42.

Finch, A.A., Klein, J., 1999. The causes and petrological significance of cathodoluminescence emissions from alkali feldspars. Contributions to Mineralogy and Petrology 135, 234-243.

Garcia-Guinea, J., Rendell, H.M., Sanchez-Muñoz, L., 1996. Luminescence spectra of alkali feldspars: some relationships between structural features and luminescence emission. Radiation Protection Dosimetry 66, 395-398.

Garcia-Guinea, J., Townsend, P.D., Sanchez-Muños, Rojo, J.M., 1999. Ultraviolet-blue ionic luminescence of alkali feldspars from bulk and interfaces. Physics and Chemistry of Minerals 26, 658-667.

Geake, J.E., Walker, G., Mills, A.A., Garlick, G.F.J., 1971. Luminescence of Apollo lunar samples. Proceedings of the Second Lunar Science Conference 3, 2265-2275.

Govindaraju, K., 1995. Update (1984-1995) on two GIT-IWG geochemical reference samples: Albite from Italy, Al-I and iron formation sample from Greenland, IF-G. Geostandards Newsletter 19, 55-96.

Guérin, G., Visocekas, R., 2015. Volcanic feldspars anomalous fading: Evidence for two different mechanisms. Radiation Measurements 81, 218-223.

Harrison, T.N., Parsons, I., Brown, P.E., 1990. Mineralogical evolution of fayalite-bearing rapakivi granites from the Prins Christians Sund pluton, South Greenland. Mineralogical Magazine 54, 57-66.

Huntley, D.J., Lamothe, M., 2001. Ubiquity of anomalous fading in K-feldspars and the measurement and correction for it in optical dating. Canadian Journal of Earth Sciences 38, 1093-1106.

Huntley, D.J., 2006. An explanation of the power-law decay of luminescence. Journal of Physics: Condensed Matter 18, 1359-1365.

Huntley, D.J., Lian, O.B., 2006. Some observations on tunnelling of trapped electrons in feldspars and their implications for optical dating. Quaternary Science Reviews 25, 2503-2512.

Huntley, D.J., Baril, M.R., Haider, S., 2007. Tunnelling in plagioclase feldspars. Journal of Physics D: Applied Physics 40, 900-906.

Jain, M., Guralnik, B., Andersen, M. T., 2012. Stimulated luminescence emission from localized recombination in randomly distributed defects. Journal of Physics: Condensed Matter 24, 385-402.

Jenkins, G.T.H., Duller, G.A.T., Roberts, H.M., Chiverrell, R.C., Glasser, N.F., 2018. A new approach for luminescence dating glaciofluvial deposits – High precision optical dating of cobbles. Quaternary Science Reviews 192, 263-273.

Kars, R.H., Wallinga, J., Cohen, K.M., 2008. A new approach towards anomalous fading correction for feldspar IRSL dating – tests on samples in field saturation. Radiation Measurements 43, 786-790.

King, G.E., Herman, F., Guralnik, B., 2016. Northward migration of the eastern Himalayan syntaxis revealed by OSL thermochronometry. Science 353, 800-804.

Kook, M.H., Lapp, T., Murray, A.S., Thiel, C., 2012. A Risø XRF Attachment for Major Element Analysis of Aliquots of Quartz and Feldspar Separates. UK Luminescence and ESR Meeting, Aberystwyth, pp. 37 September 2012 (abstract).

Krbetschek, M.R., Götze, J., Dietrich, A., Trautmann, T., 1997. Spectral infor-

mation from minerals relevant for luminescence dating. Radiation Measurements 27, 695-748.

Lambert, R., 2018. Investigating Thermal decay in K-Feldspar for the Application of IRSL Thermochronometry on the Mont Blanc massif. University of Lausanne.

Lapp, T., Kook, M., Murray, A.S., Thomsen, K.J., Buylaert, J.-P., Jain, M., 2015. A new luminescence detection and stimulation head for the Risø TL/OSL reader. Radiation Measurements 81, 178-184.

Lee, M.R., Waldron, K.A., Parsons, I., 1995. Exsolution and alteration microtextures in alkali feldspar phenocrysts from the Shap granite. Mineralogical Magazine 59, 63-78.

Lee, M.R., Parsons, I., 1997. Dislocation formation and albitization in alkali feldspars from the Shap Granite. Mineralogical Magazine 82, 557-570.

Li, B., Li, S.-H., 2011. Thermal stability of infrared stimulated luminescence of sedimentary K-feldspar. Radiation Measurements 46, 29-36.

Neudorf, C.M., Roberts, R.G., Jacobs, Z., 2012. Sources of overdispersion in a K-rich feldspar sample from north-central India: Insights from De, K content and IRSL age distributions for individual grains. Radiation Measurements 47, 696-702.

Parsons, I., 1978. Feldspars and fluids in cooling plutons. Mineralogical Magazine 42, 1-17.

Parsons, I., 2010. Feldspars defined and described: a pair of posters published by the Mineralogical Society. Sources and supporting information. Mineralogical Magazine, 74(3), 529-551.

Parsons, I., FitzGerald, J.D., Lee, M.R., 2015. Routine characterization and interpretation of complex alkali feldspar intergrowth. American Mineralogist 100, 1277-1303.

Polymeris, G.S., Theodosoglou, E., Kitis, G., Tsirliganis, N.C., Koroneos, A., Paraskevopoulos, K.M., 2013. Preliminary results on structural state characterization of K-feldspars by using thermoluminescence. Mediterranean Archaeology and Archaeometry 13, 155-161.

Prasad, A.K., Lapp, T., Kook, M., Jain, M., 2016. Probing luminescence centres in Na rich feldspars. Radiation Measurements 90, 292-297.

Prasad, A.K., 2017. Understanding defect related luminescence processes in wide bandgap materials using low temperature multi-spectroscopic techniques. PhD Thesis, Technical University of Denmark, 196 p.

Reimann, T., Thomsen, K.J., Jain, M., Murray, A.S., Frechen, M., 2012. Single-grain dating of young sediments using the pIRIR signal from feldspar. Quaternary Geochronology 11, 28-41.

Rendell, H.M., Clarke, M.L., 1997. Thermoluminescence, radioluminescence and cathodoluminescence spectra of alkali feldspars. Radiation Measurements 27, 263-272.

Riedesel, S., Brill, D., Roberts, H.M., Duller, G.A.T., Garrett, E., Zander, A.M., King, G.E., Tamura, T., Burow, C., Cunningham, A., Seeliger, M., De Batist, M., Heyvaert, V.M.A., Fujiwara, O., Brückner, H. and the QuakeRecNankai Team, 2018. Single-grain luminescence chronology of historical extreme-wave event deposits recorded in a coastal lowlands, Pacific coast of central Japan. Quaternary Geochronology 45, 37–49.

Riedesel, S., King, G.E., Prasad, A.K., Kumar, R., Finch, A.A., Jain, M., 2019. Optical determination of the width of the band-tail states, and the excited and ground state energies of the principal dosimetric trap in feldspar. Radiation Measurements 125, 40-51.

Şahiner, E., Kitis, G., Pagonis, V., Meriç, N., Polymeris, G.S., 2017. Tunnelling recombination in conventional, post-inrared and post-infrared multi-elevated temperature IRSL signals in microcline feldspar. Journal of Luminescence 188, 514-

523.

Sanderson, D.C.W., 1988. Fading of thermoluminescence in feldspars: Characteristics and corrections. Nuclear Tracks and Radiation Measurements 14, 155-161.

Smedley, R.K., Glasser, N.F., Duller, G.A.T., 2016. Luminescence dating of glacial advances at lago Buenos Aires (∼46°S), Patagonia. Quaternary Science Reviews 134, 59-73.

Speit, B., Lehmann, G., 1976. Hole centers in the feldspar sanidine. Physica Status Solidi 36, 471-481.

Speit, B., Lehmann, G., 1982a. Radiation Defects in Feldspars. Physics and Chemistry of Minerals 8, 77-82.

Speit, B., Lehmann, G., 1982b. A comparative study of thermoluminescence and isothermal destruction of radiation defects in feldspars. Journal of Luminescence 27, 127-136.

Spooner, N.A., 1992. Optical dating: Preliminary results on the anomalous fading of luminescence from feldspars. Quaternary Science Reviews 11, 139-145.

Spooner, N.A., 1994. The anomalous fading of infrared-stimulated luminescence from feldspars. Radiation Measurements 23, 625-632.

Stevens, T., Buylaert, J.-P., Thiel, C., Ujavri, G., Yi, S., Murray, A.S., Frechen, M., 2018. Ice-volume-forced erosion of the Chinese Loess Plateau global Quaternary stratotype site. Nature Communications 9: 983.

Telfer, D.J., Walker, G., 1978. Ligand field bands of Mn^{2+} and Fe^{3+} luminescence centres and their site occupancy in plagioclase feldspars. Modern Geology 6, 199-210.

Templer, R.H., 1986. The localised transition model of anomalous fading. Radiation Protection Dosimetry 17, 493-497.

Thiel, C., Buylaert, J.-P., Murray, A.S., Terhorst, B., Hofer, I., Tsukamoto, S., Frechen, M., 2011. Luminescence dating of the Stratzing loess profile (Austria) – Testing the potential of an elevated temperature post-IR IRSL protocol. Quaternary International 234, 23-31.

Thomsen, K.J., Murray, A.S., Jain, M., Bøtter-Jensen, L., 2008. Laboratory fading rates of various luminescence signals from feldspar-rich sediment extracts. Radiation Measurements 43, 1474-1486.

Trauerstein, M., Lowick, S., Preusser, F., Rufer, D., Schlunegger, F., 2012. Exploring fading in single grain feldspar IRSL measurements. Quaternary Geochronology 10, 327-333.

Ussher, W.A.E., Barrow, G., McAlister, D.A., 1909. The Geology of the country around Bodmin and St. Austell. Memoirs of the Geological Survey England and Wales – Explanation of Sheet 347.

Valla, P.G., Lowick, S.E., Herman, F., Champagnac, J.-D., Steer, P., Guralnik, B., 2016. Exploring $IRSL_{50}$ fading variability in bedrock feldspars and implications for OSL thermochronometry. Quaternary Geochronology 36, 55-66.

Visocekas, R., 1985. Tunnelling radiative recombination on labradorite: Its association with anomalous fading of thermoluminescence. Nuclear Tracks and Radiation Measurements 10, 521-529.

Visocekas, R., Zink, A., 1995. Tunneling afterglow and point defects in feldspars. Radiation Effects and Defects in Solids 134, 265-272.

Visocekas, R., Zink, A., 1999. Use of the red TL emission band of alkali feldspars for dosimetry and dating. Quaternary Geochronology 18, 271-278.

Visocekas, R., Barthou, C., Blanc, P., 2014. Thermal quenching of far-red Fe^{3+} thermoluminescence of volcanic K-feldspars. Radiation Measurements 61. 52-73.

Wintle, A.G., 1973. Anomalous fading of thermoluminescence in mineral samples. Nature 245, 143-144.

Wintle, A.G., 1977. Detailed study of a thermoluminescent mineral exhibiting anomalous fading. Journal of Luminescence 15, 385-393.

Xiao, Y., Kirkpatrick, J., Hay, R.L., Kim, Y.J., Phillips, B.L., 1995. Investigation of Al,Si order in K-feldspars using ^{27}Al and ^{29}Si MAS NMR. Mineralogical Magazine 59, 47-61.

Supplementary Material - Exploring sources of variation in thermoluminescence emissions and anomalous fading in alkali feldspars

This chapter contains supplementary material to the article in revision for publication in *Radiation Measurements* as

Riedesel, S., Bell, A.M.T., Duller, G.A.T., Finch, A.A., Jain, M., King, G.E., Pearce, N.J., Roberts, H.M., 2021. *Exploring sources of variation in thermoluminescence emissions and anomalous fading in alkali feldspars.* Radiation Measurements 141, 106541.

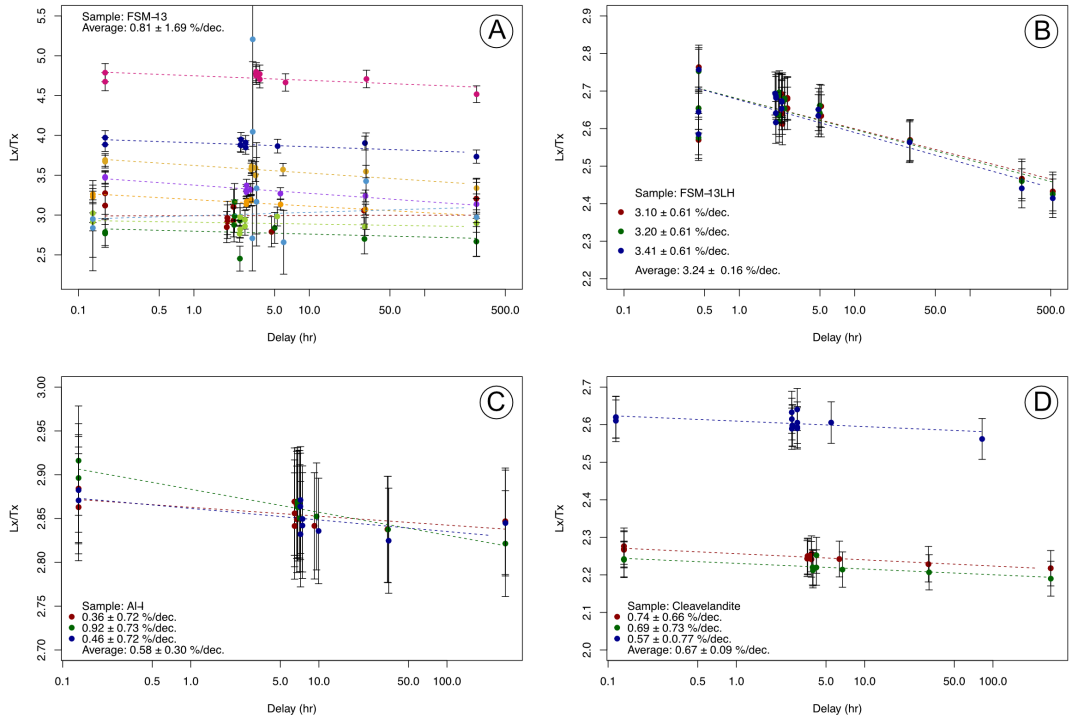

Figure S6.1: *Fading results as Lx/Tx versus delay time for FSM-13 (A), FSM-13LH (B), Al-I (C) and CLBR (D).*

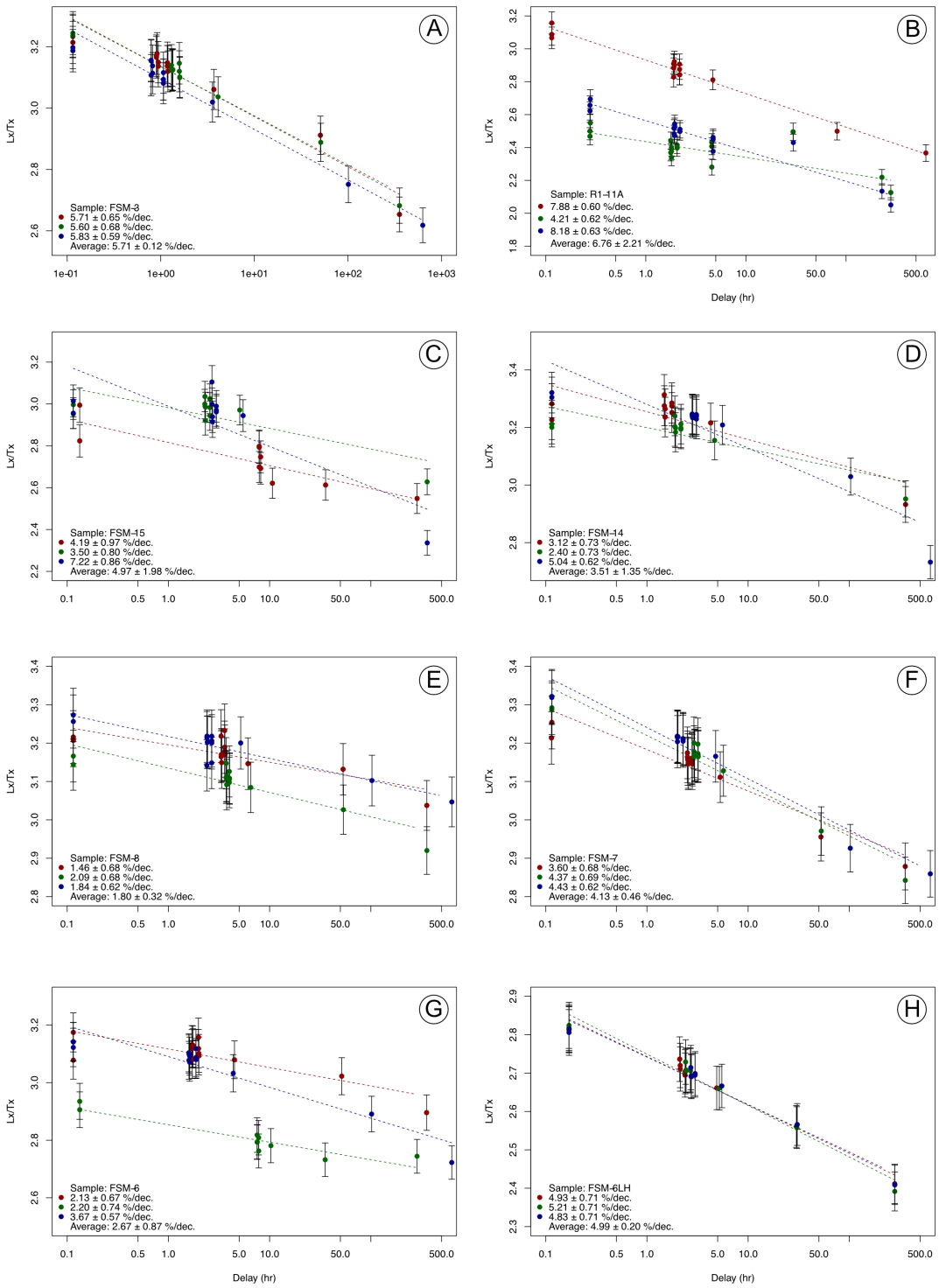

Figure S6.2: *Fading results as Lx/Tx versus delay time for FSM-3 (A), R1-11A (B), FSM-15 (C) FSM-14 (D), FSM-8 (E), FSM-7 (F), FSM-6 (G) and FSM-6LH (H).*

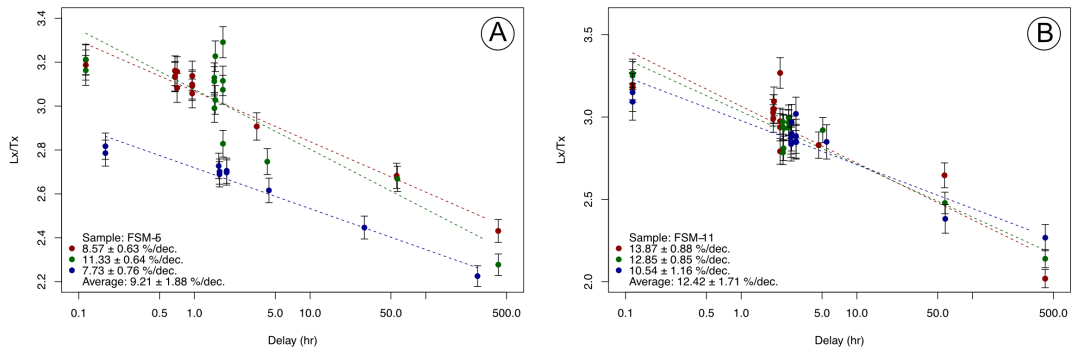

Figure S6.3: *Fading results as Lx/Tx versus delay time (hours) for FSM-5 (A) and FSM-11 (B).*

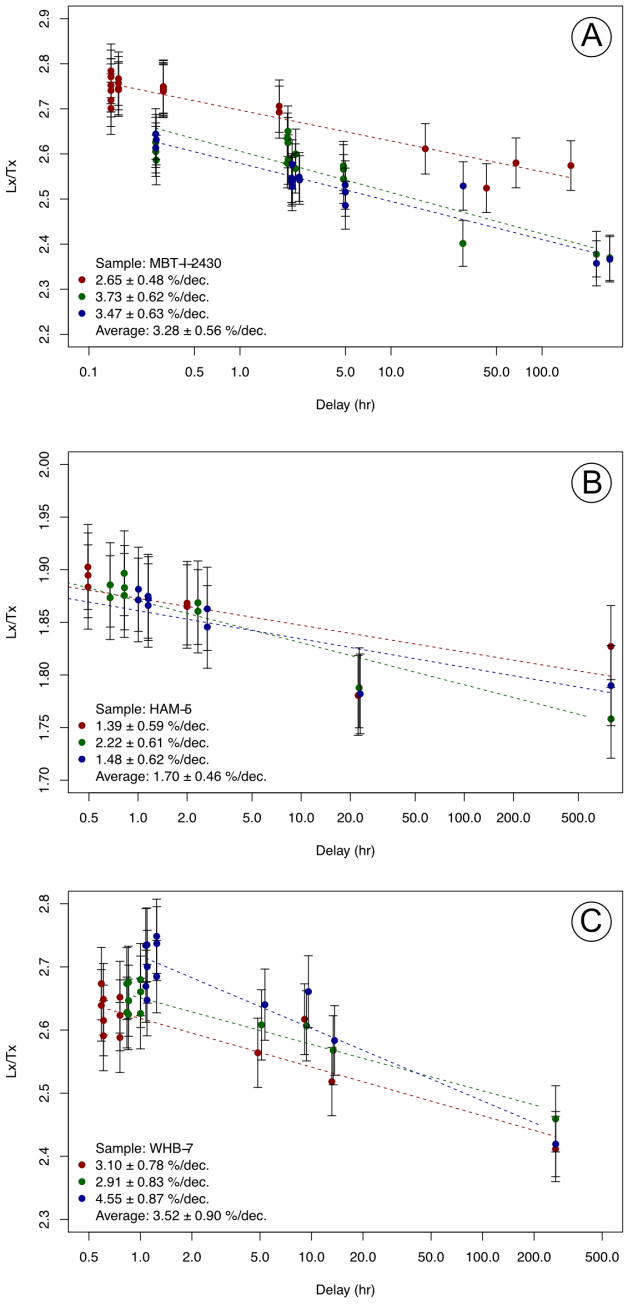

Figure S6.4: *Fading results as Lx/Tx versus delay time (in hours) for MBT-I-2430 (A), HAM-5 (B) and WHB-7 (C).*

Seven

Conclusions and outlook

The overall aim of this thesis was to provide a better understanding of luminescence production in feldspars by exploring luminescence properties of chemically and structurally different feldspars. Luminescence is the product of trapping (or re-trapping) of electrons within defects functioning as electron trapping centres, or of the recombination of electrons and holes. Both processes result in the emission of luminescence, if the relaxation of electrons from an excited state within an electron trap during trapping or within the hole trap during recombination is radiative (Bøtter-Jensen et al., 2003, p. 1–2; Yukihara and McKeever, 2011, p. 1–4). To be able to improve our understanding of luminescence production in feldspar, this thesis focussed on electron trapping and recombination centres and the electron transitions involved in trapping and recombination. This thesis combined a detailed literature review (Chapter 3) with experimental work (Chapter 4 to Chapter 6) consisting of excitation spectroscopy, photoluminescence measurements, various types of emission spectroscopy and fading measurements of the IRSL signal. Here the findings of each of the chapters of this thesis are summarised. Additionally, the overall conclusions are drawn by answering the research questions introduced in Chapter 1 and potential directions for further research are discussed.

7.1 Summary of individual chapters

Chapter 3: Excitation and emission spectroscopy of feldspars — Insights into luminescence production in feldspars

Chapter 3 summarised the current state of knowledge on excitation and emis-

sion spectroscopy of feldspars and how these methods have been used to constrain physical parameters, such as defects responsible for certain luminescence emissions, that govern luminescence production in feldspars. It has been shown that excitation spectroscopy is a powerful tool to constrain defect related parameters, e.g. trap depth and optical resonances associated with electron traps and hole traps and the band gap energy of feldspars. Based on excitation spectroscopy, the band-gap in feldspar is estimated at ∼7.7 eV (Malins et al., 2004). The ground state of a type of electron trap seems to be located ∼2 eV (e.g. Kars et al., 2013) below the edge of the conduction band and the first excited state of this trap is located at an energy level of ∼1.45 eV (e.g. Baril and Huntley, 2003) above the ground state of the trap.

Various types of emission spectroscopy (e.g. thermoluminescence, infrared stimulated or radioluminescence emission spectroscopy) have revealed emissions in the UV, blue, green-yellow, red and infrared region of the electromagnetic spectrum (e.g. Krbetschek et al., 1997). The actual crystal defects have only been identified for a few of these emissions. The red emission has been correlated to Fe^{3+} ions substituting for Al^{3+} ions on tetrahedral sites in the crystal (e.g. Telfer and Walker, 1978; Prasad and Jain, 2018). It has been proposed that the green-yellow emission arises due to Mn^{2+} (Telfer and Walker, 1978), however this is still under debate (Prasad et al., 2016). For the blue luminescence emission different sources for alkali feldspar and plagioclase have been proposed, with a hole centre on Al-bridging O ions as the defect responsible for the blue emission in alkali feldspar (Finch and Klein, 1999), and potentially Eu^{2+} substituting for Ca^{2+} ions on M sites in plagioclase (Götze et al., 1999). For the UV emission no actual defect has been proposed, but the emission is likely to be linked to metastable Na accumulation at the interfaces, and could thus be explained by ion motion rather than electron-hole-recombination, which would also explain the low stability of the signal (e.g. Garcia-Guinea et al., 1999).

The review in Chapter 3 showed open questions, some of which were explored in the framework of this thesis, in particular questions regarding the properties of electron trapping centres, electron trap ground and excited state energies, the width and influence of the band-tail states, but also regarding the blue emission and anomalous fading of this emission.

Chapter 4: Optical determination of the width of the band-tail

states, and the excited and ground state energies of the principal dosimetric trap in feldspars

In this chapter parameters involved in the eviction of trapped electrons from electron traps in feldspar were explored. The combined use of excitation and emission spectroscopy enabled the measurements of electron trap gound and excited state energies and the width of the sub-conduction band-tail states in feldspars. From the excitation spectra it became evident that the IR resonance peak is invariant between samples and located 1.44 ± 0.02 eV above the ground state. This result is in good agreement with previous experimental work (e.g. Baril and Huntley, 2003), and suggestions made on the basis of quantum mechanics (Poolton et al., 1995; Poolton et al., 2002). Minimum trap depth values were obtained for most of the samples ranging from 1.99 eV to 2.15 eV. Whilst only little variation between samples was seen for the trap depth and the IR resonance peak, sample-to-sample variabilities in band-tail states width were observed. Two different methods were used to obtain information on the width of the sub-conduction band-tail states: (1) parts of the excitation spectrum were fitted to obtain the width of the sub-conduction band-tails states accessible from the ground state of the trap (ΔE) and (2) an excitation energy-dependent emission observed in photoluminescence experiments was used to constrain the full width of the sub-conduction band-tail states (E_u). However, for the latter the obtained values should be regarded as the densest 37 % of the band-tail states, since in this method the width corresponds to 1/e. Values for ΔE range from 0.22 eV to 0.47 eV and for E_u from 0.26 eV to 0.81 eV. Interestingly the difference between ΔE and E_u is greater for samples with low K-content, potentially indicating that recombination efficiency could vary more with band-tail energy in K-poor feldspars. The similarities observed in ground and excited state energies of the electron trap in feldspar led to the suggestion that the defect functioning as the electron trap in feldspar is located on the Si,Al-framework. Variable widths of the band-tail states potentially indicate that the band-tail states might influence the stability of trapped electrons in feldspars.

Chapter 5: Site-selective characterisation of electron trapping centres in relation to chemistry, structural state and mineral phases present in single crystal alkali feldspars

The experiments presented in this chapter are based on the findings in Chapter 4. Chapter 4 focussed on chemically different samples, but used mainly grain mixtures extracted from sediments and bedrock. In contrast, samples used in this chapter are single-crystal specimens, which allowed an investigation of electron trap parameters of samples of different structural state, single phase specimen and perthites, and of different chemical compositions. Here the novel technique of IRPL excitation-emission spectroscopy (Kumar et al., 2020) was used. In agreement with Kumar et al. (2020) and Erfurt (2003), IRPL and IR-RL emissions centred around 1.3 eV and 1.41 eV were found, and for the first time at 1.2 eV, were identified, but not all emissions were present in all samples. It is suggested that the $IRPL_{1.41}$ trapping centre and related $IRPL_{1.41}$ and $IR\text{-}RL_{1.41}$ emissions are linked to the presence of K^+ ions on M sites in the crystal. In contrast, the $IRPL_{1.3}$ trapping centre and related emissions were found to be independent of the chemical composition of the crystal. Changes to the distribution of Al^{3+} ions on the Si,Al-framework of the feldspars only had little effect on trap depth and emissions of $IRPL_{1.3}$ and $IRPL_{1.41}$ centres.

It is also shown that $IRPL_{1.3}$ and $IRPL_{1.41}$ emissions reacted differently to optical resetting, and that large residuals found in some samples for the $IRPL_{1.41}$ even after 18 hours in the solar simulator indicate potential challenges for using this signal in luminescence dating.

The results in presented in Chapter 5 support the suggestions by Kumar et al. (2018, 2020) that the two types of IRPL trapping centres represent the same type of crystal defect, and that it is located in two different lattice environments. In addition to the two previously identified IRPL centres, this chapter revealed the presence of a third trapping centre ($IRPL_{1.2}$).

Chapter 6: Exploring sources of variation in thermoluminescence emissions and anomalous fading in alkali feldspars

Whilst the previous two chapters focussed on the electron trapping site and related parameters, this chapter explored the recombination site in feldspars, particularly sources of variation in the blue emission of feldspars and fading rates. The results in this chapter show that the blue luminescence emission is strongest in disordered alkali feldspar specimen and perthites; this emission is relatively weak in K-, Na-feldspar end members, compared to the green-yellow emission. It is suggested that the blue luminescence intensity is proportional to the popula-

tion of Al-O-Al bridges, which increases with Al-Si disorder and that the defect giving rise to blue luminescence is located on an Al-bridging oxygen ion. As a result, fading rates are greater for disordered feldspar specimens and perthites, and highest fading rates are found in macroperthites. The high fading rates in macroperthites are suggested to be caused by defect clustering associated with semi-coherent perthite interfaces.

The research presented in this chapter supports previous suggestions of the blue luminescence emission arising due to a hole trap located on an Al-bridging oxygen ion (Speit und Lehmann, 1982; Finch and Klein, 1999). TL emission spectra paired with anomalous fading measurements of chemically and structurally different alkali feldspars and their end members reveals that the intensity of the blue emission and its fading rate are coupled with the population of Al-O-Al bridges and that the corresponding defect is densest in disordered feldspar (in agreement with e.g. Wintle, 1973; Visocekas and Zink, 1995; Guérin and Visocekas, 2015) and perthites, leading to the conclusion that the only feldspars that might show a non-fading blue luminescence signal are single phase specimens. Unfortunately, due to the nature of feldspar, particularly the process of exsolution, single-phase specimens are rare and thus overcoming fading in feldspars might remain a challenge.

7.2 Research questions and answers

This thesis was aimed at answering multiple research questions, which are hoped to contribute to the further understanding of luminescence production in feldspars.

Question 1: Electron trapping centres

Q.1.1: Where in the feldspar crystal are the defects functioning as electron trapping centres located?

Based on similarities observed for ground and excited state energies of a type of electron trap in feldspars, and based on variations in relaxation energies and trap depth due to changes in the sample chemistry and the structural state of the sample, it is proposed that the electron trapping centres investigated are located on the Si,Al-framework. A comparison of the effect of framework disorder on electron trapping centres and related IRPL and IR-RL emission and on the blue

luminescence emission revealed that the blue emission is affected significantly by disorder of the framework, whilst the electron trapping centres and their emission are only affected to a small extend. Thus, whilst the blue emission is linked to a defect on Al-bridging O ions, such a lattice location seems rather unlikely for the electron trapping centres investigated here. The M site cation occupancy of K^+ ions influences the presence of the $IRPL_{1.41}$ trapping centre, but no effect is seen on the $IRPL_{1.3}$ centre. This may exclude M sites as a potential location for the electron trapping centres investigated.

Q.1.2: What are the physical properties of electron trapping centres? More particular: What are the energies of the ground and excited state of the electron trap and do they vary between samples? If these energies vary between samples, what are the driving forces for changes in energy level?

The explored type of electron trap has an optical trap depth varying between 2 eV and 2.4 eV. The IR resonance peak position, which likely reflects the first excited state of the trap has an energy of ∼1.45 eV. Interestingly, sample-to-sample variations in ground state energies are observed, but the IR resonance peak is invariant between samples. This could either indicate that the IR resonance peak does not correspond to the first excited state of the trap, or that the measured trap depth might not purely reflect the ground state to conduction band energy. Variations in measured trap depth might be related to changes in the width of the sub-conduction band-tail states.

Q.1.3: IRPL, as the result of radiative relaxation within electron trapping centres has been shown to result in emissions at ∼1.3 eV and at ∼1.41 eV. Are both emissions present in all types of structurally and chemically different feldspars, or are these emissions related to specific properties of the material?

IRPL emissions occur at 1.2 eV, 1.3 eV and 1.41 eV. However, not all these emissions are present in all samples, but the same emissions are present in IRPL and IR-RL emission spectra of the same sample. The emission at 1.3 eV is independent of the presence of K^+ ions on M sites in the crystal. In contrast the emission at 1.41 eV is only observed in samples, which contain K^+ ions. Changes to the tetrahedral site occupancy by Al^{3+} ions has only little influence on the IRPL and IR-RL relaxation energies.

Question 2: Band-tail states

Q.2: How far do the band-tail states extend below the conduction band (band-tail states width) and does the width vary between chemically and structurally different feldspars?

The band-tail states widths range from 0.2 eV to 0.8 eV dependent on the sample. Two different methods were used to constrain the width of the band-tail states: One constrains the width of these states accessible from the ground state of the trap (referred to as ΔE). The other method constrains the full width of the sub-conduction band-tail states (E_u). It is shown that for samples with higher K-content, values for ΔE and E_u agree with each other. Larger differences between these two variables are obtained for K-poor feldspars. On this basis it is suggested that the luminescence efficiency could be more variable in K-poor feldspars, due to the potentially varying influence of the band-tail states.

Question 3: Blue luminescence emission and recombination centres

Q.3: In which chemical and structural feldspars is the blue luminescence present and what controls the intensity of this emission?

The blue luminescence is present as a broad emission, overlapping with the green-yellow emission, in perthites. The emission is relatively weak in single-phase feldspars; in this thesis these samples are one single-phase microcline and two single-phase albite specimens. Disorder of Al^{3+} on the framework increases the intensity of the blue luminescence significantly. In accordance with previous studies (Speit and Lehmann, 1982; Finch and Klein, 1999) it is suggested that the blue luminescence arises from a hole trap located on Al-bridging oxygen ions on the framework and that framework disorder increases the number of these hole traps.

Question 4: Anomalous fading of the blue luminescence signal

Q.4.1: Is anomalous fading ubiquitous for the blue luminescence emission in all feldspars?

Fading was observed in all perthitic samples, but to a varying degree. Macroperthite fade more than micro- and cryptoperthite. Single-phase feldspars, such as albite and microcline show only little fading (g-values <1 %/decade) in the experiments in this thesis. Artificially disordered feldspars fade more than their ordered counter parts.

Q.4.2: Can the fading rate be linked to properties of the sample, e.g. the sample chemistry or the structural state?

The fading rate seems to be related to the same parameters that influence the intensity of the blue emission. Fading increases with increased disorder of Al^{3+} on the framework. Additionally, fading seems to be linked to the phase-interfaces in perthites, particularly to semi-coherent interfaces in macroperthites; potentially due to a high density of defects along these interfaces.

7.3 Potential future directions

This thesis contributes to the growing body of methodological work focussing on luminescence production in feldspars. Results presented in this thesis show the importance of combining a thorough sample characterisation with multiple luminescence techniques to obtain further information on the luminescence properties of feldspar. It is hoped that the research presented in this PhD thesis will inspire future research towards a better understanding of luminescence production in feldspar.

Coupling detailed mineralogical characterisation with spatially resolved luminescence

In order to chemically and mineralogically characterise the samples used in this thesis, they were examined using a combination of visible inspection using a hand lens and an optical microscope, X-ray fluorescence (XRF) and X-ray diffraction (XRD). These methods allowed the characterisation of the bulk sample material. However, this thesis has shown that some luminescence emissions in feldspars are influenced by order and disorder of Al^{3+} ions on the silicate framework (Chapters 5 and 6) and by defects located along the phase-interfaces in

perthites (Chapter 6). Whilst XRD only allows the analysis of long-range order-disorder (over multiple unit cells), nuclear magnetic resonance (NMR) would enable the analysis of potential effects of short-range disorder on luminescence intensity and signal stability. Thus, combining luminescence and NMR measurements of Al and Si nuclei could be a potential next step towards further exploring the effect of framework disorder on the blue luminescence emission and fading rates in feldspars.

The potential role of phase-interfaces in perthites on luminescence are so far only explored on the basis that the samples examined were identified as perthites (Chapter 6). Further work could include spatially resolved luminescence on coarsely perthitic feldspars, preferably in rock slices or thin sections. This might allow the identification of possible defect clusters along interfaces. However, high-resolution luminescence measurements on the micrometre to sub-micrometre scale would be necessary to identify such potential defect clusters. Baril (2004) explored spatially resolved luminescence with a resolution of 38 μm, for different IRSL emissions of slices of single crystal feldspar specimens and grain mixtures and found a that luminescence emissions, and thus the related defects, are non-uniformly distributed within the single crystal specimens, indicating potential defect clusters within feldspars. More recent research by Thomsen et al. (2018) has shown that spatially resolved luminescence (resolution of ∼25 µm) of rock slices, combined with major element chemistry can help in identifying luminescent grains and correlate those with a two-dimensional map of the measured elements. Similar observations were made by Sellwood et al. (2019), who investigated spatially resolved (resolution of 140 μm) variations in IRPL signal intensities with depth into a rock. These examples show that spatially resolved luminescence measurements are possible, however, in most cases the resolution is too poor to enable associations of luminescence signal intensities and mineralogical properties, particularly when investigating individual grains (Baril, 2004). In contrast to spatially resolved infrared stimulated (photo)luminescence used by the Baril (2004), Thomsen et al. (2018) and Sellwood et al. (2019) used, research using cathodoluminescence showed luminescence emissions on a higher resolution (sub-μm scale) and with the possibility of examining different luminescence emissions within one measurement (e.g. Götze et al., 1999). Recently, spatially resolved cathodoluminescence measurements have been applied to feldspars, to identify potential sources of the two different IRPL emissions (Kumar et al., 2020a). These different studies show the potential of spatially resolved

luminescence measurements, however, more detailed work using high resolution instrumentation on well-characterised feldspars is necessary to potentially identify crystallographic sources of luminescence in feldspars.

Single or multiple electron trapping centres in feldspars?

As shown in the discussion in Chapter 3, different opinions exist on whether TL, IRSL and IRPL arise from a single type of electron trapping centre or from multiple types of electron trapping centres (e.g. Strickertsson, 1985; Clark and Sanderson, 1994; Baril and Huntley, 2003; Jain and Ankjærgaard, 2011; Andersen et al., 2012; Kumar et al., 2020b). Similarities in trap depth observed for chemically different feldspars in this thesis (Chapter 4 and 5) resulted in the suggestion that the investigated types of electron trapping centre could be located on the Si,Al-framework, since this is similar across the alkali feldspar group (Chapter 4). However, changing the distribution of Al^{3+} ions on the framework by artificially heating the samples had only little effect on the measured trap depths (Chapter 5). Larger differences, particularly regarding the $IRPL_{1.41}$ centre, were observed, for samples with different contents of K^+ ions on M sites (Chapter 5). Potentially indicating that the presence of K^+ ions changes the environment of the this type of trapping centre. The question arises if the same type of defect, but in two different lattice environments classifies still as a single type of electron trap (Kumar et al., 2020) or as two different types of electron trapping centres. Infrared and UV bleaching and pulse anneal experiments of the two different IRPL emissions performed by Kumar et al. (2020b) revealed different optical and thermal stabilities of the $IRPL_{1.3}$ and $IRPL_{1.41}$ emissions. Despite these observations, and primarily based similar lifetimes and dose response curves, Kumar et al. (2020b) inferred that the emissions arise from the same type of defect, but which is located in two different lattice environments. However, since the defect(s) are still unknown, no definite explanation can yet be given, whether the variations in emission energy (1.3 vs. 1.41 eV) as well as the different optical and thermal resetting behaviour, are due to variations in the lattice environment, or if actually different defects (e.g. different vacancies or different impurity ions) are the source of the different IRPL emissions.

Another question arises in regard to the physical meaning of the often broad and rather featureless TL curve of feldspars. It has been proposed that the TL curve represents a distribution of electron traps with different ground state energies (e.g. Strickertsson, 1985; Pagonis et al., 2014), a distribution of dis-

tances between donor and acceptor pairs (Polymeris et al., 2017; Pagonis and Brown, 2019) or different recombination routes (Jain and Ankjærgaard, 2011). Interestingly, TL curves extracted for different emissions of artificially disordered samples showed very similar shapes at all emission wavelengths investigated. The recorded TL spectra of unheated and heated sample material of a perthitic alkali feldspar and a single-phase microcline showed that heating changes the TL curves for all emissions in a similar way for the single-phase microcline sample (Chapter 6). For the perthitic sample similar TL curves were measured for the emissions at 410 nm, 550 nm and 710 nm; the emission at 300 nm shows the same broad peak, but with a different peak temperature, compared to the other emissions. After heating the perthite, the 710 nm and 300 nm showed a similar behaviour, but a different shape compared to the emissions at 410 and 550 nm. This is interesting and has implications for the different suggested physical meanings of the TL curve shape: If the TL curve represents a distribution of ground state energies, then observing similar shapes for different emissions would mean that similar thermal activation energies are needed to result in charge eviction from electron traps and subsequent recombination at different emission centres. If instead the TL curve represents a distribution of donor-acceptor pair differences or different recombination routes, then similarities in TL curve shape for different emissions would indicate that the same distances are present between the defects acting as electron trapping centres and the different recombination centres responsible for different emissions. In light of the observed changes in signal intensity due to artificial disordering of the sample material, this is rather unlikely. Whilst the blue emission increases significantly in intensity due to artificial disordering, other emission intensities are less affected. The increase in blue TL emission intensity was assigned to an increase in recombination centre density (Chapter 6), which would in turn shorten the donor-acceptor distance. It is difficult to evaluate the possibility of the TL curve shape to represent the recombination pathway (excited state tunnelling or band-tail state hopping, cf. Jain and Ankjærgaard, 2011). However, Chapter 6 shows that the fading rate, as a proxy for the tunnelling probability, increases in disordered samples. In such samples the TL curve maximum moves to higher temperatures. This higher temperature TL was suggested to represent band-tail states hopping (Jain and Ankjærgaard, 2011), however, this would mean that excited state tunnelling is less likely in such samples, which is in contrast to the higher fading rates observed.

No conclusion can be reached regarding the physical meaning of the TL curve

shape. Further investigations on TL curve shapes of chemically and structurally different feldspars, preferably also of feldspars whose chemistry and structure has been altered under laboratory conditions (e.g. doping or artificial disordering), are necessary to get further insights into this problem. Potential effects of defect densities could for example be explored by populating different numbers of defects by irradiating a sample to different doses and measuring the TL signal afterwards, ideally for different emissions. If the TL curve shape changes with increasing irradiation doses, then this could help in identifying the driver behind the broad and rather featureless TL curve of feldspars. Should the different emissions respond similarly to the irradiation experiment then this could likely indicated the role of electron trapping centres on the TL curve shape.

Further investigations on the width of the band-tail states

It has been shown that the band-tail states below the conduction band influence luminescence production in feldspars and impact measurements of physical parameters, such as measurements of electron trap depths (see Chapters 4 and 5, as well as Poolton et al., 2009). However, in this thesis the width has only been constrained for chemically different feldspar grain mixtures. Future research could further explore the width of the sub-conduction band-tail states in structurally different feldspars and their influence on charge recombination processes in feldspars. This would be particularly interesting to be performed on the set of samples explored in Chapter 5, as this would help to investigate the sources of variations seen in the ground state energies of these samples (Chapter 5). The measurements of sub-conduction band-tail states width could be achieved by combining the measurements of band-tail states width presented in Chapter 4 at different temperatures (e.g. at cryogenic and room temperature) with luminescence measurements at varying elevated temperatures (e.g. IRSL isothermal holding experiments or IRPL pulse anneal experiments), to evaluate the impact of the band-tail states width on the thermal stability of electrons within the electron trap.

Origin of anomalous fading in feldspars

Fading as the major limitation in luminescence dating of feldspars has been of interest since the 1970s and different mechanisms have been proposed (e.g. Wintle, 1977; Visocekas, 1985; Templer, 1986; Sanderson, 1988). Quantum mechanical tunnelling is the most widely accepted explanation for anomalous fading (Vi-

socekas, 1985). Huntley (2006) linked the fading rate to the density of recombination centres, however, in 1988 Sanderson calculated the density of defects needed to enable proximity models, such as the one proposed by Huntley (2006), and concluded that defect concentrations on the ppm to percent level would be needed. Instead, inferred from the integrated luminescence light sum, Sanderson (1988) proposed that only 107 to 108 charge carriers (such as electrons) are involved in luminescence of samples which contain ∼1020 atoms. Subsequently Sanderson (1988) noted the possibility of defect clusters in feldspars, which could allow tunnelling processes. This suggestion would, however, contradict more recent luminescence models, which are based on a random distribution of defects within the crystal (e.g. Huntley, 2006; Jain et al., 2012). Results presented in Chapter 6 of this thesis proposed that phase-interfaces in perthites influence the rate of fading in feldspars, with the highest fading rates observed in macroperthites in which semi-coherent interfaces might form defect clusters (Chapter 6). These observations from Chapter 6 are in agreement with theoretical calculations by Sanderson (1988). Additionally, high fading rates were also observed in disordered alkali feldspars (Chapter 6). Here one would expect a rather homogeneous distribution of defects due to disordering of the entire crystal. However, it is unknown, if the heating experiment conducted on samples used in Chapter 5 and 6, caused disorder in all unit cells of the samples or if also here defects are clustered in specific areas of the crystal. Spatially resolved luminescence could yet again help in regard to this problem, as defect clusters may be identified when using high resolution luminescence microscopy.

Luminescence properties of plagioclases

This thesis focussed on the alkali feldspar group, but plagioclase feldspar could also help to understand luminescence production in feldspars. Initial experiments on plagioclase samples in the framework of this PhD revealed low IRPL, TL and IRSL emission intensities (data not shown in this thesis) for which reason the samples were not further explored. However, the observation of low luminescence signal intensities is an interesting observation and could be explored further in future research. Luminescence experiments on a large sample set, including a variety of chemically different plagioclase samples could not only help to understand luminescence production in plagioclases, but also in alkali feldspar, as there are structural and chemical differences between the two feldspar solid solutions, for example the different Si:Al ratio on tetrahedral sites and M site occupancy

by Ca^{2+}, compared to K^{+} or Na^{+}.

Previous investigations on fading in plagioclase feldspars (Huntley and Lian, 2006; Huntley et al., 2007) have revealed relationships between fading rates and Ca or Fe content of the samples. This could either indicated an influence of the M site cation occupancy or the charge balancing effect of the framework, by including two Al^{3+} ions, to balance the charge difference introduced by Ca^{2+} ions on M sites. Götze et al (1999) suggested that the blue emission (∼400 nm) is activated by a defect associated with Eu^{2+} ions on M sites. This would suggest a different source of the blue emission in plagioclase feldspars compared to alkali feldspars (Chapter 6).

In plagioclases the yellow-green emission (∼550 nm) has been assigned to Mn^{2+} substituting for Ca^{2+} on M sites (e.g. Telfer and Walker, 1978). However, this emission has also been found in a single-phase microcline sample (Chapter 6), which did not contain any detectable amount of MnO in XRF measurements. Additionally, relaxation lifetimes for Mn^{2+} defects on M sites should be on the ms scale, but shorter lifetimes have been found for this emission (e.g. Clark and Bailiff, 1998; Prasad et al., 2016). Thus further research is needed into potentially different sources for various emissions, their relaxation lifetimes and thermal and athermal stabilities.

References

Andersen, M.T., Jain, M., Tidemann-Lichtenberg, P., 2012. Red-IR stimulated luminescence in K-feldspar: single or multiple trap origin? Journal of Applied Physics 112, 043507.

Baril, M.R., Huntley, D.J., 2003. Optical excitation spectra of trapped electrons in irradiated feldspars. Journal of Physics: Condensed Matter 15, 8011-8027.

Baril, M.R., 2004. CCD imaging of the infra-red stimulated luminescence of feldspars. Radiation Measurements 38, 81-86.

Clark, R.J., Sanderson, D.C.W., 1994. Photostimulated luminescence excitation spectroscopy of feldspars and micas. Radiation Measurements 23, 641-646.

Clark, R.J., Bailiff, I.K., 1998. Fast time-resolved luminescence emission spectroscopy in some feldspars. Radiation Measurements 29, 553-560.

Bøtter-Jensen, L., McKeever, S. W. S., Wintle, A. G., 2003. Optically Stimulated Luminescence Dosimetry. Elsevier, Amsterdam, 375 p.

Erfurt, G., 2003. Infrared luminescence of Pb^{+} centres in potassium-rich feldspars. Physica Status Solidi 200, 429-438.

Finch, A.A., Klein, J., 1999. The causes and petrological significance of cathodoluminescence emissions from alkali feldspars. Contributions to Mineralogy and Petrology 135, 234-243.

Garcia-Guinea, J., Townsend, P.D., Sanchez-Munoz, L., Rojo, J.M., 1999. Ultraviolet-blue ionic luminescence of alkali feldspars from bulk and interfaces. Physics and Chemistry of Minerals 26, 658-667.

Götze, J., Habermann, D., Neuser, R.D., Richter, D.K., 1999. High-resolution spectrometric analysis of rare earth elements-activated cathodoluminescence in feldspar minerals. Chemical Geology 153, 81-91.

Guérin, G., Visocekas, R., 2015. Volcanic feldspars anomalous fading: Evidence for two different mechanisms. Radiation Measurements 81, 218-223.

Huntley, D.J., Lian, O.B., 2006. Some observations on tunnelling of trapped electrons in feldspars and their implications for optical dating. Quaternary Science Reviews 25, 253-2512.

Huntley, D.J., Baril, M.R., Haidar, S., 2007. Tunnelling in plagioclase feldspars. Journal of Physics D: Applied Physics 40, 900-906.

Jain, M., Ankjærgaard, C., 2011. Towards a non-fading signal in feldspar: Insight into charge transport and tunnelling from time-resolved optically stimulated luminescence. Radiation Measurements 46, 292-309.

Jain, M., Guralnik, B., Andersen, M.T., 2012. Stimulated luminescence emission from localized recombination in randomly distributed defects. Journal of Physics: Condensed Matter 24, 385402.

Kars, R.H., Poolton, N.R.J., Jain, M., Ankjærgaard, C., Dorenbos, P., Wallinga, J., 2013. On the trap depth of the IR-sensitive trap in Na- and K-feldspar, Radiation Measurements 59, 103-113.

Krbetschek, M.R., Götze, J., Dietrich, A., Trautmann, T., 1997. Spectral information from minerals relevant for luminescence dating. Radiation Measurements 27, 695-748.

Kumar, R., Kook, M., Murray, A.S., Jain, M., 2018. Towards direct measurement of electrons in metastable states in K-feldspar: Do infrared-photoluminescence and radioluminescence probe the same trap? Radiation Measurements 120, 7-13.

Kumar, R., Martin, L.I.D.J., Poelman, D., Vandenberghe, D., De Grave, J., Kook, M., Jain, M., 2020a. Site-selective mapping of metastable states using electron-beam induced luminescence microscopy. Scientific Reports 10, 15650.

Kumar, R., Kook, M., Jain, M., 2020b. Understanding the metastable states in K-Na aluminosilicates using novel site-selective excitation-emission spectroscopy.

Journal of Physics D: Applied Physics 53, 465301.

Malins, A.E.R., Poolton, N.R.J., Quinn, F.M., Johnsen, O., Denby, P.M., 2004. Luminescence excitation characteristics of Ca, Na and K-aluminosilicates (feldspars) in the stimulation range 5-40 eV: determination of the band gap energies. Journal of Physics D: Applied Physics 37, 1439-1450.

Pagonis, V., Morthekai, P., Kitis, G., 2014. Kinetic analysis of thermoluminescence glow curves in feldspar: evidence for a continuous distribution of energies. Geochronometria 41, 168-177.

Pagonis, V., Brown, N., 2019. On the unchanging shape of thermoluminescence peaks in preheated feldspars: Implications for temperature sensing and thermochronometry. Radiation Measurements 124, 19-28.

Polymeris, G.S., Pagonis, V., Kitis, G., 2017. Thermoluminescence glow curves in preheated feldspar samples: An interpretation based on a random defect distribution. Radiation Measurements 97, 20-27.

Poolton, N.R.J., Bøtter-Jensen, L., Johnsen, O., 1995. Influence on donor electron energies of the chemical composition of K, Na and Ca aluminosilicates. Journal of Physics: Condensed Matter 7, 4751-4762.

Poolton, N.R.J., Wallinga, J., Murray, A.S., Bulur, E., Bøtter-Jensen, L., 2002. Electrons in feldspar I: on the wavefunction of electrons trapped at simple lattice defects. Physics and Chemistry of Minerals 29, 210-216.

Poolton, N.R.J., Kars, R.H., Wallinga, J., Bos, A.J.J., 2009. Direct evidence for the participation of band-tails and excited-state tunneling in the luminescence of irradiated feldspars. Journal of Physics: Condensed Matter 21, 1–10.

Prasad, A.K., Lapp, T., Kook, M., Jain, M., 2016. Probing luminescence centers in Na rich feldspar. Radiation measurements 90, 292-297.

Prasad, A.K., Jain, M., 2018. Dynamics of the deep red Fe^{3+} photoluminescence emission in feldspar. Journal of Luminescence 196, 462-469.

Sanderson, D.C.W., 1988. Fading of thermoluminescence in feldspars: Characteristics and corrections. Nuclear Tracks and Radiation Measurmenets 14, 155-161.

Sellwood, E.L., Guralnik, B., Kook, M., Prasad, A.K., Sohbati, R., Hippe, K., Wallinga, J., Jain, M., 2019. Optical bleaching front in bedrock revealed by spatially-resolved infrared photoluminescence. Scientific Reports 9, 2611.

Speit, B., Lehmann, G., 1982. Radiation Defects in Feldspars. Physics and Chemistry of Minerals 8, 77-82.

Strickertsson, K., The thermoluminescence of potassium feldspars – glow curve characteristics and initial rise measurements. Nuclear Tracks 10, 613-617.

Telfer, D.J., Walker, G., 1978. Ligand field bands of Mn^{2+} and Fe^{3+} luminescence centres and their site occupancy in plagioclase feldspars. Modern geology 6, 199-210.

Thomsen, K.J., Kook, M., Murray, A.S., Jain, M., 2018. Resolving luminescence in spatial and compositional domains. Radiation Measurements 120, 260-266.

Visocekas, R., 1985. Tunnelling radiative recombination in labradorite: its association with anomalous fading of thermoluminescence. Nuclear tracks and Radiation Measurements 10, 521-529.

Visocekas, R., Zink, A., 1995. Tunnelling afterglow and point defects in feldspars. Radiation Effects and Effects in Solids 134, 265-272.

Wintle, A.G., 1973. Anomalous fading of thermoluminescence in minerals samples. Nature 245, 143-145.

Yukihara, E.G., McKeever, S.W.S., 2011. Optically stimulated luminescence: fundamentals and applications. John Wiley and Sons Ltd, Chichester, United Kingdom.

Wintle, A.G., 1973. Anomalous fading of thermoluminescence in mineral sam-

ples. Nature 245, 143-145.